UNIVERSITY OF NOVA GORICA
GRADUATE SCHOOL

NUMERICAL MODELLING OF DENDRITIC SOLIDIFICATION BASED ON PHASE FIELD FORMULATION AND ADAPTIVE MESHLESS SOLUTION PROCEDURE

DISSERTATION

Tadej Dobravec

Mentor: Prof. Dr. Božidar Šarler

Nova Gorica, 2021

UNIVERZA V NOVI GORICI
FAKULTETA ZA PODIPLOMSKI ŠTUDIJ

NUMERIČNO MODELIRANJE DENDRITSKEGA STRJEVANJA NA PODLAGI FORMULACIJE FAZNEGA POLJA IN PRILAGODLJIVEGA BREZMREŽNEGA REŠITVENEGA POSTOPKA

DISERTACIJA

Tadej Dobravec

Mentor: prof. dr. Božidar Šarler

Nova Gorica, 2021

UNIVERSITY OF NOVA GORICA
GRADUATE SCHOOL

Tadej Dobravec, *Numerical modelling of dendritic solidification based on phase field formulation and adaptive meshless solution procedure*, Dissertation, 2021

Acknowledgements

I would like to express my great gratitude to my mentor, Prof. Dr. Božidar Šarler, for his guidance during my doctoral study. I would like to sincerely thank him for his limitless advice and ideas, encouraging words, and careful reading of the dissertation.

Next, I would like to thank my unofficial co-mentor, Dr. Boštjan Mavrič, for his advice and help in the development of the solution procedure and for the careful proofreading of the dissertation.

Special thanks go to my former and current co-workers from the Laboratory for Simulation of Materials and Technology at the Institute of Metals and Technology and from the Laboratory for Fluid Dynamics and Thermodynamics at the Faculty of Mechanical Engineering, especially to Dr. Vanja Hatić, Grega Belšak, Dr. Robert Vertnik, and Dr. Jurij Gregorc. I would also like to thank visiting researcher Mahboubeh Najafi for the interesting discussions regarding the mathematical theory of the meshless methods.

This work was funded by the Slovenian Research Agency (ARRS) in the framework of research program P2-0162, applied research project L2-9246, co-sponsored by the company Štore Steel, and basic research project J2-1718. This work was also funded by the Slovenian Ministry of Education, Science and Sport and the European Structural and Investment Funds in the framework of the project MARTIN.

I would like to thank my loving wife Nataša for her support and encouragement during the writing of this dissertation. A special thanks goes also to my beautiful children, Iva and Oliver, who brought so much happiness to my life and motivated me to finish the dissertation. I would also like to thank my brothers, Blaž and Vid, and my friends.

Finally, I would like to express a special gratitude to my parents, France and Marija, who encouraged me to study physics in the first place and kindly supported me throughout this long journey ...

Numerical modelling of dendritic solidification based on phase field formulation and adaptive meshless solution procedure

Abstract

The main aim of the dissertation is to develop a novel numerical approach for an accurate and computationally efficient modelling of dendritic solidification, which is one of the most commonly observed phenomena in the industrial casting of the metallic alloys. The size and the morphology of dendritic structures as well as the distribution of the solute within them critically effect the mechanical and the electro-chemical properties of the solidified material. The numerical modelling of dendritic solidification can be applied for an in-depth understanding and optimisation of the casting process under various solidification conditions and chemical compositions of the alloy under consideration.

The dendritic solidification of pure materials and dilute multi-component alloys with negligible attachment-kinetics effects is considered in the dissertation. The externally imposed temperature approximation is applied in modelling the solidification of dilute multi-component alloys. The approximation is valid when the diffusion of heat is a few orders of magnitude faster than the diffusion of the solutes – a typical situation in metallic alloys.

The phase field formulation is applied for the modelling of dendritic solidification. The formulation is based on the introduction of the continuous phase field variable that is constant in the bulk of the solid and liquid phases. The phase field variable has a smooth transition from the value denoting the solid phase to the value denoting the liquid phase at the solid-liquid interface over the characteristic interface thickness. A phase field model yields a system of coupled non-linear parabolic partial differential equations that govern the evolution of the phase field and other thermodynamic variables. The thin-interface limit is applied to determine the parameters of the phase field model. The characteristic interface thickness is the only free parameter of the phase field model in the thin-interface limit. The phase field model correctly

captures the underlying physics of solidification when the interface thickness is much smaller than the smallest (or only) diffusion length of the system.

The meshless radial basis function-generated finite-differences (RBF-FD) method is used for the spatial discretisation of the system of partial differential equations. The forward Euler scheme is applied for the temporal discretisation. Fifth-degree polyharmonic splines are used as the shape functions in the RBF-FD method. A second-order accurate RBF-FD method is achieved by augmenting the shape functions with monomials up to the second degree.

The adaptive solution procedure is developed in order to speed-up the calculations. The procedure is based on the quadtree domain decomposition of a rectangular computational domain into rectangular computational sub-domains of different sizes. Each quadtree sub-domain is extended to ensure overlap communication between the neighbouring sub-domains. Each extended quadtree sub-domain has its own regular or scattered distribution of computational nodes in which the RBF-FD method and the forward Euler scheme apply for the discretisation of the system of partial differential equations. The h-adaptivity is ensured by the constant product between the density of the computational nodes and the area of the rectangular quadtree sub-domain. The adaptive solution procedure dynamically ensures the prescribed highest density of the computational nodes at the solid-liquid interface and the lowest-possible density in the bulk of the solid and liquid phases while sustaining a balanced quadtree. The adaptive time-stepping is employed to further speed-up the calculations. The stable time step in the forward Euler scheme depends on the density of the computational nodes; hence, different time steps can be used in quadtree sub-domains with different node densities.

The accuracy and the computational efficiency of the developed adaptive numerical approach is tested for the modelling of the dendritic solidification of undercooled pure melts for arbitrary preferential growth directions. The dendritic growth into an infinite domain is considered. The steady-state growth velocity is compared with the velocity obtained by the microscopic solvability theory. The phase field model is solved first by the basic solution procedure with the uniform node density in the whole computational domain in order to obtain reference numerical data for the assessment of the accuracy and computational efficiency of the adaptive solution procedure. The impact of the size of the local sub-domains in the RBF-FD method by using the regular and

the scattered node distributions is analysed. It turns out that the solution is much more sensitive to the size of a local sub-domain in the case of regular node distribution. The use of the regular node distribution in comparison to the use of the scattered node distribution is much more prone to mesh-induced anisotropy when the growth for arbitrary preferential growth directions is considered. The solution of an identical physical problem is repeated by using the adaptive solution procedure. The accuracy of the solution obtained by the regular node distribution remains almost unchanged. The accuracy of the solution obtained by the scattered node distribution is, however, compromised due to rectangular quadtree domain decomposition. An increase of the ratio between the side length of a quadtree sub-domain and the characteristic spacing between the scattered nodes mitigates the undesirable effect of regularity due to the rectangular domain decomposition. The adaptive solution procedure speeds up the considered calculations by approximately ten times. The speed-up is generally an increasing function of the size of the computational domain and a decreasing function of the length of the solid-liquid interface.

The adaptive numerical approach is further analysed for the modelling of the isothermal dendritic solidification of a supersaturated binary alloy for arbitrary preferential growth directions. The dendritic growth into an infinite domain is considered. The steady-state growth velocity and the concentration in the solid phase are compared to the reference solution from the paper in which the phase field model for solidification in binary alloys was originally developed. It turns out that the solution is even more sensitive to the size of a local sub-domain in the case of a regular node distribution in comparison to the modelling of the solidification of pure materials. The use of the scattered node distribution provides higher accuracy, except for the configuration with thirteen nodes in a local sub-domain by using the regular node distribution where the highest accuracy is observed. An increase of the ratio between the side length of a quadtree sub-domain and the characteristic spacing between the scattered nodes proves once again to be beneficial for the mitigation of the effect of regularity due to rectangular domain decomposition.

The solidification of an Al-1wt.%Cu alloy with a constant cooling rate is

simulated. The growth velocity as a function of time is compared to the reference solution, based on the finite-difference method. The size of a local sub-domain and the regular- or scattered-type of node distribution critically determine the morphology of a dendrite. A quantitative discrepancy between our results and the reference results is observed. The discrepancy is attributed to the difference between the considered partial differential equations, which otherwise describe the same physical problem, and to the use of different numerical methods.

The main originality of the present work is the use of the RBF-FD method for the thorough analysis of the impact of the type of the node distribution and the size of a local sub-domain to the accuracy when the phase field modelling of dendritic solidification for arbitrary preferential growth directions is considered. It is shown how the use of the scattered node distribution reduces the undesirable mesh-induced anisotropy effects, present when the partial differential equations are discretisied on a regular node distribution. The main advantage of the RBF-FD method for the phase field modelling of dendritic growth is the simple discretisation of the partial differential equations on the scattered node distributions. The RBF-FD method is, for the first time, used in combination with the spatial-temporal adaptive solution procedure based on the quadtree domain decomposition. The adaptive solution procedure successfully speeds-up the calculations; however, the advantages of the use of the scattered node distribution are compromised due to the impact of regularity in the quadtree domain decomposition. An increase of the ratio between the side length of a quadtree sub-domain and the characteristic spacing between the scattered nodes mitigates the undesirable effect of the regularity; however, the increase of the ratio reduces the speed-up of the adaptive solution procedure. This turns out to be one of the most serious limitations of the newly developed adaptive numerical approach.

Keywords dendritic solidification, phase field method, meshless methods, RBF-FD, adaptive solution procedure

Numerično modeliranje dendritskega strjevanja na podlagi formulacije faznega polja in prilagodljivega brezmrežnega rešitvenega postopka

Povzetek

Glavni cilj disertacije je razvoj novega numeričnega pristopa za natančno in računsko učinkovito modeliranje dendritskega strjevanja. Dendritsko strjevanje je eden najpogosteje opaženih pojavov pri industrijskem ulivanju kovinskih zlitin. Velikost in morfologija dendritskih struktur ter porazdelitev topljencev v njih ključno vplivajo na mehanske in elektro-kemijske lastnosti strjenega materiala. Numerično modeliranje dendritskega strjevanja se lahko uporablja za poglobljeno razumevanje in optimizacijo procesa ulivanja pri različnih pogojih strjevanja in pri različnih kemijskih sestavah obravnavane zlitine.

V disertaciji obravnavamo dendritsko strjevanje čistih snovi in razredčenih več-sestavinskih zlitin z zanemarljivim učinkom kinetike pripenjanja. Strjevanje razredčenih več-sestavinskih zlitin modeliramo v približku zunanje privzete temperature. Približek velja, kadar je difuzija toplote za nekaj velikostnih razredov hitrejša od difuzije topljencev – tipična situacija v primeru kovinskih zlitin.

Za modeliranje dendritskega strjevanja uporabimo formulacija faznega polja. Formulacija temelji na uvedbi zvezne spremenljivke faznega polja, ki je konstantna v trdni in kapljeviti fazi. Spremenljivka faznega polja ima na medfaznem robu zvezen prehod preko značilne debeline medfaznega roba od vrednosti, ki označuje trdno fazo, do vrednosti, ki označuje kapljevito fazo. Model faznega polja poda sistem sklopljenih nelinearnih paraboličnih parcialnih diferencialnih enačb, ki opisujejo časovni razvoj faznega polja in ostalih termodinamskih spremenljivk. Za določitev parametrov modela faznega polja uporabimo limito tankega medfaznega roba. V limiti tankega medfaznega roba je karakteristična debelina medfaznega roba edini prosti parameter modela faznega polja. Model faznega polja pravilno opiše obravnavano fiziko

strjevanja, kadar je karakteristična debelina medfaznega roba veliko manjša od najmanjše (oziroma edine) difuzijske dolžine v sistemu.

Za krajevno diskretizacijo sistema parcialnih diferencialnih enačb uporabimo brezmrežno metodo z radialnimi baznimi funkcijami generiranih končnih razlik (RBF-KR). Za časovno diskretizacijo uporabimo eksplicitno Eulerjevo shemo. Poliharmonične zlepke petega reda uporabimo kot oblikovne funkcije v metodi RBF-KR. Natančnost drugega reda metode RBF-KR dosežemo z dodajanjem monomov do vključno drugega reda k oblikovnim funkcijam.

Za pospešitev izračunov razvijemo prilagodljiv rešitveni postopek. Postopek temelji na razdelitvi pravokotne računske domene na pravokotne računske pod-domene različnih velikosti z uporabo štiriškega drevesa. Vsaka pod-domena štiriškega drevesa je razširjena, s čimer je zagotovljena komunikacija na podlagi prekrivanja med sosednjimi pod-domenami. Vsaka pod-domena na štiriškem drevesu vsebuje svojo lastno regularno ali razmetano porazdelitev računskih točk, v katerih z uporabo metode RBF-KR in eksplicitne Eulerjeve sheme diskretiziramo sistem parcialnih diferencialnih enačb. h-prilagodljivost je zagotovljena s konstantnim produktom med gostoto računskih točk in površino pravokotne pod-domene štiriškega drevesa. Prilagodljiv rešitveni postopek dinamično zagotavlja predpisano najvišjo gostoto računskih točk na trdno-kapljevitem medfaznem robu in najmanjšo možno gostoto v notranjosti trdne in kapljevite faze, obenem pa vzdržuje uravnoteženo štiriško drevo. Za dodatno pohitritev izračunov uporabimo prilagodljivo časovno korakanje. Stabilen časovni korak v eksplicitni Eulerjevi shemi je odvisen od gostote računskih točk, zaradi česar lahko uporabimo različne časovne korake v pod-domenah štiriškega drevesa z različnimi gostotami točk.

Natančnost in računska učinkovitost razvitega prilagodljivega numeričnega pristopa je najprej preizkušena za modeliranje dendritskega strjevanja podhlajenih čistih talin pri poljubnih preferenčnih smereh rasti. Obravnavamo dendritsko rast v neskončno veliko domeno. Hitrost rasti v ustaljenem stanju primerjamo s hitrostjo pridobljeno v mikroskopski teoriji rešljivosti. Model faznega polja najprej rešimo z osnovnim rešitvenim postopkom z enakomerno gostoto računskih točk v celotni računski domeni z namenom zagotovitve referenčnih numeričnih podatkov, ki jih uporabimo za oceno natančnosti

in računske učinkovitosti prilagodljivega rešitvenega postopka. Preučimo vpliv velikosti lokalnih pod-domen v metodi RBF-KR pri uporabi regularne ali razmetane porazdelitve računskih točk. Izkaže se, da je rešitev v primeru regularne razporeditve računskih točk mnogo bolj občutljiva na izbiro velikosti lokalne pod-domene kot v primeru razmetane porazdelitve. Uporaba regularne porazdelitve računskih točk je v primerjavi z uporabo razmetane porazdelitve računskih točk veliko bolj nagnjena k mrežni anizotropiji pri obravnavi rasti v poljubnih preferenčnih smereh. Analizo identičnega fizikalnega problema ponovimo z uporabo prilagodljivega rešitvenega postopka. Natančnost rešitve, pridobljene z uporabo regularne porazdelitve računskih točk, ostane skorajda nespremenjena. Natančnost rešitve, pridobljene z uporabo razmetane porazdelitve računskih točk, se zmanjša zaradi pravokotne razdelitve računske domene s štiriškim drevesom. Povečava razmerja med dolžino stranice pod-domene štiriškega drevesa in karakteristično razdaljo med razmetanimi računskimi točkami ublaži neželjen vpliv regularnosti, kot posledice pravokotne razdelitve računske domene. Prilagodljiv rešitveni postopek za približno desetkrat pohitri obravnavane izračune. Pohitritev je v splošnem naraščajoča funkcija velikosti računske domene in padajoča funkcija dolžine trdno-kapljevitega medfaznega roba.

Numerična metoda je nadalje analizirana za modeliranje izotermnega dendritskega strjevanja prenasičenih dvo-sestavinskih zlitin pri poljubno usmerjenih preferenčnih smereh rasti. Obravnavamo dendritsko rast v neskončno veliko domeno. Hitrost rasti v ustaljenem stanju in koncentracijo v trdni fazi primerjamo z referenčno rešitvijo iz članka, v katerem je bil prvotno razvit model faznega polja za strjevanje v dvo-sestavinskih zlitinah. Izkaže se, da je rešitev pri uporabi regularne razporeditve računskih točk še bolj občutljiva na velikost računske pod-domene v primerjavi z modeliranjem strjevanja čistih snovi. Uporaba razmetane razporeditve računskih točk zagotavlja višjo natančnost, razen v primeru s trinajstimi točkami v lokalni pod-domeni pri uporabi regularne razporeditve računskih točk, pri katerem je opažena najvišja natančnost. Povečava razmerja med dolžino stranice pod-domene štiriškega drevesa in karakteristično razdaljo med razmetanimi računskimi točkami se ponovno izkaže za dober način blaženja neželjenega vpliva regularnosti, kot posledice pravokotne razdelitve računske domene.

Simuliramo tudi strjevanje zlitine Al-1wt.%Cu pri konstantni hitrosti

ohlajanja. Hitrost rasti kot funkcijo časa primerjamo z referenčno rešitvijo, pridobljeno z metodo končnih razlik. Velikost lokalnih pod-domen in regularni ali razmetani tip porazdelitve računskih točk kritično vplivata na morfologijo dendrita. Opazimo neskladje med našo in referenčno rešitvijo. Razlog za neskladje je razlika v obravnavanih parcialnih diferencialnih enačbah, ki opisujejo drugače identičen fizikalni problem, in uporaba različnih numeričnih metod.

Glavna novost predstavljenega dela je v uporabi metode RBF-KR za temeljito analizo vpliva tipa porazdelitve računskih točk in velikosti lokalnih pod-domen na natančnost pri modeliranju dendritskega strjevanja pri poljubnih preferenčnih smereh rasti z uporabo metode faznega polja. Pokažemo, kako uporaba razmetanih računskih točk zmanjša neželjen vpliv mrežne anizotropije, ki je prisotna, kadar parcialne diferencialne enačbe diskretiziramo na regularni porazdelitvi računskih točk. Glavna prednost metode RBF-KR za modeliranje dendritskega strjevanja je preprosta diskretizacija parcialnih diferencialnih enačb na razmetanih porazdelitvah računskih točk. Metoda RBF-KR je prvič uporabljena v kombinaciji s krajevno-časovnim prilagodljivim rešitvenim postopkom, ki temelji na razdelitvi računske domene s štiriškim drevesom. Prilagodljiv rešitveni postopek uspešno pohitri izračune, vendar se prednosti uporabe razmetane porazdelitve računskih točk zmanjšajo zaradi vpliva regularnosti pri razdelitvi računske domene s štiriškim drevesom. Povečava razmerja med dolžino stranice pod-domene štiriškega drevesa in karakteristično razdaljo med razmetanimi računskimi točkami ublaži neželjen vpliv regularnosti, vendar povečava razmerja zmanjša pohitritev prilagodljivega rešitvenega postopka. Izkaže se, da je to ena izmed najbolj pomembnih omejitev na novo razvitega prilagodljivega numeričnega pristopa.

Ključne besede dendritsko strjevanje, metoda faznega polja, brezmrežne metode, RBF-KR, prilagodljiv rešitveni postopek

Contents

List of Figures

List of Tables

List of Symbols

Acronyms

$\mathrm{ERT}_{\mathrm{ASP}}$	Elapsed real time in the case of adaptive solution procedure
$\mathrm{ERT}_{\mathrm{BSP}}$	Elapsed real time in the case of basic solution procedure
$\mathrm{ERT}_{\mathrm{PREP}}$	Preparation elapsed real time
1-D	One-dimension
2-D	Two-dimensions
3-D	Three-dimensions
ASP	Adaptive solution procedure
BEM	Boundary element method
BSP	Basic solution procedure
ERT	Elapsed real time
FDM	Finite difference method
FEM	Finite element method
FFT	fast Fourier transformation
FVM	Finite volume method
LGK	Lipton-Glicksman-Kurz
LRBFCM	Local radial basis function collocation method
MQ	Multiquadric
MST	Microscopic solvability theory

NUFFT	non-uniform fast Fourier transformation
PA	Point automata
PDE	Partial differential equation
PF	Phase field
PFM	Phase field method
PHS	Polyharmonic splines
RBF	Radial basis function
RBF-FD	Radial basis function-generated finite-differences
RE	Richardson extrapolation
RND	Regular node distribution
SND	Scattered node distribution

Subscripts

$_s$	solid phase
$_\ell$	liquid phase
$_i$	i-th component
$_{ref}$	reference value

Greek Letters

α	solid phase determined by crystal structure of pure solvent A
$\alpha_{\Delta t}$	forward Euler scheme stability parameter
$\bar{\phi}$	order parameter at extremum
β	solid phase determined by crystal structure of pure solute B
β_k	rescaled attachment-kinetic coefficient
$\beta_{k,ref}$	reference rescaled attachment-kinetic coefficient

Δ	initial undercooling
ϵ	measure of the anisotropy of the surface energy
η	general field
Γ	boundary of computational domain
Γ_i	boundary of quadtree sub-domain
Γ_i^*	boundary of extended quadtree sub-domain
$\Gamma_{s\ell}$	Gibbs-Thomson coefficient
κ	curvature of the solid-liquid interface
λ	coupling parameter
μ	chemical potential
μ_k	attachment-kinetic coefficient
ν_m	molar volume
Ω	computational domain
Ω_i	quadtree sub-domain
Ω_i^*	extended quadtree sub-domain
Ω_i^j	child sub-domain of Ω_i
ϕ_0	equilibrium phase field profile
$\phi_{\boldsymbol{G}}$	order parameter of reciprocal lattice vector
ψ_i	phase field convergence parameter
ρ	density
ρ_i	computational node density in Ω_i^*
σ	surface energy
τ	characteristic attachment time

τ_0	constant characteristic attachment time
θ	dimensionless temperature
θ_0	angle between the x-axis and one of the preferential growth directions
Υ	initial supersaturation
φ	general angle
ξ	random variable
${}_l\alpha_i$	interpolation coefficient in sub-domain
${}_l\gamma_i$	value of field or boundary condition
${}_l\Omega$	local sub-domain
${}_l\Phi_i$	radial basis function in sub-domain
${}_l\Psi_i$	radial basis function or monomial in sub-domain

Latin Letters

$\bar{a}$	lattice size
$\bar{D}$	dimensionless diffusivity
$\bar{D}_i$	dimensionless solute diffusivity
$\bar{D}_T$	dimensionless thermal diffusivity
$\bar{D}_{\ell,ref}$	dimensionless reference diffusivity of solute in the liquid phase
$\boldsymbol{g}$	reciprocal lattice vector
$\boldsymbol{I}$	identity matrix
$\boldsymbol{j}$	diffuse mass flux
$\boldsymbol{K}$	thermal conductivity tensor
$\boldsymbol{n}$	normal to the solid-liquid interface

$\boldsymbol{n}'$	normal to the interface in dendrite coordinate system
$\boldsymbol{n}_0$	preferential growth direction
$\boldsymbol{q}$	diffuse heat flux
$\boldsymbol{R}$	rotation matrix
$\boldsymbol{r}_i$	positions, used to calculate l_{tip}
$\boldsymbol{r}_{nuc}$	center of nucleus
$\boldsymbol{v}^*$	growth velocity
Δh	spacing between nodes
Δh_i	characteristic spacing in Ω_i^*
Δh_{min}	minimum characteristic spacing
ΔT	undercooling
Δt	time step
Δt^{mea}	time step between two measurements
Δt_0	reference time step
ΔT_c	curvature undercooling
ΔT_k	kinetic undercooling
Δt_{max}	maximum current time step
$\Delta\mathcal{N}$	level difference
ϵ_4	strength of cubic anisotropy
$\hat{g}$	rescaled tilting function
$\mathcal{B}$	operator of linear boundary condition
$\mathcal{D}$	linear differential operator
$\mathcal{F}$	phenomenological free-energy density

$\mathcal{M}$	ratio between freezing ranges
$\mathcal{N}$	node's depth
$\mathcal{N}_{max}$	maximum level
$\mathcal{N}_{min}$	minimum level
$\mathcal{N}_{parent}$	parent's depth
$\mathcal{N}_{root}$	root's depth
$\mathcal{S}$	seed of pseudo-random numbers
$\tilde{\boldsymbol{q}}$	dimensionless conserved noise flux
$\tilde{F}$	free-energy functional integrand
$\tilde{v}_{tip}$	dimensional growth velocity of a dendrite
A	temperature dependent constant in statical distribution
a	anisotropy of surface energy
a_0, a_2, a_4	coefficients in Taylor series of free energy density
a_0^2, a_2^0, a_4^0	constants in coefficients in Taylor series of free energy density
a_i	anti-trapping parameter
b	value of linear boundary condition
C	concentration (mass fraction)
C^e	equilibrium concentration (mass fraction)
C_0	initial composition in binary alloy
C_s^{steady}	steady-state concentration in the solid-phase
C_{eut}	eutectic concentration
c_p	specific heat
C_{RE}	constant in the Richardson extrapolation

C_{sol}	solubility limit in the solid phase
D	mass diffusivity
d_0	thermal capillary length
d_c	chemical capillary length
D_T	thermal diffusivity
$D_{\ell,ref}$	reference diffusivity of solute in the liquid phase
D_ℓ	diffusivity of solute in the liquid phase
D_{ij}	component of mass diffusivity tensor
D_s	diffusivity of solute in the solid phase
E	internal energy
F	Helmholtz free energy
f	Landau free-energy density
F_u	magnitude of the noise
f_{dw}	double-well potential
F_{eq}	equilibrium bulk free-energy
g	tilting function
h	specific enthalpy
k	thermal conductivity
k_1, k_2	indices of discrete frequencies
k_b	Boltzmann constant
k_0	partition coefficient
L	side length of square Ω
L_i	side length of square Ω_i

L_m	latent heat of melting
L_{int}	length of the solid-liquid interface
l_{tip}	distance between the center and the tip of a dendrite
$l_{tip}^{end,RE}$	final distance between the center and the tip of a dendrite in the Richardson extrapolation
$l_{tip}^{end,RND}$	final distance between the center and the tip of a dendrite obtained on the regular node distribution
l_{tip}^{end}	final distance between the center and the tip of a dendrite
M	mass mobility
m	order of polyharmonic spline
$m_{\Delta t}$	time step restriction parameter
m_ℓ	slope of liquidus line
m_Ω	ratio between the side length of quadtree sub-domain and the characteristic spacing
N	number of nodes in local sub-domain
n	degree of polyharmonic spline
n^*	overlapping parameter
N_b	number of boundary nodes in Ω_i^*
N_c	number of components in multi-component alloy
N_i	number of inner nodes in Ω_i^*
N_p	number of Ω_i domains in Ω
n_x, n_y	components of the normal to the interface
$N_{\mathcal{N}}$	number of sub-domains on level $\mathcal{N}$
N_Ω	number of nodes in computational domain

N_{all}	number of all nodes Ω_i^*
N_{at}	number of atoms
N_{aug}	number of augmentation monomials
N_{cores}	number of processor cores
N_{dim}	number of dimensions
N_{ib}	number of first inner boundary nodes in Ω_i^*
N_{real}	number of realisations of noise
n_{side}	overlapping parameter in direction $side$
P	highest degree of augmentation monomials
R	gas constant
R_c	cooling rate
R_{nuc}	radius of nucleus
R_{tip}	radius of curvature at the tip of a dendrite
S	entropy
T	temperature
T^e	equilibrium temperature
t_0	initial time
T_c	critical temperature
t_i^{mea}	time at which measuring is performed
T_m	melting temperature
$t_{\mathcal{N}}$	simulation time on level $\mathcal{N}$
t_{end}	final simulation time
t_{eq}	equilibrium time

T_{eut}	eutectic temperature
T_{liq}	liquidus temperature
$T_{m,A}$	melting temperature of solvent A
$T_{m,B}$	melting temperature of solute B
t_{start}	initial simulation time
t_{tip}^{max}	time at which maximum growth velocity occurs
U	supersaturation
V	volume
v^*	absolute value of growth velocity
v_{tip}	growth velocity of a dendrite
v_{tip}^{max}	maximum growth velocity
v_{tip}^{steady}	steady-state growth velocity of a dendrite
W	interface thickness
W_0	constant interface thickness
W_ϕ	surface energy parameter
n'_x, n'_y	components of the normal to the interface in dendrite coordinate system
${}_l\boldsymbol{r}$	computational node
${}_lh$	characteristic size of local sub-domain
${}_lp_i$	monomials in sub-domain
${}_lw_k$	finite-difference-like coefficient of differential operator

Superscripts

*	solid-liquid interface

1 Introduction

1.1 Dendritic solidification

Dendritic solidification is one of the most common and consequently most studied phenomenon in the solidification of metallic alloys (Dantzig and Rappaz, 2017; Glicksman, 2011). It attracts the attention of both scientists and engineers due to its interesting pattern selection and useful industrial applications. The term dendrite originates from the Greek word *dendron*, which means tree. Like a tree, a dendrite consists of a primary trunk and side branches, as seen in Fig. 1.1.

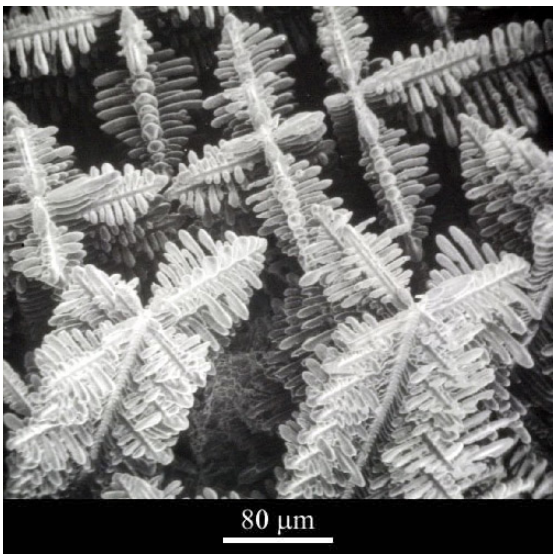

FIGURE 1.1: An image of the 3-D structure of dendrites in a cobalt-samarium-copper alloy, taken with a scanning electron microscope. Author: Prof. Dr. W. Kurz, EPFL, Lausanne, Switzerland. URL: `www.doitpoms.ac.uk/miclib/micrograph_record.php?id=617`.

The microstructure evolution during the casting of metallic alloys has a significant effect on the mechanical, physical, and chemical properties of the solidified material (Campbell, 2003). In the case of dendritic solidification, grain size, interdendritic spacing, and distribution of the solute, for example, critically effect the hardness (Ruan et al., 2016) and corrosion resistance (Goulart et al., 2007) of the material. The prediction of the microstructure's evolution under various casting conditions is therefore crucial for the design and production of high-quality castings for scientific and industrial use.

Dendritic solidification occurs at a thermodynamically metastable state when the material remains in the liquid phase, even below the solid-liquid equilibrium temperature. Such a state is usually achieved in the industrial casting of metallic alloys, which explains why dendritic solidification is so commonly observed. Solidification below the solid-liquid equilibrium temperature is initialized by homogeneous or heterogeneous nucleation (Dantzig and Rappaz, 2017). In the former case, the first solid phase forms spontaneously from a homogeneous melt, while in the latter case, the solidification starts on the domain boundaries or on the particles already present in the melt. The latter type of nucleation usually takes place during the casting of metals.

The stability of the solid-liquid interface during solidification can be analysed by performing a *linear stability analysis* (Dantzig and Rappaz, 2017). The morphological stability of a particle growing by diffusion or heat flow (Mullins and Sekerka, 1963) and stability of a planar interface during solidification of a dilute binary alloy (Mullins and Sekerka, 1964) were originally analysed by Mullins and Sekerka in the 1960s. Comprehensive overview of the linear stability of a solidifying spherical particle and planar front according to the original articles is given in (Dantzig and Rappaz, 2017). In the case of the solidification of a spherical particle growing into a supercooled or supersaturated melt, the stability shows, that the spherical geometry becomes unstable to small perturbations at a certain particle threshold size and that the selected length scale is proportional to the geometric mean of the length scales associated with diffusion and capillarity. In the case of the solidification of a planar interface in a dilute binary alloy, characterised by the constant growth velocity and thermal gradient, three regimes are observed. Firstly, the planar interface is stable if the growth velocity is so low that constitutional supercooling does not occur, i.e., a thermodynamically metastable state is not achieved. Secondly, as the growth

velocity increases, the interface becomes unstable over a range of wavelengths that depend on the growth velocity, and finally, the planar interface is stable again if the growth velocity is above the critical velocity, dependent on the solid-liquid interface energy.

In the case of dendritic solidification, the linear stability analysis only applies during the initial stage of solidification and yields conditions for which the solid-liquid interface becomes unstable. After that, the solid phase starts to grow faster in the preferential growth directions, determined by the crystal structure of the solid phase, due to the anisotropy of the solid-liquid surface energy and the anisotropy of the attachment of atoms on different crystallographic planes. For example, solidified aluminium or copper has a face-centered cubic crystal structure, yielding six equivalent $\langle 100 \rangle$ preferential growth directions, as seen in Fig. 1.1. Faster growth in the preferential growth directions results in the evolution of the solid trunks and side branches, represented in the mathematical analysis by the so-called *needle crystal shape* (Dantzig and Rappaz, 2017), i.e., a nearly parabolic shape with a small but important correction at the tip.

The heat-diffusion equation during the growth of a parabola in 2-D and the paraboloid of revolution in 3-D into an infinite supercooled pure melt when the solid-liquid interface is held at the melting temperature was first solved by Ivantsov (Ivantsov, 1947) and later by Horvay and Cahn (Horvay and Cahn, 1961). The solution yields the result $v^* R_{tip} = const.$, where v^* and R_{tip} stand for the growth velocity and the radius of curvature at the tip of a dendrite, respectively. The result suggests an infinite number of pairs (v^*, R_{tip}) for a given supercooling ΔT. This contradicts the experiments (Glicksman, 1984) which show that a unique pair (v^*, R_{tip}) is always selected at a given ΔT and that as ΔT increases, v^* increases and R_{tip} decreases.

In contrast to the Ivantsov solution, which does not consider any curvature effects, Temkin (Temkin, 1960) and later Nash and Glicksman (Nash and Glicksman, 1974) also took into account the Gibbs-Thomson condition with an isotropic surface energy at the solid-liquid interface; however, their results for v^* and R_{tip} were several orders of magnitude far from the experimental results. Oldfield (Oldfield, 1973) performed the first numerical simulation of the growth of a parabolic dendrite and found that a needle shape with the applied Gibbs-Thomson condition is unstable. He proposed a heuristic stability

condition $v^* R_{tip}^2 = const.$; however, the selection of the constant in the relation remained an open question. Langer and Muller-Krumbhaar (Langer and Müller-Krumbhaar, 1978) also showed that growing a needle crystal with a finite isotropic surface energy is unstable. They set the constant in the relation $v^* R_{tip}^2 = const.$ in such a way that R_{tip} was equal to the minimum wavelength in the stability analysis of a planar front (Mullins and Sekerka, 1964). This selection is known as the *marginal stability criterion* and produces results that are actually very close to the experimental values observed by Glicksman.

After that approximate models for dendrite growth were developed independently by two research groups (Ben-Jacob et al., 1983; Ben-Jacob et al., 1984; Brower et al., 1984; Kessler and Levine, 1988). They both found stable solutions only if the surface energy is anisotropic. The models yield a finite number of pairs (v^*, R_{tip}) where only the solution with the highest v^* is stable. The models also yield the relation $v^* R_{tip}^2 = const.$ similar to the one in the marginal stability criterion. Kessler and Levine (Kessler and Levine, 1986) performed a numerical stability analysis of a model incorporating a full diffusion equation and an anisotropic surface energy. In their solution, the calculated shape of a dendrite can generally have a cusp at the tip. The requirement for the smoothness of the solid-liquid interface at the tip of a dendrite is known as the *microscopic solvability condition*. Using an iterative procedure, a unique solution (v^*, R_{tip}) is found when the condition is fulfilled. Numerical experiments according to the theory yield the result $v^* R_{tip}^2 = C(\epsilon)$, where ϵ stands for the measure of the anisotropy of the surface energy. Saito et al. (Saito et al., 1988) and Barbieri and Langer (Barbieri and Langer, 1989) showed that $C(\epsilon)$ is roughly proportional to ϵ in the framework of the microscopic solvability theory; however, this results has not been yet validated experimentally.

An example of an approximate analytical model for the growth of a needle crystal in binary alloys, incorporating the heat and solute transport, is the famous LGK model (Lipton et al., 1984; Lipton et al., 1987) proposed in the 1980s by Lipton, Glicksman and Kurz. The model is capable of predicting a unique pair (v^*, R_{tip}) for a given supercooling ΔT and initial composition C_0. In the model, the Ivantsov solution (Ivantsov, 1947) is used for the temperature and concentration profiles in the liquid phase. The supercooling of the solid-liquid interface at the tip of a dendrite ΔT takes into account the

thermal, constitutional, and curvature effects. The marginal stability selection criterion (Langer and Müller-Krumbhaar, 1978) is used for the estimation of R_{tip}. The model yields a system of two coupled non-linear equations that can be iteratively solved to obtain (v^*, R_{tip}) at a given $(\Delta T, C_0)$. A significant simplification (Dantzig and Rappaz, 2017) can be made in the very common case of negligible thermal and curvature effects, yielding $v^* \propto \Delta T^{5/2}/C_0^{3/2}$ and $R_{tip} \propto C_0^{1/4}/\Delta T^{5/4}$.

The literature overview from this sub-section only briefly describes the history of modelling of dendritic solidification. A comprehensive overview can be found in the recently published articles on modelling of dendrite growth from 1700 to 2000 (Kurz et al., 2019) and from 2001 to 2018 (Kurz et al., 2021). Especially in the modelling of dendrite growth during rapid solidification with and without the consideration of convective flow, a significant contribution has been made by Peter Galenko and his co-workers (Galenko and Sobolev, 1997; Galenko and Danilov, 1999; Galenko et al., 2017; Galenko et al., 2007).

1.2 Phase field modelling

In the 1980s the phase field method (PFM) was introduced in the field of modelling free-boundary problems in materials science (Chen, 2002; Boettinger et al., 2002). There are two main reasons why the PFM became the method of choice for the modelling of this phenomenon. Firstly, it has fundamental origins in thermodynamics, and secondly, it does not require explicit tracking of the interfaces between the phases in contrast to the analytical approximate models reviewed in the previous section. The main hallmark of the PFM is the introduction of a phase field (PF) or order parameter, a continuous field representing phases (Provatas and Elder, 2010). The PF is constant in the bulk of each phase and varies across the thin boundary layer between the phases, as schematically shown in Fig. 1.2.

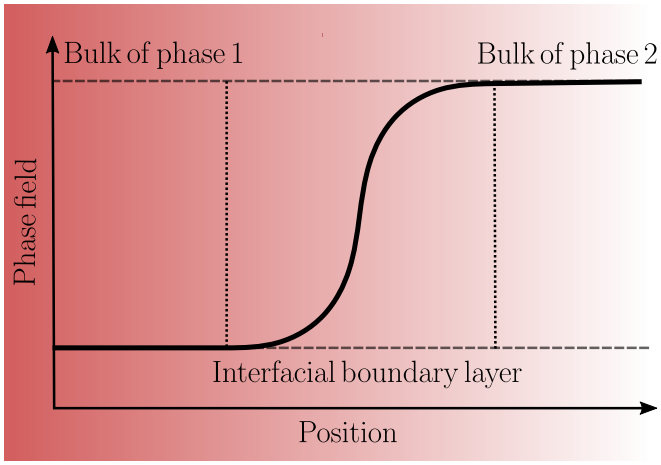

FIGURE 1.2: Representation of the solid-liquid interface by the PFM.

From the point of view of condensed-matter physics, the PF can be seen as a degree of crystallinity or atomic order in a phase, while the thin boundary layer represents an atomically diffuse interface. From the point of view of mathematical modelling, the PF represents a tool for describing the time evolution of phases as the tracking of an exact position for the interfaces between phases is no longer necessary. The link between the PF and other relevant thermodynamics variables, e.g., temperature, solute concentration, etc., is given by the free-energy functional (Provatas and Elder, 2010). A minimisation of the functional yields a set of partial differential equations (PDEs) describing the movement of interfaces between the phases and the heat and mass transfer.

The name *phase field model* was introduced in the realm of modelling free-boundary problems in material science in the 1980s, when scientists modelling the solidification in a pure melt were trying to avoid the explicit tracking of the solid-liquid interface by introducing a diffuse interface (Fix, 1982; Collins and Levine, 1985; Langer, 1986). The idea was not new; nearly a century ago, Van der Waals proposed a diffuse-interface description of a density field in a liquid-gas system (Rowlinson, 1979). A similar approach was used in the magnetic domain theory by Landau and Lifshitz in 1935 (Haar, 2013). In 1958, Cahn and Hilliard introduced the diffuse-interface theory (Cahn and Hilliard, 1958), which was first used in two famous diffuse-interface models of dynamics. In the first, the dynamics of the phases with a conserved order parameter is considered in the work on spinodal decomposition by Cahn from

1961 (Cahn, 1961). In the second, the dynamics of a non-conserved long-range order parameter is studied in the work of Allen and Cahn from 1977 (Cahn and Allen, 1977). Both models with added thermal noise were also studied in the work of Hohenberg and Halperin on critical dynamics from 1977 (Hohenberg and Halperin, 1977).

One of the most important issues in the modelling of microstructure evolution by the PFM is the appropriate selection of the free PF parameters and the interpolation functions in order to correctly capture the underlying physics. In the case of solidification in pure materials, the parameters have to be selected in a way to properly describe the kinetics of the Stefan problem (Šarler, 1995). This was first achieved by performing the so-called *sharp-interface limit* of the PF equations (Caginalp, 1989), which assumes that the interface thickness is small compared to the thermal capillary length. The limit experiences two major drawbacks. The incapability of simulating the important physical limit when kinetic supercooling in the Stefan Problem can be neglected and the requirement for very small interface widths and, consequently, time-consuming simulations on large computational domains. Both problems were overcome by the derivation of the so-called *thin-interface limit* of the PF equations (Karma and Rappel, 1998). The limit assumes that the interface thickness is small compared to the diffusion length and the radius of curvature, but can be of the same order as the thermal capillary length. This is a huge advantage as far as numerical efficiency is concerned (Karma and Rappel, 1998).

The formalism of the thin-interface limit, originally developed for the PF model describing solidification in pure materials (Karma and Rappel, 1998), has been successfully applied in other PF models, e.g., in the PF models describing the solidification in dilute binary alloys (Karma, 2001; Echebarria et al., 2004), multi-component alloys with arbitrary kinetics (Kim, 2007), and dilute multi-component alloys (Ohno, 2012). In the models, describing the solidification in alloys, it is, however, impossible to correctly capture the underlying physics solely by minimisation of the free-energy functional of the system and the appropriate selection of the free parameters and interpolation functions. The correct results are only obtained if so-called *anti-trapping current* (Karma, 2001) is added to the diffusion equation, compensating for the non-physical effects due to the artificially enlarged interface thickness at the thin-interface limit.

Besides the PF modelling of solidification (Dong et al., 2017), the PFM has been successfully applied in other research areas, e.g., for modelling solid-state phase transformations (Zhu et al., 2019; Duong et al., 2020; Kovačević and Šarler, 2005), coarsening and grain growth (Bhaskar, 2018; Perumal et al., 2019), crack propagation (Lu et al., 2019; Moshkelgosha and Mamivand, 2020), and two-phase flow (Talat et al., 2018a; Talat et al., 2018b).

Quantitative PF simulations of experimentally relevant situations are to a great extent possible due to rapid growth of computational capabilities (Karma and Tourret, 2016; Dong et al., 2017). A large number of different computational approaches have been developed in the last 20 years, e.g., 1. adaptive mesh refinement (Provatas et al., 1998; Greenwood et al., 2018), 2. parallel simulations using graphic processing units (Shimokawabe et al., 2011), 3. hybrid finite-difference and random-walk algorithms (Plapp and Karma, 2000), 4. implicit time-stepping and multi-grid approaches (Guo et al., 2012; Bollada et al., 2015), and 5. up-scaling techniques (Berghoff et al., 2013). However, the development of new techniques for an accurate and computationally effective solution of PF models is always welcome and represents the focus of this dissertation.

1.3 Meshless methods

A PF model yields a system of PDEs that have to be numerically solved in order to predict a microstructure's evolution. This is usually done with numerical models based on the finite difference method (FDM) (Trefethen, 1996), the finite volume method (FVM) (Versteeg and Malalasekera, 2007), or the finite element method (FEM) (Lewis et al., 1996). These methods are characterised as *mesh-based* methods since they require a predefined mesh for the domain discretisation. They represent a powerful tool for the solution of PDEs and have been successfully used in the vast majority of scientific and engineering applications. However, the mesh-based methods experience some drawbacks (Liu and Gu, 2005), e.g., only a regular node distribution can be used in the FDM and polygonisation of the computational domain is required in the case of the FVM or the FEM.

Meshless methods (Atluri, 2004; Atluri and Shen, 2002; Liu, 2009; Li and Liu, 2004; Liu and Gu, 2005; Li and Mulay, 2013; Fasshauer, 2007; Buhmann,

2003; Wendland, 2010; Dyn et al., 2001; Chen et al., 2006; Chen et al., 2014; Belinha, 2014; Sladek and Sladek, 2006; Šarler and Atluri, 2010; Atluri and Sladek, 2009; Leitao et al., 2007; Griebel and Schweitzer, 2017) represent an alternative to the mesh-based methods in a way that a predefined mesh is not a prerequisite for the discretisation of the computational domain. The domain is represented solely by the computational nodes where the information regarding the relationship between them is not required for the approximation of the field variables. The difference between the representations of the computational domain by the mesh-based and meshless approaches is schematically shown in Fig. 1.3. Some advantages of the meshless methods in comparison to the mesh-based methods are (Nguyen et al., 2008) simpler development of h-adaptive algorithms, easier treatment of free-boundary problems, no mesh-alignment sensitivity, and higher accuracy. Also, the expensive creation of the mesh is not necessary in the meshless methods. Naturally, the meshless methods also experience some drawbacks in comparison to the mesh-based methods, e.g., the treatment of essential boundary conditions can be problematic and computational efficiency is, in general, lower in comparison to mesh-based methods. The meshless methods can be classified (Liu and Gu, 2005) according to the used formulation procedures, function approximation or interpolation techniques, and the domain representation.

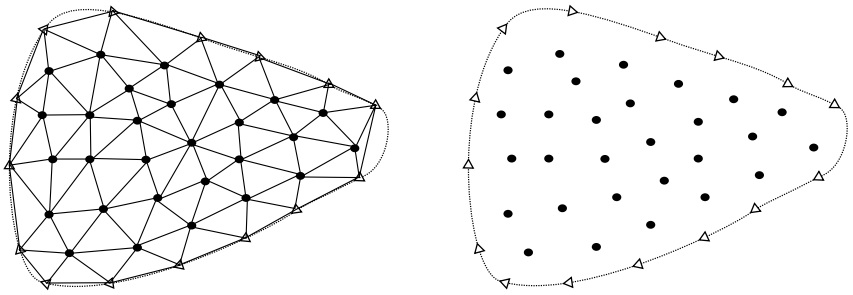

FIGURE 1.3: An example of mesh-based (left) and meshless (right) representations of the computational domain. The boundary of the computational domain is marked by a dotted line. Circles and triangles represent the inner and boundary computational nodes, respectively.

According to the used formulation procedure we distinguish the meshless *weak-form* methods, the meshless *strong-form* methods, and the meshless methods based on the combination of weak- and strong-form techniques.

Examples of the meshless weak-form methods are the element-free Galerkin method (Belytschko et al., 1994), the radial point-interpolation method (Liu and Gu, 2001a), the reproducing kernel particle method (Liu et al., 1995), the meshless local Petrov-Galerkin (Atluri, 2004), etc. In the group of the meshless strong-form methods, also known as the meshless *collocation* methods, we find the general finite-difference method (Perrone and Kao, 1975; Liszka and Orkisz, 1980), the meshless-collocation method (Kansa, 1990a; Kansa, 1990b), the finite-point method (Oñate et al., 1996), the diffusive-approximate method (Sadat and Prax, 1996; Hatić et al., 2018; Hatić et al., 2019; Talat et al., 2018a; Reuther et al., 2012; Reuther and Rettenmayr, 2014), the radial basis function-generated finite-differences (RBF-FD) method (Flyer et al., 2016; Bayona et al., 2017; Dobravec et al., 2020) also known as the local radial basis function collocation method (LRBFCM) (Šarler and Vertnik, 2006; Kosec and Šarler, 2011; Vertnik et al., 2019; Mramor et al., 2014; Hanoglu and Šarler, 2018; Mavrič and Šarler, 2015), etc. The meshless methods based on the combination of weak- and strong-form formulations are the meshless weak-strong method (Liu and Gu, 2003) and the smoothed particle hydrodynamics methods (Liu and Liu, 2003).

According to the function approximation or interpolation techniques we distinguish meshless methods based on the *moving least squares* approximation, *integral representation method* for approximation, and *point interpolation method*. The moving least-squares approximation is used, for instance, in the the element-free Galerkin method (Belytschko et al., 1994) and the meshless local Petrov-Galerkin method (Atluri and Zhu, 1998). An example of meshless methods based on the integral representation method for the function approximation is the smoothed particle hydrodynamics method (Liu and Liu, 2003). Examples of the methods based on the point-interpolation methods are the point-interpolation method (Liu and Gu, 2001b) and the meshless-collocation method (Kansa, 1990a; Kansa, 1990b).

The final classification of the meshless methods can be made according to the domain representation. In this classification, we differ between the domain-type and boundary-type meshless methods. All the previous paragraphs mentioned methods that are the domain-type methods, since the whole computational domain is represented by the computational nodes. In the case

of the boundary-type methods, the computational nodes only have to be distributed on the boundary of the computational domain. The same distinction can be made in the case of mesh-based methods between the FDM, FVM, and FEM, on the one hand, and the boundary element method (BEM) (Wrobel and Aliabadi, 2002), on the other. Examples of boundary-type meshless methods are the boundary-node method (Mukherjee and Mukherjee, 1997), the local boundary integral equation method (Zhu et al., 1998), the boundary point interpolation method (Gu and Liu, 2002), the boundary radial point interpolation method (Gu and Liu, 2003), non-singular method of fundamental solutions (Liu and Šarler, 2018), method of regularized sources (Wang et al., 2016), etc.

1.3.1 RBF-FD method

In the dissertation, the meshless RBF-FD method (Flyer et al., 2016; Bayona et al., 2017; Dobravec et al., 2020) is applied for the solution of the PF models for dendritic solidification. In the literature, the RBF-FD is also known as the LRBFCM method (Šarler and Vertnik, 2006). The method is based on the strong-form meshless collocation method originally proposed by Kansa (Kansa, 1990a; Kansa, 1990b). He used interpolation with radial basis functions (RBFs) for the evaluation of differential operators for the first time and successfully applied his approach for the solution of parabolic, hyperbolic and elliptic PDEs. For some choices of RBFs, augmentation with monomials (Fasshauer, 2007) is additionally required to ensure well-posed interpolation matrices in the method. The interpolation with RBFs proved to be very accurate, however, Kansa's method uses all the computational nodes in the domain to construct the interpolation, which results in dense and ill-conditioned interpolation matrices. Consequently, the method cannot be used to solve large-scale physical problems.

Due to very good interpolation properties, RBFs were used for interpolation in the meshless weak-form local radial point interpolation method (Liu and Gu, 2001a). The idea of a local approach was shortly after that also applied in the strong-form meshless methods (Tolstykh and Shirobokov, 2003; Lee et al., 2003; Liu et al., 2002; Šarler and Vertnik, 2006) since the construction of a local interpolation effectively mitigates the problems with dense matrices

and ill-conditioning in Kansa's original method. The local LRBFCM/RBF-FD approach has been successfully applied to many different scientific and engineering problems, e.g., turbulent combined forced and natural convection problems (Vertnik and Šarler, 2011), simulation of laminar backward facing step flow under a magnetic field (Mramor et al., 2014), simulation of macrosegregation (Kosec and Šarler, 2014), h-adaptive solution of partial differential equations (Kosec and Šarler, 2011), r-adaptive solution of PF model for dissolution of primary particles in binary aluminium alloys (Kovačević and Šarler, 2005), simulation of linear and transient thermo-elasticity (Mavrič and Šarler, 2015; Mavrič and Šarler, 2017), multi-pass hot-rolling simulation (Hanoglu and Šarler, 2018), the numerical simulation of the PF crystal models (Dehghan and Mohammadi, 2016), solution of multi-dimensional Cahn-Hilliard, Swift-Hohenberg and PF crystal equations (Dehghan and Abbaszadeh, 2017), and PF modelling of dendritic solidification (Dobravec et al., 2020).

In the Kansa's original method (Kansa, 1990a) and in many application of the RBF-FD method to different physical problems (Kosec and Šarler, 2011; Vertnik and Šarler, 2011; Mavrič and Šarler, 2015; Hanoglu and Šarler, 2018; Mramor et al., 2014), multiquadrics (MQs) are used as RBFs. The use of MQs produces very good results; however, a MQ introduces a free shape parameter, which greatly influences the performance of the method. There are several techniques for the optimal shape-parameter search (Rippa, 1999; Mavrič, 2017). The search has to be performed for each computational node independently, which can lead to long computational times, especially for large engineering problems.

In recent years, shape parameter-free polyharmonic splines (PHS) have gained popularity as RBFs (Flyer et al., 2016; Bayona et al., 2017) in the RBF-FD methods. Flyer and co-workers (Flyer et al., 2016; Bayona et al., 2017) have recently shown that not PHS or any other RBFs, but the highest-order monomial controls the h-convergence of the RBF-FD method. Influenced by the results of Flyer and co-workers, an interpolation with PHS as RBFs, augmented with monomials up to the selected order of h-convergence, is also used in the RBF-FD method in this dissertation.

1.4 Adaptive solution procedure

The idea behind the adaptive solution procedure is to develop an algorithm that dynamically changes the computational nodes during a simulation in order to reduce the overall computational work and memory usage while sustaining the accuracy of the solution. Several different adaptive techniques have been developed in the last few decades for the speed-up of the solution of PDEs. One possibility is an r-adaptive algorithm (Kovačević and Šarler, 2005) where the positions of the computational nodes in the domain vary in order to fulfil the refinement criteria while the total number of nodes remains unchanged. Another one is an h-adaptive algorithm (Kosec and Šarler, 2011; Dobravec et al., 2017a), where the nodes are added or removed from the computational domain. The pioneering work on the adaptive mesh-refinement techniques is the algorithm by Berger and co-workers (Berger and Oliger, 1984; Berger and Colella, 1989), which is in its original form nowadays known as the block-structured adaptive mesh refinement (Dubey et al., 2014) and is used for the solution of various physical problems in astrophysics, cosmology, general relativity, combustion, climate science, subsurface flow, turbulence, fluid–structure interactions, plasma physics, and particle accelerators.

Many different adaptive techniques have been applied for the solution of PF models (Provatas et al., 1999; Provatas et al., 1998; Guo and Xiong, 2015; Bollada et al., 2015; Li and Kim, 2012; Greenwood et al., 2018). In the framework of the present dissertation, a novel 2-D h-adaptive algorithm based on the work by Greenwood et al. (Greenwood et al., 2018) is developed. The algorithm can be seen as an adaptive domain decomposition (Mathew, 2008) where the computational domain is dynamically decomposed into sub-domains of different size. The constant product between the area and the node density of a sub-domain yields an h-adaptivity. The algorithm dynamically ensures that the evolving solid-liquid interface always lies in the sub-domains with the highest node density. In contrast to the algorithm by Greenwood et al. (Greenwood et al., 2018), the RBF-FD method is used instead of the FDM for the spatial discretisation of the PDEs. This selection provides enhanced flexibility regarding the shape of a sub-domain and the type of the node distribution in it.

1.5 Goals

The main goal of the dissertation is to apply and thoroughly analyse the RBF-FD method for the spatial discretisation of PDEs arising from the PF models while using a simple forward Euler scheme for the temporal discretisation (Dobravec et al., 2020). The method is applied for the solution of PF models describing solidification in pure materials (Karma and Rappel, 1998), in dilute binary alloys (Echebarria et al., 2004), and in an Al-1wt.%Cu alloy with a constant cooling rate (Boukellal et al., 2018). Special emphasis is given to the issue of *mesh-induced anisotropy* (Mullis, 2006), which is present in the solution of the PF models using mesh-based methods. The RBF-FD method can be used on regular and scattered node distributions and therefore provides the perfect tool to assess the influence of the arrangement of the node distribution on the anisotropy of the solution of PDEs.

The developed numerical model is 2-D, however, the extension to 3-D is straightforward and planned for the continuation of the research, presented herein. A thorough analysis and testing of the newly developed numerical method in 2-D before moving onto the highly computationally challenging 3-D cases is standard procedure for mesh-based and meshless methods. For the same reason, simple regular domains are used for the testing of the method, although the method can be, in principal, used for complex domains, at least in 2-D. The use of regular computational domains for the PF simulations of dendritic solidification also makes sense from the practical point of view. Even with the use of the fastest supercomputers (Shimokawabe et al., 2011), it is impossible to perform such simulations in the whole computational domain with complex domain boundaries, e.g., during the direct-chill casting of aluminium alloys (Šarler et al., 2019). The PF models apply on much smaller scales, for which the complexity of the domain boundary is not relevant. Although straightforward coping with complex-shaped domains is one of the main advantages and reasons for the use of meshless methods, we apply the meshless RBF-FD method due to its high accuracy and freedom in the selection of the type of the node distribution.

Another important goal of the dissertation is the development of an h-adaptive solution procedure (Greenwood et al., 2018) in order to speed-up the calculations and to reduce the memory usage. In the solution procedure, the

computational domain is dynamically decomposed into sub-domains of different sizes where the product between the node density and the size is kept constant to ensure h-adaptivity. Since regular domains are used in the model, the decomposition can be easily performed by the quadtree (Dobravec et al., 2017a), which can be in 3-D replaced by the octree (Greenwood et al., 2018) algorithm.

The developed model can be incorporated into the simulation system for the direct-chill casting of aluminium alloys (Šarler et al., 2019) or continuous casting of steel (Vertnik et al., 2019) for the prediction of dendritic morphology and micro-segregation. In our previous work (Dobravec et al., 2017b; Šarler et al., 2019), the morphology of dendrites was predicted on the millimetre scale using a Point Automata (PA) model (Lorbiecka and Šarler, 2010). The model, developed in the framework of the doctoral dissertation, is able to resolve the dendritic morphology on the micrometre scale, providing a useful numerical tool for the precise prediction of the microstructure's evolution. With such a model, the impact of the process parameters on the quality of the solidified alloys can be assessed. Also, the free parameters of the computationally more effective PA model can be calibrated with the use of the newly developed PF model.

2 Physical model

Solidification is mathematically represented by the transport equations of the relevant thermodynamic variables and the appropriate boundary conditions at the solid-liquid interface. The basic balance is used to derive those equations, i.e., the change of any quantity in a volume is equal to the sum of the flux of a quantity through the surface of a volume and the production of the quantity in a volume. Consequently, the equations are known as *balance equations*. In the dissertation, only the diffusion of quantities is considered in the balance equations. The balance equations for the energy and solute during solidification are also known as *Stefan problems* (Šarler, 1995) in honour of the Slovenian physicist Jožef Stefan who made several pioneering contributions in solid-liquid phase-change research in the 19th century.

When the transport equations are solved, the exact position of the solid-liquid interface, at which the boundary conditions apply, has to be known. However, the position of the solid-liquid interface is determined by solving the transport equations. This problem is known as the *free-boundary problem* and can be analytically solved only for very simple cases (Dantzig and Rappaz, 2017), e.g., constant growth of a sphere, planar front or paraboloid. The direct numerical solution of the balance equations in the case of realistic complex shapes of the solid-liquid interface, e.g., during the growth of highly branched dendrites, is very challenging, especially in 3-D. To overcome this problem, a diffuse-interface PFM (Chen, 2002; Boettinger et al., 2002) was introduced in the 1980s for the solution of the free-boundary problems. In the PFM, the tracking of the exact position of the solid-liquid interface is avoided at the expense of an extra transport equation for the continuous PF variable, which is coupled to the appropriately modified transport equations.

In the chapter, the balance equations for the energy and solute are first presented in Section 2.1. In Section 2.2, the origin and the basics of the PFM are given. In section 2.3, the diffuse-interface PF versions of the balance equations from Section 2.1 are presented. The diffuse-interface PF version of the energy

balance equations is presented for the case of solidification from pure melts. The diffuse-interface PF version of the solute balance equations is presented in the case of solidification of dilute multi-component alloys in the frozen temperature approximation, i.e., externally imposed temperature approximation.

In the PF models for modelling of solidification of *dilute multi-component alloys* (Ohno, 2012; Sun et al., 2019), only the interaction between solvent and solutes is considered while the interaction between solutes is neglected. Such approximation is reasonable for dilute alloys with small amount of solutes (Sun et al., 2019). The multi-component system is divided into several binary system, hence, the model could be also called the *multi-binary* PF model. The model for dilute multi-component alloys (Ohno, 2012) is constructed in the same manner as the model for dilute binary alloys (Karma, 2001; Echebarria et al., 2004) which is extensively used in the PF community (Tourret et al., 2017; Greenwood et al., 2018; Bollada et al., 2015; Boukellal et al., 2018) for the modelling of solidification of dilute binary alloys. In the dilute version of the free energy of a phase, the contributions of different alloying elements are simply summed (see Section 2.3). We are well aware that the PF model should be used with caution only for dilute multi-component alloys since it only considers the contributions of melting point depression of different alloying elements. Solidification of general multi-component alloys should be considered with much more complex PF models (Kim, 2007; Nestler and Choudhury, 2011; Nestler et al., 2005) based on CALculation of PHAse Diagram (CALPHAD) thermodynamic database.

In the *frozen temperature approximation*, the infinitely fast diffusivity of the heat is assumed in relation to the species diffusion, hence, the temperature can be considered as an input parameter. The approximation can be applied if the diffusivity of the heat is few orders of magnitude faster than the diffusivity of the solute, e.g., in steels and aluminium alloys, which is the foreseen application of the present work.

2.1 Balance equations

2.1.1 Energy balance

The heat diffusion equation takes into account the change of the energy in a system due to the diffusion of heat into and out of a system

$$\frac{\partial(\rho h)}{\partial t} = -\nabla \cdot \boldsymbol{q}, \tag{2.1}$$

where ρ, h, and $\boldsymbol{q}$ stand for the density, the specific enthalpy, and the heat flux, respectively. The convective effects are not taken into account in the whole work. The heat flux is given by Fourier's Law

$$\boldsymbol{q} = -\boldsymbol{K} \cdot \nabla T, \tag{2.2}$$

where $\boldsymbol{K}$ and T are the thermal conductivity tensor and the temperature, respectively. In the case of isotropic materials, where $\boldsymbol{K} = k\boldsymbol{I}$ and k and $\boldsymbol{I}$ are the thermal conductivity and the identity matrix, respectively, the combination of Eqs. (2.1) and (2.2) yields

$$\frac{\partial(\rho h)}{\partial t} = \nabla \cdot (k \nabla T). \tag{2.3}$$

Conditions at the solid-liquid interface

The boundary condition for the heat flux at the solid-liquid interface is given by *Stefan condition*

$$\rho_s L_m \boldsymbol{v}^* \cdot \boldsymbol{n} = k_s \nabla T_s|^* \cdot \boldsymbol{n} - k_\ell \nabla T_\ell|^* \cdot \boldsymbol{n}, \tag{2.4}$$

where L_m stands for the latent heat of melting, the asterisk * denotes the value at the solid-liquid interface, and subscripts $_s$ and $_\ell$ denote the solid and liquid phase, respectively. The normal to the solid-liquid interface in the direction of the liquid phase and the growth velocity are denoted by $\boldsymbol{n}$ and $\boldsymbol{v}^*$, respectively.

The boundary condition for the temperature at the solid-liquid interface $T^* = T_s^* = T_\ell^*$ takes into account the capillary and the attachment-kinetics effects

$$T^* = T_m - \Delta T_c - \Delta T_k, \tag{2.5}$$

where T_m, ΔT_c, and ΔT_k stand for the melting temperature, the curvature undercooling, and the attachment-kinetics undercooling, respectively. A scheme of the boundary conditions for the heat flux and the temperature at the solid-liquid interface is shown in Fig. 2.1. The attachment-kinetics undercooling is given as

$$\Delta T_k = \boldsymbol{v}^* \cdot \boldsymbol{n} / \mu_k(\boldsymbol{n}), \tag{2.6}$$

where μ_k stands for the attachment-kinetics coefficient. The curvature undercooling is given according to Herring's relation (Dantzig and Rappaz, 2017). In 2-D, the relation is given as

$$\Delta T_c = \Gamma_{s\ell} \left(a(\boldsymbol{n}) + \mathrm{d}^2 a(\boldsymbol{n}) / \mathrm{d}\varphi^2 \right) \kappa, \tag{2.7}$$

where $\Gamma_{s\ell}$, κ, and a stand for the Gibbs-Thomson coefficient, the curvature of the solid-liquid interface, and the function accounting for the anisotropy of the interfacial energy, respectively. The angle φ is defined as $\varphi = \arctan(n_y/n_x)$, where $\boldsymbol{n} = (n_x, n_y)$. The expression for ΔT_c in 3-D is obtained in a similar way.

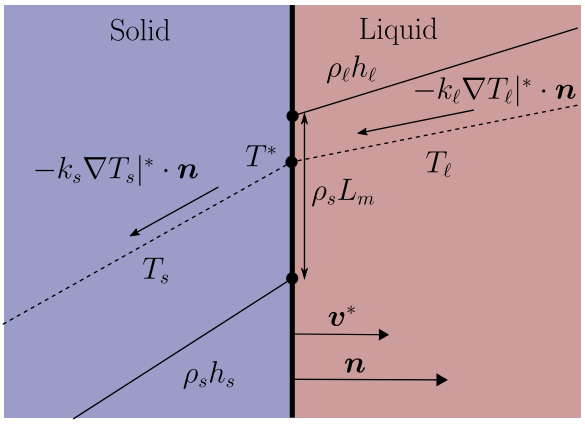

FIGURE 2.1: A scheme of the boundary conditions for the heat flux and the temperature at the solid-liquid interface.

Dimensionless symmetric model

In a simplified case, especially relevant for the verification of different numerical techniques for the simulation of solidification, the so-called *symmetric model*, assuming the constant and equal values of the material properties in

both phases, is used

$$\rho_s = \rho_\ell = \rho, \quad c_{ps} = c_{p\ell} = c_p, \quad k_s = k_\ell = k, \tag{2.8}$$

where c_p is the specific heat at constant pressure. By introducing the dimensionless temperature $\theta = (T - T_m)/(L_m/c_p)$, Eqs. (2.3), (2.4), and (2.5) are elegantly rewritten as

$$\frac{\partial \theta}{\partial t} = D_T \nabla^2 \theta, \tag{2.9}$$

$$\boldsymbol{v}^* \cdot \boldsymbol{n} = D_T \left(\nabla \theta_s |^* \cdot \boldsymbol{n} - \nabla \theta_\ell |^* \cdot \boldsymbol{n} \right), \tag{2.10}$$

$$\theta^* = -d_0 \left(a(\boldsymbol{n}) + \mathrm{d}^2 a(\boldsymbol{n}) / \mathrm{d}\varphi^2 \right) \kappa - \beta_k(\boldsymbol{n}) \boldsymbol{v}^* \cdot \boldsymbol{n}, \tag{2.11}$$

where $d_0 = \Gamma_{s\ell}/(L_m/c_p)$, $\beta_k(\boldsymbol{n}) = 1/(\mu_k(\boldsymbol{n}) L_m/c_p)$, and $D_T = k/(\rho c_p)$ are the thermal capillary length, the re-scaled attachment-kinetics coefficient, and the diffusivity of heat, respectively.

2.1.2 Solute balance

Similar to the diffusion of heat, the diffusion of the i-th component in a multi-component alloy with N_c components is described as

$$\frac{\partial (\rho C_i)}{\partial t} = -\nabla \cdot \boldsymbol{j}_i, \tag{2.12}$$

where C_i and $\boldsymbol{j}_i$ stand for the concentration and the diffusive mass flux of the i-th component, respectively. The concentration C_i is defined as the mass fraction of the i-th element, the quantity ρC_i therefore represents the mass of the i-th component per unit volume in a phase with density ρ. The diffusive mass flux is given by Fick's first law, which states that $\boldsymbol{j}_i$ is proportional to the gradient of the chemical potential of the i-th component. The flux can be written as (Dantzig and Rappaz, 2017)

$$\boldsymbol{j}_i = -\rho \sum_{j=1}^{N_c} D_{ij} \nabla C_j + \frac{M_i C_i \mu_i}{T^2} \nabla T, \tag{2.13}$$

where M_i and μ_i stand for the mobility and the chemical potential of the i-th component, respectively. D_{ij} is the element of the diffusivity tensor. In the case of solidification (Dantzig and Rappaz, 2017), the most basic version of Fick's

law can be used where the off-diagonal elements in the diffusivity tensor and a term proportional to ∇T are neglected. The diffusion is therefore given as

$$\frac{\partial(\rho C_i)}{\partial t} = \nabla(\rho D_i \nabla C_i), \tag{2.14}$$

where the notation $D_i = D_{ii}$ can be applied due to the diagonal diffusivity matrix. Only the diffusion of solute elements is usually considered, since the concentration of the solvent can be calculated from

$$\sum_{i=1}^{N_c} C_i = 1. \tag{2.15}$$

Conditions at the solid-liquid interface

The boundary condition for the mass flux at the solid-liquid interface is given as

$$\rho_s C^*_{\ell,i}(1 - k_{0,i})\boldsymbol{v}^* \cdot \boldsymbol{n} = \rho_s D_{s,i} \nabla C_{s,i}|^* \cdot \boldsymbol{n} - \rho_\ell D_{\ell,i} \nabla C_{\ell,i}|^* \cdot \boldsymbol{n}, \tag{2.16}$$

where $k_{0,i}$ is the partition coefficient of the i-th component, defined as $C^*_{s,i} = k_{0,i} C^*_{\ell,i}$. The values $C^*_{\ell,i}$ and $k_{0,i}$ at a given temperature are determined by the phase diagram of the alloy. The temperature at the solid-liquid interface is given as

$$T^* = T_{liq}(\{C^*_{\ell,i}\}) - \Delta T_c - \Delta T_k, \tag{2.17}$$

where T_{liq} stands for the liquidus temperature and ΔT_k and ΔT_c are given by Eqs. (2.6) and (2.7), respectively.

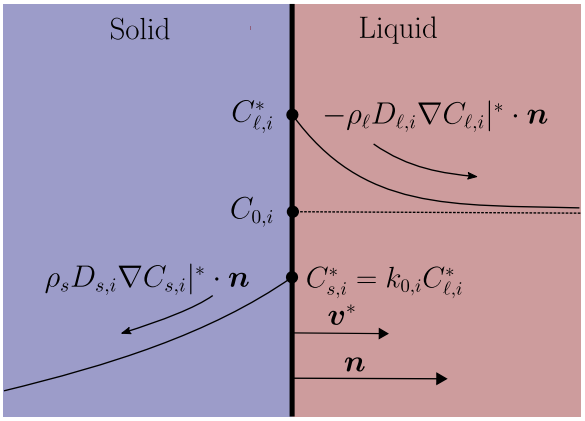

FIGURE 2.2: A scheme of the boundary conditions for the solute flux and the concentration of the i-th component at the solid-liquid interface.

Phase diagrams

The main aim of the dissertation is the simulation of the dendritic solidification of the primary solid phase in dilute eutectic alloys. A schematic binary eutectic phase diagram at constant pressure is shown in Fig. 2.3. The alloy consists of solvent A and solute B with melting temperatures $T_{m,A}$ and $T_{m,B}$, respectively. The solid phases α and β are determined by the crystal structure of the pure elements A and B, respectively. The solubility limit of the solid phases α and β are $C_{sol,A}$ and $C_{sol,B}$, respectively. In the regions $\alpha + \ell$ and $\beta + \ell$, the solid and liquid phase coexist. At the eutectic point (C_{eut}, T_{eut}), two solid phases and the liquid phase coexist. In the region $\alpha + \beta$, both solid phases coexist. The *liquidus* of the phase α is the line connecting the points $(C = 0, T = T_{m,A})$ and $(C = C_{eut}, T = T_{eut})$ (and similar for the phase β). The *solidus* of the phase α is the line connecting the points $(C = 0, T = T_{m,A})$ and $(C = C_{sol,A}, T = T_{eut})$ (and similar for the phase β). At T_{eut}, the partition coefficient in the phase α is equal to $k_{0,\alpha} = C_{sol,A}/C_{eut}$.

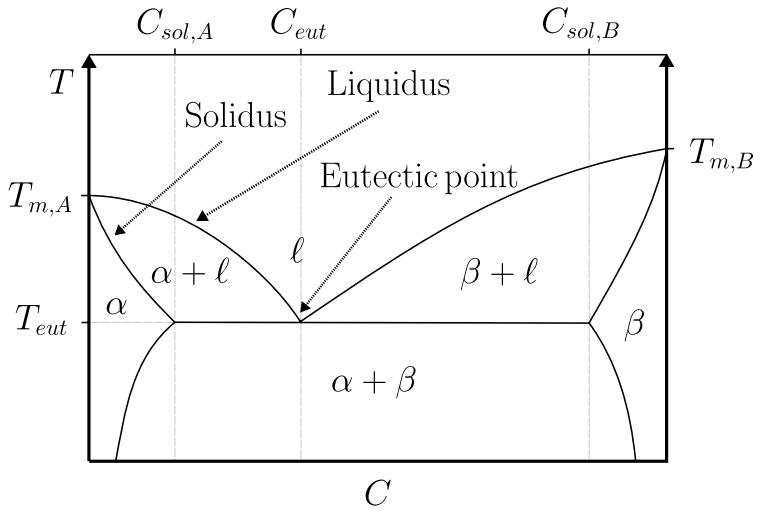

FIGURE 2.3: Scheme of a binary eutectic phase diagram at constant pressure.

In the case of binary alloys, the concentrations C_ℓ^* and C_s^* from Eq. (2.16) at a given temperature are easily obtained using the phase diagram as intersections of the horizontal line $T = const.$ with liquidus and solidus lines, respectively. The index in the concentration has been dropped since there is only one solute element. For a dilute binary alloy, the liquidus temperature from Eq. (2.17) is simply given as

$$T_{liq}(C_\ell^*) = T_m + m_\ell C_\ell^*, \tag{2.18}$$

where m_ℓ is the constant slope of the liquidus line.

For multi-component alloys with more than one solute element ($N_c > 2$), the determination of the values $C_{\ell,i}^*$ and $C_{s,i}^*$ at a given temperature is more complicated (Dantzig and Rappaz, 2017). In the case of dilute multi-component alloys, however, Eq. (2.18) can be generalized to obtain the liquidus temperature from Eq. (2.17)

$$T_{liq}(\{C_{\ell,i}^*\}) = T_m + \sum_{i=1}^{N_c-1} m_{\ell,i} C_{\ell,i}^*, \tag{2.19}$$

where $m_{\ell,i}$ is the constant slope of the liquidus line in the binary phase diagram of the solvent and the i-th solute component.

Dimensionless model for dilute alloys in a frozen temperature approximation

It is convenient for the verification of different numerical techniques for the simulation of solidification to rewrite the balance equations in a dimensionless form by introducing dimensionless supersaturations and the dimensionless undercooling with respect to the equilibrium state. The constant and equal values of density are used in both phases.

The equilibrium state is defined by the equilibrium temperature

$$T^e = T_m + \sum_{i=1}^{N_c-1} m_{\ell,i} C^e_{\ell,i}, \tag{2.20}$$

where $C^e_{\ell,i}$ is the equilibrium concentration in the liquid phase. The dimensionless supersaturation of the i-th component is defined as

$$U_i = \frac{C_i - C^e_{\nu,i}}{z_{\nu,i}(1-k_{0,i})C^e_{\ell,i}}, \tag{2.21}$$

where $z_{s,i} = k_{0,i}$ and $z_{\ell,i} = 1$. The freezing range ΔT_i, which is used to define the dimensionless undercooling, is given as

$$\Delta T_i = -m_{\ell,i}(1-k_{0,i})C^e_{\ell,i}. \tag{2.22}$$

The dimensionless temperature is given as

$$\theta = \frac{T - T^e}{\Delta T_{ref}}, \tag{2.23}$$

where the selection of the reference freezing range ΔT_{ref} among the values ΔT_i, $i = 1, ..., N_c - 1$ is arbitrary.

The dimensionless versions of Eqs. (2.14), (2.16), and (2.17) are given as

$$\frac{\partial U_i}{\partial t} = \nabla \cdot (D_i \nabla U_i), \tag{2.24}$$

$$(1 + (1-k_{0,i})U^*_i))\, \boldsymbol{v}^* \cdot \boldsymbol{n} = k_{0,i} D_{s,i} \nabla U_{s,i}|^* \cdot \boldsymbol{n} - D_{\ell,i} \nabla U_{\ell,i}|^* \cdot \boldsymbol{n}, \tag{2.25}$$

$$\theta^* + \sum_{i=1}^{N_c-1} \mathcal{M}_i U^*_i = -d_{c,ref} \left(a(\boldsymbol{n}) + \mathrm{d}^2 a(\boldsymbol{n})/\mathrm{d}\varphi^2 \right) \kappa - \beta_{k,ref}(\boldsymbol{n}) \boldsymbol{v}^* \cdot \boldsymbol{n}, \tag{2.26}$$

where $\mathcal{M}_i = \Delta T_i/\Delta T_{ref}$, $\beta_{k,ref}(\boldsymbol{n}) = 1/(\mu_k(\boldsymbol{n})\Delta T_{ref})$ and $d_{c,ref} = \Gamma/\Delta T_{ref}$ are the ratio between the freezing ranges, the reference re-scaled kinetics-attachment coefficient, and the reference chemical capillary length, respectively. The ratio $\mathcal{M}_i$ can be also written as $\mathcal{M}_i = d_{c,ref}/d_{c,i}$ where $d_{c,i} = \Gamma/\Delta T_{ref}$.

2.2 Introduction to phase field modelling

The main aim of this sub-section is a presentation of the theoretical basics of the PF modelling that are used in all PF models describing various free-boundary problems in materials science and engineering, e.g., solidification, solid-state phase transformations, crack propagation, etc. The theory behind the PF methodology has its origins in the mean field theory of first- and second-order phase transitions, especially in the Landau theory of phase transformations presented in Section 2.2.1. The formalism from Section 2.2.1 considers only the bulk properties of the phases, while the equilibrium interfaces between the phases are studied in Section 2.2.2. The first two sections deal with equilibrium systems, while the non-equilibrium kinetics of phase transitions is presented in Section 2.2.3.

2.2.1 Landau's theory

Landau's phenomenological theory (Barrat and Hansen, 2003) represents a unified framework for studying phase transitions, characterized by a macroscopic order parameter ϕ. The order parameter represents an average measure of the global symmetry of a phase. The phases at high temperature are in the most cases fully disordered ($\phi = 0$) on the atomic scale and have a high degree of translation symmetry (homogeneity) and rotation symmetry (isotropy) of the macroscopic properties. The symmetry is said to be broken at low temperatures as long-range translational or orientational order spontaneously appears in the phases, i.e., ϕ takes non zero values, dependent on the thermodynamic state variables. The example is the transition between the paramagnetic and ferromagnetic phases at a critical (Curie) temperature T_c. The symmetry is broken from fully rotational at $T > T_c$ to cylindrical around the orientation of spontaneous magnetization at $T < T_c$. In some cases, two phases in the system

experience the same symmetry. In that case a thermodynamic order parameter can be introduced, e.g., the difference in density between the two liquids or the difference in concentration between two species in a binary alloy. The vanishing of ϕ at a phase transition indicates the order of the phase transition. A discontinuous change of ϕ indicates the first order, while the continuous change of ϕ signals a second-order phase transition.

Simple example of Landau free-energy construction

In the framework of Landau's theory, the Helmholtz free energy F is used to describe a system

$$F = E - TS, \tag{2.27}$$

where E and S stand for the internal energy and the entropy, respectively. For example, the thermodynamics of spinodal decomposition in binary alloys or the transition between the paramagnetic and ferromagnetic phases at T_c (Ising model) can be, in the most simple case, described by Landau free-energy density as (Provatas and Elder, 2010)

$$f(\phi, T) = F(\phi, T)/V = a_0(T) + \frac{a_2(T)}{2}\phi^2 + \frac{a_4(T)}{4}\phi^4, \tag{2.28}$$

where a_0, a_2, and a_4 are the coefficients in the Taylor expansion of the free energy and V is the volume of the system, while ϕ represents the concentration of the solute or the mean magnetisation. The free energy from Eq. (2.28) considers systems that are invariant under the inversion $\phi \leftrightarrow -\phi$, hence, only even powers of ϕ are non-zero. The expected values of the order parameter are obtained by minimization

$$\frac{\partial f}{\partial \phi} = 0 \rightarrow \bar{\phi} = \left(0, \pm\sqrt{\frac{-a_2(T)}{a_4(T)}}\right), \tag{2.29}$$

where $\bar{\phi}$ denotes the value of ϕ at the minimum. The phases above the critical temperature T_c are fully disordered, hence, $\bar{\phi} = 0$ has to be the only real root in Eq. (2.29) requiring $a_2(T) > 0$ and $a_4(T) > 0$. Below T_c, ϕ takes non-zero values, hence, the second root in Eq. (2.29) has to be real, which is true if $a_2(T) < 0$ and $a_4(T) > 0$. These requirements can be, near T_c , simply fulfilled

by the following approximation

$$a_2(T) \approx a_2^0(T - T_c), \quad a_4(T) \approx a_4^0, \tag{2.30}$$

where a_2^0 and a_4^0 are the positive constants. Landau's theory therefore predicts two stable phases below (and near) T_c

$$\bar{\phi} \approx \pm\sqrt{\frac{a_2^0}{a_4^0}(T_c - T)}. \tag{2.31}$$

Eq. (2.31) shows that the transition of the expected value of the order parameter from $\bar{\phi} \neq 0$ to $\bar{\phi} = 0$ at T_c is continuous, which indicates a second-order phase transition. The Landau free-energy density as a function of the order parameter at different values of the temperature is shown in Fig. 2.4. The parameters in Eqs. (2.28) and (2.30) are simply selected as

$$a_0(T) = 0, \quad a_2^0 = a_4^0 = 1. \tag{2.32}$$

As the temperature is dropping, f is becoming flatter and flatter, till the symmetry is spontaneously broken below $T = T_c$, as the minimum at $\bar{\phi} = 0$ breaks into two minima $\bar{\phi} \pm \bar{\phi}(T) \neq 0$.

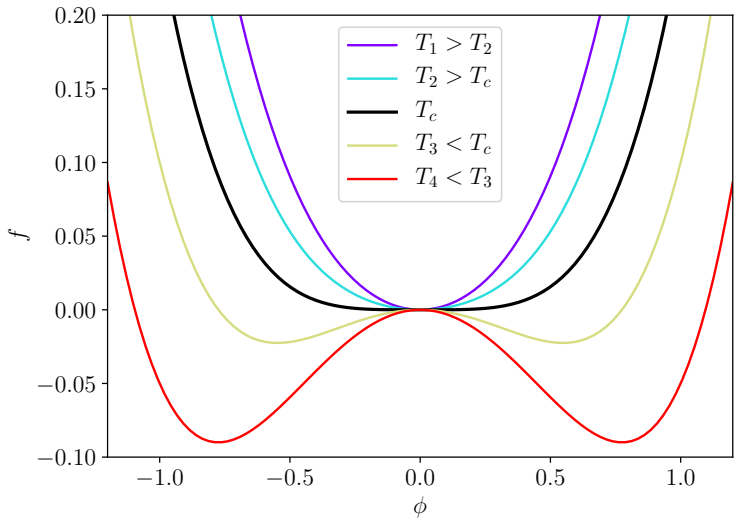

FIGURE 2.4: Landau free-energy density as a function of the order parameter near the critical temperature.

2.2.2 Spatial variations and interfaces

In the previous section, only the bulk properties of the phases are discussed. By considering the interfaces between the phases, ϕ and T become space dependent. In that case, the free energy of the system is given by the Ginzburg-Landau or Cahn-Hilliard free energy (Provatas and Elder, 2010)

$$F[\phi, T] = \int_V \left(\frac{1}{2} |W_\phi \nabla \phi(\boldsymbol{r})|^2 + f(\phi(\boldsymbol{r}), T(\boldsymbol{r})) \right) \mathrm{d}V, \tag{2.33}$$

where the parameter W_ϕ accounts for the effects of the surface energy. The thermodynamic equilibrium is assured by minimizing the thermodynamic potential with respect to intensive thermodynamic variables, as seen in Section 2.2.1. Similarly, the thermodynamic equilibrium is assured by the function $\phi_0(\boldsymbol{r})$, which minimizes the Ginzburg-Landau free-energy functional from Eq. (2.33). Minimization of Eq. (2.33) is achieved through the *functional* or *variational derivative*, which relates the change in the functional to the change in a function, on which the functional depends on. By using the variational derivative notation, the equilibrium condition is given as

$$\frac{\delta F[\phi]}{\delta \phi} = 0. \tag{2.34}$$

The variational derivative of the functional $F[\phi]$ is defined as

$$\frac{\delta F}{\delta \phi} = \frac{\partial \tilde{F}}{\partial \phi} - \sum_{\xi=x,y,z} \partial_\xi \left(\frac{\partial \tilde{F}}{\partial_\xi \phi} \right), \quad F[\phi] = \int_V \tilde{F}(\phi, \partial_x \phi, \partial_y \phi, \partial_z \phi) \mathrm{d}V. \tag{2.35}$$

For example, the equilibrium function for a system described by the free-energy density from Eq. (2.28) is calculated by combining Eqs. (2.33), (2.34) and (2.35), which in 1-D yields

$$W_\phi^2 \frac{\mathrm{d}^2 \phi_0}{\mathrm{d}x^2} - a_2(T)\phi_0 - a_4(T)\phi_0^3 = 0. \tag{2.36}$$

After applying some mathematical analysis (Provatas and Elder, 2010), the solution of Eq. (2.36) is given as

$$\phi_0(x) = \sqrt{\frac{|a_2(T)|}{a_4(T)}} \tanh\left(\frac{x}{\sqrt{2}W_0}\right), \tag{2.37}$$

where $W_0 = W_\phi/\sqrt{|a_2(T)|}$ stands for the interface thickness. The equilibrium function $\phi_0(x)$ at different values of temperature is shown in Fig. (2.5) where approximations for $a_2(T)$ and $a_4(T)$ from Eqs. (2.30) and (2.32) have been used. The interface thickness W_0 is becoming narrower and narrower as the temperature is dropping, while $\phi_0(\pm\infty) = \pm\sqrt{|a_2(T)|/a_4(T)}$. As T is approaching T_c, W_0 is approaching infinity and $\phi_0(x)$ is approaching zero.

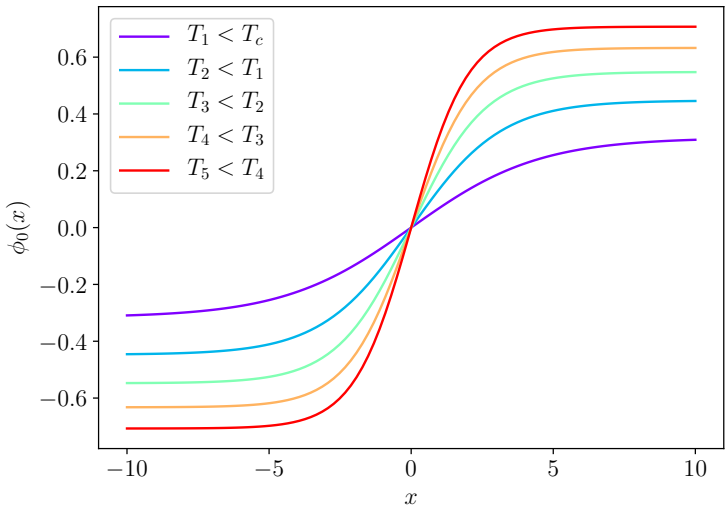

FIGURE 2.5: Equilibrium order parameter as a function of position at different values of temperature below T_c.

Surface energy of equilibrium profile

The *surface energy* σ, also known as the *surface tension*, can be seen as the resistance of the system to any increase of the surface area. The constant W_ϕ in the (penalty) term $|W_\phi \nabla\phi|^2/2$ and the parameters of the free-energy density $f(\phi, T)$ in the Ginzburg-Landau free energy from Eq. (2.33) should therefore be somehow linked to the surface energy. σ can be defined as the excess of the free energy in a system due to the presence of the interface (Provatas and

Elder, 2010). For an equilibrium profile $\phi_0(x)$ in 1-D, σ can be defined as

$$\sigma = F - F_{eq} = \int_{-\infty}^{\infty} \left[\frac{1}{2} W_\phi^2 \left(\frac{\mathrm{d}\phi_0}{\mathrm{d}x} \right)^2 + f(\phi_0) \right] \mathrm{d}x - \int_{-\infty}^{\infty} f\left(\phi_0(-\infty)\right) \mathrm{d}x, \quad (2.38)$$

where F_{eq} represents the equilibrium bulk free energy. After applying some mathematical analysis (Provatas and Elder, 2010), the surface energy is given as

$$\sigma = W_\phi^2 \int_{-\infty}^{\infty} \left(\frac{\mathrm{d}\phi_0}{\mathrm{d}x} \right)^2 \mathrm{d}x. \quad (2.39)$$

Although Eq. (2.39) represents the surface energy in 1-D, the unit $1/\mathrm{m}$ of the integral is independent of the problem dimension, hence, it is clear that σ has units of surface energy since $[W_\phi] = \sqrt{\mathrm{J}} \rightarrow [\sigma] = \mathrm{J/m}$ in 2-D and $[W_\phi] = \sqrt{\mathrm{J/m}} \rightarrow [\sigma] = \mathrm{J/m^2}$ in 3-D.

2.2.3 Non-equilibrium dynamics

Equilibrium systems with spatially dependent order parameter have been studied in the previous section. The next important aspect in the PF modelling of phase transitions is the examination of the temporal dependence of the order parameter. In the framework of the mathematical modelling of non-equilibrium dynamics, space can be seen as a set of volume cells, each large enough to be assumed in the thermodynamic equilibrium, although small enough to spatially resolve the microstructure evolution. Local thermodynamic driving forces govern the system towards the global equilibrium. Kinetic equations for the order parameter can be either conserved of non-conserved. An example of the conserved order parameter is the concentration in a binary alloy model, while the mean magnetisation in the Ising model is an example of a non-conserved order parameter. The latter is govern by Langevin-type equations, while the governing equations for the conserved order parameter are diffusion-like.

Dynamics of conserved order parameter

We are considering the dynamics of a general conserved order parameter. An example of such an order parameter is the solute concentration in a binary alloy, represented by the free-energy curve from Eq. (2.28). The local chemical

potential μ has to be derived from the Ginzburg-Landau free energy functional from Eq. (2.33) in order to calculate the solute flux. Cahn and Hilliard (Cahn and Hilliard, 1958) used the following definition

$$\mu = \frac{\delta F[\phi]}{\delta \phi}. \tag{2.40}$$

In the limit of the mean field theory where the spatial gradients are neglected, Eq. (2.40) is reduced to the classic definition of the chemical potential. At equilibrium, when the free energy depends on the spatial gradients, Eq. (2.40) yields a differential equation for the equilibrium profile of ϕ. The order parameter ϕ, representing the solute concentration in binary alloys has to obey the mass-conservation equation

$$\frac{\partial \phi}{\partial t} = -\nabla \cdot \boldsymbol{j}, \quad \boldsymbol{j} = -M \nabla \mu \tag{2.41}$$

where $\boldsymbol{j}$ and M are the solute flux and the mobility of the solute, respectively. The combination of Eqs. (2.40) and (2.41) yields the famous *Cahn-Hilliard equation* (Cahn and Hilliard, 1958) or *Model B* (Hohenberg and Halperin, 1977)

$$\frac{\partial \phi}{\partial t} = \nabla \cdot \left(M \nabla \frac{\delta F}{\delta \phi} \right). \tag{2.42}$$

Eq. (2.42) can be used for the simulation of spinodal decomposition using Eq. (2.28) for the free energy in the bulk. By combining Eq. (2.42), the definition of the variational derivative from Eq. (2.35), and the definition of the Ginzburg-Landau functional from Eq. (2.33) we obtain a PDE for the propagation of the conserved order parameter

$$\begin{aligned} \frac{\partial \phi}{\partial t} &= M \nabla^2 \left(-W_\phi^2 \nabla^2 \phi + \frac{\partial f}{\partial \phi} \right) \\ &= M \nabla^2 \left(-W_\phi^2 \nabla^2 \phi + a_2(T) \phi + a_4(T) \phi^3 \right), \end{aligned} \tag{2.43}$$

where the constant mobility M is assumed.

Dynamics of the non-conserved order parameter

The order parameter can also represent the non-conserved variables, e.g., the mean magnetisation in the Ising model or the atomic order during solidification from a pure melt. A glass full of pure water will completely freeze below the freezing temperature as the zero mean order parameter before freezing will change to a non-zero value after the freezing is complete. Since ϕ does not need to be conserved, the simplest dissipative dynamics is given by Langevin-type kinetics

$$\frac{\partial \phi}{\partial t} = -M \frac{\delta F}{\delta \phi} = M \left(W_\phi^2 \nabla^2 \phi - \frac{\partial f(\phi, T)}{\partial \phi} \right), \tag{2.44}$$

where M is related to the attachment time of the particles from the phase with $\phi = 0$ to the phase $\phi \neq 0$. Eq. (2.44) is also know as *Allen-Cahn equation* (Cahn and Allen, 1977) or *Model A* (Hohenberg and Halperin, 1977). Eq. (2.44) can be used to simulate the spontaneous formation of local domains with non-zero magnetisation in the Ising model below the Curie temperature with PDE

$$\frac{\partial \phi}{\partial t} = M \left(W_\phi^2 \nabla^2 \phi - a_2(T)\phi - a_4(T)\phi^3 \right). \tag{2.45}$$

Equilibrium fluctuations of the order parameter

Although a system is in equilibrium, the order parameter and all the other quantities in a system continuously fluctuate in time and space due to thermal fluctuations. Thermal fluctuations are taken into account by adding a stochastic noise term $\eta(\boldsymbol{r}, t)$ to the Cahn-Hilliard and Allen-Cahn equations

$$\frac{\partial \phi}{\partial t} = \frac{\partial \phi}{\partial t} + \eta(\boldsymbol{r}, t). \tag{2.46}$$

The term $\eta(\boldsymbol{r}, t)$ describes the thermal fluctuations on length scales of the order of Å, i.e., on scales much smaller than the interface thickness W_0 over which the phase change occurs, and on time scales of the order of ps. In the case of the Allen-Cahn equation from Eq. (2.44), $\eta(\boldsymbol{r}, t)$ is chosen from statistical distribution, obeying

$$\langle \eta(\boldsymbol{r}, t) \eta(\boldsymbol{r}', t') \rangle = A \delta(\boldsymbol{r} - \boldsymbol{r}') \delta(t - t'), \tag{2.47}$$

where δ is the Dirac delta function and A stands for a temperature-dependent constant, equal to (Provatas and Elder, 2010)

$$A = 2Mk_bT, \tag{2.48}$$

where k_b is the Boltzmann constant. In the case of the Cahn-Hilliard equation from Eq. (2.42), $\eta(\boldsymbol{r}, t)$ is chosen from a statistical distribution obeying

$$\langle \eta(\boldsymbol{r}, t)\eta(\boldsymbol{r}', t')\rangle = A\nabla^2\delta(\boldsymbol{r} - \boldsymbol{r}')\delta(t - t'), \tag{2.49}$$

with the same constant A from Eq. (2.48).

2.3 Phase field modelling of solidification

In the previous section, two examples of the order parameter are discussed: the mean magnetisation in the Ising model and the concentration of solute in a binary alloy. In this section, the definition of the order parameter for solidification is first presented, followed by the PF models describing solidification in pure materials and dilute multi-component alloys.

2.3.1 Definition of the order parameter

We are considering a crystal with N_{at} atoms. The instantaneous solid density in a crystal is given as

$$\rho(\boldsymbol{r}, t) = \sum_{n=1}^{N_{at}} \delta(\boldsymbol{r} - \boldsymbol{r}_n(t)), \tag{2.50}$$

where $\boldsymbol{r}_n(t)$ is the position of the n-th atom in a crystal. The temporal or ensemble average of the density is calculated as (Provatas and Elder, 2010)

$$\langle \rho(\boldsymbol{r}, t)\rangle_{\text{time}} = \langle \rho(\boldsymbol{r}, t)\rangle_{\text{ensemble}} = \frac{\bar{\rho}}{N_{at}} \sum_{\boldsymbol{g}} \phi_{\boldsymbol{g}} \exp(-\mathrm{i}\boldsymbol{g} \cdot \boldsymbol{r}), \tag{2.51}$$

where $\bar{\rho}$ is the average atomic number density, $\boldsymbol{g}$ the reciprocal lattice vector, and $\phi_{\boldsymbol{g}}$ the order parameter of $\boldsymbol{g}$. The order parameter is defined as (Provatas

and Elder, 2010)

$$\phi_{\boldsymbol{g}} = \left\langle \sum_{n=1}^{N_{at}} \exp(\mathrm{i}\boldsymbol{g} \cdot \boldsymbol{r}_n(t)) \right\rangle . \tag{2.52}$$

In the 1-D case, $\boldsymbol{g}$ and $\boldsymbol{r}_n$ become scalars $g = 2\pi m/\bar{a}$ and $r_n(t) = (n + \xi(t))\bar{a}$, where $\bar{a}$ and ξ represent the the lattice size and the Gaussian random number accounting for the thermal fluctuations, respectively. It can be easily show, that in the solid phase

$$\left\langle e^{igr_n} \right\rangle = 1, \quad \phi_g \sim N_{at}, \tag{2.53}$$

since $\sin(2\pi mn) = 0$, $\cos(2\pi mn) = 1$, and $\langle \sin(2\pi m\xi) \rangle = 0$ and $\langle \cos(2\pi m\xi) \rangle = 1$ due to $\langle \xi \rangle = 0$. Positions $r_n(t)$ are, in the liquid phase, totally uncorrelated, hence

$$\left\langle e^{igr_n} \right\rangle = 0, \quad \phi_g = 0. \tag{2.54}$$

The order parameter is therefore equal to a non-zero constant in the solid phase and zero in the liquid phase, with continuous change at the solid-liquid interface.

The above considerations are only valid in the case when the order parameter varies over length scales much larger than the atomically diffuse solid-liquid interface thickness and on time scales much larger than time scales of the atomic vibrations.

Free energy functional for solidification

In the framework of classic density functional theory (Kalikmanov, 2001), the free-energy functional can be derived in terms of $\langle \rho(\boldsymbol{r}, t) \rangle$, i.e., $F = F(\langle \rho(\boldsymbol{r}, t) \rangle, T)$. This definition of functional can be "homogenized" or "coarse-grained" into an effective free-energy functional, valid on the scales much larger than a single atom, but small enough to resolve metallurgically relevant length scales (Provatas and Elder, 2010). The homogenized version of the functional can be written as

$$F[\langle \rho(\boldsymbol{r}, t) \rangle, T] \to F[\{\phi_{\boldsymbol{g}}\}, T], \tag{2.55}$$

where $F[\{\phi_{\boldsymbol{g}}\}, T]$ can be seen as the Ginzburg-Landau free-energy functional, dependent on the multiple complex order parameters $\{\phi_{\boldsymbol{g}}\}$. By using such a functional, it is possible to describe how elasto-plastic phenomena effect the

microstructure's evolution. At higher temperatures, elasto-plastic effects can often be neglected, leading to a description of the solidification with a single real order parameter

$$F[\{\phi_{\boldsymbol{g}}\}, T] \rightarrow F[\phi, T], \tag{2.56}$$

represented by the Ginzburg-Landau free-energy functional from Eq. (2.33).

2.3.2 Pure materials

In this section, the diffuse-interface version of the dimensionless model from Eqs. (2.9), (2.10), and (2.11), based on the energy balance, is presented. The PF model (Karma and Rappel, 1998) can be derived from a single free-energy functional in the variational formulation (VF) where the temperature and the PF are considered as conserved and non-conserved order parameters, respectively. Alternatively, the governing equations can be derived in the isothermal variational formulation (IVF) where only the governing equation for the PF is derived from a free-energy functional. The IVF is used to derive the PF model in the dissertation.

In the IVF, the phenomenological free-energy functional is given as

$$\mathcal{F} = \int \left(\frac{1}{2} |W \nabla \phi|^2 + f_{dw}(\phi) + \lambda \hat{g}(\phi) \theta \right) \mathrm{d}V \tag{2.57}$$

where W is the interface thickness, f_{dw} the double-well potential, $\hat{g}$ the tilting function, and λ is the coupling parameter. The dimensionless temperature $\theta = (T - T_m)/(L_m/c_p)$ has been defined in Section 2.1.1. The functional $\mathcal{F}$ is constructed in such a way that the integrand in Eq. (2.57) is dimensionless. The standard choice of PF functions is

$$f_{dw}(\phi) = -\frac{1}{2}\phi^2 + \frac{1}{4}\phi^4 \quad \hat{g}(\phi) = \phi - \frac{2}{3}\phi^3 + \frac{1}{5}\phi^5. \tag{2.58}$$

This selection keeps the minima of the free energy at values $\phi = \pm 1$ as $\phi = 1$ and $\phi = -1$ determine the solid and liquid phase, respectively. The bulk free energy with $\lambda = 1$ is shown in Fig. 2.6. At the melting temperature ($\theta = 0$), the free energy has two global minima at $\phi = \pm 1$. The global minimum of the free energy above ($\theta > 0$) and below ($\theta < 0$) the melting temperature is in the liquid ($\phi = -1$) and in the solid ($\phi = 1$) phases, respectively.

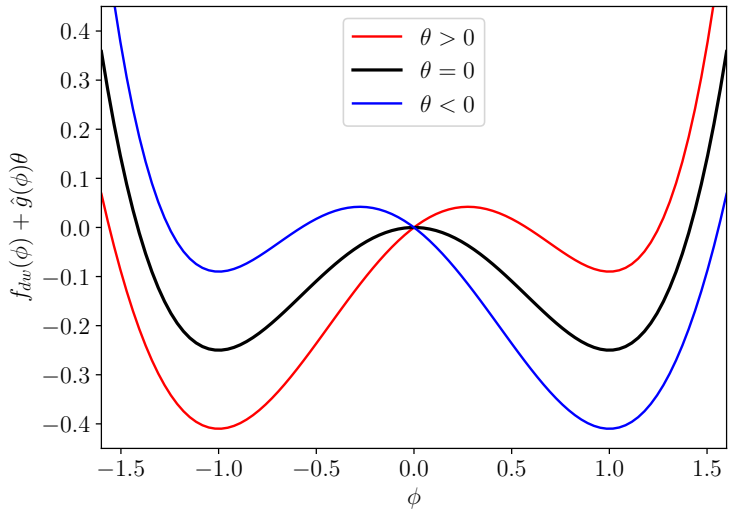

FIGURE 2.6: The dimensionless bulk free energy for three values of the dimensionless temperature.

The governing equations for the PF and temperature are, in the IVF, obtained as

$$\tau \frac{\partial \phi}{\partial t} = -\frac{\delta \mathcal{F}}{\delta \phi}, \tag{2.59}$$

$$\frac{\partial \theta}{\partial t} = D_T \nabla^2 \theta + \frac{1}{2} h'(\phi) \frac{\partial \phi}{\partial t}, \tag{2.60}$$

where τ is the characteristic time of the attachment of atoms at the interface. The function $h(\phi) = \phi$ is used in the calculations which turns out to be the most computationally effective (Karma and Rappel, 1998). By applying the definition of the functional derivative, the governing equation for the PF is given as

$$\begin{aligned} \tau(\boldsymbol{n}) \frac{\partial \phi}{\partial t} = & -f'_{dw}(\phi) - \lambda \hat{g}'(\phi)\theta + \nabla \cdot \left(W^2(\boldsymbol{n}) \nabla \phi \right) \\ & + \sum_{\xi = x,y} \partial_\xi \left(|\nabla \phi|^2 W(\boldsymbol{n}) \frac{\partial W(\boldsymbol{n})}{\partial (\partial_\xi \phi)} \right), \end{aligned} \tag{2.61}$$

where we have taken into account that W and τ can be anisotropic, which is the case when the capillary length d and the attachment-kinetics coefficient β_k are anisotropic. The notation $\partial_\xi \equiv \partial / \partial \xi$ is used through the dissertation in the "anisotropy term" of the governing equations for PF, e.g., in the last term in

Eq. (2.61). The "anisotropy term" vanishes from the governing equation if the interface thickness is isotropic.

Determination of the free parameters

In order to find the free parameters W, τ, and λ, for which the model correctly captures the physics described by the balance equations, the *matched asymptotic analysis* (Caginalp, 1989; Karma and Rappel, 1998; Echebarria et al., 2004; Ohno, 2012) of the governing equations has to be performed. The analysis was first performed in the framework of the *sharp-interface limit* (Caginalp, 1989) which requires that the interface thickness is much smaller than the capillary length, i.e., $W \ll d$. The limit yields the following relations

$$d = \alpha_1 \frac{W}{\lambda}, \tag{2.62}$$

$$\beta_k = \alpha_1 \frac{\tau}{\lambda W}, \tag{2.63}$$

where α_1 is the constant determined by the selection of the PF functions. The requirement $W \ll d$ makes the sharp-interface limit computationally ineffective since the spacing between the computational nodes has to be of the order of W. Additionally, the very common case of negligible attachment kinetics during solidification cannot be simulated in this limit since $\tau \to 0$ when $\beta_k \to 0$ according to Eq. (2.63).

The drawbacks of the sharp-interface limit have been successfully overcome with the derivation of the *thin-interface limit* (Karma and Rappel, 1998). The limit requires that the interface thickness is much smaller than the diffusion length of solidification, i.e., $W \ll D_T/(\boldsymbol{v}^* \cdot \boldsymbol{n})$, while the ratio W/d can be of the order of unity, which significantly enhances the computational efficiency in comparison to the sharp-interface limit. In the limit, the relation from Eq. (2.63) is modified as

$$\beta_k = \alpha_1 \left(\frac{\tau}{\lambda W} - \alpha_2 \frac{W}{D_T}, \right), \tag{2.64}$$

while the relation from Eq. (2.62) remains the same. Similar to α_1, the constant α_2 is determined by the selection of the PF functions. For the selection from Eq. (2.58) and $h(\phi) = \phi$, the constants are determined as $\alpha_1 = 0.8839$ and $\alpha_2 = 0.6267$ (Karma and Rappel, 1998).

Dimensionless PF model

In the dissertation, the PF model with zero interface kinetics and an anisotropic capillary length is considered. This case is especially relevant for solidification of metallic alloys. Eqs. (2.62) and (2.64) yield the following relations if $\beta_k = 0$ and $d(\boldsymbol{n}) = d_0 a(\boldsymbol{n})$

$$W(\boldsymbol{n}) = W_0 a(\boldsymbol{n}), \quad \tau(\boldsymbol{n}) = \tau_0 a^2(\boldsymbol{n}), \quad \lambda = \frac{D_T \tau_0}{\alpha_2 W_0^2}. \tag{2.65}$$

By rescaling time and Cartesian coordinates as

$$t \to t/\tau_0, \quad x \to x/W_0, \quad y \to y/W_0, \tag{2.66}$$

the dimensionless PF model for solidification in pure materials is given as

$$\begin{aligned} a^2(\boldsymbol{n})\frac{\partial \phi}{\partial t} = &-f'_{dw}(\phi) - \lambda\theta\hat{g}'(\phi) + \nabla \cdot \left(a^2(\boldsymbol{n})\nabla\phi\right) \\ &+ \sum_{\xi=x,y} \partial_\xi \left(|\nabla\phi|^2 a(\boldsymbol{n}) \frac{\partial a(\boldsymbol{n})}{\partial(\partial_\xi \phi)} \right), \end{aligned} \tag{2.67}$$

$$\frac{\partial \theta}{\partial t} = \bar{D}_T \nabla^2 \theta + h'(\phi)\frac{\partial \phi}{\partial t}, \tag{2.68}$$

where $\bar{D}_T = D_T \tau_0 / W_0^2$. The dimensionless PF model from Eqs. (2.67) and (2.68) has only one free parameter since the dimensionless $\bar{D}_T$ and λ are linked as $\bar{D}_T = \lambda \alpha_2$ according to Eq. (2.65). The free parameter has to be chosen according to the validity condition of the thin-interface limit, i.e., the interface thickness has to be much smaller than the diffusion length of solidification.

Incorporation of the thermal noise

It is possible to incorporate the thermal noise in the PF simulations by appropriately reformulating the PF model from Eqs. (2.67) and (2.68). In general, the interface noise term, originating from the exchange of atoms between the two phases, is added to Eq. (2.67) and the bulk noise, originating from the fluctuations in the heat current, is added to Eq. (2.68). In the pioneering work on the incorporation of thermal noise in the PF simulations (Karma and Rappel, 1999), the calculations were performed with the both noises and with the bulk noise only. Authors found out that the time-averaged morphology characteristics of

a dendrite were identical, indicating that the fluctuations which become amplified to affect the morphology of a dendrite are on the length scales much larger than the interface thickness. Hence, it is enough to include only bulk noise by reformulating Eq. (2.68) as

$$\frac{\partial \theta}{\partial t} = \frac{\partial \theta}{\partial t} - \nabla \cdot \tilde{\boldsymbol{q}}(\boldsymbol{r}, t), \tag{2.69}$$

where $\tilde{\boldsymbol{q}} = (\tilde{q}_m, \tilde{q}_n)$ stands for the dimensionless conserved noise with

$$\langle \tilde{q}_m(\boldsymbol{r}, t)\tilde{q}_n(\boldsymbol{r}', t')\rangle = 2\bar{D}_T F_u \delta_{mn}\delta(\boldsymbol{r} - \boldsymbol{r}')\delta(t - t'), \tag{2.70}$$

where F_u stands for the magnitude of the noise. The magnitude is calculated as (Karma and Rappel, 1999)

$$F_u = \frac{k_b T_m^2 c_p}{L_m^2 W_0^{N_{dim}}}, \tag{2.71}$$

where k_b and N_{dim} stand for the Boltzmann constant and the number of the dimensions, respectively.

2.3.3 Dilute multi-component alloys

In this section the diffuse-interface version of the solute-balance-obtained dimensionless model from Eqs. (2.24), (2.25), and (2.26) is presented. The PF model used in the dissertation (Ohno, 2012) is based on the PF model for solidification in binary alloys (Kim et al., 1999). The model (Ohno, 2012) originally describes the non-isothermal solidification where the diffusion of heat is also considered. In the dissertation, the model has been recast in the framework of the frozen temperature approximation where the temperature is considered as an input parameter.

As in the PF model for solidification in pure materials, the PF values $\phi = 1$ and $\phi = -1$ determine the solid and liquid phases, respectively. In the model, the concentration of the i-th element is given as $C_i = [1 + g(\phi)]C_{s,i}/2 + [1 - g(\phi)]C_{\ell,i}/2$ where the interpolation function $g(\phi)$ satisfies $g(\pm 1) = \pm 1$ and $g'(\pm 1) = 0$. Function $g(\phi) = (15/8)(\phi - (2/3)\phi^3 + \phi^5/5)$ is used in this study.

The phenomenological free energy is given as

$$\mathcal{F} = \int \left(\frac{1}{2}|W\nabla\phi|^2 + f_{dw}(\phi) + \frac{1}{\omega} f(T, \{C_{s,i}\}, \{C_{\ell,i}\}) \right) \mathrm{d}V, \tag{2.72}$$

where ω is the constant. The bulk free-energy density is given as $f = [1 + g(\phi)]f_s(T, \{C_{s,i}\})/2 + [1 - g(\phi)]f_\ell(T, \{C_{\ell,i}\})/2$. In the PF model, the chemical potentials of the solid and liquid are assumed to be the same at each local point, i.e., $\partial f_s/\partial C_{s,i} = \partial f_\ell/\partial C_{\ell,i} = \mu_i$ which yields

$$\begin{aligned} \tau\frac{\partial\phi}{\partial t} = -\frac{\delta\mathcal{F}}{\delta\phi} &= W^2\nabla^2\phi - f'_{dw}(\phi) \\ &- \frac{1}{2\omega}g'(\phi)\left[f_s - f_\ell - \sum_{i=1}^{N_c-1} \mu_i \left(C_{s,i} - C_{\ell,i} \right) \right] \end{aligned} \tag{2.73}$$

where we have temporarily assumed the isotropic surface properties. In the thermodynamic equilibrium, the last term on the right in Eq. (2.73) vanishes, which makes the profile of ϕ determined solely by W and f_{dw}. Consequently, the profile of ϕ and the corresponding surface energy are independent of the concentration fields (Kim et al., 1999; Ohno, 2012), which is the main advantage of the PF model used.

Free energy density of a dilute alloy

The free-energy density of a phase ν is given as

$$f_\nu(T, \{C_{\nu,i}\}) = f_{\nu,0}(T) + \sum_{i=1}^{N_c-1} \left[\Omega_{\nu,i}(T)C_{\nu,i} + \frac{RT}{\nu_m}\left(C_{\nu,i}\ln C_{\nu,i} - C_{\nu,i} \right) \right], \tag{2.74}$$

where $f_{\nu,0}(T)$, ν_m, and R stand for the free energy of a pure solvent, the molar volume, and the gas constant, respectively. $\Omega_{\nu,i}(T) = (RT/\nu_m)\ln\hat{\gamma}_{\nu,i}$, where $\hat{\gamma}_{\nu,i}$ is a constant. The condition $\partial f_s/\partial C_{s,i} = \partial f_\ell/\partial C_{\ell,i} = \mu_i$ yields $C_{s,i} = k_{0,i}C_{\ell,i}$ where $k_{0,i} = \hat{\gamma}_{\ell,i}/\hat{\gamma}_{s,i}$ is the partition coefficient. Substitution of Eq. (2.74) in Eq.

(2.73) yields the following expression for the thermodynamic driving force

$$\begin{aligned} & f_s - f_\ell - \sum_{i=1}^{N_c-1} \mu_i \left(C_{s,i} - C_{\ell,i}\right) \\ & \quad = f_{s,0}(T) - f_{\ell,0}(T) + (RT/\nu_m) \sum_{i=1}^{N_c-1} (1 - k_{0,i}) C_{\ell,i}. \end{aligned} \tag{2.75}$$

The approximation $f_{s,0}(T) - f_{\ell,0}(T) \approx (L_m/T_m)(T - T_m)$ can be applied near the melting temperature. Also, the temperature in the third term on the right in Eq. (2.75) can be approximated by T_m. The expression from Eq. (2.75) should vanish in the equilibrium when $T = T^e = T_m + \sum m_{\ell,i} C^e_{\ell,i}$ and $C_{\ell,i} = C^e_{\ell,i}$, which yields the definition of the liquidus slope $m_{\ell,i} = -RT_m^2(1 - k_{0,i})/(L_m \nu_m)$. Finally, by using the definition of the equilibrium temperature, the driving force of solidification can be written as

$$\begin{aligned} & f_s - f_\ell - \sum_{i=1}^{N_c-1} \mu_i \left(C_{s,i} - C_{\ell,i}\right) \\ & \quad \approx \frac{L_m}{T_m}(T - T^e) + (RT_m/\nu_m) \sum_{i=1}^{N_c-1} (1 - k_{0,i}) \left(C_{\ell,i} - C^e_{\ell,i}\right). \end{aligned} \tag{2.76}$$

Determination of the free parameters

As for pure materials, the focus of this study is the simulation of solidification with negligible attachment kinetics. The thin-interface limit for dilute multi-component alloys (Ohno, 2012) yields similar relations as in the case of pure materials (Karma and Rappel, 1998). The thermal capillary length is replaced by the reference chemical capillary length, which has been defined in Section 2.1.2

$$W(\boldsymbol{n}) = W_0 a(\boldsymbol{n}), \quad W_0 = \frac{\lambda}{\alpha_1} d_{c,ref}. \tag{2.77}$$

The attachment kinetics is negligible when

$$\tau(\boldsymbol{n}) = \tau_0 \Xi(\{U_i\}) a^2(\boldsymbol{n}), \quad \tau_0 = \frac{\alpha_2 \lambda W_0^2}{D_{\ell,ref}}, \tag{2.78}$$

where the function $\Xi(\{U_i\})$ is in the frozen temperature approximation ($D_T \to \infty$) given as

$$\Xi(\{U_i\}) = \sum_{i=1}^{N_c-1} \frac{[1 + (1 - k_{0,i})U_i]\mathcal{M}_i\psi_i}{D_{\ell,i}/D_{\ell,ref}}, \tag{2.79}$$

where $D_{\ell,ref}$ is the reference diffusivity of the solute in the liquid phase and the parameter $\mathcal{M}_i = d_{c,ref}/d_{c,i} = \Delta T_i/\Delta T_{ref}$ has been defined in Section 2.1.2. The parameter ψ_i controls the convergence of the model. The dimensionless temperature and supersaturation are given as

$$\theta = \frac{T - T^e}{\Delta T_{ref}}, \quad U_i = \frac{C_{\ell,i} - C^e_{\ell,i}}{(1 - k_{0,i})C^e_{\ell,i}}. \tag{2.80}$$

which have also been defined in Section 2.1.2. The constants $\alpha_1 = 0.8839$ and $\alpha_2 = 0.6267$ (Ohno, 2012) are identical to the constants from the case of pure materials (Karma and Rappel, 1998), since the same PF interpolation functions are applied.

Anti-trapping current

The driving force of solidification is written in terms of $C_{\ell,i}$, while the concentration in the solid phase is determined as $C_{s,i} = k_{0,i}C_{\ell,i}$. The diffusion of the i-th element is described as

$$\frac{\partial C_i}{\partial t} = \nabla \cdot (D_i(\phi)\nabla C_{\ell,i}), \tag{2.81}$$

where the diffusivity should satisfy $D_i(+1) = k_{0,i}D_{s,i}$ and $D_i(-1) = D_{\ell,i}$. Diffusivity $D_i(\phi) = [k_{0,i}D_{s,i} + D_{\ell,i} + (k_{0,i}D_{s,i} - D_{\ell,i})\phi]/2$ is used in the study. The solution of the system of equations defined by Eq. (2.73) and (2.81) is prone to many anomalous interface effects (Karma, 2001; Echebarria et al., 2004), e.g., solute trapping, interface stretching, surface diffusion, etc. These effects can be eliminated if the so-called *anti-trapping current* (Karma, 2001) is added to Eq. (2.81)

$$\frac{\partial C_i}{\partial t} = \nabla \cdot \left(D_i(\phi)\nabla C_{\ell,i} + a_i(\phi)W(C_{\ell,i} - C_{s,i})\frac{\partial \phi}{\partial t}\frac{\nabla \phi}{|\nabla \phi|} \right), \tag{2.82}$$

where the function $a_i(\phi)$ is defined as

$$a_i(\phi) = \frac{1}{2\sqrt{2}} \left(1 - \frac{k_{0,i} D_{s,i}}{D_{\ell,i}}\right) \psi_i. \tag{2.83}$$

Dimensionless model

By re-scaling the time by τ_0 and the Cartesian coordinates by W_0 according to Eq. (2.66), the dimensionless governing equation for the PF in terms of θ and U is given as

$$\begin{aligned} \Xi(\{U_i\}) a^2(\boldsymbol{n}) \frac{\partial \phi}{\partial t} = -f'_{dw}(\phi) - \hat{g}'(\phi)\lambda \left(\theta + \sum_{i=1}^{N_c-1} \mathcal{M}_i U_i\right) \\ + \nabla \cdot \left(a^2(\boldsymbol{n}) \nabla \phi\right) + \sum_{\xi=x,y} \partial_\xi \left(|\nabla \phi|^2 a(\boldsymbol{n}) \frac{\partial a(\boldsymbol{n})}{\partial(\partial_\xi \phi)}\right), \end{aligned} \tag{2.84}$$

where the same functions $f'_{dw}(\phi) = -\phi + \phi^3$ and $\hat{g}'(\phi) = (1-\phi^2)^2$ as for pure materials from Eq. (2.58) are used. The governing equation for the supersaturation is given as

$$\begin{aligned} &\frac{1}{2}\left(1 + k_{0,i} - (1-k_{0,i}) h(\phi)\right) \frac{\partial U_i}{\partial t} = \frac{1}{2}\left(1 + (1-k_{0,i}) U_i\right) h'(\phi) \frac{\partial \phi}{\partial t} \\ &+ \nabla \cdot \left(\bar{D}_i(\phi) \nabla U_i + a_i(\phi)(1 + (1-k_{0,i}) U_i) \frac{\partial \phi}{\partial t} \frac{\nabla \phi}{|\nabla \phi|}\right), \end{aligned} \tag{2.85}$$

where $\bar{D}_i(\phi) = D_i(\phi)\tau_0 / W_0^2$. The function $h(\phi) = \phi$ is used instead of $g(\phi)$ in the definition of the concentration $C_i = [1 + h(\phi)]C_{s,i}/2 + [1 - h(\phi)]C_{\ell,i}/2$ in the governing equation for U_i due to the better convergence properties of the PF model (Karma and Rappel, 1998). This replacement is allowed since the restrictions $g(\pm 1) = \pm 1$ and $g'(\pm 1) = 0$ have to be applied in the governing equation for PF to ensure an equilibrium solution at $\phi = \pm 1$, while only the restriction $g(\pm 1) = \pm 1$ applies in the governing equation for U_i (Echebarria et al., 2004). The PF model correctly captures the physics of solidification of dilute multi-component alloys if the interface thickness is much smaller than the lowest characteristic diffusivity length. The PF model has only one free parameter ($\bar{D}_{\ell,ref} = \alpha_2 \lambda$), which has to be set according to this condition.

3 Numerical method

The governing equations from Section 2.3 require temporal and spatial discretisations. The forward Euler scheme and the meshless RBF-FD method are used for the temporal and spatial discretisation of PDEs. They are described in Sections 3.1 and 3.2. Discretisation of the conserved thermal noise in the case of solidification of pure materials is presented in Section 3.3. The adaptive solution procedure is presented in Section 3.4.

3.1 Forward Euler scheme

The forward Euler scheme is used for the time-marching of governing equations. The time derivative of a general variable η at t_0, a time at which the solution of η is known, is approximated as

$$\frac{\partial \eta}{\partial t}\Big|_{t_0} \approx \frac{\eta^{t_0+\Delta t} - \eta^{t_0}}{\Delta t}, \tag{3.1}$$

where Δt is the time step. The formula from Eq. (3.1) results in a first-order accurate scheme. The stable time step of the method has to be determined according to the considered system of PDEs and the method for spatial discretisation. If the PF model for solidification is spatially discretisied in 2-D by the FVM with square volumes having side length Δh, the forward Euler scheme is stable when (Provatas and Elder, 2010)

$$\Delta t < \Delta t_0, \quad \Delta t_0 = \frac{1}{4}\frac{\Delta h^2}{\max(\bar{D}, 1/a(\boldsymbol{n}))}, \tag{3.2}$$

where Δt_0 is the reference time step. $\bar{D}$ and $a(\boldsymbol{n})$ are the dimensionless diffusivity of heat (pure materials) or solute (alloys) and the anisotropy function, respectively. Such a condition is formally derived by using a linear stability analysis (Provatas and Elder, 2010). The derivation of the stable time step as

the RBF-FD is used for spatial discretisation of the considered PDEs is not the focus of this dissertation. The stable time step is simply set as

$$\Delta t = \alpha_{\Delta t} \Delta t_0, \tag{3.3}$$

where the stability parameter $\alpha_{\Delta t} < 1$ is determined experimentally. The stability and convergence of the forward Euler scheme is analysed in the range $\alpha_{\Delta t} \in [10^{-2}, 1]$.

3.2 RBF-FD method

The interpolation with RBFs represents the core of the RBF-FD method. The interpolation procedure is presented first, followed by the presentation of the procedure for the evaluation of spatial operators in the computational nodes. For simplicity, the method is presented for the case of scalar fields; however, the same procedure is also used for the case of vector and tensor fields.

3.2.1 Local interpolation with RBFs

We are considering a computational domain Ω with the boundary Γ. The domain is represented by N_Ω nodes ${}_l\boldsymbol{r} \in \Omega \cup \Gamma$, $l = 1, ..., N_\Omega$. A local sub-domain ${}_l\Omega$ consists of N nodes ${}_l\boldsymbol{r}_i \in {}_l\Omega$, $i = 1, ..., N$ where ${}_l\boldsymbol{r}_1 = {}_l\boldsymbol{r}$ and ${}_l\boldsymbol{r}_i \in {}_l\Omega$, $i = 2, ..., N$ are the nearest nodes to ${}_l\boldsymbol{r}$. A local sub-domain is schematically shown in Fig. 3.1. The details of the construction of a local sub-domain are presented in (Mavrič, 2017). The characteristic size of ${}_l\Omega$ is defined as

$${}_lh = \sqrt{\sum_{i=2}^{N} \frac{|{}_l\boldsymbol{r}_i - {}_l\boldsymbol{r}|^2}{N-1}}. \tag{3.4}$$

An arbitrary scalar field η at $\boldsymbol{r} \in \Omega \cup \Gamma$ is approximated as

$$\eta(\boldsymbol{r}) \approx \sum_{i=1}^{N} {}_l\alpha_i \, {}_l\Phi_i(\boldsymbol{r}), \tag{3.5}$$

where ${}_l\boldsymbol{r}$ is the computational node closest to $\boldsymbol{r}$. Constants ${}_l\alpha_i$, $i = 1, ..., N$ are the interpolation coefficients and the function ${}_l\Phi_i$ is a RBF centered at ${}_l\boldsymbol{r}_i$. The

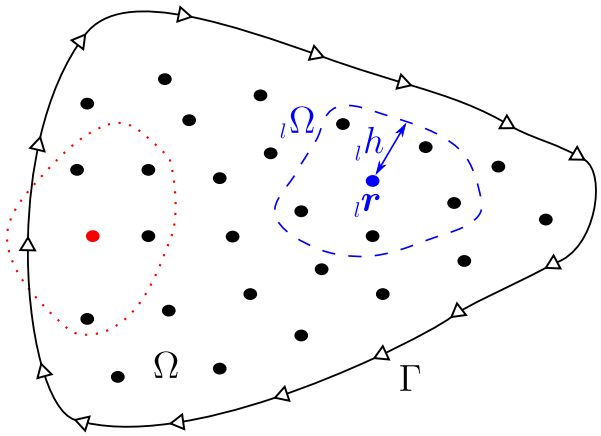

FIGURE 3.1: Illustration of a computational domain Ω and boundary Γ. The solid circles and the empty triangles represent the interior and the boundary computational nodes, respectively. The dashed line represents the boundary of a local sub-domain $_l\Omega$ containing six interior nodes. The boundary of a local sub-domain containing five interior and a boundary node is represented by the dotted line.

application of Eq. (3.5) at each $_l\boldsymbol{r}_i$ from $_l\Omega$ yields a system of equations for coefficients $_l\alpha_i$

$$\begin{bmatrix} {}_l\Phi_1({}_l\boldsymbol{r}_1) & {}_l\Phi_2({}_l\boldsymbol{r}_1) & \dots & {}_l\Phi_N({}_l\boldsymbol{r}_1) \\ {}_l\Phi_1({}_l\boldsymbol{r}_2) & {}_l\Phi_2({}_l\boldsymbol{r}_2) & \dots & {}_l\Phi_N({}_l\boldsymbol{r}_2) \\ \vdots & \vdots & \ddots & \vdots \\ {}_l\Phi_1({}_l\boldsymbol{r}_N) & {}_l\Phi_2({}_l\boldsymbol{r}_N) & \dots & {}_l\Phi_N({}_l\boldsymbol{r}_N) \end{bmatrix} \begin{bmatrix} {}_l\alpha_1 \\ {}_l\alpha_2 \\ \vdots \\ {}_l\alpha_N \end{bmatrix} = \begin{bmatrix} {}_l\eta_1 \\ {}_l\eta_2 \\ \vdots \\ {}_l\eta_N \end{bmatrix}, \tag{3.6}$$

where $_l\eta_i = \eta({}_l\boldsymbol{r}_i)$ are the known field values in the nodes from $_l\Omega$. The system of equations from Eq. (3.6) is well-posed and therefore yields a unique solution if the used RBFs are strictly positive definite functions (Fasshauer, 2007). If conditionally positive or negative definite functions are used, RBFs have to be augmented with monomials to ensure a well-posed interpolation problem

$$\eta(\boldsymbol{r}) \approx \sum_{i=1}^{N} {}_l\alpha_i \, {}_l\Phi_i(\boldsymbol{r}) + \sum_{i=1}^{N_{aug}} {}_l\alpha_{N+i} \, {}_lp_i(\boldsymbol{r}), \tag{3.7}$$

where

$${}_lp_1(\boldsymbol{r}) = 1, \quad {}_lp_2(\boldsymbol{r}) = \frac{x - {}_lx}{{}_lh}, \quad {}_lp_3(\boldsymbol{r}) = \frac{y - {}_ly}{{}_lh}, \quad \dots . \tag{3.8}$$

The number N_{aug} as a function of the highest degree of the augmentation monomials P and the number of dimensions N_{dim} is given as

$$N_{aug} = \frac{(P + N_{dim})!}{P!\, N_{dim}!}. \tag{3.9}$$

The system of equations constructed solely according to Eq. (3.7) is underdetermined and therefore requires additional relations which are obtained from the condition that the vector of RBF coefficients ${}_l\alpha_i$ is orthogonal to the polynomials evaluated at the nodes from ${}_l\Omega$ (Iserles, 2000)

$$\sum_{i=1}^{N} {}_l p_1({}_l\boldsymbol{r}_i)\,{}_l\alpha_i = 0, \quad \sum_{i=1}^{N} {}_l p_2({}_l\boldsymbol{r}_i)\,{}_l\alpha_i = 0, \quad \ldots \quad \sum_{i=1}^{N} {}_l p_{N_{aug}}({}_l\boldsymbol{r}_i)\,{}_l\alpha_i = 0. \tag{3.10}$$

It is mathematically proven (Fasshauer, 2007) that the interpolation with conditionally positive definite RBFs of order $m \geq 2$ is well-posed if the augmentation with monomials at least up to the order $m - 1$ is used. While the positions of the nodes in ${}_l\Omega$ is totally arbitrary in the interpolation by RBFs (Fasshauer, 2007), the nodes have to be unisolvent (Iserles, 2000) if the interpolation problem is augmented by monomials. If a node from ${}_l\Omega$ lies on the boundary Γ where the linear boundary condition $\mathcal{B}(\boldsymbol{r})\eta(\boldsymbol{r}) = b(\boldsymbol{r})$ applies, $\mathcal{B}$ is simply applied to Eq. (3.7) at that node in the construction of the system of equations. The system of equations which accounts for the augmentation with N_{aug} monomials and the boundary condition applied at the node ${}_l\boldsymbol{r}_i \in \Gamma$ reads as

$${}_l\boldsymbol{A}\,{}_l\boldsymbol{\alpha} = {}_l\boldsymbol{\gamma}, \tag{3.11}$$

where

$$
{}_l\boldsymbol{A} = \begin{bmatrix}
{}_l\Phi_1({}_l\boldsymbol{r}_1) & \dots & {}_l\Phi_N({}_l\boldsymbol{r}_1) & {}_lp_1({}_l\boldsymbol{r}_1) & \dots & {}_lp_{N_{aug}}({}_l\boldsymbol{r}_1) \\
{}_l\Phi_1({}_l\boldsymbol{r}_2) & \dots & {}_l\Phi_N({}_l\boldsymbol{r}_2) & {}_lp_1({}_l\boldsymbol{r}_2) & \dots & {}_lp_{N_{aug}}({}_l\boldsymbol{r}_2) \\
\vdots & \vdots & \vdots & \vdots & \ddots & \vdots \\
{}_l\Phi_1({}_l\boldsymbol{r}_{i-1}) & \dots & {}_l\Phi_N({}_l\boldsymbol{r}_{i-1}) & {}_lp_1({}_l\boldsymbol{r}_{i-1}) & \dots & {}_lp_{N_{aug}}({}_l\boldsymbol{r}_{i-1}) \\
\mathcal{B}({}_l\boldsymbol{r}_i){}_l\Phi_1({}_l\boldsymbol{r}_i) & \dots & \mathcal{B}({}_l\boldsymbol{r}_i){}_l\Phi_N({}_l\boldsymbol{r}_i) & \mathcal{B}({}_l\boldsymbol{r}_i){}_lp_1({}_l\boldsymbol{r}_i) & \dots & \mathcal{B}({}_l\boldsymbol{r}_i){}_lp_{N_{aug}}({}_l\boldsymbol{r}_i) \\
{}_l\Phi_1({}_l\boldsymbol{r}_{i+1}) & \dots & {}_l\Phi_N({}_l\boldsymbol{r}_{i+1}) & {}_lp_1({}_l\boldsymbol{r}_{i+1}) & \dots & {}_lp_{N_{aug}}({}_l\boldsymbol{r}_{i+1}) \\
\vdots & \vdots & \vdots & \vdots & \ddots & \vdots \\
{}_l\Phi_1({}_l\boldsymbol{r}_N) & \dots & {}_l\Phi_N({}_l\boldsymbol{r}_N) & {}_lp_1({}_l\boldsymbol{r}_N) & \dots & {}_lp_{N_{aug}}({}_l\boldsymbol{r}_N) \\
{}_lp_1({}_l\boldsymbol{r}_1) & \dots & {}_lp_1({}_l\boldsymbol{r}_N) & 0 & \dots & 0 \\
\vdots & \vdots & \vdots & \vdots & \ddots & \vdots \\
{}_lp_{N_{aug}}({}_l\boldsymbol{r}_1) & \dots & {}_lp_{N_{aug}}({}_l\boldsymbol{r}_N) & 0 & \dots & 0
\end{bmatrix}, \tag{3.12}
$$

$$
{}_l\boldsymbol{\alpha} = \begin{bmatrix} {}_l\alpha_1 \\ \vdots \\ {}_l\alpha_N \\ {}_l\alpha_{N+1} \\ \vdots \\ {}_l\alpha_{N+N_{aug}} \end{bmatrix}, \quad {}_l\boldsymbol{\gamma} = \begin{bmatrix} {}_l\eta_1 \\ \vdots \\ {}_l\eta_{i-1} \\ b({}_l\boldsymbol{r}_i) \\ {}_l\eta_{i+1} \\ \vdots \\ {}_l\eta_N \\ 0 \\ \vdots \\ 0 \end{bmatrix}, \tag{3.13}
$$

where ${}_l\boldsymbol{A}$ is the interpolation matrix, ${}_l\boldsymbol{\alpha}$ is the interpolation coefficients vector, and ${}_l\boldsymbol{\gamma}$ stands for the vector of field values in the sub-domain ${}_l\Omega$.

3.2.2 Evaluation of differential operators

The approximation from Eq. (3.7) is used for the evaluation of any linear differential operator $\mathcal{D}$ applied to a scalar field η in ${}_l\boldsymbol{r} \in \Omega \cup \Gamma$, while the boundary condition in ${}_l\boldsymbol{r} \in \Gamma$ is analytically satisfied in the interpolation problem from

Eqs. (3.11), (3.12) and (3.13). Applying $\mathcal{D}$ to Eq. (3.5) yields

$$\mathcal{D}\eta(\boldsymbol{r}) \approx \sum_{i=1}^{N+N_{aug}} {}_l\alpha_i \mathcal{D}\Psi_i(\boldsymbol{r}), \tag{3.14}$$

since ${}_l\alpha_i$ are constants. ${}_l\boldsymbol{r}$ is the computational node closest to $\boldsymbol{r}$. The function ${}_l\Psi_i$ is either a RBF ($i \leq N$) or a monomial ($i > N$). By calculating the inverse of the matrix ${}_l\boldsymbol{A}$ from Eq. (3.12), Eq. (3.14) applied at ${}_l\boldsymbol{r}$ can be rewritten as

$$\mathcal{D}\eta({}_l\boldsymbol{r}) \approx \sum_{k=1}^{N+N_{aug}} {}_l\gamma_k \sum_{i=1}^{N+N_{aug}} {}_lA_{ik}^{-1} \mathcal{D}\Psi_i({}_l\boldsymbol{r}). \tag{3.15}$$

Eq. (3.15) can now be written in a standard finite-difference-like manner as

$$\mathcal{D}\eta({}_l\boldsymbol{r}) \approx \sum_{k=1}^{N} {}_lw_k \, {}_l\gamma_k, \tag{3.16}$$

where ${}_lw_k$ are the finite-difference-like coefficients of the operator $\mathcal{D}$, defined as

$${}_lw_k = \sum_{i=1}^{N+N_{aug}} {}_lA_{ik}^{-1} \mathcal{D}\Psi_i({}_l\boldsymbol{r}). \tag{3.17}$$

The summation in Eq. (3.16) goes from $k = 1$ to $k = N$, since ${}_l\gamma_k = 0$ for $k > N$ according to Eq. (3.13). For inner local sub-domains, without nodes on the boundary of the computational domain, Eq. (3.16) is reduced to

$$\mathcal{D}\eta({}_l\boldsymbol{r}) \approx \sum_{k=1}^{N} {}_lw_k \, {}_l\eta_k. \tag{3.18}$$

3.2.3 Polyharmonic splines (PHS)

In the dissertation, radial-powers-based PHS are used as RBFs in the interpolation problem. PHS are defined as

$${}_l\Phi_i(\boldsymbol{r}) = \left(\frac{|\boldsymbol{r} - {}_l\boldsymbol{r}_i|}{{}_lh} \right)^n, \quad n = 1, 3, 5, \ldots, \tag{3.19}$$

where n is the (odd) PHS degree. The linear and cubic PHS are shown in Fig. 3.2.

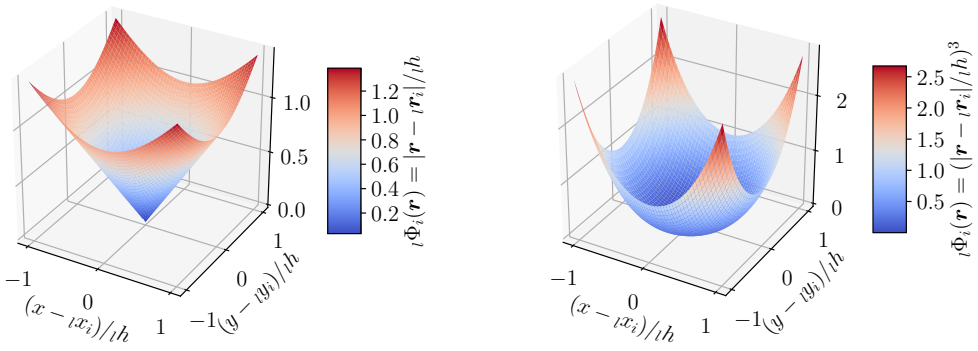

FIGURE 3.2: Linear (left) and cubic (right) PHS centered at the origin ${}_l\boldsymbol{r}_i = ({}_l x_i, {}_l y_i) \in \mathbb{R}^2$.

There are several reasons why the use of PHS augmented by monomials has gained popularity in recent years (Flyer et al., 2016; Bayona et al., 2017):

- the absence of the stagnation error (present if MQs or Gaussian functions are used as RBFs),
- the accuracy of the method is very good,
- no need for a search of the optimal shape parameter (needed if MQs or Gaussian functions are used as RBFs).

The PHS are conditionally positive definite RBFs with order $m = \lceil n/2 \rceil$ (Fasshauer, 2007). For instance, PHS with $n = 3$ have order $m = \lceil 3/2 \rceil = 2$; hence, the interpolation with such PHS is well-posed if augmentation with monomials up to at least the first order is used. It has been shown (Flyer et al., 2016) that the convergence rate of the method is determined by the highest order of the augmentation monomials. It is therefore beneficial to use augmentation with as many monomials as possible to achieve high convergence rates; however, a large number of augmentation monomials requires larger local sub-domains and correspondingly large simulation times. One might rightfully wonder if the polynomial least-squares would provide the same accuracy as the RBF-FD method since the monomials dictate the convergence rate of the method. It has been shown in the same work (Flyer et al., 2016) that the convergence rates are indeed the same if the same polynomials as in polynomial least-squares are used as augmentation in the

RBF-FD method; however, the accuracy of the RBF-FD method is much higher. Additionally, the PHS play an important role in preventing singularities if unusual node distributions are used. The PHS degree has little or no impact on the accuracy of the interpolation. However, if the derivatives of a field value are evaluated, the PHS degree has to be high enough to avoid singularities in the PHS derivative in the collocation points.

In the solution of PDEs by the RBF-FD method, large errors can occur near the boundaries of the computational domain due to one-sided local sub-domains. The use of ghost nodes is one possibility to avoid large errors near the computational boundary. Another possibility is to increase the number of nodes in a local sub-domain. It has been shown (Bayona et al., 2017) that without any special treatment of the boundary, the accuracy of the RBF-FD method is not altered due to one-sided sub-domains if $N \gtrsim 2N_{aug}$.

Selection of the parameters of the RBF-FD method

The focus of the dissertation is not in a detailed study of all the parameters of the RBF-FD method on the performance, since this has already been done in other studies (Flyer et al., 2016; Bayona et al., 2017). We have decided to use the second-order RBF-FD method, which is realised by augmentation with six monomials according to Eq. (3.9). To avoid the problems near the boundaries (Bayona et al., 2017), the best accuracy is expected for $N \gtrsim 12$ in that case. The first and second derivatives have to be evaluated to spatially discretise PDEs from the PF models. In order to avoid the complications in the evaluation of the second derivative at the center of PHS for degree $n = 3$, degree $n = 5$ is used instead. As stated before (Flyer et al., 2016), the choice of the degree does not alter the accuracy of the method. The well-posed interpolation problem for $n = 5$ is already ensured by the second-order augmentation with monomials.

3.3 Discretisation of the conserved thermal noise

In the case of the RND (Karma and Rappel, 1999), the conserved noise is discretised by generating two independent numbers per computational node ${}_{l}\boldsymbol{r}$ at each discretizied time $t_j = j\Delta t$. The numbers are chosen from a Gaussian

distribution with variance

$$\langle q_{l,j} q_{l',j'} \rangle = \frac{2\bar{D}_T F_u}{\Delta t \Delta h^2} \delta_{ll'} \delta_{jj'}. \tag{3.20}$$

In the case of totally independent random numbers, each frequency in the power spectrum $S(k_1, k_2)$ of the random numbers has to have the same magnitude, where k_1 and k_2 represent indices of discrete frequencies in the (regular) two dimensional frequency domain. In order to verify that the discretisation of thermal noise for the RND (Karma and Rappel, 1999) can also be applied if the SND is being used, we calculate $S(k_1, k_2)$ of the random numbers on RND and on SND by using Fourier transformation. The classical two dimensional fast Fourier transformation (FFT) can only be used in the case of RND. In order to calculate power spectrum in the case of SND, non-uniform FFT (NUFFT) (Lee and Greengard, 2005; Greengard and Lee, 2004) has to be used.

In our test case, we construct a RND with $N_{all} = 100 \times 100$ computational nodes in the square computational domain $[-\pi, \pi] \times [-\pi, \pi]$. In the same computational domain, a SND with the same number of computational nodes is constructed. For simplicity, we set $F_u = \Delta t \Delta h^2 / (2\bar{D}_T)$ and generate N_{real} realisations of the noise according to Eq. (3.20). For each realisation, $S(k_1, k_2)$ is calculated by NUFFT (naturally, NUFFT also works for RND). Finally, we perform averaging of $S(k_1, k_2)$ at each pair (k_1, k_2) over N_{real} realisations and plot the minimum, the maximum and the mean value as a function of N_{real} as shown in Fig. 3.3. The expected magnitude in the spectrum is $1/N_{all}$, hence, we multiplied the spectrum values by N_{all} in order to have expected value at $N_{all}/N_{real} \sum^{N_{real}} S(k_1, k_2) = 1$. The average value of the spectrum is for both realisations at 1, while the minimum and the maximum values converge to 1 with convergence rate $1/\sqrt{N_{real}}$. It is evident, that the procedure for discretisation of the conserved thermal noise on a RND (Karma and Rappel, 1999) can also be used on uniform SND.

3.4 Adaptive algorithm

The PF modelling of dendritic growth is a computationally very expensive task. The PF model correctly captures the underlying physics of solidification when the spacing between the computational nodes Δh is smaller than

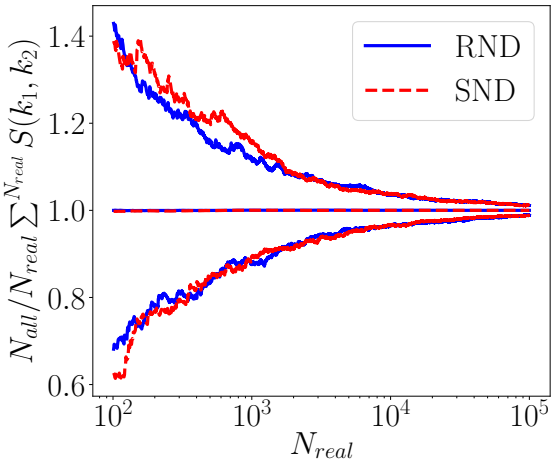

FIGURE 3.3: The mean, minimum, and maximum of averaged power spectrum (over number of realisations) as a function of number of realisations. The spectrum is multiplied by the number of the nodes in the computational domain in order to have expected value at 1.0.

the interface thickness W (Karma and Rappel, 1998; Karma, 2001; Echebarria et al., 2004; Ohno, 2012) although slightly larger values $\Delta h \gtrsim W$ (Tourret and Karma, 2015; Boukellal et al., 2018) can be used if the PF equations are re-scaled by the preconditioned PF (Glasner, 2001). The length scale of the final microstructure of interest is usually at least a few orders of magnitude larger than W, which results in a large number of computational nodes and consequently large computational times if fixed node distributions are used. The requirement for small values of Δh applies only in the areas at and near the solid-liquid interface where the highest gradients of the variables are observed. In the bulk of each phase, much larger values of Δh can be used, which in turn has given rise to the development of adaptive techniques (Provatas et al., 1998; Greenwood et al., 2018; Bollada et al., 2015) that dynamically assure a high density of computational nodes near the solid-liquid interface and a low density in the bulk of phases.

In this section, the adaptive solution procedure, developed in the framework of the dissertation, is presented. The procedure is based on the algorithm from (Greenwood et al., 2018) with three major distinctions:

- the RBF-FD method is used instead of the FD method for the spatial discretisation of the governing equations,
- along with the regular node distribution, the scattered node distribution is applied,
- along with the spacing Δh, the time step Δt is also adaptive.

A scheme of the adaptive solution procedure is shown in Fig.3.4. The solution procedure is based on the quadtree domain decomposition of the computational domain into quadtree sub-domain of different size. Node distribution is generated in each quadtree sub-domain. The h-adaptivity is ensured by keeping the ratio between the side length of a quadtree sub-domain and the spacing between the computational nodes fixed. The adaptive time-stepping is employed to further speed-up the calculations. The stable time step in the forward Euler scheme depends on the density of the computational nodes, hence, different time steps can be used in quadtree sub-domains with different node densities.

The core of the adaptive algorithm is the quadtree data structure presented in Section 3.4.1. The quadtree data structure is used for the dynamic domain decomposition of the computational domain presented in Section 3.4.2. The refinement and de-refinement procedures are formulated in Section 3.4.3 and 3.4.4, respectively. The refinement/de-refinement procedure for the case of PF modelling of solidification is presented in Section 3.4.5. Adaptive time-stepping is formulated in Section 3.4.6. The final solution procedure and the numerical implementation are presented in Sections 3.4.7 and 3.4.8. For the reasons of clarity, the adaptive procedure is presented for the case of square computational domains, although the procedure for rectangular computational domains is exactly the same. The procedure can be extended to describe arbitrary shapes of the computational domain; however, this is not the focus of dissertation.

3.4.1 Quadtree data structure

A tree is a data structure consisting of nodes and links without having any cycles (Knuth, 1997). The nodes are hierarchically organized, so that every

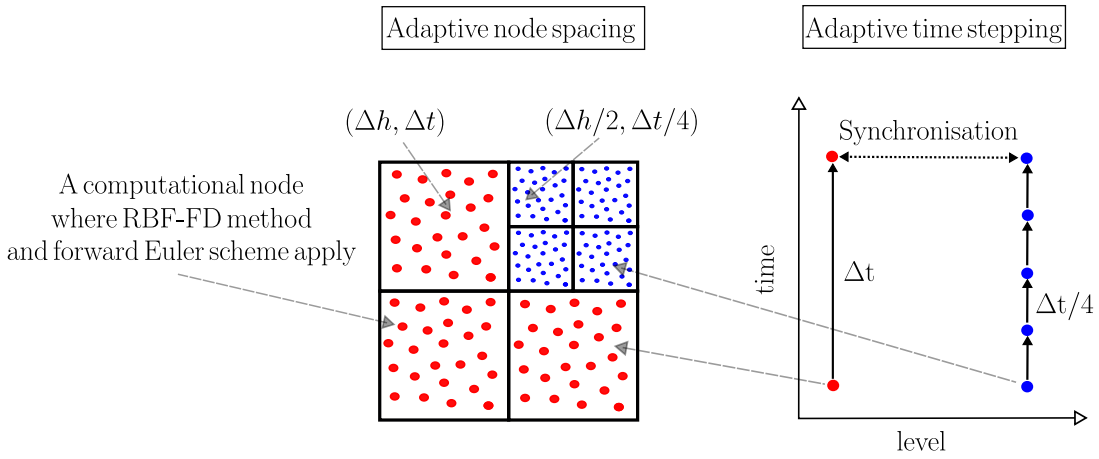

FIGURE 3.4: Scheme of the adaptive solution procedure. The quadtree domain decomposition of computational domain (left). Computational nodes in the quadtree sub-domains on two successive levels of a quadtree are marked red and blue. Time stepping on different levels on a quadtree (right). Different time steps can be applied in quadtree sub-domains since the stable time step in the forward Euler scheme is a function of the node spacing. Time stepping and synchronisation between neighbouring quadtree sub-domains on different levels are marked by solid arrows and the dotted two-way arrow, respectively.

node has at most one parent and an arbitrary number of children. There are three possible types of nodes:

- *root*: a node without a parent,
- *inner node*: a node with a parent and children,
- *leaf*: a node without children.

The level (or depth) $\mathcal{N}$ of the node is defined as

$$\mathcal{N} = \mathcal{N}_{parent} + 1, \quad \mathcal{N}_{root} = 0, \tag{3.21}$$

where $\mathcal{N}_{root}$ and $\mathcal{N}_{parent}$ stand for the root's level and the level of the node's parent, respectively.

Quadtree is a tree data structure in which the root and inner nodes have exactly four children (Finkel and Bentley, 1974). Each node represents a square (or a rectangle), which is divided by the children into four equal sized squares (rectangles) as seen in Fig. 3.5.

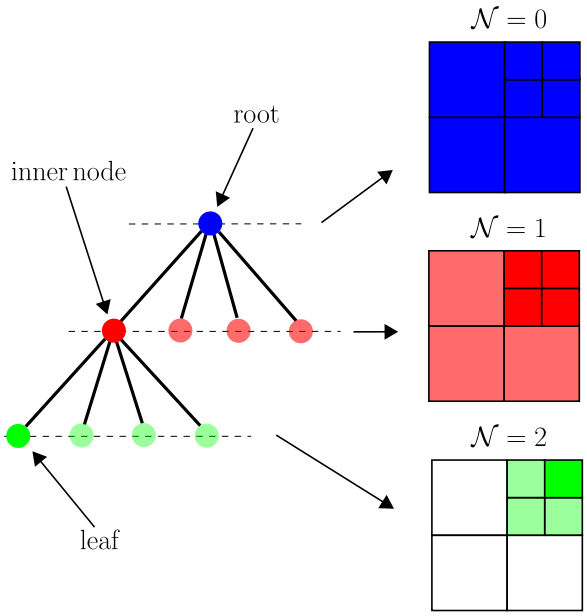

FIGURE 3.5: Scheme of a quadtree data structure.

The quadtree data structure is especially appealing since it allows straightforward dynamical refinement and de-refinement of critical and non-critical areas in the computational domain, i.e., refinement of the areas at the solid-liquid interface and de-refinement of the areas in the bulk of phases. Another appealing feature of the quadtree is the simple and computationally effective search of the nearest neighbours (Samet, 1989).

3.4.2 Quadtree domain decomposition

The quadtree algorithm (Dobravec et al., 2017a) decomposes a square computational domain Ω with side length L into N_p computational sub-domains Ω_i, $i = 1, \dots N_p$ represented by the leaves on a tree. The side length L_i of a square Ω_i is determined according to the level of a leaf as

$$L_i = L/2^{\mathcal{N}}. \tag{3.22}$$

The neighbourhood of a Ω_i is defined as a set of sub-domains $\{\Omega_j\}$, $i \neq j$ which have a common edge or vertex with Ω_i. The neighbourhood is easily determined by the recursive nearest-neighbours search (Samet, 1989). The difference in levels between neighbouring sub-domains defines whether a quadtree is balanced or non-balanced. In a balanced quadtree, this difference is at most one, as shown in Fig. 3.6.

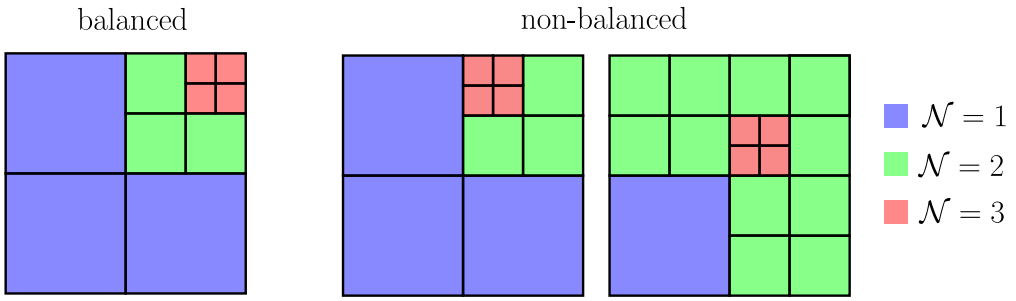

FIGURE 3.6: Examples of balanced and non-balanced quadtrees for non-periodic boundary conditions.

Each Ω_i is discretised by a uniform node distribution with the density of the computational nodes

$$\rho_i = 1/\Delta h_i^2, \tag{3.23}$$

where Δh_i is the characteristic spacing between the neighbouring computational nodes in Ω_i. The h-adaptivity is ensured by the constant product between the density and the area of Ω_i

$$\rho_i L_i^2 = \text{const.} \rightarrow L_i/\Delta h_i = \text{const.}, \tag{3.24}$$

as schematically shown in Fig. 3.7. In order to prevent excessive jumps of the density of computational nodes, care is taken to keep the quadtree balanced.

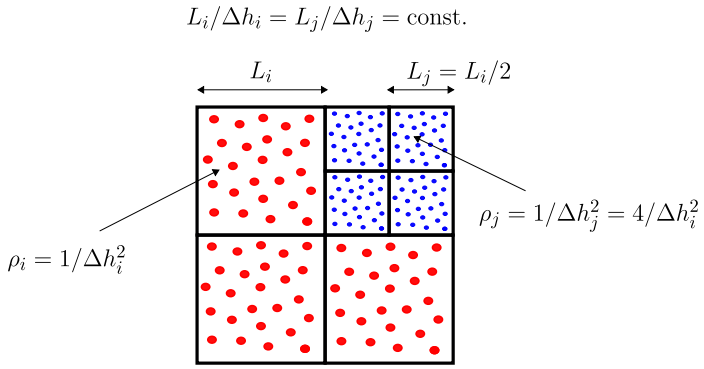

FIGURE 3.7: Scheme of computational nodes in quadtree sub-domains.

Extension of a quadtree sub-domain

The actual computational sub-domain, where the governing equations are solved, is obtained by extending Ω_i to Ω_i^* as shown in Fig 3.8 in order achieve accurate interpolation of the communication field values. The communication between neighbouring sub-domains can in principle be done without extension, however, the overlapping sub-domains make the method much more robust and accurate. Ω_i is extended as

$$L_i \times L_i \rightarrow [L_i + (n^*_{west} + n^*_{east})\Delta h_i] \times [L_i + (n^*_{south} + n^*_{north})\Delta h_i]\,, \tag{3.25}$$

where $n^*_{side} = n^*$ or $n^*_{side} = 0$ and n^* is the overlapping parameter. The choice of $n^*_{side} = 0$ or $n^*_{side} = n^*$ depends on the position of Ω_i in Ω as shown in Fig. 3.8. An interior quadtree sub-domain (third case in Fig. 3.8) is extended in all four sides. A boundary quadtree sub-domain (first two cases in Fig. 3.8) can not be extended outside of Ω which makes $n^*_{side} = 0$ for certain sides.

The governing equations are solved on each Ω_i^* independently. The boundary condition on $\Gamma_i^* \cap \Gamma$ is given by the physical problem, while the condition on $\Gamma_i^* \cap \Omega_j^*$, $i \neq j$ is provided by the interpolation from Ω_j^* to Γ_i^*. That is how communication between two neighbouring domains is achieved.

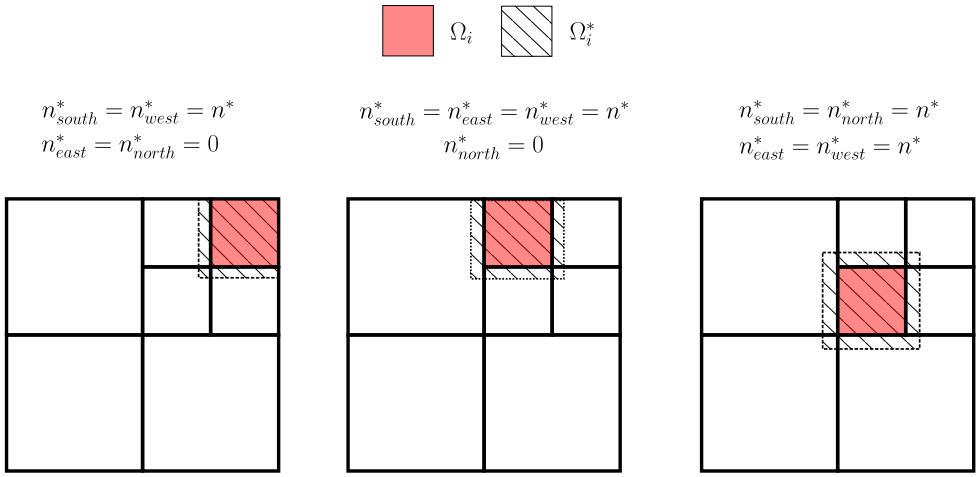

FIGURE 3.8: Extension of a boundary sub-domain with two sides (left) and one side (middle) on the boundary of the computational domain. Extension of an interior sub-domain (right).

Computational node arrangement

The size of Ω_i^* is according to Eq. (3.25) determined by the level $\mathcal{N}$ of Ω_i ($L_i = L/2^{\mathcal{N}}$), the position of Ω_i in Ω, and the prescribed overlapping parameter n^*. The density of computational nodes $\rho_i = 1/\Delta h_i^2$ in Ω_i^* is set according to the prescribed ratio

$$m_\Omega = \frac{L_i}{\Delta h_i}. \tag{3.26}$$

Regular node distribution (RND) or scattered node distribution (SND) is generated in each Ω_i^*. The node distributions are illustrated in Fig. 3.9.

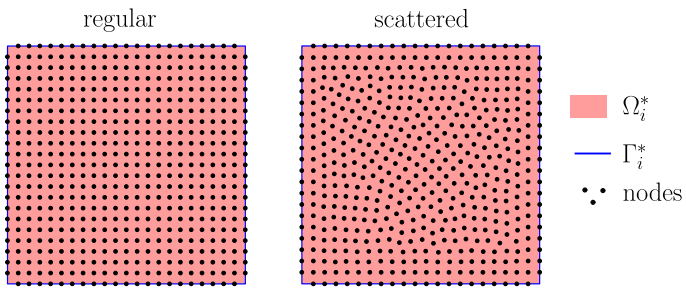

FIGURE 3.9: Discretisation of Ω_i^* and Γ_i^* with regular and scattered node distributions.

While the construction of RND with the spacing Δh_i is straightforward, the generation of SND (Mavrič, 2017; Hatić, 2019) is more complex:

1. Firstly, N_b computational nodes (marked red in Fig. 3.10) are positioned on the boundary Γ_i^* with the spacing Δh_i. The nodes are not positioned at the corners of Ω_i^*.

2. Secondly, N_{ib} first inner nodes (marked blue in Fig. 3.10) are positioned in Ω_i^*. Each boundary node has one first inner node in the opposite direction to the outward-facing normal at the boundary node. The distance between them is Δh_i.

3. Thirdly, $N_i = N_{all} - N_b - N_{ib}$ inner nodes (marked black in Fig. 3.10) are randomly positioned into a polygon determined by the first inner nodes, where N_{all} is the total number of computational nodes in Ω_i^* determined according to the density ρ_i and the area of Ω_i^*.

4. Finally, the positions of randomly distributed inner nodes are adjusted in a minimization process, similar to the one in the node repel algorithm from (Fornberg and Flyer, 2015) in order to obtain locally isotropic node distribution.

The nodes after each of four steps in the generation of uniform node distribution in Ω_i^* are shown in Fig. 3.10. A SND has two parameters: the node density ρ_i and the seed $\mathcal{S}$ of pseudo-random numbers used for the generation of randomly positioned nodes. The different seeds $\mathcal{S}$ yield different SNDs.

3.4.3 Refinement procedure

The refinement procedure ensures the prescribed minimum node spacing Δh_{min} in all sub-domains Ω_i in which the refinement condition is fulfilled as presented in Algorithm 1. The refinement conditions in the case of PF modelling of solidification are discussed in sub-section 3.4.5.

In the refinement algorithm, the refinement condition is checked in each Ω_i^* on the quadtree for which $\Delta h_i > \Delta h_{min}$. The sub-domains in which the condition is fulfilled are flagged (*Step 1* in Algorithm 1). A quadtree is checked again multiple times in order to prevent potential non-balancing. A sub-domain is flagged if a quadtree would become non-balanced after the refinement of

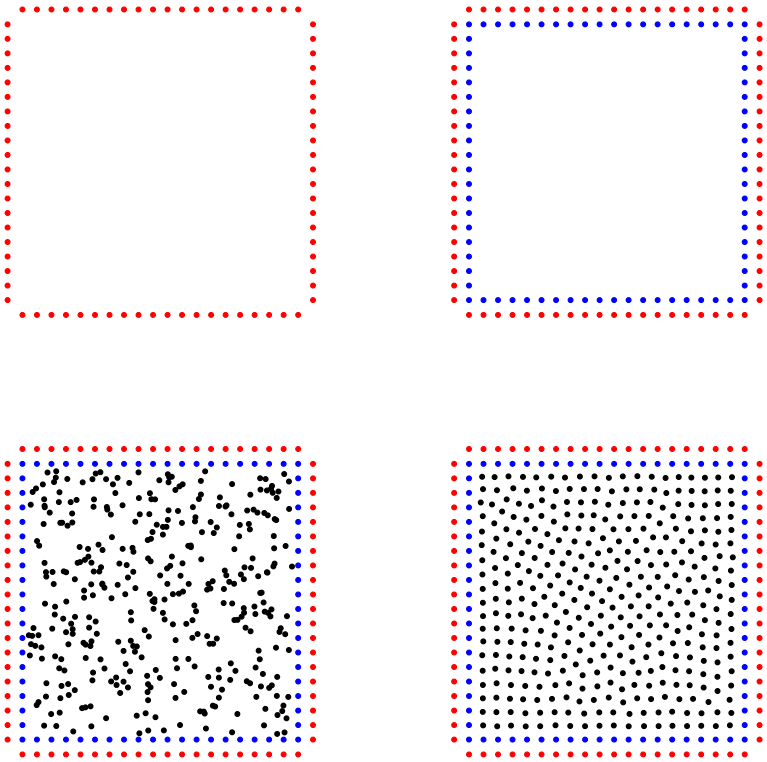

FIGURE 3.10: Nodes after first (top-left), second (top-right), third (bottom-left), and fourth (bottom-right) step in the generation of a scattered node distribution with the uniform density of the computational nodes.

Algorithm 1: Refinement algorithm.

Result: $\Delta h_i = \Delta h_{min}$ in those Ω_i^* where the refinement condition is fulfilled

Step 1: Flag each Ω_i^* with $\Delta h_i > \Delta h_{min}$ in which the refinement condition is fulfilled;

while $\#\text{flags} > 0$ **do**

  Step 2: Flag additional domains to ensure the balancing;

  Step 3: Refinement of each flagged Ω_i^* by four children sub-domains $\{\Omega_i^{j*}\}$;

  Repeat *Step 1*;

end

already flagged sub-domains (*Step 2* in Algorithm 1) as shown in Fig. 3.11. In the refinement (*Step 3* in Algorithm 1), each flagged Ω_i^* is divided by four

child sub-domains $\{\Omega_i^{j*}\}$. The whole procedure is repeated until the number of flagged sub-domains due to the refinement condition in *Step 1* in Algorithm 1 is equal to zero.

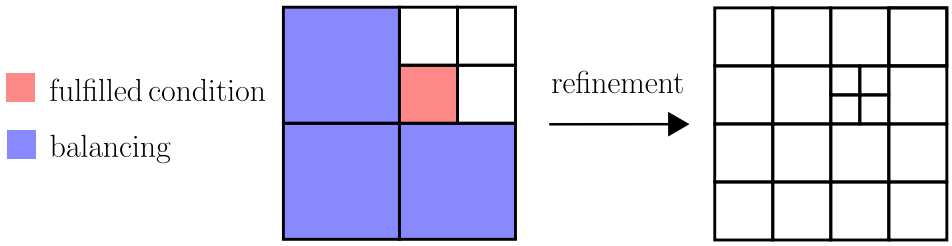

FIGURE 3.11: Refinement of a quadtree sub-domain (red) and an additional refinement of the neighbouring sub-domains (blue) to ensure a balanced quadtree.

When a flagged Ω_i^* is refined by four forming child sub-domains $\{\Omega_i^{j*}\}$, the following steps are performed

1. the computational node distribution is generated in the child sub-domains $\{\Omega_i^{j*}\}$,
2. the governing equations are discretisied in child sub-domains $\{\Omega_i^{j*}\}$ by the RBF-FD method and the forward Euler scheme,
3. the field values in the child sub-domains $\{\Omega_i^{j*}\}$ are interpolated from Ω_i^* and its neighbours,
4. the stored data for the solution of governing equations and interpolation in Ω_i^* is freed.

3.4.4 De-refinement procedure

The de-refinement algorithm ensures the maximum allowed node spacing $\Delta h_i \leq \Delta h_{max}$ in all sub-domains Ω_i^* in which the de-refinement condition is fulfilled as presented in Algorithm 2. The de-refinement conditions in the case of PF modelling of solidification are discussed in sub-section 3.4.5.

In the de-refinement algorithm, the de-refinement condition is checked in each Ω_i^* on the quadtree for which $\Delta h_i < \Delta h_{max}$. The sub-domains in which

Algorithm 2: De-refinement algorithm.

Result: Maximum possible Δh_i in those Ω_i^* where the de-refinement condition is fulfilled

Step 1: Flag each Ω_i^* with $\Delta h_i < \Delta h_{max}$ in which the de-refinement condition is fulfilled if the balancing is sustained after the de-refinement;

while $\#\text{flags} > 0$ **do**

  Step 2: De-refine flagged domains;

  Repeat *Step 1*;

end

the condition is fulfilled are flagged only if the quadtree remains balanced after the potential de-refinement (*Step 1* in Algorithm 2) as shown in Fig. 3.12. In the de-refinement (*Step 2* in Algorithm 2), each flagged Ω_i^* is removed from the quadtree if its siblings are flagged for de-refinement too. The whole procedure is repeated until the number of flagged sub-domains due to the de-refinement condition from *Step 1* in Algorithm 2 is equal to zero.

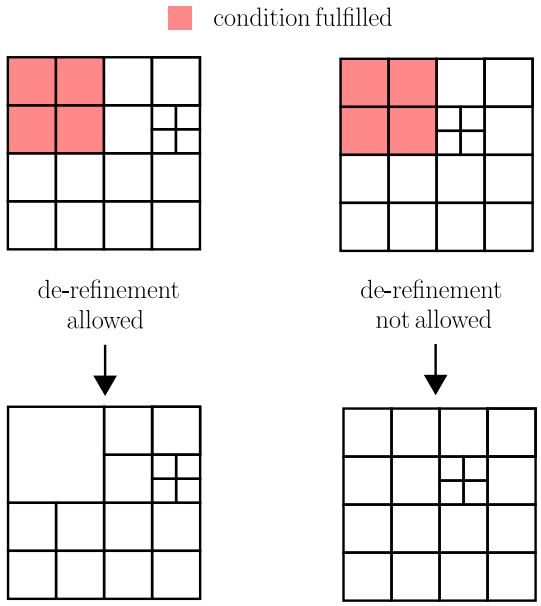

FIGURE 3.12: Sub-domains with allowed refinement (left) and a case of sub-domains with prohibited de-refinement (right) by the constraints imposed by a balanced quadtree.

When the flagged siblings $\{\Omega_i^{j*}\}$ are de-refined, the following steps are performed

1. the computational node distribution is generated in their parent Ω_i^*,
2. the governing equations are discretisied in their parent Ω_i^* by the RBF-FD method and the forward Euler scheme,
3. the field values in the parent Ω_i^* are set by the interpolation from the children $\{\Omega_i^{j*}\}$ and their neighbours.
4. the stored data for the solution of the governing equations and interpolation in siblings $\{\Omega_i^{j*}\}$ is freed.

3.4.5 Refinement/de-refinement conditions

In the PF modelling of solidification, different strategies have been applied to determine the refinement/de-refinement conditions. For instance, the adaptation is triggered when the gradients of the fields exceed a threshold value (Greenwood et al., 2018). In this dissertation, very simple refinement and de-refinement conditions are applied. The conditions were obtained from the preliminary numerical experiments. The accuracy in comparison to the solution, obtained on the uniform node distribution in the whole computational domain, has been analysed in the derivation of the conditions.

The refinement condition ensures the minimum node spacing Δh_{min} in the areas where the PF rapidly changes from $\phi = -1$ to $\phi = 1$. On the other hand, the de-refinement condition ensures the maximum possible spacing (with the upper limit Δh_{max}) in the bulk of the solid and liquid phases. The refinement and de-refinement conditions apply in each $\boldsymbol{r}_i^* \in \Omega_i$, where $\boldsymbol{r}_i^*$ is a node from the computational node distribution generated in the extended sub-domain Ω_i^*. We distinguish two types of refinement conditions. The first type ensures the refinement in the vicinity of the evolving solid-liquid interface, while the second type ensures the refinement according to the initial condition.

Refinement condition

A quadtree sub-domain Ω_i is flagged for the refinement during the simulation if

$$|\phi(\boldsymbol{r}_i^*)| < 0.95, \tag{3.27}$$

for any $\boldsymbol{r}_i^* \in \Omega_i$. The condition from Eq. (3.27) ensures refinement in the vicinity of the evolving solid-liquid interface.

Initial refinement condition

The initial condition for the PF is a solid nucleus with the origin $\boldsymbol{r}_{nuc}$ and the radius R_{nuc}. The condition from Eq. (3.27) is at the beginning of the simulation applied to the computational nodes at the coarsest level with large spacings between the computational nodes. The refinement condition from Eq. (3.27) can fail in the refinement of the initial condition for the PF since all of the computational nodes lie only in the bulk of the phases. An additional refinement condition is therefore applied at the beginning of the simulation. A quadtree sub-domain Ω_i with node spacing h_i is flagged for refinement if

$$\left| |\boldsymbol{r}_i^* - \boldsymbol{r}_{nuc}| - R_{nuc} \right| < 2h_i, \tag{3.28}$$

for any $\boldsymbol{r}_i^* \in \Omega_i$. The condition from Eq. (3.28) ensures refinement in the vicinity of the initial solid-liquid interface.

De-refinement condition

A Ω_i is flagged for de-refinement if

$$|\phi(\boldsymbol{r}_i^*)| > 0.99, \tag{3.29}$$

for all $\boldsymbol{r}_i^* \in \Omega_i$. The condition from Eq. (3.29) ensures de-refinement of the areas in the liquid and solid phase where the PF is almost constant.

An example of the refinement/de-refinement algorithm

An example of the refinement/de-refinement during the solidification of a spherical particle from a pure supercooled melt is shown in Fig. 3.13. The red and blue colors represent the solid ($\phi = 1$) and liquid ($\phi = -1$) phases, respectively, while the white color denotes the solid-liquid interface ($\phi = 0$). The boundaries of the quadtree sub-domains are denoted by a green colour. The PF and the boundaries of the quadtree sub-domains $\{\Omega_i\}$ are plotted for the initial configuration and the next two changes in the quadtree.

In the initial configuration, the algorithm adapts the area around the nucleus according to Eq. (3.28). As the nucleus starts to grow, the condition from Eq. (3.29) is fulfilled in the center of the solid particle which results in de-refinement. When the solid circle is large enough, additional sub-domains in the liquid phase are refined according to Eq. (3.27).

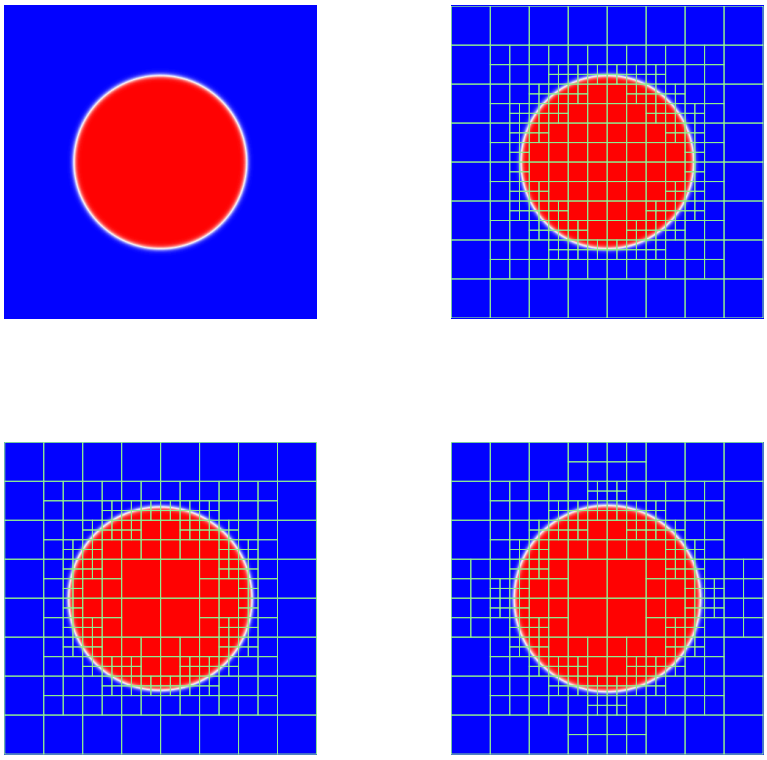

FIGURE 3.13: Initial condition for PF at $t = 0$ (top-left), initial refinement at $t = 0$ (top-right) according to Eq. (3.28), de-refinement at $t = t_1 > 0$ (bottom-left) according to Eq. (3.29), and refinement at $t = t_2 > t_1$ (bottom-right) according to Eq. (3.27) during the solidification of a circular particle.

The refinement and de-refinement conditions apply in the nodes $\boldsymbol{r}_i^* \in \Omega_i$ shown in Fig. 3.14. The conditions do not apply in the nodes $\boldsymbol{r}_i^* \notin \Omega_i$, i.e., the nodes from Ω_i^* which lie in the neighbouring sub-domains. A RND or SND with the constant ratio $L_i/\Delta h_i = 10$ is generated in each Ω_i^* in the example from Fig. 3.14.

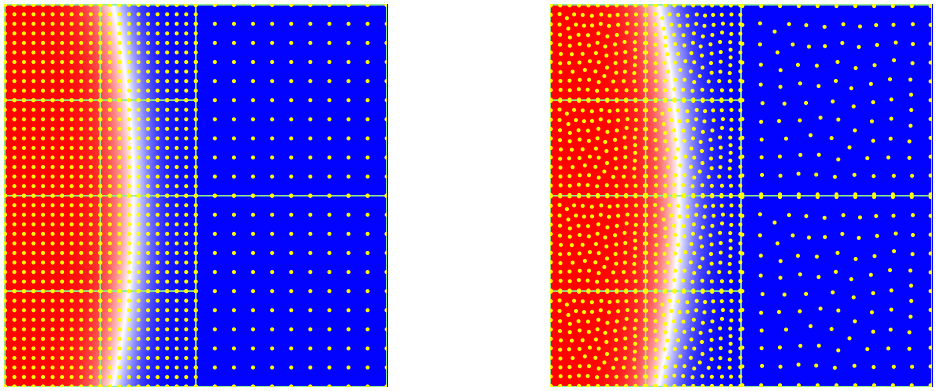

FIGURE 3.14: PF, the boundaries of sub-domains Γ_i (green), and computational nodes $\boldsymbol{r}_i^* \in \Omega_i$ (yellow) from the node distribution generated in extended sub-domains Ω_i^* in the case of RND (left) and SND (right).

3.4.6 Adaptive time-stepping

Time step in the forward Euler scheme

Different time steps can be used in sub-domains with different node densities since the stable time step in the forward Euler scheme is a function of the spacing Δh_i according to Eqs. (3.2) and (3.3). In theory, the maximum stable time step can be used in each Ω_i^* according to the value of Δh_i; however, this is not feasible in practice. The ratio between two stable time steps in the sub-domains with the level difference $\Delta\mathcal{N}$ is $2^{2\Delta\mathcal{N}}$. For example, during one time step in the sub-domains on the level $\mathcal{N}$, 1024 time steps are performed in the sub-domains on the level $\mathcal{N}+5$. Because the solution procedure is designed in such a way that the time stepping on all the computational sub-domains is performed first, followed by the refinement and de-refinement algorithms, the solidification front may "escape" from the sub-domains with Δh_{min} in 1024 iterations, which yields large errors and can even cause the collapse of the calculation. To overcome this problem, the maximum allowed time step is imposed in Ω_i^* as

$$\Delta t_i = \min\left[\, \Delta t(\Delta h_i), \Delta t(2^{m_{\Delta t}} \Delta h_{min})\right], \tag{3.30}$$

where the integer $m_{\Delta t} \geq 0$ stands for the time-step restriction parameter. The same time step $\Delta t_i = \Delta t(\Delta h_{min})$ is used in all the sub-domains if $m_{\Delta t} = 0$. The maximum allowed value of $m_{\Delta t}$ depends on the physical problem. In the cases which are considered in this dissertation, values $m_{\Delta t} = 1$ and $m_{\Delta t} = 2$ are used to ensure the stability of the calculations. Preliminary numerical experiments showed that the values $m_{\Delta t} > 2$ can be problematic, especially at high growth velocities. The introduction of parameter $m_{\Delta t}$ reduces the computational efficiency of the solution procedure in order to ensure stability. Since only very small values of $m_{\Delta t}$ are permitted in the examples considered in the dissertation, the analysis of the impact of $m_{\Delta t}$ on the computational efficiency is not specifically analysed.

Adaptive time-stepping and synchronisation between levels

The adaptive time-stepping is presented using an example with three levels of refinement, as shown in Fig. 3.15. The time step on level $\mathcal{N}$ is two times larger than on level $\mathcal{N} + 1$ in this example. The sequence of events for the case from Fig. 3.15 is

1. A time step is evaluated on level $\mathcal{N} = 1$.
2. A time step is evaluated on level $\mathcal{N} = 2$.
3. Two time steps are evaluated on level $\mathcal{N} = 3$.
4. Synchronisation of levels $\mathcal{N} = 2$ and $\mathcal{N} = 3$.
5. A time step is evaluated on level $\mathcal{N} = 2$.
6. Two time steps are evaluated on level $\mathcal{N} = 3$.
7. Synchronisation of levels $\mathcal{N} = 1$ and $\mathcal{N} = 2$ and $\mathcal{N} = 2$ and $\mathcal{N} = 3$.

During the synchronisation, the field values on the boundary Γ_i^* of an extended quadtree sub-domain Ω_i^* on level $\mathcal{N}$ are interpolated from the neighbouring extended sub-domains on level $\mathcal{N} + 1$ and vice versa. The synchronisation is also done between neighbouring sub-domains on the same level after each time step as seen in the example from Fig. 3.16. The example considers three neighbouring quadtree sub-domains, one on level $\mathcal{N} = 1$ and two on level $\mathcal{N} = 2$.

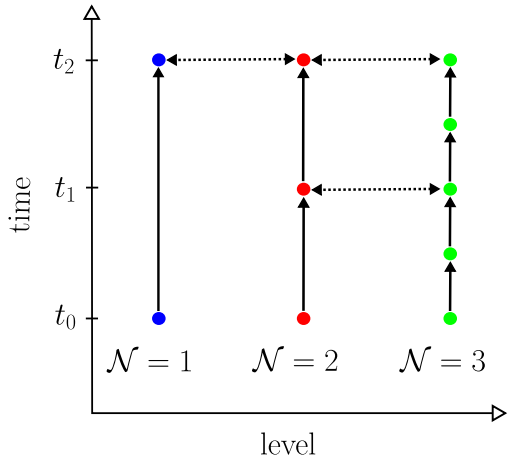

FIGURE 3.15: An example of adaptive time-stepping algorithm for three levels when the time-step on the level $\mathcal{N}$ is two times larger than the time step on the level $\mathcal{N}+1$. A solid arrow represents a time step on a level, while a dotted two-way arrow represents synchronisation between levels. Firstly, one time step on levels $\mathcal{N}=1$ and $\mathcal{N}=2$ and two time steps on level $\mathcal{N}=3$ are evaluated, followed by $\mathcal{N}=2 \leftrightarrow \mathcal{N}=3$ level synchronisation at $t=t_1$. Secondly, one time step on level $\mathcal{N}=2$ and two time steps on level $\mathcal{N}=3$ are evaluated, followed by $\mathcal{N}=1 \leftrightarrow \mathcal{N}=2$ and $\mathcal{N}=2 \leftrightarrow \mathcal{N}=3$ level synchronisation at $t=t_2$.

Adaptive time-stepping algorithm

The time-stepping with different time steps on different levels is implemented by Algorithm 3. In the time-stepping procedure, the extended sub-domains $\{\Omega_i^*\}$ from a quadtree are segmented into sets $\{\Omega_i^*\}_{\mathcal{N}}$ of $N_{\mathcal{N}}$ sub-domains on the level $\mathcal{N}$. Evaluation of a time step in a quadtree sub-domain $\Omega_i^* \in \{\Omega_i^*\}_{\mathcal{N}}$ is independent of the evaluation of a time step in all the other sub-domains from $\{\Omega_i^*\}_{\mathcal{N}}$. Time-stepping in domains $\{\Omega_i^*\}_{\mathcal{N}}$ (*Time step* in Algorithm 3) is therefore performed in parallel. `OpenMP` (Chapman et al., 2008) application programming interface for shared-memory multiprocessing programming is applied for the parallel evaluation of a single time step on level $\mathcal{N}$.

The levels $\mathcal{N}$ and $\mathcal{N}+1$ are synchronised when the solutions on levels $\mathcal{N}$ and $\mathcal{N}+1$ are at the same time. Recursion (*Recursion* in Algorithm 3) is therefore applied to achieve synchronisation between levels $\mathcal{N}$ and $\mathcal{N}+1$.

During the communication, the interpolation of field values is done in Ω_i^* in each boundary node $\boldsymbol{r}_k \in \{\Omega_j^*\}_i^{neigh}$ which lies in Ω_i^*. The neighbourhood

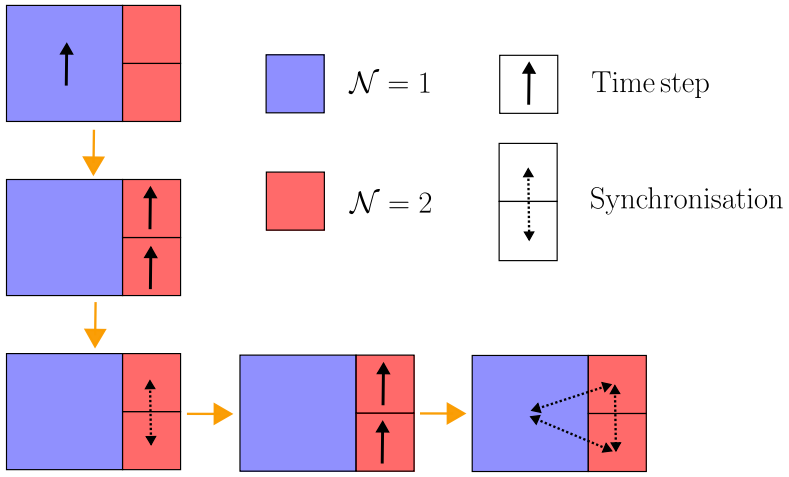

FIGURE 3.16: An example of adaptive time-stepping for three neighbouring quadtree sub-domains on levels $\mathcal{N} = 1$ and $\mathcal{N} = 2$. The solid arrow represents a time step in a sub-domain while the dotted two-way arrow represents the synchronisation between two sub-domains. The time-step on level $\mathcal{N}$ is two times larger than the time step on $\mathcal{N} + 1$ in this example. In the sequence of tasks denoted by orange arrows, a time step in a sub-domain on level $\mathcal{N} = 1$ is evaluated first, followed by a time step in two sub-domains on level $\mathcal{N} = 2$. Next, synchronisation between two sub-domains on level $\mathcal{N} = 2$ is performed, followed by another time step evaluation in these two sub-domains. Finally, synchronisation among all three sub-domains is performed.

$\{\Omega_j^*\}_i^{neigh}$ of each extended sub-domain Ω_i^* is straightforwardly determined by the nearest neighbours search (Samet, 1989) after each change on a quadtree. The neighbouring quadtree sub-domains of a quadtree sub-domain on level $\mathcal{N}$ can lie on levels $\{\mathcal{N} - 1, \mathcal{N}, \mathcal{N} + 1\}$ since a balanced quadtree is used. Interpolation of the field values during the communication (*Communication* in Algorithm 3) in a quadtree sub-domain $\Omega_i^* \in \{\Omega_i^*\}_{\mathcal{N}}$ is also independent of the interpolation of the field values during the communication in all the other sub-domains from $\{\Omega_i^*\}_{\mathcal{N}}$ and is therefore also performed in parallel by `OpenMP`.

3.4.7 Solution procedure

The RBF-FD method and the forward Euler scheme are used for the spatial and the temporal discretisations of the governing equations in each Ω_i^*. The

Algorithm 3: Recursive time-stepping algorithm.

Result: Evaluate a time step on level $\mathcal{N}$
Time step: Evaluate a time step in each $\Omega_i^* \in \{\Omega_i^*\}_{\mathcal{N}}$ in parallel;
if $\mathcal{N} < \mathcal{N}_{max}$ **then**
  while Levels $\mathcal{N}$ and $\mathcal{N}+1$ are not synchronised **do**
    Recursion: Run Algorithm 3 on level $\mathcal{N}+1$;
  end
else
  do nothing;
end
Communication: Interpolate field values to each boundary node $\boldsymbol{r}_k \in \{\Omega_j^*\}_i^{neigh}$ which lies in Ω_i^* for each extended neighbouring quadtree sub-domain $\Omega_i^* \in \{\Omega_i^*\}_{\mathcal{N}}$ in parallel;
.

RBF-FD method is also used for the interpolation of the field values to the boundary nodes in the communication between neighbouring sub-domains and in the interpolation during the refinement/de-refinement procedure. The solution procedure is presented in the Algorithm 4. Firstly, the parameters of the numerical method are set. Next, the refinement according to the initial condition is made. Finally, the iteration starts where each iteration consists of three steps:

- adaptive time-stepping,
- refinement, and
- de-refinement.

3.4.8 Numerical implementation

The novel numerical approach is implemented in the programming language `Fortran` and compiled with the Intel Visual Studio Compiler 19.0. The `Fortran` libraries for the spatial discretisation of the PDEs by meshless methods, for the temporal discretisation, and for the generation of scattered node distribution were already developed in the framework of previous dissertations (Mavrič, 2017; Hatić, 2019) at the Institute of Metals and Technology in Ljubljana, Slovenia. In the framework of this dissertation, the adaptive

Algorithm 4: Solution procedure.

Result: Solution of the governing equations in Ω in the time interval $t \in [t_{start}, t_{end}]$
Initialize RBF-FD method: N, n, P;
Initialize forward Euler scheme: $\alpha_{\Delta t}$;
Initialize adaptive algorithm: Δh_{min}, Δh_{max}, m_Ω, n^*, $m_{\Delta t}$;
Initialize node distribution: $\mathcal{S}$ (for SND);
Initial refinement: execution of Algorithm 1 according to the initial condition;
$t = t_{start}$;
while $t \leq t_{end}$ **do**
    Adaptive time-stepping: execution of Algorithm 3;
    Refinement: execution of Algorithm 1;
    De-refinement: execution of Algorithm 2;
    $t = t + \Delta t_{max}$ (Δt_{max} is the maximum current time step);
end

solution procedure has been developed. Previously developed `Fortran` libraries have been applied for the

- generation of RND or SND in each Ω_i^*, and
- spatial and temporal discretisation of the governing equations in each Ω_i^*.

As already mentioned, the `OpenMP` interface has been used for the shared-memory parallel computations.

Five new modules were developed in the framework of the dissertation:

1. `Cloud`: module for generation of Ω_i^* (computational node distribution, discretisation of PDEs, interpolation, ...).
2. `Qtree`: implementation of quadtree data structure.
3. `QtreeCloud`: extension of quadtree data structure for the use with `Cloud` module.
4. `Communicator`: implementation of communication between `Clouds`.
5. `CloudStructure`: generation of sets $\{\Omega_i^*\}_{\mathcal{N}}$ and implementation of adaptive time-stepping.

Programming language `Python` with the libraries `Matplotlib` and `Numpy` was used for the processing and for the graphical presentation of the numerical results.

4 Numerical experiments

The performance of the developed numerical approach in terms of accuracy and computational efficiency is thoroughly analysed by considering the following numerical experiments:

- solidification from an undercooled pure melt (Karma and Rappel, 1998),
- isothermal solidification from a dilute binary alloy (Karma, 2001), and
- solidification from a dilute Al-Cu alloy with constant cooling rate (Boukellal et al., 2018).

The first two examples are quite standard in the verification of the numerical methods for the PF simulation of solidification. The third example is less standard; however, it is very important and relevant for the PF modelling of dendritic solidification in commercial aluminium alloys and steels.

All the cases consider the growth of a dendrite in 2-D with the cubic anisotropy function

$$a(\boldsymbol{n}) = (1 - 3\epsilon_4)\left(1 + \frac{4\epsilon_4}{1 - 3\epsilon_4}\left({n'}_x^4 + {n'}_y^4\right)\right), \tag{4.1}$$

where ϵ_4 stands for the strength of the cubic anisotropy and $\boldsymbol{n}' = ({n'}_x, {n'}_y)$ is the normal $\boldsymbol{n}$ in the dendrite coordinate system

$$\boldsymbol{n}' = \boldsymbol{R}^{\mathrm{T}}(\theta_0)\boldsymbol{n}, \tag{4.2}$$

where

$$\boldsymbol{R}(\theta_0) = \begin{bmatrix} \cos\theta_0 & -\sin\theta_0 \\ \sin\theta_0 & \cos\theta_0 \end{bmatrix}, \tag{4.3}$$

is the rotation matrix. The dendrite coordinate system is determined according to the preferential growth direction $\boldsymbol{n}_0 = (\cos\theta_0, \sin\theta_0)$, where θ_0 stands for the angle between the x-axis of the computational coordinate system and $\boldsymbol{n}_0$.

In the considered PF examples (Karma and Rappel, 1998; Karma, 2001; Boukellal et al., 2018), the growth of a dendrite that is aligned with the computational coordinate system is considered, i.e., $\boldsymbol{R}$ is the identity matrix ($\boldsymbol{n}' = \boldsymbol{n}$). The first two examples are extended to the growth for an arbitrary preferential growth direction in the present dissertation. More precisely, the growth at values $\theta_0 \in [0, \pi/4]$ is considered due to the cubic anisotropy function. The accurate simulation of growth for arbitrary preferential directions is especially important during the solidification of multiple, differently oriented dendrites, which is the case in the industrial casting of aluminium alloys and steels.

The first example of dendritic solidification is used for the comprehensive analysis of the accuracy and the computational efficiency of the numerical model in Section 4.1. This example is solved by two solution procedures:

- basic solution procedure (BSP): uniform node distribution with constant Δh and Δt in the whole Ω„
- adaptive solution procedure (ASP): adaptive node distribution with dynamic Δh and Δt.

The four possible distributions of computational nodes in Ω are shown in Fig. 4.1. The BSP is used to test the temporal and spatial convergence properties and the accuracy of the method for arbitrary preferential growth directions. The results from the BSP are used to assess the accuracy and speed-up when the ASP is used. The ASP only is used to consider the other two examples from Sections 4.2 and 4.3.

4.1 Solidification of pure materials

In this section, the solidification of pure materials is considered. A 2-D example with dimensionless undercooling $\Delta = 0.65$ and the strength of anisotropy $\epsilon_4 = 0.05$, consistent with data from (Karma and Rappel, 1998), is chosen to verify our newly developed numerical model. In the article, the thin-interface limit of the PF model for the solidification of pure materials is originally formulated. The PF model is numerically solved and successfully verified by the results of the microscopic solvability theory for different values of Δ and ϵ_4.

The problem definition of the solidification of pure materials is given in Section 4.1.1. The time step in the forward Euler scheme is determined in Section

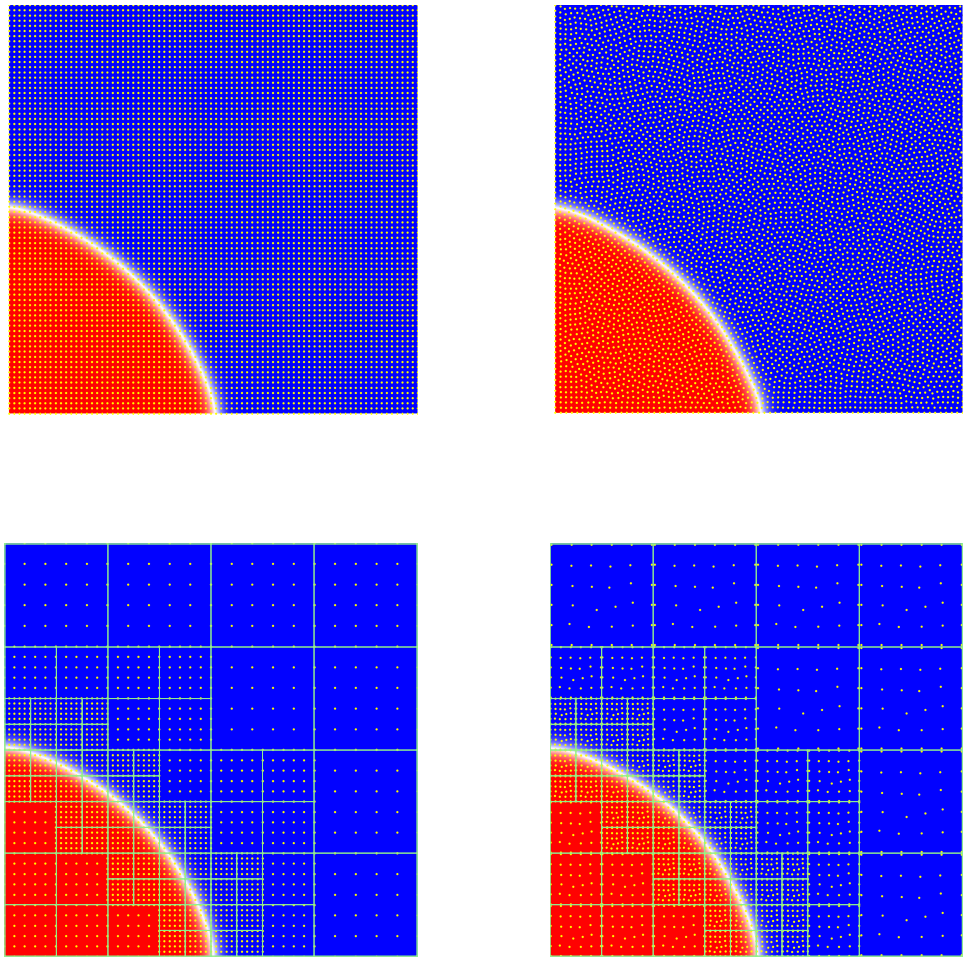

FIGURE 4.1: Four possible distributions of computational nodes (marked yellow) for the PF modelling of dendritic solidification: RND in the case of BSP (top-left), SND in the case of BSP (top-right), RND in the case of ASP (bottom-left), and SND in the case of ASP (bottom-right). Red and blue represent solid and liquid phases, while white denotes the solid-liquid interface. The boundaries of the quadtree sub-domains are marked in green. Value $m_\Omega = 5$ is used in the ASP.

4.1.2. A typical simulation result is shown in Section 4.1.3. Characterisation of the simulation results for the purpose of verification is presented in Section 4.1.4. In Section 4.1.5, the dendritic solidification of pure materials is simulated by using BSP in order to test the accuracy of the forward Euler scheme and the RBF-FD method. The solution obtained by BSP is used to assess the accuracy

and the speed-up of the ASP in Section 4.1.6.

4.1.1 Problem definition

The computational domain Ω with the boundary Γ is a square with the south-west vertex $\boldsymbol{r}_{sw}$ and the side length L, as shown in Fig. 4.2. Solidification of a dendrite from an undercooled pure melt is considered. The system of two coupled governing equations for PF ϕ and the dimensionless temperature θ is given by Eqs. (2.67) and (2.68)

$$\begin{aligned} a^2(\boldsymbol{n})\frac{\partial \phi}{\partial t} = &-\phi(\phi^2-1) - \lambda\theta(1-\phi^2)^2 + \nabla\cdot\left(a^2(\boldsymbol{n})\nabla\phi\right) \\ &+ \sum_{\xi=x,y}\partial_\xi\left(|\nabla\phi|^2 a(\boldsymbol{n})\frac{\partial a(\boldsymbol{n})}{\partial(\partial_\xi\phi)}\right), \end{aligned} \tag{4.4}$$

$$\frac{\partial \theta}{\partial t} = \alpha_2\lambda\nabla^2\theta + \frac{\partial \phi}{\partial t}. \tag{4.5}$$

The anisotropy function $a(\boldsymbol{n})$ is given by Eq. (4.1). The parameter α_2 is constant, which leaves λ as the only free parameter of the PF model. According to the thin-interface relations from Eqs. (2.62) and (2.64), the spatial and temporal coordinates are measured in units of

$$W_0 = d_0\frac{1}{\alpha_1}\lambda, \tag{4.6}$$

and

$$\tau_0 = \frac{d_0^2}{D_T}\frac{\alpha_2}{\alpha_1^2}\lambda^3. \tag{4.7}$$

The initial condition for the dimensionless temperature assumes the constant undercooling in the whole domain Ω

$$\theta(t=0) = -\Delta, \tag{4.8}$$

where Δ stands for the initial dimensionless undercooling. The initial condition for the PF is a circular nucleus with the origin $\boldsymbol{r}_{nuc}$ and the radius R_{nuc}

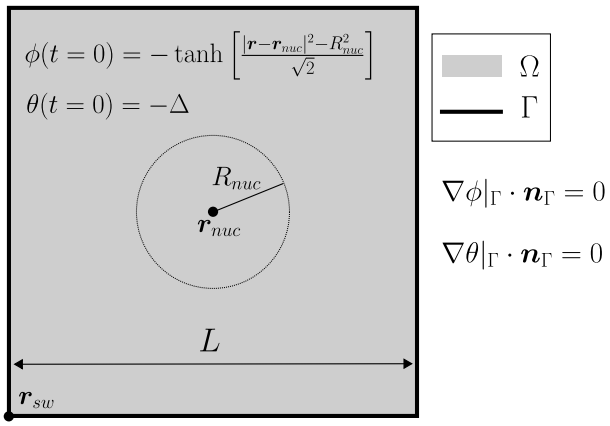

FIGURE 4.2: Illustration of a square computational domain Ω with boundary Γ. A domain is defined by the south-west coordinate $\boldsymbol{r}_{sw}$ and the side length of a square L. Solidification from an undercooled melt is initialized by a small nucleus with radius R_{nuc} and center $\boldsymbol{r}_{nuc}$. Zero flux Neumann boundary conditions are proposed for ϕ and θ.

(Provatas and Elder, 2010)

$$\phi(t=0) = -\tanh\left[\frac{|\boldsymbol{r}-\boldsymbol{r}_{nuc}|^2 - R_{nuc}^2}{\sqrt{2}}\right]. \tag{4.9}$$

In the dissertation, the steady-state growth of a dendrite into an infinite undercooled melt is simulated. A pseudo-infinite undercooled melt is ensured by a large enough Ω with zero flux Neumann boundary conditions for the PF

$$\nabla\phi|_\Gamma \cdot \boldsymbol{n}_\Gamma = 0, \tag{4.10}$$

and for the dimensionless temperature

$$\nabla\theta|_\Gamma \cdot \boldsymbol{n}_\Gamma = 0, \tag{4.11}$$

where $\boldsymbol{n}_\Gamma$ stands for the normal to the boundary Γ. The zero-flux boundary conditions also account for the symmetry if only one-quarter (or one-half) of a dendrite is considered in order to reduce the computational cost of the simulation.

In the dissertation, the example with the undercooling $\Delta = 0.65$ and the

strength of anisotropy $\epsilon_4 = 0.05$ is considered. As already mentioned, this is one of the examples from (Karma and Rappel, 1998) in which the PF model from Eqs. (4.4) and (4.5) is derived. In the same study, the PF free parameter is set to $\lambda = 1/\alpha_2$. In this way, the PF model correctly captures the physics of the Stefan problem with negligible interface kinetics. The simulation parameters used in the study are shown in Table 4.1.

TABLE 4.1: Simulation parameters.

Physical problem parameters	
Strength of anisotropy (ϵ_4)	0.05
Undercooling (Δ)	0.65
Center of nucleus ($\boldsymbol{r}_{nuc}$)	$(0, 0)$
Radius of nucleus (R_{nuc})	10
PF parameters	
Constant (α_1)	0.8839
Constant (α_2)	0.6267
Coupling parameter (λ)	$1/\alpha_2$

4.1.2 Stability criterion in the forward Euler scheme

In the case of pure materials, the time step is given as

$$\Delta t(\Delta h) = \alpha_{\Delta t} \frac{1}{4} \frac{\Delta h^2}{\max(\bar{D}_T, 1/a(\boldsymbol{n}))} \tag{4.12}$$

The term $1/a(\boldsymbol{n})$ from Eq. (4.12) varies as a function of the normal $\boldsymbol{n}$; hence, the minimum of the anisotropy function is used in the stability criterion. The anisotropy function from Eq. (4.1) has minimum $1-\epsilon_4$ at $\boldsymbol{n} = (\cos \pi/4, \sin \pi/4)$. The time step is therefore given as

$$\Delta t(\Delta h) = \alpha_{\Delta t} \frac{1}{4} \frac{\Delta h^2}{\max(\bar{D}_T, 1/(1-\epsilon_4))} \tag{4.13}$$

The parameters from Table 4.1 yield

$$\Delta t(\Delta h) = \alpha_{\Delta t}(1-\epsilon_4)\Delta h^2/4, \tag{4.14}$$

since $\bar{D}_T = \lambda\alpha_2 = 1$ and therefore $\bar{D}_T < 1/(1-\epsilon_4)$. The actual time step in a extended quadtree sub-domain Ω_i^* with spacing Δh_i is according to Eq. (3.30) from the sub-section 3.4.6 given as

$$\Delta t_i(\Delta h_i) = \alpha_{\Delta t}(1-\epsilon_4)\min\left(\Delta h_i^2, 2^{2m_{\Delta t}}\Delta h_{min}^2\right)/4, \tag{4.15}$$

since the restriction parameter has to be additionally considered in the ASP.

4.1.3 Solution of PF model

The solution of the PF model with the simulation parameters from Table 4.2 is shown in Figs. 4.3 and 4.4. Due to symmetry, only one quarter of a dendrite is considered. The solid ($\phi = 1$) and liquid ($\phi = -1$) phases are marked red and blue, respectively. The solid-liquid interface ($\phi = 0$) is marked white. The boundaries of the quadtree sub-domains are marked green.

At the beginning of the simulation, the whole Ω is undercooled below the melting temperature ($\theta < 0$). As the growth starts, the latent heat is released to both the solid and liquid phases, as seen in Fig. 4.4 at $t = 25$. The temperature in the solid phase quickly reaches the melting temperature ($\theta = 0$). From then on, the latent heat is released only in the liquid phase and away from the solid-liquid interface.

4.1.4 Characterisation of simulation results

A very important issue in the verification of numerical models is the appropriate characterisation of the simulation results from Fig. 4.3 and 4.4. The steady-state growth velocity v_{tip}^{steady} of a dendrite growing into an undercooled, infinitely large, domain turns out to be the most suitable observable (Jokisaari et al., 2018) for the verification of different numerical methods. The numerically calculated v_{tip}^{steady} can be directly compared to the v_{tip}^{steady} obtained in the framework of the microscopic solvability theory (Kessler and Levine, 1986) for dendritic solidification.

In order to estimate the dimensionless growth velocity $v_{tip}(t)$ during a PF simulation, the dimensionless distance l_{tip} between the center and the tip of a dendrite as a function of time has to be measured. The distance l_{tip} at an arbitrary preferential growth direction is calculated with the following procedure:

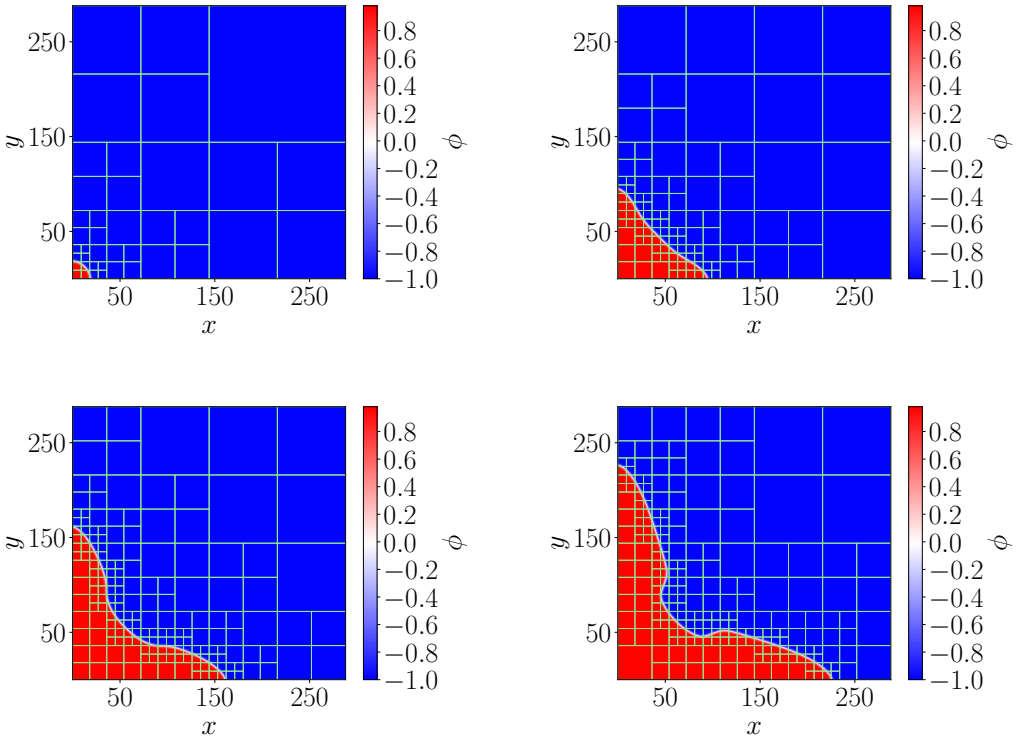

FIGURE 4.3: PF at $t = 25$ (top-left), $t = 850$ (top-right), $t = 1675$ (bottom-left), and $t = 2500$ (bottom-right). Red and blue represent the solid and liquid phases, respectively. White represents the solid-liquid interface, while the boundaries of the quadtree sub-domains are marked green.

- The preferential growth direction $\boldsymbol{n}_0$ is discretisied as

$$\boldsymbol{r}_i = \boldsymbol{r}_{nuc} + i\Delta h_{min}\boldsymbol{n}_0 \quad i = 1, 2, 3, \ldots . \tag{4.16}$$

- The phase field is interpolated to the points from Eq. (4.16) and the values are checked, until two sequential points for which $\phi(\boldsymbol{r}_i) > 0$ and $\phi(\boldsymbol{r}_{i+1}) < 0$ are found.

- We take into account that the solution of the PF model in one dimension is the $\tanh$ function and estimate l_{tip} as the solution to the following system of two equations with two unknowns

$$\phi(\boldsymbol{r}_k) = -\tanh\left(\frac{|\boldsymbol{r}_k - \boldsymbol{r}_{nuc}| - l_{tip}}{\sqrt{2}W_0}\right), \quad k = i, i+1. \tag{4.17}$$

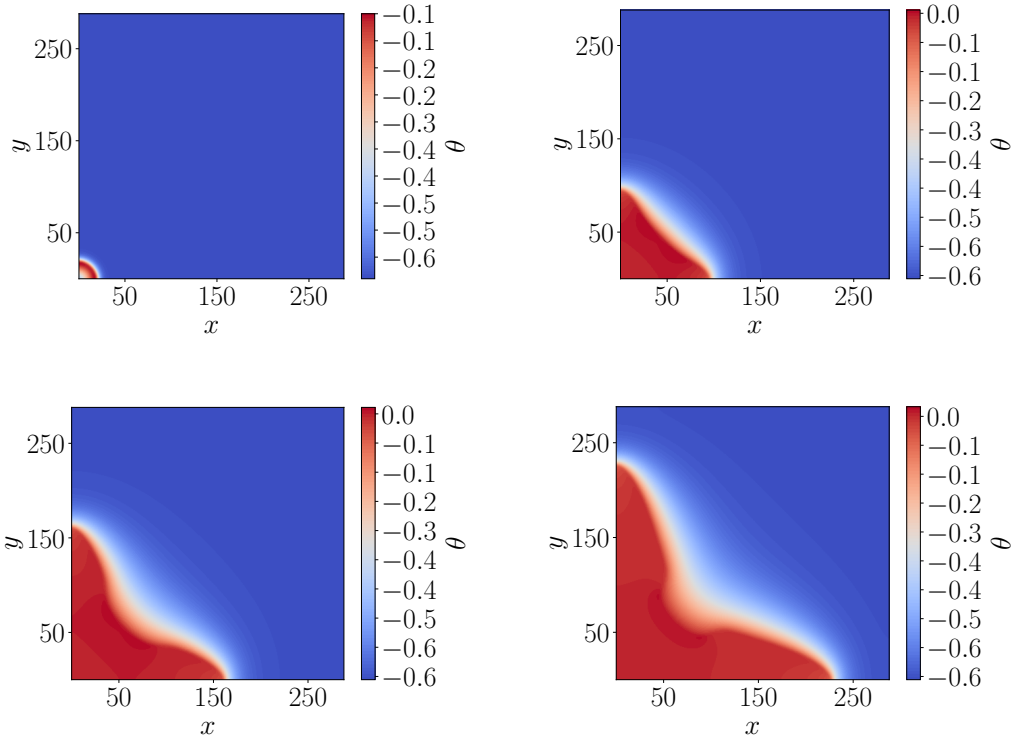

FIGURE 4.4: Dimensionless temperature at $t = 25$ (top-left), $t = 850$ (top-right), $t = 1675$ (bottom-left), and $t = 2500$ (bottom-right).

The distance l_{tip} is measured at discrete times

$$t_i^{mea} = t_0^{mea} + i\Delta t^{mea},\ i = 0, 1, 2, 3, \ldots, \tag{4.18}$$

where t_i^{mea} and Δt^{mea} stand for the i-th dimensionless measuring time and the dimensionless time difference between the two measuring times, respectively. In our case, the values $t_0^{mea} = 10$ and $\Delta t^{mea} = 10$ are used. The growth velocity is simply calculated as

$$v_{tip}(t_i^{mea}) = \frac{l_{tip}(t_{i+1}^{mea}) - l_{tip}(t_i^{mea})}{t_{i+1}^{mea} - t_i^{mea}}. \tag{4.19}$$

For the purpose of the verification of numerical methods, it is convenient to re-scale the dimensional growth velocity $\tilde{v}_{tip} = v_{tip}W_0/\tau_0$ in such a way that the solution no longer depends on the capillary length d_0 and the diffusivity D_T, but solely on the undercooling Δ and the strength of the anisotropy ϵ_4 (Karma

TABLE 4.2: Simulation parameters for the results from Figs. 4.3 and 4.4.

Preferential growth direction	
Growth angle (θ_0)	$0°$
Computational domain parameters	
Side length (L)	288
South-west coordinate ($\boldsymbol{r}_{sw}$)	$(0, 0)$
Simulation time	
Initial simulation time (t_{start})	0
Final simulation time (t_{end})	2500
Forward Euler scheme	
Stability parameter ($\alpha_{\Delta t}$)	0.3
Time step (Δt)	$\alpha_{\Delta t}(1-\epsilon_4)\Delta h^2/4$
RBF-FD method	
Number of nodes in sub-domain (N)	13
PHS power (n)	5
Highest monomial order (P)	2
Adaptive algorithm	
Type of node distribution	RND
Sub-domain size/spacing ratio (m_Ω)	15
Overlapping parameter (n^*)	1
Minimum spacing (Δh_{min})	0.6
Maximum spacing (Δh_{max})	$L/(2m_\Omega)$
Time step-restriction parameter ($m_{\Delta t}$)	2

and Rappel, 1998)

$$\tilde{v}_{tip} \to \tilde{v}_{tip} d_0/D_T, \tag{4.20}$$

The re-scaled dimensional velocity is according the definition of W_0 and τ_0 (see Eqs. (4.6) and (4.7)) calculated as

$$\tilde{v}_{tip} = v_{tip}\frac{W_0}{\tau_0}\frac{d_0}{D_T} = v_{tip}\frac{\alpha_1}{\alpha_2}\frac{1}{\lambda^2}. \tag{4.21}$$

The observables l_{tip} and v_{tip} are obtained by the post-processing of the simulation results. The post-processing itself introduces an error; however, the post-processing error of l_{tip} is much smaller than the post-processing error of

the derivative $v_{tip} = \mathrm{d}l_{tip}/\mathrm{d}t$. The distance l_{tip} at different values of the numerical parameters is therefore considered when the convergence of the numerical method is discussed. The velocity v_{tip} at the converged solution is then compared to the result of the microscopic solvability theory.

The distance l_{tip} and velocity v_{tip} as a function of time for the example from Section 4.1.3 are shown in Fig. 4.5. At the beginning of the growth, a transient with a rapid decrease of the velocity is observed, followed by the steady-state growth. In the calculation of l_{tip}, a small error is introduced, which is further amplified in the calculation of $v_{tip} = \mathrm{d}l_{tip}/\mathrm{d}t$. The averaging with five points from the data set $\{t_i^{mea}, v_{tip}(t_i^{mea})\}$ is therefore applied in the representation of the velocity $v_{tip}(t)$, as shown in Fig. 4.5.

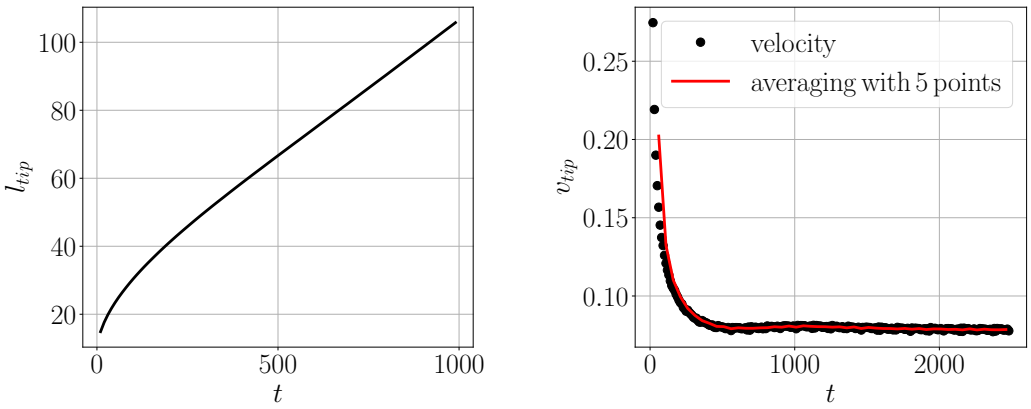

FIGURE 4.5: Distance between the origin and the tip of a dendrite (left) and the growth velocity as a function of time (right). The growth velocity, calculated at discrete times according to Eq. (4.19), is marked black. Averaging with five points of those values is marked red.

4.1.5 BSP

The numerical model is first tested on the BSP in order to later evaluate the accuracy and computational efficiency of the ASP. The results from this subsection were published in (Dobravec et al., 2020).

Convergence of the forward Euler scheme

The aim of this section is to determine the stable time step in the forward Euler scheme, while the second-order accurate RBF-FD method with different values of N is used for the spatial discretisation of the PDEs on RND and SND. To achieve this goal, the cases with the simulation parameters from Table 4.3 are considered. The values N represent symmetric stencils when using a RND. The origin of the dendrite is set in the middle of the left side of the square, since we want to have the interpolation points from Eq. (4.16) inside the computational domain (not on the boundary). The interpolation to the boundary is actually an extrapolation that can likely result in large errors.

TABLE 4.3: Simulation parameters for the analysis of the forward Euler scheme.

Preferential growth direction	
Growth angle (θ_0)	0°
Computational domain parameters	
Side length (L)	240
South-west coordinate ($\boldsymbol{r}_{sw}$)	$(0, -L/2)$
Time	
Initial time (t_{start})	0
Final time (t_{end})	1500
Forward Euler scheme	
Stability parameter ($\alpha_{\Delta t}$)	$0.3, 0.15, 0, 075, 0.0375, 0.01875$
Time step (Δt)	$\alpha_{\Delta t}(1-\epsilon_4)\Delta h^2/4$
RBF-FD method	
Number of nodes in sub-domain (N)	$9, 13, 21$
PHS power (n)	5
Highest monomial order (P)	2
Node distribution	
Type of node distribution	RND, SND (fixed $\mathcal{S}$)
Spacing (Δh)	0.5

We are simulating the steady-state growth of a dendrite into an infinite undercooled melt. In order to simulate the steady state, the final simulation time has to be large enough in order to pass the initial transient regime. A

pseudo-infinite undercooled melt is ensured by a large enough Ω, for which the impact of Γ on $\tilde{v}_{tip}$ is negligible. The temperature field in Ω and the temperature as a function of x at three positions of y at the end of the simulation are shown in Fig. 4.6. The temperature at $x = L$ is not affected by the growing dendrite; hence, Γ does not alter the growing dendrite in the x-direction. The parameters from Table 4.3 therefore ensure a pseudo-infinite domain. The same size of domain Ω is also used in (Karma and Rappel, 1998).

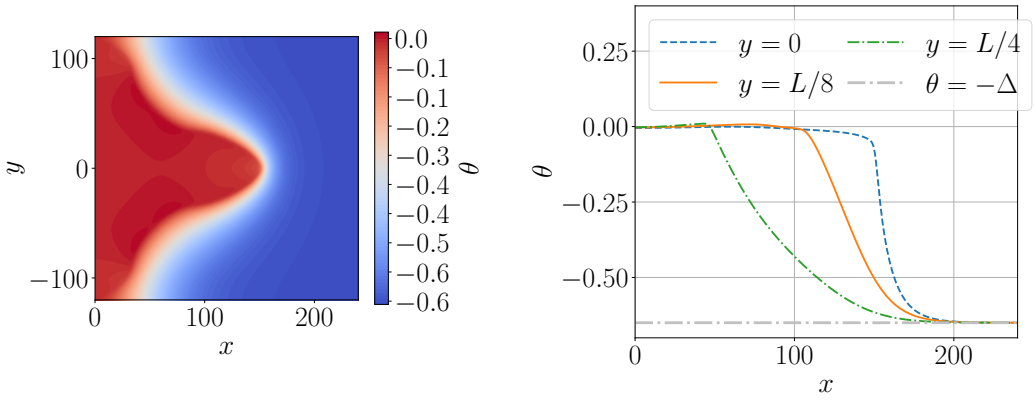

FIGURE 4.6: Temperature field (left) and temperature as a function of x at three positions of y (right) at the end of the simulation.

The model is tested for the values $\alpha_{\Delta t} \leq 0.3$ from Table 4.3. We find that the model is not stable for $\alpha_{\Delta t} > 0.3$ for each value of N. The relative error is defined as

$$\frac{\Delta l_{tip}}{l_{tip}} = \frac{|l_{tip}^{end}(\alpha_{\Delta t}) - l_{tip}^{end}(\alpha_{\Delta t} = 0.01875)|}{l_{tip}^{end}(\alpha_{\Delta t} = 0.01875)}, \tag{4.22}$$

where $l_{tip}^{end} = l_{tip}(t = t_{end})$. The relative error as a function of $\alpha_{\Delta t}$ for different values of N on RND and SND is shown in Fig. 4.7. As expected, first-order convergence is observed on both node distributions. The solution with $\alpha_{\Delta t} = 0.3$ and $N = 21$ on a RND is stable; however, inaccurate with a relative error greater than $10\,\%$. First-order convergence is observed for $\alpha_{\Delta t} \leq 0.15$ in this case.

The growth velocity at $\alpha_{\Delta t} = 0.0375$ is compared to the velocity obtained by the microscopic solvability theory (MST). The steady-state growth velocities for different values of Δ and ϵ_4, obtained by the MST (Kessler and Levine, 1986), are tabulated in (Karma and Rappel, 1998). The steady-state growth

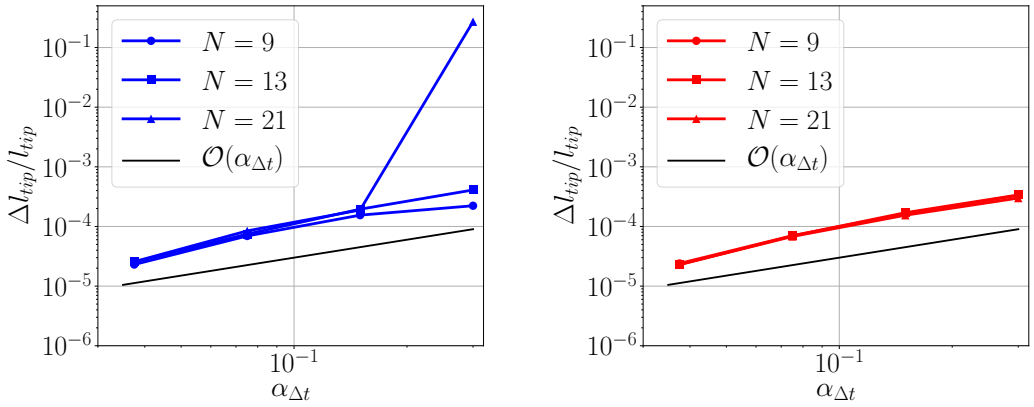

FIGURE 4.7: Relative error of l_{tip} as a function of the forward Euler scheme stability parameter $\alpha_{\Delta t}$ by using RND (left) and SND (right).

velocity for $\Delta = 0.65$ and $\epsilon_4 = 0.05$ is according to MST equal to $\tilde{v}_{tip}^{steady} = 0.0469$.

The growth velocity as a function of time for three values of N on RND and SND is shown in Fig. 4.8. In the case of RND, the solution is converging with the reduction of $\alpha_{\Delta t}$ according to Fig. 4.7; however, not to the correct value obtained by the solvability theory for $N = 9$, although a small value $\Delta h = 0.5$ is used. In the case of SND, the solution is converging with the reduction of $\alpha_{\Delta t}$ to the correct value obtained by the solvability theory for all values of N. This is an interesting observation, which is also observed in the next sections.

Convergence of the RBF-FD method

According to the study of (Bayona et al., 2017), the order of the RBF-FD method is determined by the highest order of augmentation monomials. Authors also showed that the one-sided local sub-domains near the domain boundary do not alter the accuracy of the method when the number of nodes in a local sub-domain N is approximately twice as large as the number of augmentation monomials N_{aug}. In our study, we apply second-order ($P = 2$) augmentation, which yields $N_{aug} = 6$ augmentation monomials. The convergence of the RBF-FD method on RND and SND is tested for the case with $N = 13$. Again, steady-state growth is simulated with the parameters from Table 4.4.

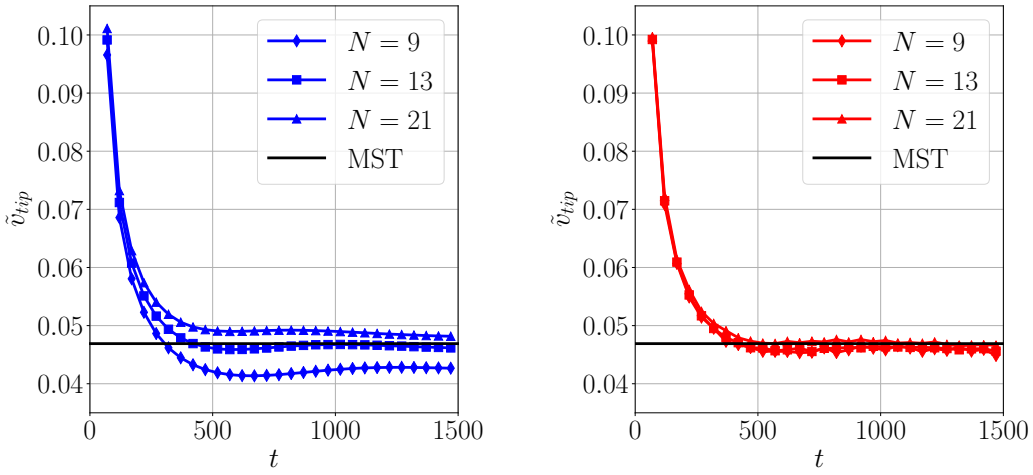

FIGURE 4.8: Re-scaled growth velocity as a function of time using RND (left) and SND (right) with $\alpha_{\Delta t} = 0.15$.

The distances $l_{tip}^{end} = l_{tip}(t = t_{end})$ are calculated on RND and SND for each value of Δh from Table 4.4. The Richardson extrapolation (RE) (Širca and Horvat, 2018) is applied to determine the order of the method since the further reduction of Δh would be computationally too expensive. In the RE, the solution $l_{tip}^{end}(\Delta h)$ is written as

$$l_{tip}^{end}(\Delta h) = l_{tip}^{end,RE} + C_{RE}\Delta h^{n_{RE}}, \tag{4.23}$$

where $l_{tip}^{end,RE}$, C_{RE}, and n_{RE} are the distance we wish to approximate, a constant, and the order of RE, respectively. The values of l_{tip}^{end} for $\Delta h \in \{0.2, 0.4, 0.6\}$ are considered in the RE to obtain a system of three non-linear equations for three unknowns $(l_{tip}^{end,RE}, C_{RE}, n_{RE})$ according to Eq. (4.23). The bisection method is used to solve the system. The results of the numerical simulations along with the results of the RE are given in Table 4.5.

As expected, second-order convergence is observed on RND. Interestingly, sixth-order convergence is observed on SND; however, this does not mean that the order of the method is actually so high. The determination of l_{tip} experiences an error which is lower in the case of RND where the computational nodes coincide with the points from Eq. (4.16) and higher in the case of SND. The distance $l_{tip}^{end,RND}$, $l_{tip}^{end,RE}$ obtained on RND, is therefore chosen as the value

TABLE 4.4: Simulation parameters for the analysis of the RBF-FD method.

Preferential growth direction	
Growth angle (θ_0)	$0°$
Computational domain parameters	
Side length (L)	240
South-west coordinate ($\boldsymbol{r}_{sw}$)	$(0, -L/2)$
Time	
Initial time (t_{start})	0
Final time (t_{end})	1500
Forward Euler scheme	
Stability parameter ($\alpha_{\Delta t}$)	0.1
Time step (Δt)	$\alpha_{\Delta t}(1-\epsilon_4)\Delta h^2/4$
RBF-FD method	
Number of nodes in sub-domain (N)	13
PHS power (n)	5
Highest monomial order (P)	2
Node distribution	
Type of node distribution	RND, SND (fixed $\mathcal{S}$)
Spacing (Δh)	$0.8, 0.6, 0.4, 0.2$

TABLE 4.5: Distance l_{tip}^{end} on RND and SND for different values of Δh and the results of RE.

Δh	RND	SND
0.8	142.54	140.93
0.6	141.99	141.12
0.4	142.57	142.67
0.2	142.93	142.81
$l_{tip}^{end,RE}$	143.06	142.81
n_{RE}	1.94	6.14

to which the solutions on both node distributions should converge to. The relative error

$$\frac{\Delta l_{tip}}{l_{tip}} = \frac{|l_{tip}^{end} - l_{tip}^{end,RND}|}{l_{tip}^{end,RND}}, \tag{4.24}$$

as a function of Δh is shown in Fig. 4.9. A small deviation from the second-order convergence is observed in the case of SND due to the previously discussed error in the determination of l_{tip}.

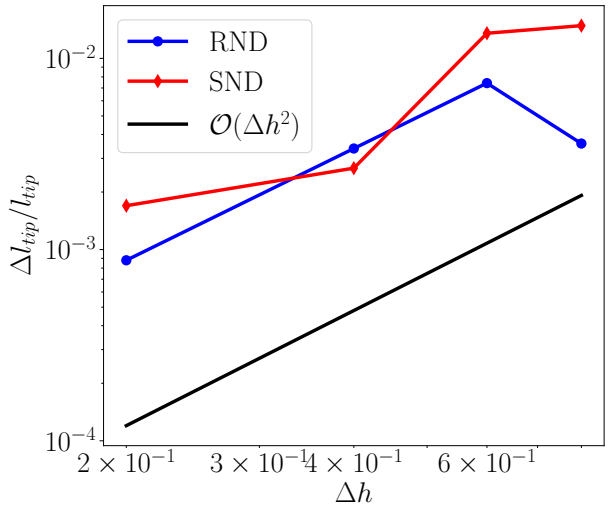

FIGURE 4.9: The relative error as a function of the spacing using RND and SND.

Performance at arbitrary preferential growth directions

In the previous two sections, the growth along the x-axis of the coordinate system is considered ($\theta_0 = 0$). In this section, the performance of the method for arbitrary preferential growth directions is studied. The solid-liquid interface at the end of the simulation for three different preferential growth directions is shown in Fig. 4.10. The origin of the solid nucleus is put in the middle of Ω in this case; hence, side L has to be twice as large. The method is tested for the values of θ_0 in the range $\theta_0 \in [0°, 45°]$ with the orientation step of $5°$, as shown in Table 4.6.

The growth velocity at the end of the simulation as a function of θ_0 for $N = 13$ and two values of Δh on RND and SND is shown in Fig. 4.11. The re-scaled growth velocity, obtained in the framework of the MST, is also plotted. In the case of RND, $\tilde{v}_{tip}^{steady}$ departures from the MST growth velocity as θ_0 increases. The departure decreases as the spacing is lowered from $\Delta h = 0.8$ to $\Delta h = 0.6$.

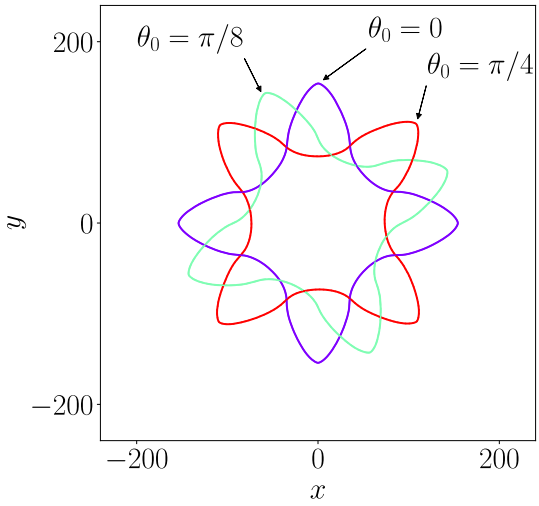

FIGURE 4.10: The solid-liquid interface at the end of the simulation for three differently oriented dendrites.

We can also see that the velocity $\tilde{v}_{tip}^{steady}$ at $\theta_0 = 0$ is slightly lowered as Δh decreases on RND. This is also observed in (Karma and Rappel, 1998).

In the case of SND, the calculation has been performed on five different SNDs defined by five different seeds $\mathcal{S}$. The minimum, the maximum and the median value of velocity $\tilde{v}_{tip}^{steady}$ at each θ_0 is plotted. The median value of velocity as a function of θ_0 is almost a constant. As Δh is decreased, the median is shifted towards the MST growth velocity and depends less on θ_0. Also, the error bar decreases as Δh is lowered.

The growth velocity at the end of the simulation as a function of θ_0 for $\Delta h = 0.8$ and three values of N on RND and SND is shown in Fig. 4.12. In the case of RND, the best result is observed for $N = 13$. The cases with $N = 9$ and $N = 21$ are very prone to the rotation of a dendrite as $N = 9$ yields the worst result. In the case of SND, the calculation was again performed on five different SNDs defined by five different seeds $\mathcal{S}$. For reasons of clarity, only the median value of velocity $\tilde{v}_{tip}^{steady}$ at each θ_0 is plotted. The growth velocity is almost independent of the orientation angle for all three values of N. The solution with $N = 21$ is closest to the solution obtained by the MST.

TABLE 4.6: Simulation parameters for the analysis of the performance for differently oriented dendrites

Preferential growth direction	
Growth angle (θ_0)	$0°, 5°, 10°, 15°, 20°, 25°, 30°, 35°, 40°, 45°$
Computational domain parameters	
Side length (L)	480
South-west coordinate ($\boldsymbol{r}_{sw}$)	$(-L/2, -L/2)$
Time	
Initial time (t_{start})	0
Final time (t_{end})	1500
Forward Euler scheme	
Stability parameter ($\alpha_{\Delta t}$)	0.1
Time step (Δt)	$\alpha_{\Delta t}(1-\epsilon_4)\Delta h^2/4$
RBF-FD method	
Number of nodes in sub-domain (N)	$9, 13, 21$
PHS power (n)	5
Highest monomial order (P)	2
Node distribution	
Type of node distribution	RND, SND (five different $\mathcal{S}$)
Spacing (Δh)	$0.8, 0.6$

Simulations with thermal noise

In this sub-section, the influence of the thermal noise on the growth is analysed. We study the influence of the magnitude of the noise F_u on the steady-state growth velocity by using RND and SND at $N = 13$ and $\Delta h = 0.8$. In the analysis, we repeat the analysis from Fig. 4.11. RND and a single SND are used in the analysis. The analysis is performed at values $F_u = 0$, $F_u = 10^{-5}$, and $F_u = 10^{-4}$, which are similar to the magnitudes in (Karma and Rappel, 1999). For $F_u > 0$, simulations with five different sets of normally distributed random numbers are performed. At each θ_0, the median, the minimum, and the maximum of the rescaled steady-state growth velocity are plotted as shown in Fig. 4.13.

In the case of the RND, the median value of $\tilde{v}_{tip}$ for $F_u > 0$ is very close

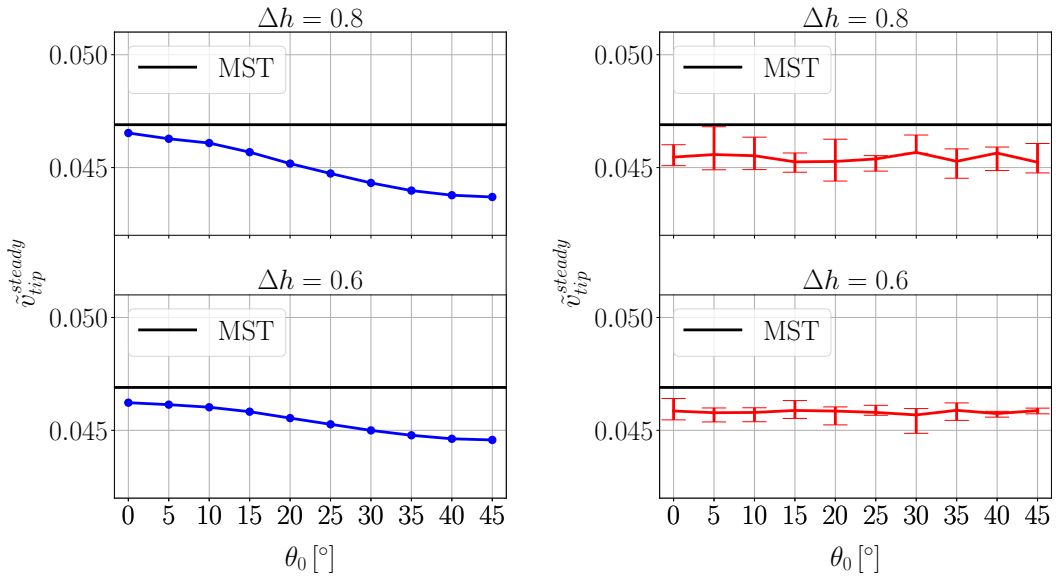

FIGURE 4.11: Steady-state growth velocity as a function of the preferential growth direction for two different spacings Δh and $N = 13$ using RND (left) and SND (right).

to $\tilde{v}_{tip}$ at $F_u = 0$ while the difference between the minimum and the maximum velocity increases with F_u. In the case of the SND, the median value as a function of θ_0 becomes more scattered as F_u increases while the the difference between the minimum and the maximum velocity increases with F_u. The difference between the maximum and the minimum is approximately twice as larger by using SND in comparison to the use of RND. This indicates that the thermal noise influences the solution obtained by using SND to a greater extent in comparison to the use of RND, especially at larger magnitudes of the thermal noise.

4.1.6 ASP

In this section the same numerical tests as in Section 4.1.5 are performed using ASP. The accuracy and computational efficiency in comparison to the BSP is assessed.

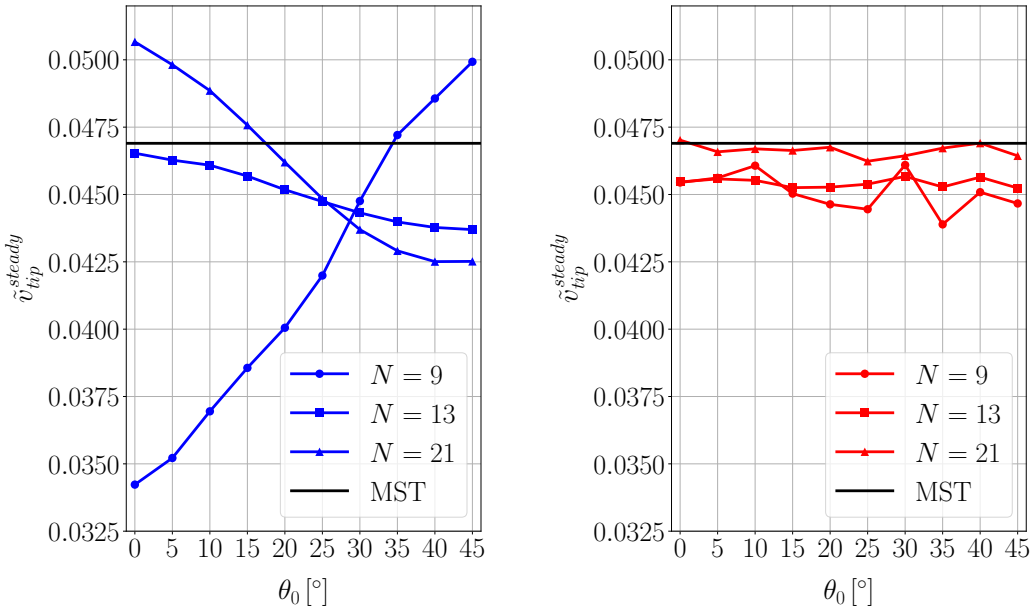

FIGURE 4.12: Steady-state growth velocity as a function of the preferential growth direction for three different sizes of local sub-domain N and $\Delta h = 0.8$ using RND (left) and SND (right).

Forward Euler scheme

The convergence of the forward Euler scheme is assessed for the same numerical parameters from Table 4.3 in Section 4.1.5. The constant spacing $\Delta h = 0.5$ from Table 4.3 is set as the minimum spacing in the ASP with the parameters from Table 4.7.

The relative error $\Delta l_{tip}/l_{tip}$ from Eq. (4.22) as a function of $\alpha_{\Delta t}$ on RND and SND for $m_\Omega = 15$ is shown in Fig. 4.14. The same behaviour as with BSP from Fig. 4.7 in Section 4.1.5 is observed for both node distributions. The re-scaled growth velocity as a function of time is shown in Fig. 4.15. In the case of RND, the same behaviour as for BSP from Fig. 4.8 is observed. In the case of SND, the situation is a little different. The quadtree domain decomposition introduces regularity in the solution on SND for $m_\Omega = 15$, which shifts the velocity away from the solution obtained by BSP. The effect of the regularity on the solution should decay with the increase of the sub-domain size/spacing ratio. The re-scaled growth velocity as a function of time on SND for the ratios $m_\Omega = 30$ and $m_\Omega = 60$ is shown in Fig. 4.16. The growth velocity for $m_\Omega = 30$ is still affected by the regularity, while the velocity for $m_\Omega = 60$ is closer to the

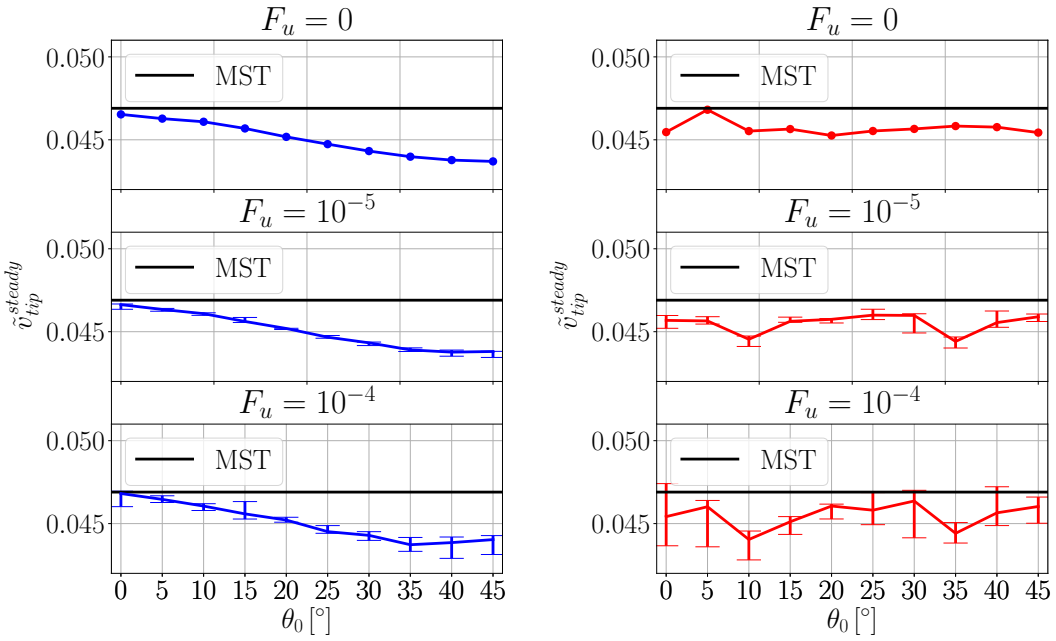

FIGURE 4.13: Steady-state growth velocity as a function of the preferential growth direction at three different magnitudes of noise F_u and $N = 13$ using RND (left) and SND (right).

velocity obtained by BSP in Figure 4.8 in Section 4.1.5.

TABLE 4.7: Parameters for the analysis of the forward Euler scheme in the adaptive algorithm.

Minimum spacing (Δh_{min})	0.5
Sub-domain size/spacing ratio (m_Ω)	$15, 30, 60$
Overlapping parameter (n^*)	1
Time step-restriction parameter ($m_{\Delta t}$)	2

RBF-FD method

The convergence of the RBF-FD method is assessed for the same numerical parameters from Table 4.4 in Section 4.1.5. Constant spacings Δh from Table 4.4 are set as the minimum spacings in the ASP with the parameters from Table 4.8. The side length of square Ω is given as

$$L = 2^{\mathcal{N}_{max}} m_\Omega \Delta h_{min}, \tag{4.25}$$

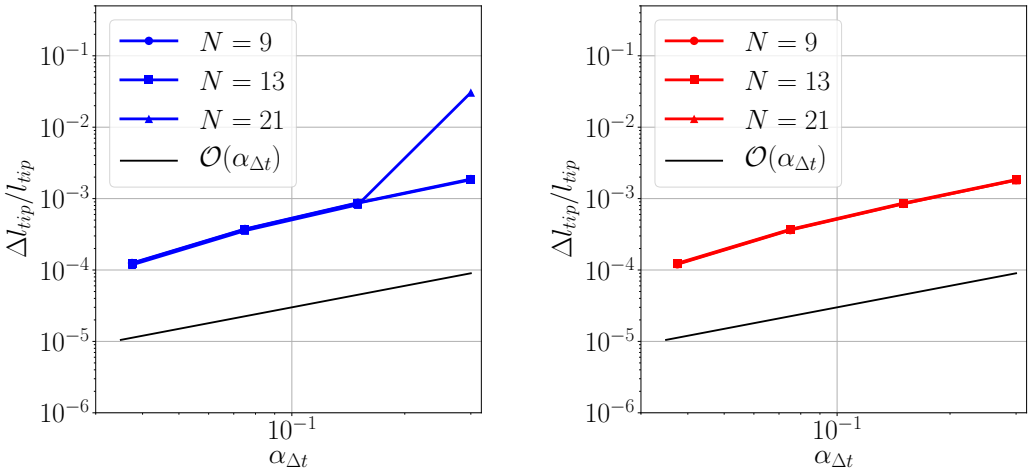

FIGURE 4.14: Relative error of l_{tip} as a function of forward Euler scheme stability parameter $\alpha_{\Delta t}$ using RND (left) and SND (right) in the case of ASP with $m_\Omega = 15$.

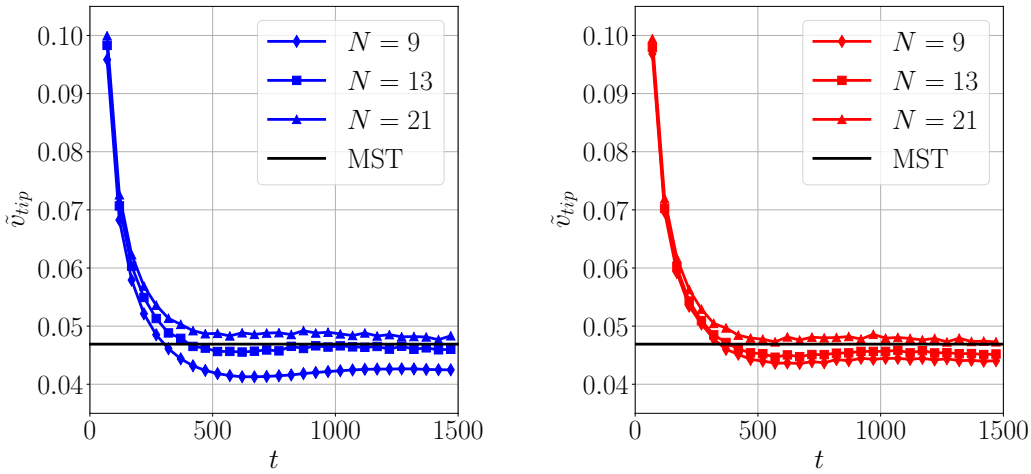

FIGURE 4.15: Rescaled growth velocity as a function of time using RND (left) and SND (right) in the case of ASP with $m_\Omega = 15$ and $\alpha_{\Delta t} = 0.15$.

in the quadtree domain decomposition. The value $L = 268.8$ is therefore used instead of $L = 240$ in the analysis of the convergence of the RBF-FD method with the parameters from Table 4.8.

The results of the RE in the case of ASP are shown in Table 4.9. The observed order of the convergence is very close to the expected second order for

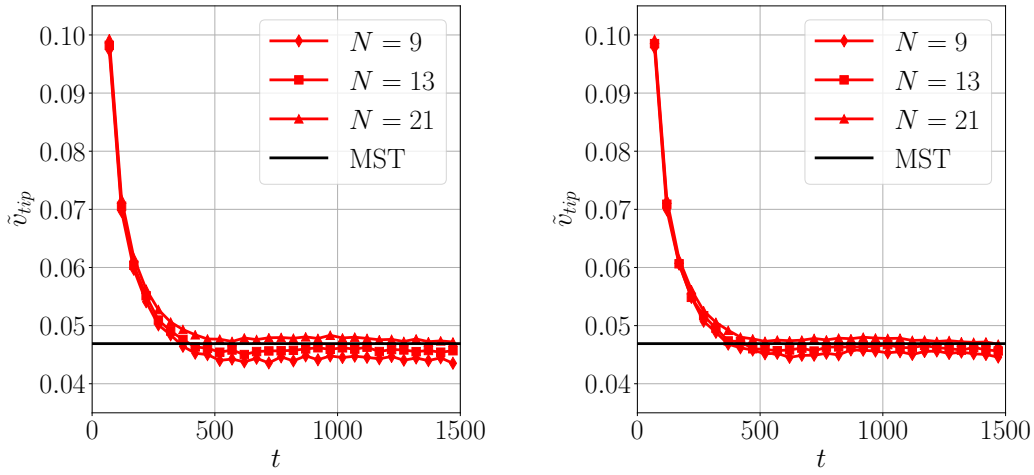

FIGURE 4.16: Rescaled growth velocity as a function of time for $m_\Omega = 30$ (left) and $m_\Omega = 60$ (right) using SND and $\alpha_{\Delta t} = 0.15$.

TABLE 4.8: Parameters for the analysis of the RBF-FD method in the adaptive algorithm. The configuration for each Δh_{min} is marked with the same colour.

Computational domain parameters	
Side length (L)	268.8
Adaptive algorithm	
Minimum spacing (Δh_{min})	0.8, 0.6, 0.4, 0.2
Sub-domain size/spacing ratio (m_Ω)	21, 28, 21, 21
Overlapping parameter (n^*)	2
Time step-restriction parameter ($m_{\Delta t}$)	2

both node distributions. In contrast to the results obtained by BSP, very similar results of RE are observed on RND and SND. The reason for this is the regular quadtree domain decomposition, which introduces some regularity in a SND. The effect of regular domain decomposition on the performance in the case of SND is further studied in the next section.

Arbitrary preferential growth directions

The analysis of the method for differently oriented dendrites is studied for the same numerical parameters from Table 4.6 in Section 4.1.5. The constant spacings from Table 4.6 are set as the minimum spacings in the ASP with the

TABLE 4.9: Distance l_{tip}^{end} on RND and SND for different values of Δh_{min} and the results of RE.

Δh_{min}	RND	SND
0.8	141.32	139.73
0.6	142.05	140.80
0.4	142.45	141.86
0.2	142.70	142.58
$l_{tip}^{end,RE}$	142.80	142.90
n_{RE}	1.87	1.72

parameters from Table 4.10. For the same reason as in the analysis of the RBF-FD method, the side length $L = 537.6$ is used instead of $L = 480$.

TABLE 4.10: Parameters for the analysis of the method in the adaptive algorithm for differently oriented dendrites. The configuration for each Δh_{min} is marked with the same colour.

Computational domain parameters	
Side length (L)	537.6
Adaptive algorithm	
Minimum spacing (Δh_{min})	0.8, 0.6, 0.8, 0.6
Sub-domain size/spacing ratio (m_Ω)	21, 28, 42, 56
Overlapping parameter (n^*)	1
Time step-restriction parameter ($m_{\Delta t}$)	2

The growth velocity at the end of the simulation as a function of θ_0 for $N = 13$ and two values of Δh_{min} on RND and SND is shown in Fig. 4.17. In the case of RND, a very similar behaviour as in Figure 4.11 from Section 4.1.5 for the BSP is observed. Interestingly, the growth velocity is slightly less affected by the orientation in the case of ASP. In the case of SND, the behaviour of the median is very similar to the behaviour in the case of BSP; however, the error bars are larger.

The growth velocity at the end of the simulation as a function of θ_0 for $\Delta h_{min} = 0.8$, $m_\Omega = 21$ and three values of N on RND and SND is shown in Fig. 4.18. For both node distributions, similar behaviour to that in Figure 4.12 from Section 4.1.5 for a BSP is observed. It is, however, evident that the solution on SND with ASP is more prone to rotation in comparison to the solution with BSP, especially for $N = 9$. The best result is again observed for $N = 21$.

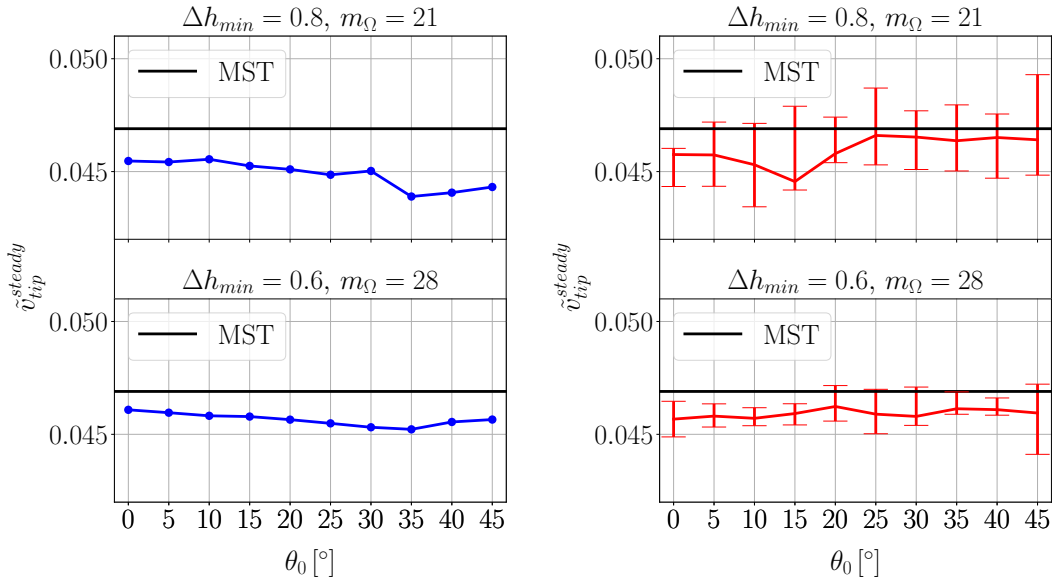

FIGURE 4.17: Steady-state growth velocity as a function of the preferential growth direction using RND (left) and SND (right) for $N = 13$ and two values of Δh_{min}.

The simulations are also performed by using SND at $m_\Omega = 42$ for $\Delta h_{min} = 0.8$ and $m_\Omega = 56$ for $\Delta h_{min} = 0.6$ as seen in Fig. 4.19. The error bars are reduced as m_Ω is increased in the study for $N = 13$ and different values of Δh_{min} in comparison to Fig. 4.17. The solution is less sensitive to the rotation at different values of N as m_Ω is increased; however, for $N = 9$ the solution is still much more prone to rotation in comparison to the BSP.

4.1.7 Computational efficiency

In the previous two sub-sections, the accuracy of the developed numerical model was studied. In this sub-section, the computational efficiency of the numerical model is analysed. First, the speed-up of the ASP is analysed, followed by an assessment of the speed-up due to `OpenMP` parallelisation. The analysis of the speed-up is made on a `HP ZBook` laptop with the hexa-core `Intel Core i7-9750H 2.6-4.5GHz` processor. The computational efficiency is tested for the case with $L = 256$ and $t_{end} = 1500$, which is similar

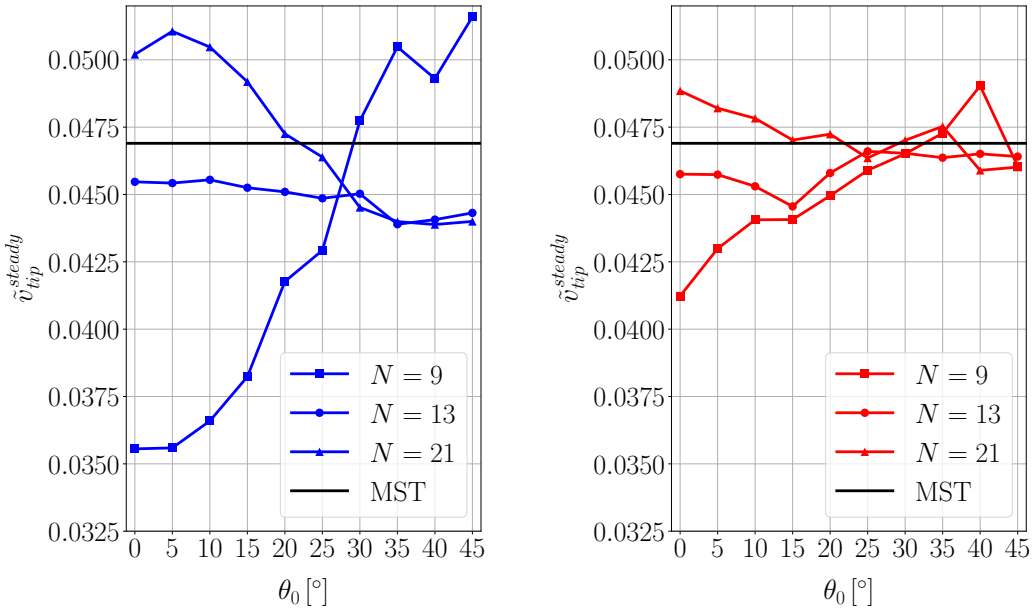

FIGURE 4.18: Steady-state growth velocity as a function of the preferential growth direction using RND (left) and SND (right) for $\Delta h_{min} = 0.8$ and $m_\Omega = 21$.

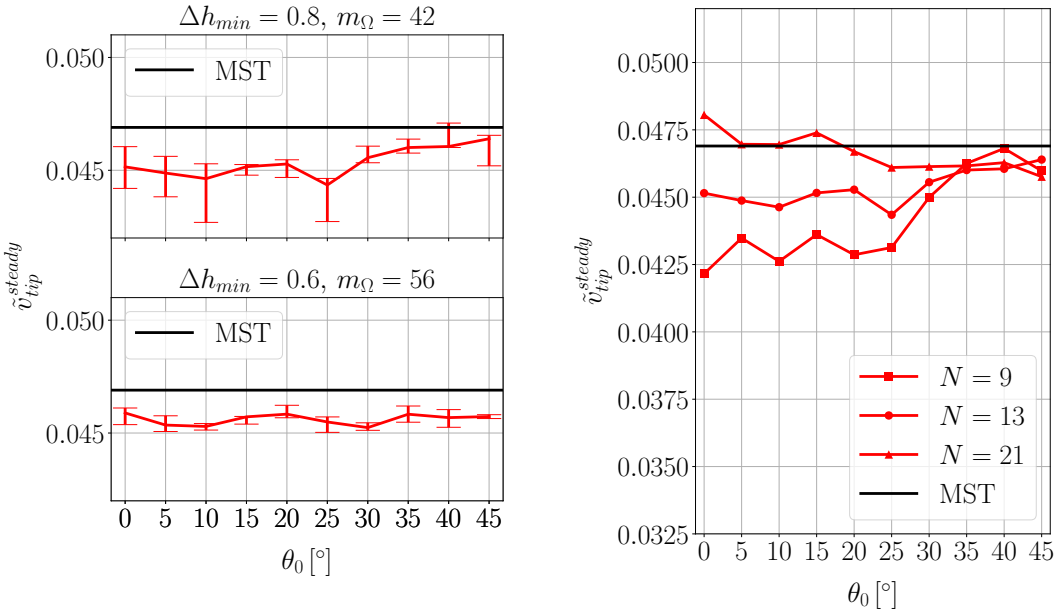

FIGURE 4.19: Steady-state growth velocity at $N = 13$ (left) and at $\Delta h_{min} = 0.8$, $m_\Omega = 42$, and three values of N (right) using SND.

to the cases from previous sections ($L = 240$ and $L = 268.8$). The used simulation parameters are given in Table 4.11. The choice of RND or SND does not change the performance of the ASP, hence, a RND is used in the analysis.

TABLE 4.11: Simulation parameters for the analysis of the computational efficiency of the numerical model.

Preferential growth direction	
Growth angle (θ_0)	0°
Computational domain parameters	
Side length (L)	256
South-west coordinate ($\boldsymbol{r}_{sw}$)	$(0, 0)$
Time	
Initial time (t_{start})	0
Final time (t_{end})	1500
Forward Euler scheme	
Stability parameter ($\alpha_{\Delta t}$)	0.3
Time step (Δt)	$\alpha_{\Delta t}(1 - \epsilon_4)\Delta h^2/4$
RBF-FD method	
Number of nodes in sub-domain (N)	13
PHS power (n)	5
Highest monomial order (P)	2
Node distribution	
Type of node distribution	RND
Adaptive algorithm	
Sub-domain size/spacing ratio (m_Ω)	$5, 10, 20, 40, 80$
Overlapping parameter (n^*)	1
Minimum spacing (Δh_{min})	$0.4, 0.8$
Maximum spacing (Δh_{max})	$L/(2m_\Omega)$
Time step-restriction parameter ($m_{\Delta t}$)	1

ASP speed-up

In order to assess the speed-up of the adaptive procedure only, the simulations are performed on a single processor core. The speed-up of the ASP is defined

as

$$\text{ASP speed-up} = \frac{\text{ERT}_{\text{BSP}}}{\text{ERT}_{\text{ASP}}}, \tag{4.26}$$

where ERT_{BSP} and ERT_{ASP} stand for the elapsed real time (ERT) in the case of the BSP and ASP, respectively. A simulation by BSP is made on a uniform RND with $\Delta h = \Delta h_{min}$. ERT_{BSP} and ERT_{ASP} for $\Delta h_{min} = 0.8$ and $m_\Omega = 5$ are shown in Fig. 4.20. The total ERT has three contributions in the case of ASP:

- Iteration ERT: time stepping with the forward Euler scheme while using the RBF-FD method for the spatial discretisation.
- Communication ERT: interpolation of boundary values by the RBF-FD method.
- Adaptation ERT: refinement/de-refinement algorithm.

Naturally, the iteration ERT represents the majority of the total ERT. The main goal of the ASP is to reduce the iteration ERT in comparison to the BSP. However, some extra computational work is introduced due to the communication and adaptation that reduce the total speed-up in comparison to the BSP.

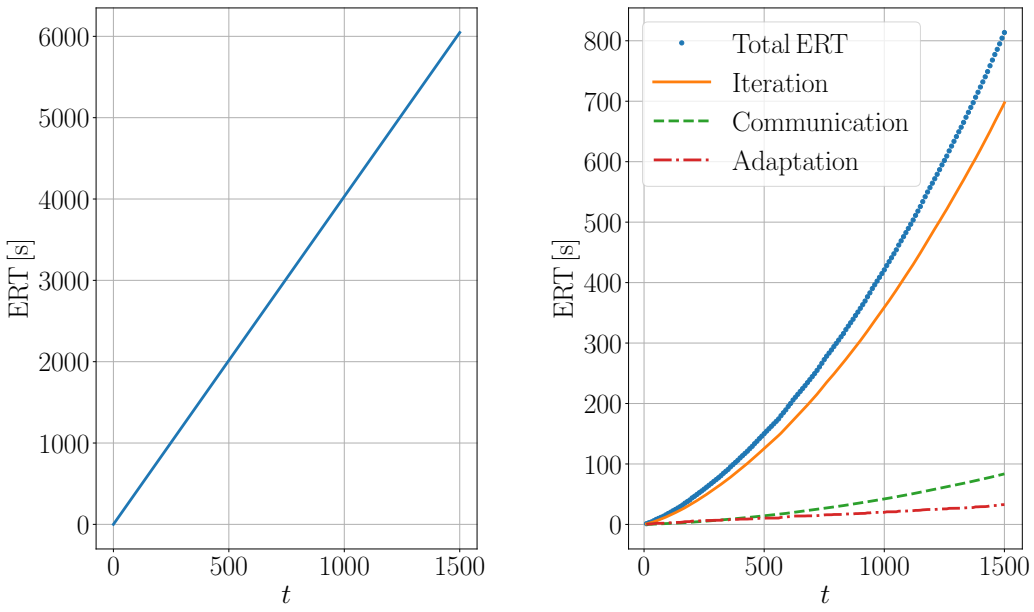

FIGURE 4.20: The ERT by using BSP (left) and ASP (right) for $\Delta h = 0.8$. ASP with $m_\Omega = 5$ is used.

The percentage of ERT for performing various tasks during simulation as a function of time for $m_\Omega = 5$ and two values of Δh_{min} is shown in Figure 4.21. The iteration of the governing equations represents the majority of the whole ERT. For $\Delta h_{min} = 0.8$, adaptation takes relatively more time in comparison to $\Delta h_{min} = 0.4$, while the percentage of communication is approximately the same for both spacings.

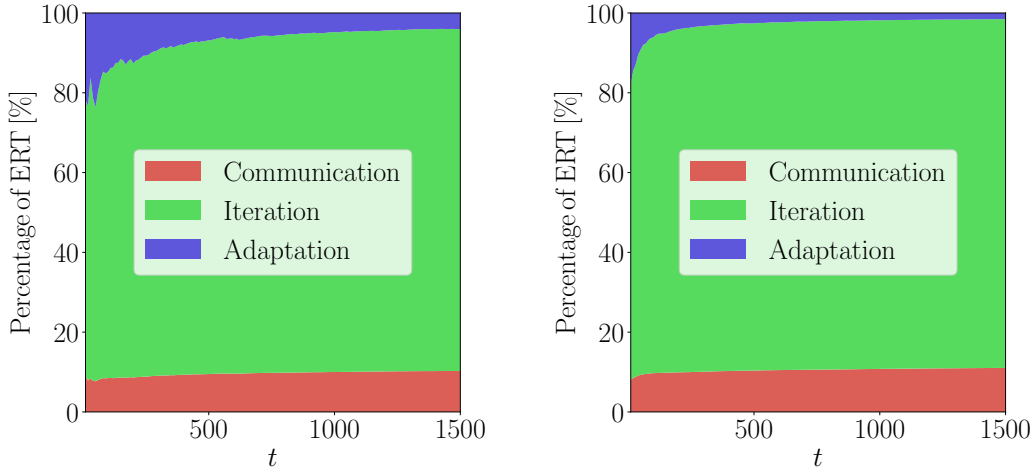

FIGURE 4.21: The percentage of ERT for performing various tasks during simulation at $\Delta h_{min} = 0.8$ (left) and $\Delta h_{min} = 0.4$ (right) for $m_\Omega = 5$.

The percentage of ERT for performing various tasks during the simulation as a function of time for $\Delta h_{min} = 0.4$ and four values of m_Ω is shown in Figure 4.22. Naturally, the ERT for the adaptation and communication decreases as m_Ω is increased. The largest percentage of ERT for adaptation at the beginning of the simulation is observed for $m_\Omega = 20$. In the initial configuration for $m_\Omega = 20$, the solid nucleus is refined by only four quadtree sub-domains with $\Delta h_{min} = 0.4$ since the size of the nucleus is equal to $R_{nuc} = 10$ and the size of the smallest quadtree sub-domain is equal to $L_i = \Delta h_{min} \times m_\Omega = 8$ as seen in Fig. 4.23. As the solid phase starts to grow, a large number of quadtree sub-domains have to be refined to ensure balancing, which explains the large percentage of the adaptation ERT. That behaviour is for the same reason observed for $\Delta h_{min} = 0.8$ and $m_\Omega = 10$. For $m_\Omega = 40$ and $m_\Omega = 80$, the adaptation does not occur until the dendrite is large enough, since a large area around the solid nucleus is refined in the initial refinement.

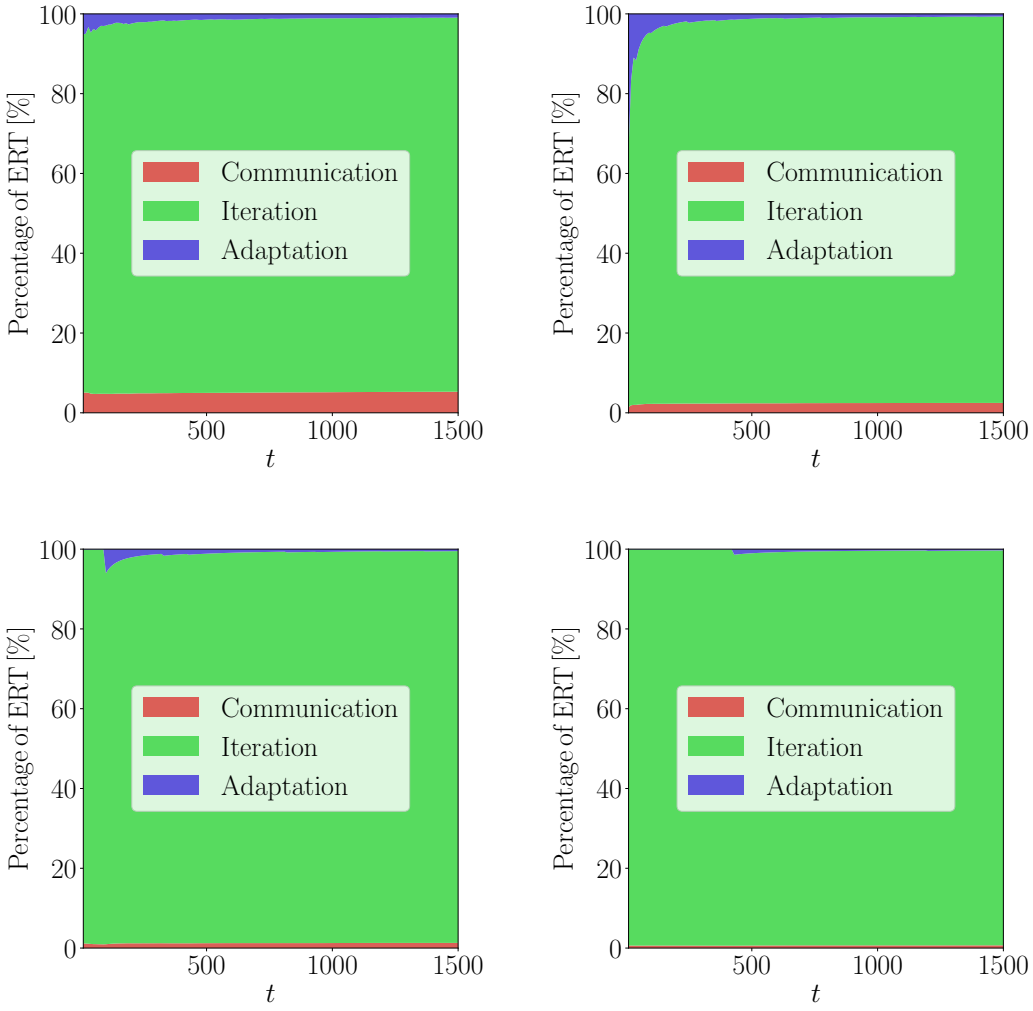

FIGURE 4.22: The percentage of ERT for performing various tasks during simulation for $m_\Omega = 10$ (top-left), $m_\Omega = 20$ (top-right), $m_\Omega = 40$ (bottom-left), and $m_\Omega = 80$ (bottom-right) at $\Delta h_{min} = 0.4$.

The speed-up as a function of time for different values of m_Ω and the final speed-up as a function of m_Ω are shown in Fig. 4.24. The speed-up is a decreasing function of time with the exception of $m_\Omega = 20$, where the maximum speed-up is shifted a little away from $t = 0$. The reason for that is the previously explained increase of the adaptation ERT for $m_\Omega = 20$ and $\Delta h_{min} = 0.4$ (and for $m_\Omega = 10$ and $\Delta h_{min} = 0.8$). The maximum final speed-up is observed for $m_\Omega = 5$ and $m_\Omega = 10$. A higher speed-up is observed for $\Delta h_{min} = 0.4$.

In Fig.4.25, the speed-up is further analysed by plotting three speed-ups

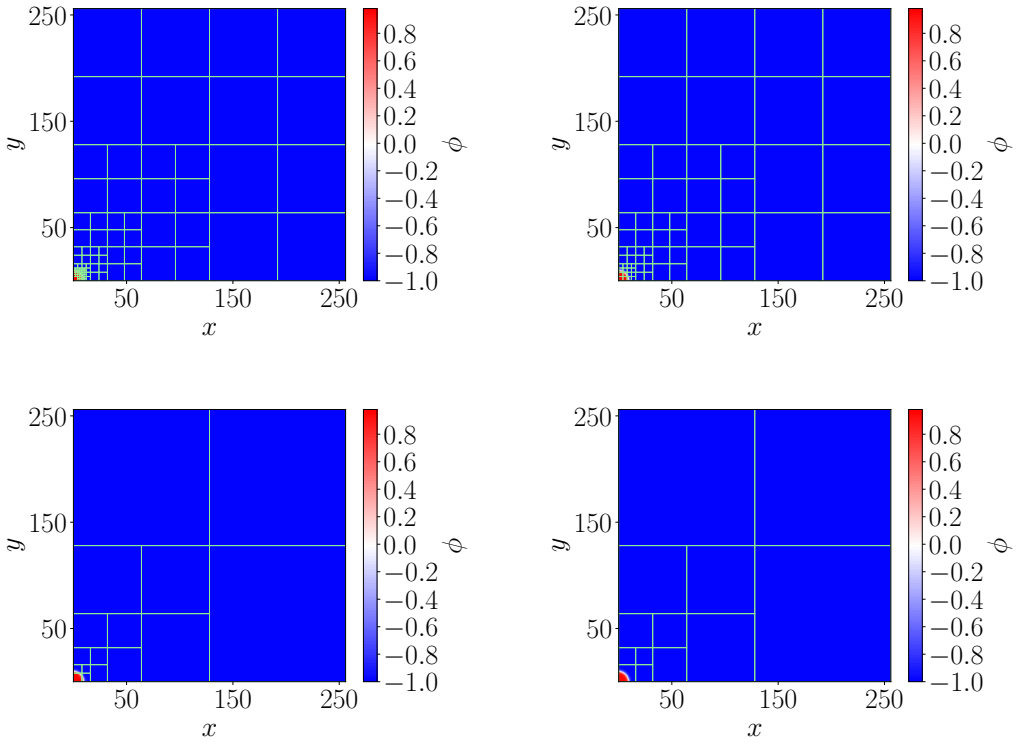

FIGURE 4.23: Initial configuration of a quadtree for $m_\Omega = 5$ (top-left), $m_\Omega = 10$ (top-right), $m_\Omega = 20$ (bottom-left), and $m_\Omega = 40$ (bottom-right) at $\Delta h_{min} = 0.4$.

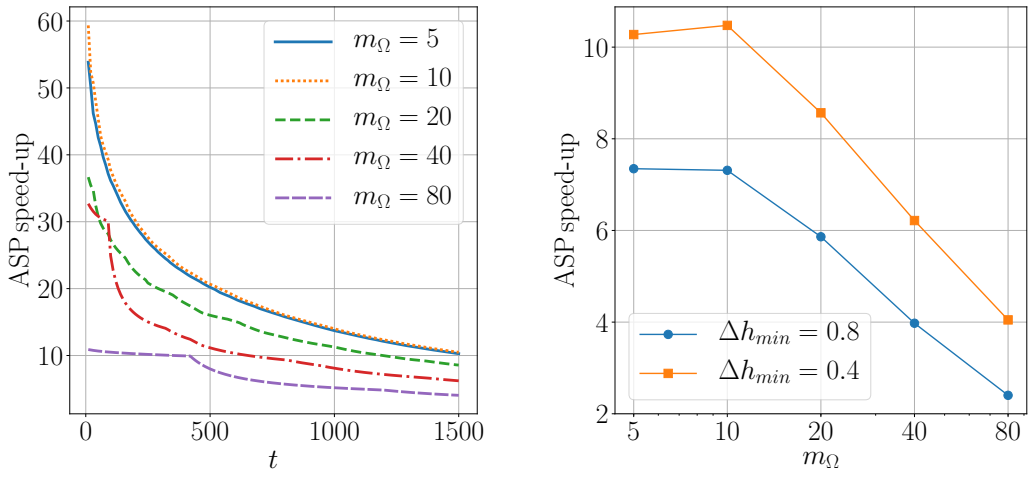

FIGURE 4.24: ASP speed-up as a function of time for $\Delta h_{min} = 0.4$ (left) and the final ASP speed-up as a function of m_Ω (right).

- ASP speed-up for iteration only (marked by Iter),
- ASP speed-up for iteration and communication (marked by +Comm),
- ASP speed-up for iteration, communication and adaptation (marked by +Comm+Adapt).

It is evident that the speed-up is decreased primarily by communication. As m_Ω increases, the reduction of the speed-up due to communication and adaptation decreases.

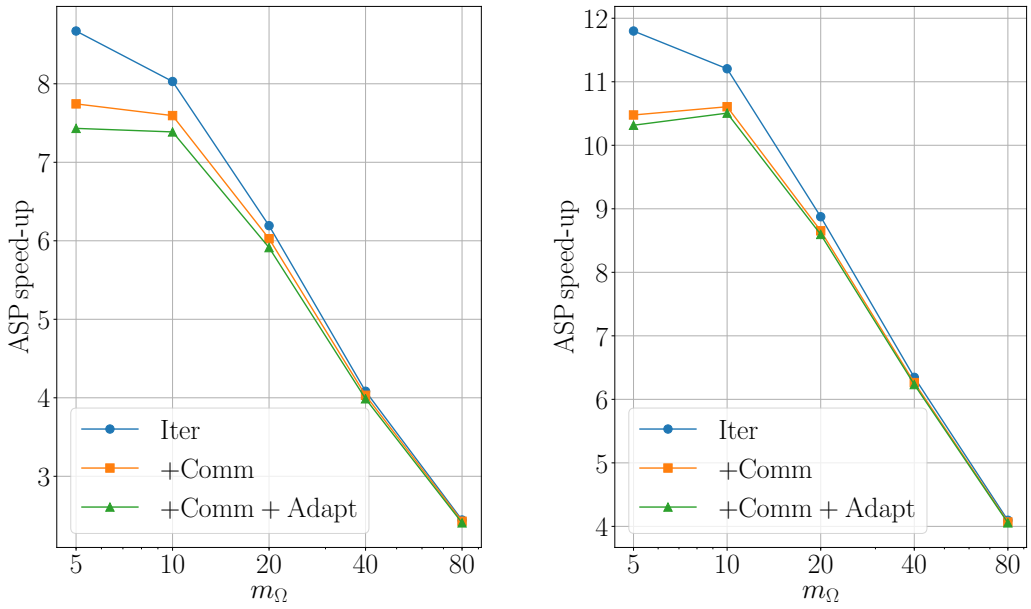

FIGURE 4.25: Contributions of communication (+Comm) and adaptation (+Adapt) in the reduction of the speed-up due to iterations (Iter) only for $\Delta h_{min} = 0.8$ (left) and $\Delta h_{min} = 0.4$ (right).

At the beginning of the simulation, the RBF-FD coefficients for each spatial operator have to be calculated according to Eq. (3.17) from Section 3.2. Preparation time $\mathrm{ERT}_{\mathrm{PREP}}$, the ERT for calculation of the RBF-FD coefficients before the time-stepping begins, has not been analysed in this section yet. In the case of BSP, the coefficients have to be calculated for each computational node in Ω, which is a computationally expensive task, especially for large number of computational nodes. In the case of ASP, the RBF-FD coefficients are calculated at the beginning of the simulation for nine possible extended sub-domains Ω_i^*

- four corner Ω_i^* (south-west, north-west, north-east, south-east) with two sides on the boundary of Ω,
- four side Ω_i^* (west, north, east, south) with one side on the boundary of Ω, and
- inner Ω_i^* without sides on the boundary of Ω.

When a new Ω_i^* is created in the refinement or de-refinement procedure during a simulation, the RBF-FD coefficients are re-scaled according to Δh_i and stored for the calculations in Ω_i^*. This hugely reduces $\mathrm{ERT}_{\mathrm{PREP}}$ and adaptation ERT. In the case of ASP, $\mathrm{ERT}_{\mathrm{PREP}}$ also accounts for the ERT of the initial refinement.

The $\mathrm{ERT}_{\mathrm{PREP}}$ for the BSP and ASP are shown in Table 4.12. In the case of ASP, $\mathrm{ERT}_{\mathrm{PREP}}$ increases with m_Ω. $\mathrm{ERT}_{\mathrm{PREP}}$ for BSP is higher than $\mathrm{ERT}_{\mathrm{PREP}}$ for ASP, especially for the smaller values of m_Ω.

TABLE 4.12: The $\mathrm{ERT}_{\mathrm{PREP}}$ for BSP and ASP.

$\Delta h_{min}/m_\Omega$	5	10	20	40	80	BSP
0.8	4 s	5 s	15 s	44 s	126 s	154 s
0.4	5 s	8 s	16 s	43 s	135 s	648 s

Parallelisation speed-up

The parallelisation speed-up is defined as

$$\texttt{OpenMP}\,\text{speed-up} = \frac{\mathrm{ERT}(\mathrm{N_{cores}} = 1)}{\mathrm{ERT}(\mathrm{N_{cores}})}, \tag{4.27}$$

where N_{cores} stands for the number of cores in the processor used to run a simulation. In the case of ASP, the parallelisation is performed over the sub-domains $\{\Omega_i^*\}_{\mathcal{N}}$ on each level $\mathcal{N}$ of a quadtree. In the case of BSP, the parallelisation is performed over the computational nodes from a computational domain.

The speed-up of ASP and BSP for two values of Δh_{min} is shown in Fig. 4.26. For $N_{cores} \leq 4$, the speed-up is quite close to the ideal speed-up for both values of Δh_{min}. For $m_\Omega = 5$ and $\Delta h_{min} = 0.8$, the speed-up is further increased at $N_{cores} = 5$ and decreased at $N_{cores} = 6$. For $m_\Omega = 10$ and $m_\Omega = 40$ with $\Delta h_{min} = 0.8$, the speed-up slightly reduced at $N_{cores} = 5$ and slightly increased

at $N_{cores} = 6$. For $m_\Omega = 20$ and $m_\Omega = 80$ with $\Delta h_{min} = 0.8$, the speed-up is slightly reduced for $N_{cores} > 4$. For $\Delta h_{min} = 0.4$ and $N_{cores} > 4$, the speed-up is further increasing as a function of N_{cores} for all values of m_Ω; however, with a lower rate for $m_\Omega = 5$ and $m_\Omega = 80$.

There are four main reasons for the observed reduction of the speed-up:

- not all the available cores are occupied when N_{cores} is higher than $N_\mathcal{N}$, which occurs at high values of m_Ω as seen in Fig. 4.23 from the previous sub-section,
- not all available cores are occupied when the remainder in the division between $N_\mathcal{N}$ and N_{cores} is greater than zero (this drawback is more prominent at low values of $N_\mathcal{N}$),
- some parts of the code for adaptation cannot be performed in parallel,
- according to the analysis with the `VTune Profiler` tool from the `Intel Parallel Studio XE 2020` software development package, the memory bandwidth represents a bottleneck of the program as the computational tasks on the processor cores cannot be performed simultaneously due to data starvation as N_{cores} is increased. This is especially limiting in our numerical model, which requires a large amount of data to be transferred from the memory to the processor to perform a single task, e.g., to evaluate a spatial operator in a computational node.

4.1.8 Discussion

In Section 4.1, the newly developed numerical approach is analysed for the PF modelling of the dendritic solidification of pure materials for arbitrary preferential growth directions. The growth velocity is compared to the reference growth velocity obtained in the framework of the MST. The accuracy of the BSP is analysed first, followed by the analysis of the accuracy of the ASP in comparison to the BSP. The ASP speed-up and `OpenMP` speed-up are analysed.

The results obtained by the BSP show, that the use of the SND provides equal or better accuracy in comparison to the use of the RND. The same accuracy is observed in the BSP and ASP by using the RND. The quadtree domain decomposition in the ASP introduces regularity in the solution obtained by

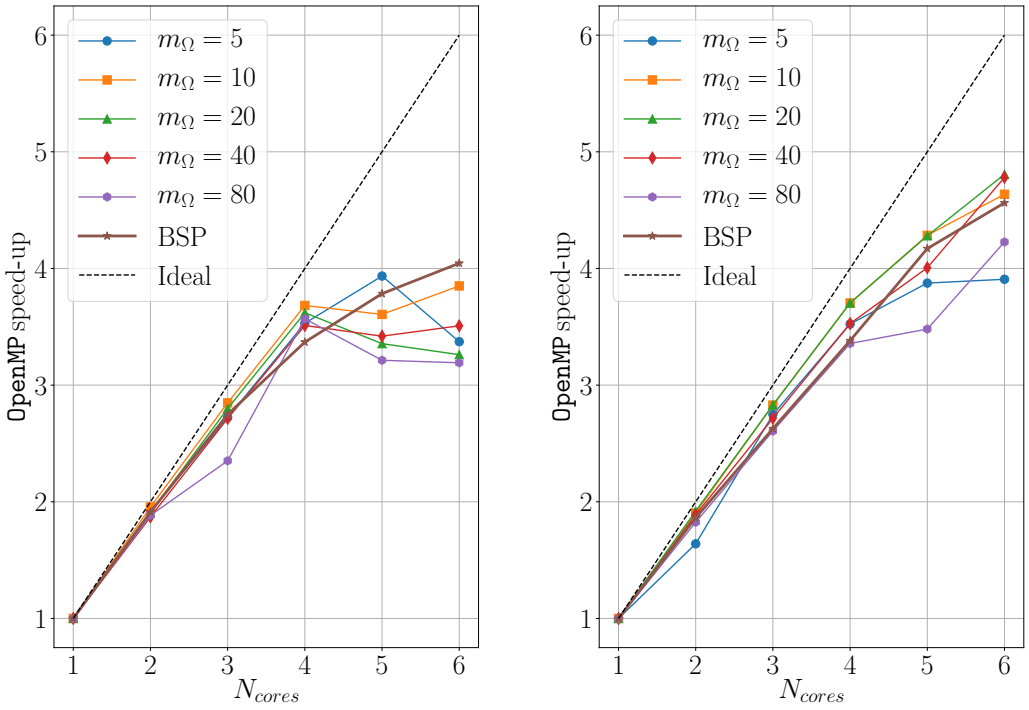

FIGURE 4.26: Parallelisation speed-up for $\Delta h_{min} = 0.8$ (left) and $\Delta h_{min} = 0.4$ (right).

using the SND. Large enough quadtree sub-domain size/spacing ratios have to be used in the ASP in order to sustain the BSP's accuracy if the SND is in use. The ASP successfully speeds-up the calculations. Smaller values of the quadtree sub-domain size/spacing ratio provide a higher ASP speed-up. `OpenMP` can be successfully used for the speed-up of the ASP. The results are further comprehensively summarized and concluded in Section 5.

4.2 Solidification of binary alloys

In this section, the isothermal solidification of binary alloys is considered. A 2-D example from (Karma, 2001) is chosen as the reference solution to which the results of our newly developed numerical approach are compared. In the article, the thin-interface limit of the PF model for the solidification of binary alloys with the introduction of the anti-trapping current is originally formulated.

The problem definition of the solidification of binary alloys is given in Section 4.2.1. The time step in the forward Euler scheme is determined in Section 4.2.2. A typical simulation result is shown in Section 4.2.3. Characterisation of the simulation results for the purpose of verification is presented in Section 4.2.4. The numerical results and the comparison with the reference solution are presented in Section 4.2.5.

4.2.1 Problem definition

The computational domain Ω with the boundary Γ is a square with the south-west vertex $\boldsymbol{r}_{sw}$ and the side length L as shown in Fig. 4.27. Isothermal solidification ($\theta = 0$) of a dendrite from a supersaturated ($U < 0$) binary alloy ($N_c = 2$) with negligible diffusivity of solute in the solid phase ($D_s = 0$) is considered. The system of two coupled governing equations for PF ϕ and dimensionless supersaturation U is given by Eqs. (2.84) and (2.85)

$$\begin{aligned}(1 + (1 - k_0)U)a^2(\boldsymbol{n})\frac{\partial \phi}{\partial t} &= \phi - \phi^3 - (1 - \phi^2)^2 \lambda U \\ &+\nabla \cdot \left(a^2(\boldsymbol{n})\nabla\phi\right) + \sum_{\xi=x,y} \partial_\xi \left(|\nabla\phi|^2 a(\boldsymbol{n}) \frac{\partial a(\boldsymbol{n})}{\partial(\partial_\xi \phi)} \right),\end{aligned} \tag{4.28}$$

and

$$\begin{aligned}&\frac{1}{2}\left(1 + k_0 - (1 - k_0)\phi\right)\frac{\partial U}{\partial t} = \frac{1}{2}\left(1 + (1 - k_0)U\right)\frac{\partial \phi}{\partial t} \\ &+ \nabla \cdot \left(\alpha_2 \lambda \frac{1 - \phi}{2} \nabla U + \frac{1}{2\sqrt{2}}(1 + (1 - k_0)U)\frac{\partial \phi}{\partial t}\frac{\nabla\phi}{|\nabla\phi|} \right),\end{aligned} \tag{4.29}$$

where the index of the i-th solute element has been dropped since the binary alloy is considered. The parameter ψ is set to one. The cubic anisotropy function $a(\boldsymbol{n})$ is given by Eq. (4.1). The parameter α_2 is constant, which leaves λ as the only free parameter of the PF model. According to the thin-interface relations from Eqs. (2.77) and (2.78), the spatial and temporal coordinates are measured in units of

$$W_0 = d_c \frac{1}{\alpha_1}\lambda, \tag{4.30}$$

and

$$\tau_0 = \frac{d_c^2}{D_\ell}\frac{\alpha_2}{\alpha_1^2}\lambda^3. \tag{4.31}$$

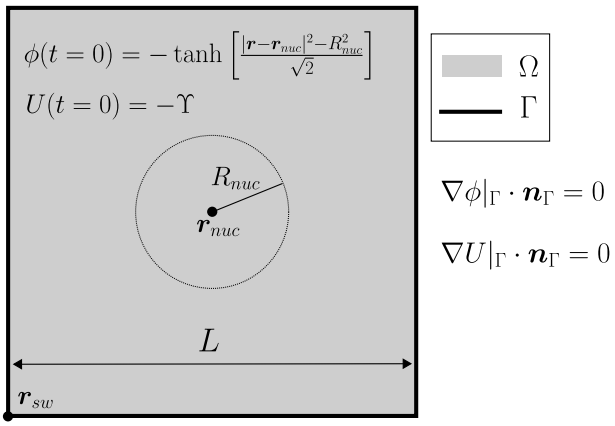

FIGURE 4.27: Illustration of a square computational domain Ω with boundary Γ. A domain is defined by the south-west coordinate $\boldsymbol{r}_{sw}$ and the side length of a square L. Solidification from a supercooled binary alloy is initialized by a small nucleus with radius R_{nuc} and center $\boldsymbol{r}_{nuc}$. Zero-flux Neumann boundary conditions are proposed for ϕ and U.

The initial condition for the supersaturation assumes the constant supersaturation in the whole Ω

$$U(t=0) = -\Upsilon, \tag{4.32}$$

where Υ stands for the initial dimensionless supersaturation. The initial condition for the PF is a circular nucleus with the origin $\boldsymbol{r}_{nuc}$ and the radius R_{nuc}, already defined in Eq. (4.9) from section 4.1. In the dissertation, the steady-state growth of a dendrite into an infinite supersaturated binary alloy is simulated. A pseudo-infinity is ensured by a large enough Ω with a zero-flux Neumann boundary condition for the PF already defined in Eq. (4.10) from Section 4.1. The same boundary condition is also used for the dimensionless supersaturation

$$\nabla U|_\Gamma \cdot \boldsymbol{n}_\Gamma = 0. \tag{4.33}$$

An example with the supersaturation $\Upsilon = 0.55$, the strength of anisotropy $\epsilon_4 = 0.02$, and the partition coefficient $k_0 = 0.15$ is considered. The PF free parameter is set to $\lambda = 2/\alpha_2$ (Karma, 2001) in order to obtain a PF model that correctly captures the physics of the Stefan problem with negligible interface kinetics. The simulation parameters used in the study are shown in Table 4.13.

TABLE 4.13: Simulation parameters.

Physical problem parameters	
Partition coefficient (k_0)	0.15
Strength of anisotropy (ϵ_4)	0.02
Initial supersaturation (Υ)	0.55
Center of nucleus ($\boldsymbol{r}_{nuc}$)	$(0, 0)$
Radius of nucleus (R_{nuc})	$22\alpha_1/\lambda$
PF parameters	
Constant (α_1)	0.8839
Constant (α_2)	0.6267
Coupling parameter (λ)	$2/\alpha_2$

4.2.2 Stability criterion in the forward Euler scheme

The time step is in the case of binary alloys given as

$$\Delta t(\Delta h) = \alpha_{\Delta t} \frac{1}{4} \frac{\Delta h^2}{\max(\bar{D}_\ell, 1/(1-\epsilon_4))} \tag{4.34}$$

The parameters from Table 4.13 yield

$$\Delta t(\Delta h) = \alpha_{\Delta t} \Delta h^2 / (4\bar{D}_\ell), \tag{4.35}$$

since $\bar{D}_\ell = \lambda\alpha_2 = 2$ and therefore $\bar{D}_\ell > 1/(1-\epsilon_4)$. The actual time step in a extended quadtree sub-domain Ω_i^* with spacing Δh_i is according to Eq. (3.30) from sub-section 3.4.6 given as

$$\Delta t_i(\Delta h_i) = \alpha_{\Delta t} \min\left(\Delta h_i^2, 2^{2m_{\Delta t}} \Delta h_{min}^2\right) / (4\bar{D}_\ell), \tag{4.36}$$

since the restriction parameter has to be additionally considered in the ASP.

4.2.3 Solution of PF model

The solution of the PF model for the concentration field with the simulation parameters from Table 4.14 is shown in Fig. 4.28. The normalised concentration as a function of U and ϕ is according to Eq. (2.80), the definition of

concentration $C = (1+\phi)C_s/2 + (1-\phi)C_\ell/2$, and relation $C_s = k_0 C_\ell$ given as

$$C/C_\ell^e = \frac{1}{2}\left(1 + U(1-k_0)\right)\left(1 + k_0 - \phi(1-k_0)\right). \tag{4.37}$$

The concentration is the highest at the solid-liquid interface where $C/C_\ell^e = 1$. Due to $D_s = 0$, the concentration is constant and approximately equal to $C/C_\ell^e = k_0$ in the solid phase. Lower solubility of the alloying element in the solid phase, i.e., $k_0 < 1$, yields the rejection of the solute in the liquid phase.

TABLE 4.14: Simulation parameters for the results from Figs. 4.28 and 4.29.

Preferential growth direction	
Growth angle (θ_0)	$0°$
Computational domain parameters	
Side length (L)	768
South-west coordinate ($\boldsymbol{r}_{sw}$)	$(0, 0)$
Time	
Initial time (t_{start})	0
Final time (t_{end})	4000
Forward Euler scheme	
Stability parameter ($\alpha_{\Delta t}$)	0.3
Time step (Δt)	$\alpha_{\Delta t}\Delta h^2/(4\bar{D}_\ell)$
RBF-FD method	
Number of nodes in sub-domain (N)	13
PHS power (n)	5
Highest monomial order (P)	2
Adaptive algorithm	
Type of node distribution	RND
Sub-domain size/spacing ratio (m_Ω)	10
Overlapping parameter (n^*)	1
Minimum spacing (Δh_{min})	0.6
Maximum spacing (Δh_{max})	$L/(2m_\Omega)$
Time step-restriction parameter ($m_{\Delta t}$)	2

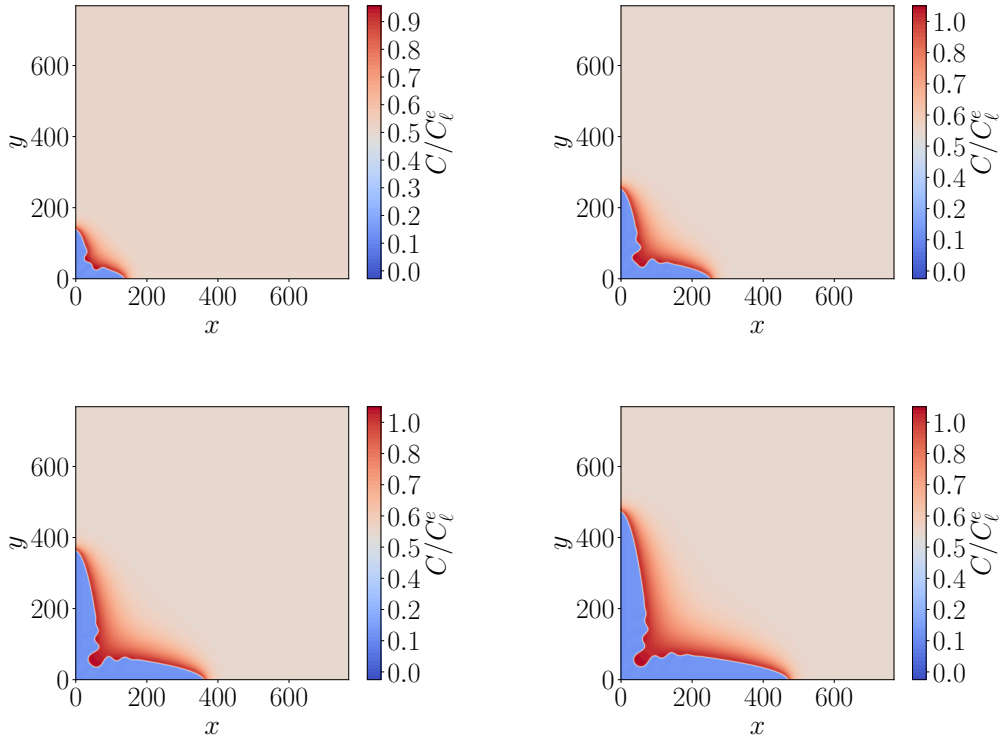

FIGURE 4.28: Normalised concentration field at $t = 1000$ (top-left), $t = 2000$ (top-right), $t = 3000$ (bottom-left), and $t = 4000$ (bottom-right).

4.2.4 Characterisation of the simulation results

The simulation results in the case of binary alloys are characterized like in the case of pure materials. Exactly the same procedure as in sub-section 4.1.4 with the parameters $t_0^{mea} = 1$ and $\Delta t^{mea} = 1$ is applied for the determination of the growth velocity. The averaging with fifteen points from the data set $\{t_i^{mea}, v_{tip}(t_i^{mea})\}$ is applied in the representation of the velocity $v_{tip}(t)$. In the case of binary alloys, the dimensional growth velocity $\tilde{v}_{tip} = v_{tip} W_0/\tau_0$ is re-scaled as

$$\tilde{v}_{tip} \rightarrow \tilde{v}_{tip} d_c / D_\ell. \tag{4.38}$$

The re-scaled dimensional velocity is according the definition of W_0 and τ_0 from Eqs. (4.30) and (4.31), respectively, calculated as

$$\tilde{v}_{tip} = v_{tip} \frac{W_0}{\tau_0} \frac{d_c}{D_\ell} = v_{tip} \frac{\alpha_1}{\alpha_2} \frac{1}{\lambda^2}. \tag{4.39}$$

Additionally to the growth velocity, the concentration in the solid phase C_s/C_ℓ^e along the x'-axis is verified, where x'-axis is the x-axis in the dendrite coordinate system determined by the preferential growth direction angle θ_0. In the comparison of our results with the reference solution from (Karma, 2001), the dimensional time $\tilde{t} = t\tau_0$ and coordinate $\tilde{x'} = x'W_0$ are re-scaled as

$$\tilde{t} \to \tilde{t}D/d_c^2, \quad \tilde{x}' \to \tilde{x}'/d_c. \tag{4.40}$$

The re-scaled $\tilde{t}$ and $\tilde{x}'$ as a function of dimensionless t and x' are given as

$$\tilde{t} = t\frac{\alpha_2}{\alpha_1^2}\lambda^3, \quad \tilde{x}' = x'\frac{1}{\alpha_1}\lambda. \tag{4.41}$$

Velocity $\tilde{v}_{tip}$ as a function of time $\tilde{t}$ and the normalised concentration C_s/C_ℓ^e in the solid phase as a function of the coordinate $\tilde{x}'$ are shown in Fig. 4.29. Like for pure materials, the steady-state growth is observed after the initial transient. The normalised concentration in the solid phase is approximately equal to $C_s/C_\ell^e = k_0 = 0.15$.

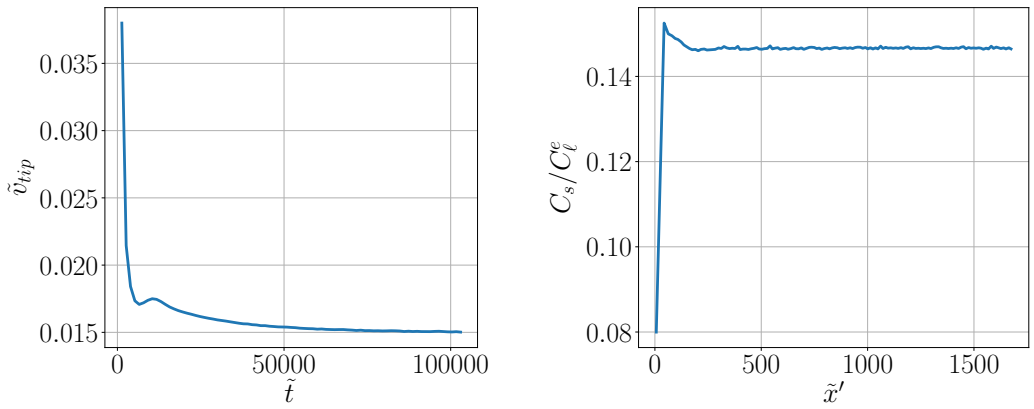

FIGURE 4.29: Growth velocity as a function of time (left) and concentration in the solid phase as a function of $\tilde{x}'$ (right).

4.2.5 Verification of the numerical model

In (Karma, 2001), the growth velocity is plotted in the range $\tilde{t} \in [0, 10000]$ and the concentration in the range $\tilde{x}' = [0, 400]$. With the parameter $\lambda = 2/\alpha_2$, these values approximately correspond to dimensionless coordinates $t \in [0, 380]$ and

$x' \in [0, 112]$. In order to compare the results, the final dimensionless coordinates are set to $t_{end} = 850$ and $L = 268.8$, as seen in Table 4.15. This choice ensures a pseudo-infinite supercooled binary alloy, for which the impact of Γ on the solidification at the end of the simulation is negligible, as seen in Fig. 4.30. The growth velocity and the re-scaled concentration in the solid phase from (Karma, 2001) are set as the reference solutions with which we compare our simulation results.

TABLE 4.15: Simulation parameters for the verification of the numerical model in the case of binary alloy. The configuration for each Δh_{min} is marked with the same colour.

Preferential growth direction	
Growth angle (θ_0)	$0°$
Computational domain parameters	
Side length (L)	268.8
South-west coordinate ($\boldsymbol{r}_{sw}$)	$(0, 0)$
Time	
Initial time (t_{start})	0
Final time (t_{end})	850
Forward Euler scheme	
Stability parameter ($\alpha_{\Delta t}$)	$0.3, 0.15, 0.075, 0.0375$
Time step (Δt)	$\alpha_{\Delta t}\Delta h^2/(4\bar{D}_\ell)$
RBF-FD method	
Number of nodes in sub-domain (N)	$9, 13, 21$
PHS power (n)	5
Highest monomial order (P)	2
Adaptive algorithm	
Type of node distribution	RND, SND
Sub-domain size/spacing ratio (m_Ω)	21, 28, 56
Overlapping parameter (n^*)	2
Minimum spacing (Δh_{min})	0.4, 0.6, 0.6
Maximum spacing (Δh_{max})	$L/(2m_\Omega)$
Time step-restriction parameter ($m_{\Delta t}$)	1

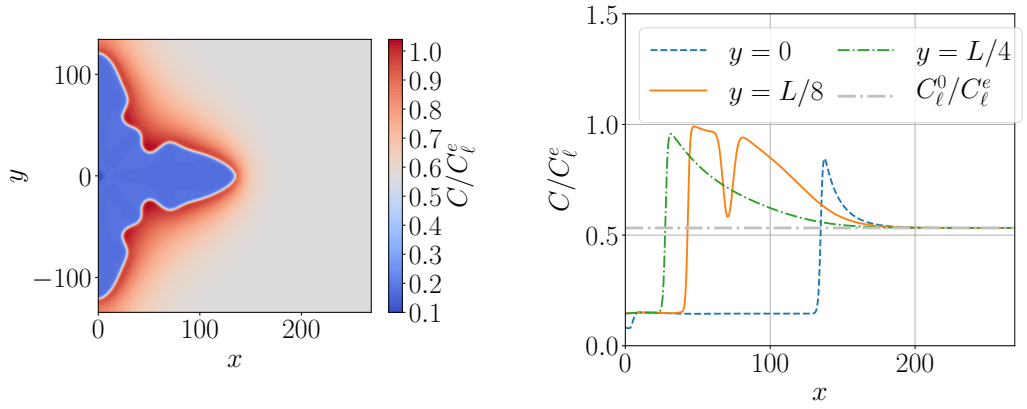

FIGURE 4.30: Concentration field (left) and the concentration as a function of x at three positions of y (right) at the end of the simulation.

Determination of the stability parameter in the forward Euler scheme

The aim of this sub-section is to determine a stable time step in the forward Euler scheme while using the second-order accurate RBF-FD method with different values of N for the spatial discretisation of the PDEs on RND and SND. To achieve this goal, the case with $\Delta h_{min} = 0.6$ and $m_\Omega = 28$ is analysed by reducing the forward Euler scheme stability parameter $\alpha_{\Delta t}$.

The model is tested for values of $\alpha_{\Delta t} \leq 0.3$ from Table 4.15. The relative error is defined as

$$\frac{\Delta l_{tip}}{l_{tip}} = \frac{|l_{tip}^{end}(\alpha_{\Delta t}) - l_{tip}^{end}(\alpha_{\Delta t} = 0.0375)|}{l_{tip}^{end}(\alpha_{\Delta t} = 0.0375)}, \tag{4.42}$$

where $l_{tip}^{end} = l_{tip}(t = t_{end})$. The relative error as a function of $\alpha_{\Delta t}$ for different values of N on RND and SND is shown in Fig. 4.31. As in the case of pure materials, we find that the model is stable with the first order of convergence for $\alpha_{\Delta t} \leq 0.3$ for each value of N. While the accuracy is approximately the same for all three values of N, in the case of SND, the accuracy is reduced as N is increased in the case of RND.

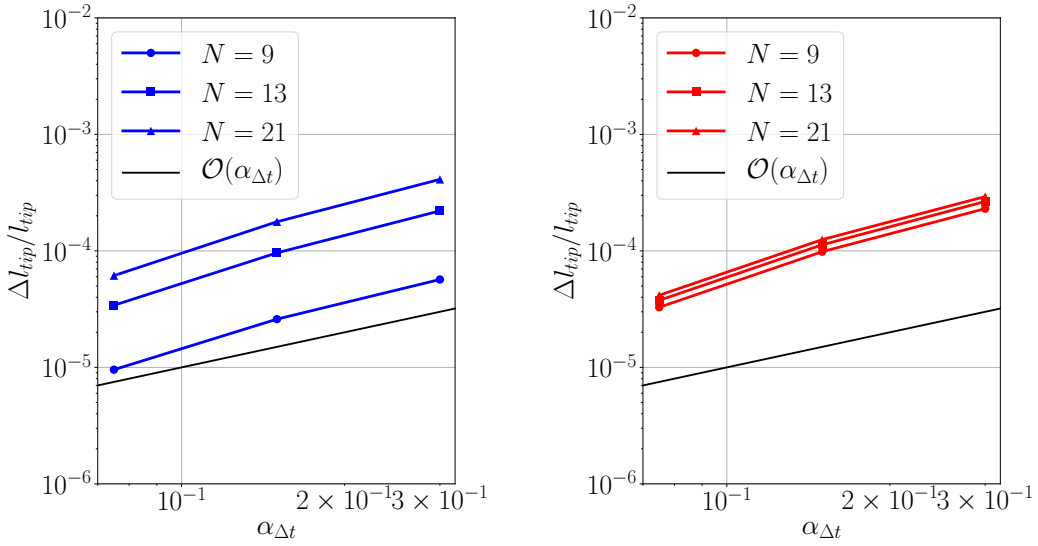

FIGURE 4.31: Relative error of l_{tip} as a function of forward Euler scheme stability parameter $\alpha_{\Delta t}$ by using RND (left) and SND (right) at $\Delta h_{min} = 0.6$ and $m_\Omega = 28$.

Verification at $\theta_0 = 0$

Re-scaled growth velocity $\tilde{v}_{tip}$ as a function of re-scaled time $\tilde{t}$ and the normalised concentration in the solid phase C_s/C_ℓ^e as a function of the re-scaled coordinate $\tilde{x}'$ are compared to the reference solutions for $\alpha_{\Delta t} = 0.3$, $\Delta h_{min} = 0.6$, and three values of N on RND and SND as shown in Figs. 4.32 and 4.33. The behaviour of the growth velocity on RND and SND is very similar to the behaviour in the case of pure materials; however, the growth velocity converges towards the steady-state growth velocity slower in comparison to the reference velocity. This observation is addressed at the end of this sub-section. On both node distributions, the best result is observed for the choice $N = 13$. In the case of RND, the values $N = 9$ and $N = 21$ yield too low and too high growth velocities, respectively. In the case of SND, the values $N = 9$ and $N = 21$ also yield too low and too high growth velocities, respectively. However, the velocities at different values of N are closer to each other in comparison to RND.

Concentration C_s/C_ℓ^e as a function of the re-scaled coordinate $\tilde{x}'$ is much less sensitive to the selection of N for both node distributions, as seen in Fig. 4.33. The concentration is slightly above the reference solution for both node

distributions. In the case of RND, the concentration is approaching the reference solution as N is increased. In the case of SND, the concentration is almost identical for all values of N.

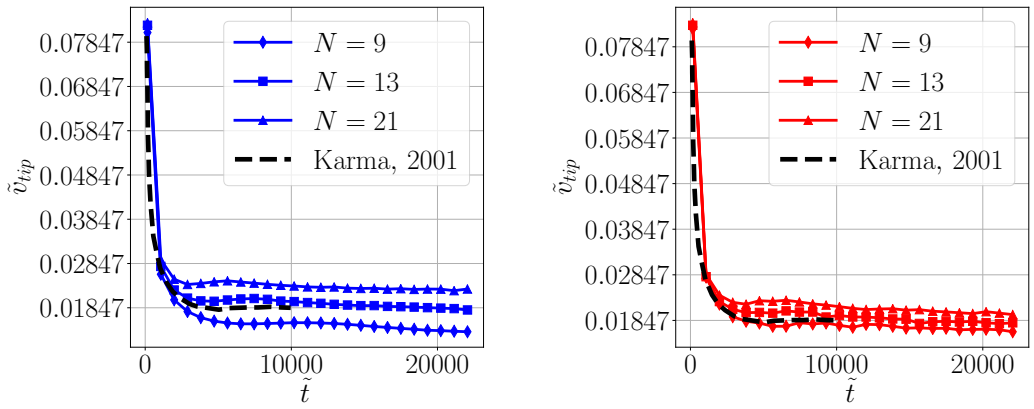

FIGURE 4.32: Re-scaled growth velocity as a function of time by using RND (left) and SND (right) at $\alpha_{\Delta t} = 0.3$, $\Delta h_{min} = 0.6$, and $m_\Omega = 28$.

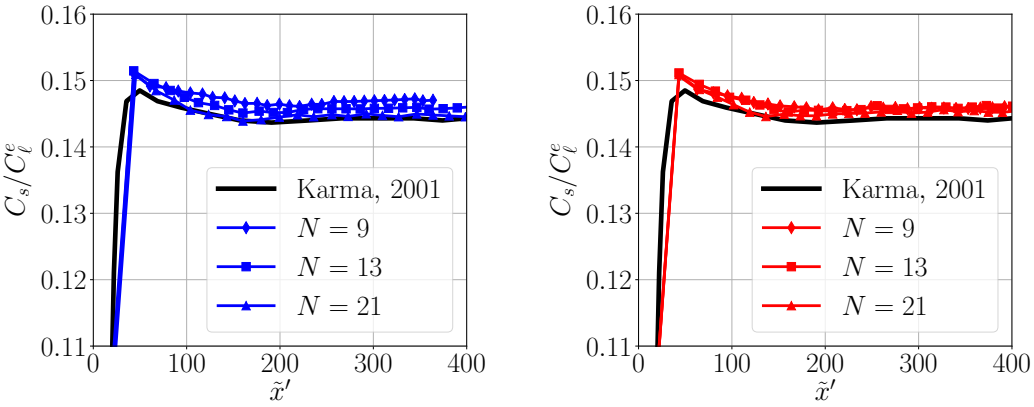

FIGURE 4.33: Normalised concentration as a function of rescaled coordinate by using RND (left) and SND (right) at $\alpha_{\Delta t} = 0.3$, $\Delta h_{min} = 0.6$, and $m_\Omega = 28$.

The influence of the scattered computational nodes on the performance is further analysed by increasing the size of a quadtree sub-domain m_Ω as shown in Fig. 4.34. As in the case of pure materials, the velocities at $N = 9$ and $N = 21$ are closer to velocity at $N = 13$ for $m_\Omega = 56$ in comparison to $m_\Omega = 28$.

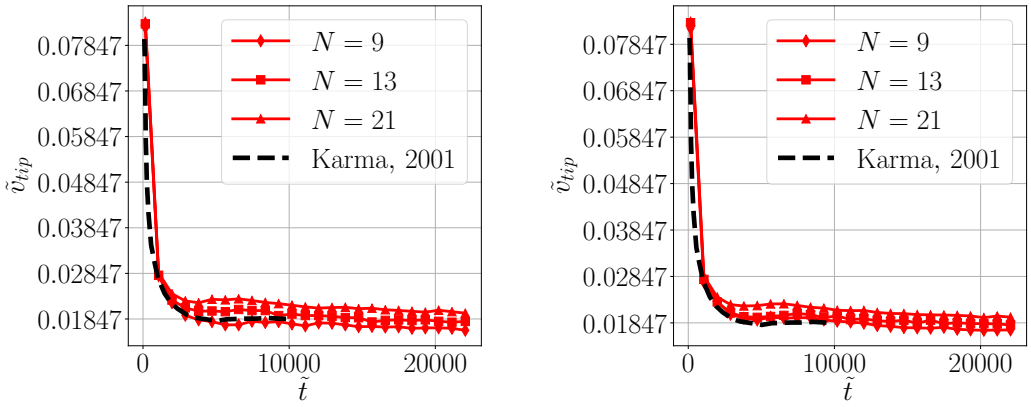

FIGURE 4.34: Rescaled growth velocity as a function of time for $m_\Omega = 28$ (left) and $m_\Omega = 56$ (right) using SND for $\alpha_{\Delta t} = 0.3$ and $\Delta h_{min} = 0.6$.

The reference velocity converges to the steady-state faster in comparison to our results. The reason is the fact that the PF model from (Karma, 2001) is not exactly identical to the PF model (Ohno, 2012) used in this dissertation. The difference between the models is function $\Xi(\{U_i\})$ from Eq. (2.79) which multiplies the left-hand side of the governing equation for ϕ from Eq. (2.84). In the case of binary alloys, the function is equal to $\Xi(\{U_i\}) = \Xi(U) = 1+(1-k_0)U$ as seen in Eq. (4.28). In (Karma, 2001), the dependence of function $\Xi(U)$ on U is not considered, i.e., $\Xi(U) = 1$. The growth velocity as a function of time for the case with $\Xi(U) = 1$ is shown in Fig. 4.35. For both node distributions with $N = 13$, the growth velocity is almost identical to the reference velocity in the interval $\tilde{t} \in [0, 10000]$. For $\tilde{t} > 10000$, the velocity is slightly reduced. For $N = 9$ and $N = 13$, the same behaviour in comparison to $N = 13$ as for $\Xi(U) = 1 + (1 - k_0)U$ is observed.

In (Karma, 2001), the finite-difference method with spacing $\Delta h = 0.4$ and forward Euler scheme with time step $\Delta t = 0.008$ are used for spatial and temporal discretisation of the governing equations. The configuration that resembles the used finite-difference method the most is $N = 13$ on RND, as evidenced in Fig. 4.35. To compare the results with the same spacing, the analysis with different values of N on RND and SND is also performed for $\Delta h_{min} = 0.4$, as seen in Fig. 4.36. While the velocity at $N = 13$ for $\Delta h_{min} = 0.4$ differs very little from the velocity at $\Delta h_{min} = 0.6$, a huge improvement is observed for

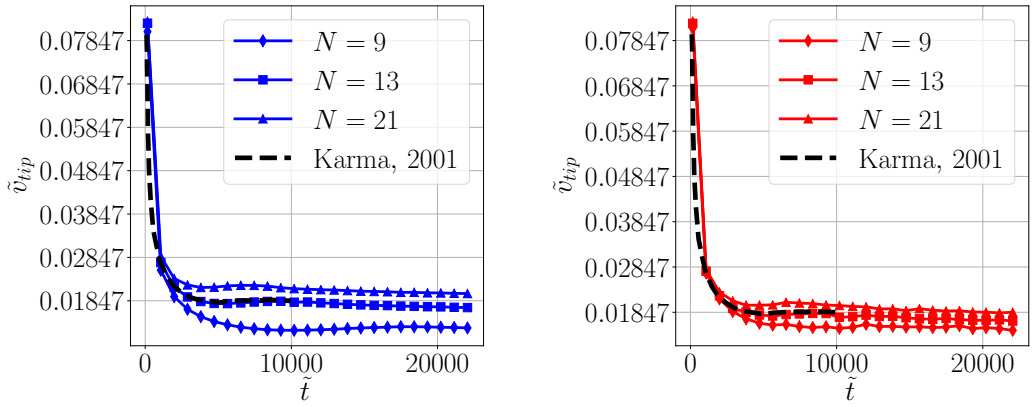

FIGURE 4.35: Rescaled growth velocity as a function of time by using RND (left) and SND (right) at $\alpha_{\Delta t} = 0.3$, $\Delta h_{min} = 0.6$, and $m_\Omega = 28$ for the case with $\Xi(U) = 1$.

$N = 9$ and $N = 21$ on both node distributions.

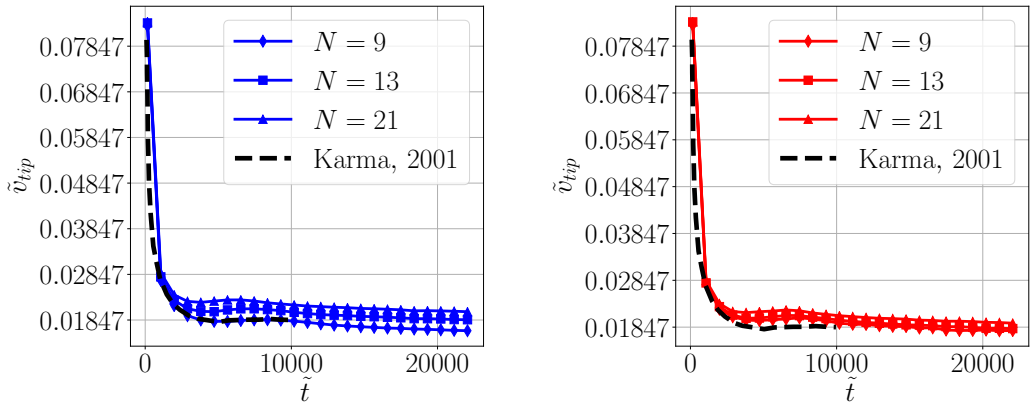

FIGURE 4.36: Re-scaled growth velocity as a function of time by using RND (left) and SND (right) at $\alpha_{\Delta t} = 0.3$, $\Delta h_{min} = 0.4$, and $m_\Omega = 21$.

Verification at $\theta_0 \geq 0$

The numerical method is analysed at different preferential growth directions with the simulation parameters from Table 4.16. The normalised concentration in Ω at four different angles θ_0 at the end of the simulation is shown in Fig. 4.37. A two-times larger computational domain is used in comparison to the

analysis at $\theta_0 = 0$, while the final time remains the same. The performance for only one SND is analysed, since the performance at multiple SNDs has already been assessed in the previous sub-section in the example of pure materials.

TABLE 4.16: Simulation parameters for the analysis of the numerical method at different growth angles in the solidification of binary alloys.

Preferential growth direction	
Growth angle (θ_0)	$0°, 5°, 10°, 15°, 20°, 25°, 30°, 35°, 40°, 45°$
Computational domain parameters	
Side length (L)	537.6
South-west coordinate ($\boldsymbol{r}_{sw}$)	$(-L/2, -L/2)$
Time	
Initial time (t_{start})	0
Final time (t_{end})	850
Forward Euler scheme	
Stability parameter ($\alpha_{\Delta t}$)	0.3
Time step (Δt)	$\alpha_{\Delta t}\Delta h^2/(4\bar{D}_\ell)$
RBF-FD method	
Number of nodes in sub-domain (N)	$9, 13, 21$
PHS power (n)	5
Highest monomial order (P)	2
Adaptive algorithm	
Type of node distribution	RND, SND
Sub-domain size/spacing ratio (m_Ω)	$28, 56$
Overlapping parameter (n^*)	2
Minimum spacing (Δh_{min})	0.6
Maximum spacing (Δh_{max})	$L/(2m_\Omega)$
Time step-restriction parameter ($m_{\Delta t}$)	1

Steady-state growth velocity $\tilde{v}_{tip}^{steady}$ as a function of preferential angle θ_0 is shown in Fig. 4.38. The behaviour of the method is very similar to the behaviour in the case of pure materials. Again, the use of SND is much less prone to the selection of N. The best result is again observed for $N = 13$ on both node distributions.

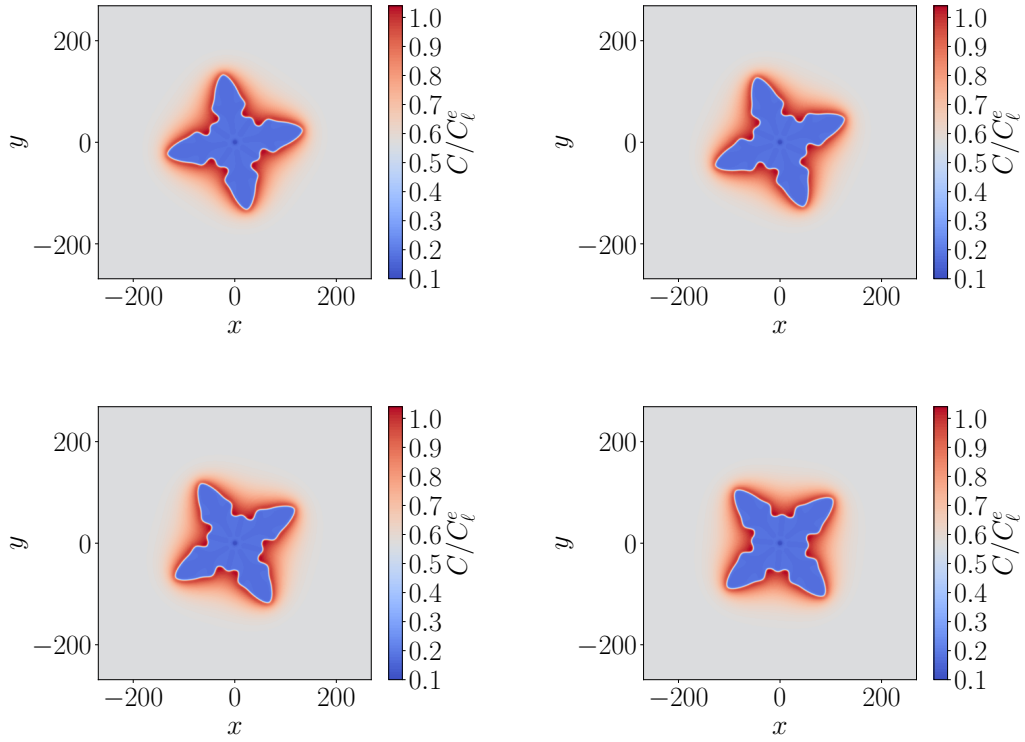

FIGURE 4.37: Normalised concentration at $\theta_0 = 10°$ (top-left), $\theta_0 = 20°$ (top-right), $\theta_0 = 30°$ (bottom-left), and $\theta_0 = 40°$ (bottom-right) for $m_\Omega = 28$ and $N = 13$ by using RND.

Normalised steady-state concentration in the solid-phase C_s^{steady}/C_ℓ^e as a function of θ_0 is shown in Fig. 4.39. In the case of RND, the concentration is independent of θ_0 for $N = 13$. For $N \neq 13$, the concentration is firstly increased and then decreased as θ_0 is increased with the maximum at $\theta_0 = 25°$ and $\theta_0 = 20°$ for $N = 9$ and $N = 21$, respectively. In the case of SND, the concentration is almost independent of θ_0 for all three values of N. The concentration is slightly increased at $\theta_0 = 40°$ and $\theta_0 = 45°$ for $N = 9$.

The influence of the scattered computational nodes on the performance for different preferential growth directions is analysed by running simulations with $m_\Omega = 56$, as shown in Fig. 4.40. The steady-state growth velocity and the concentration are both less prone to rotation, especially for $N \neq 13$. The increase of the concentration for $\theta_0 = 40°$ and $\theta_0 = 45°$ for $N = 9$ at $m_\Omega = 28$ is no longer present at $m_\Omega = 56$.

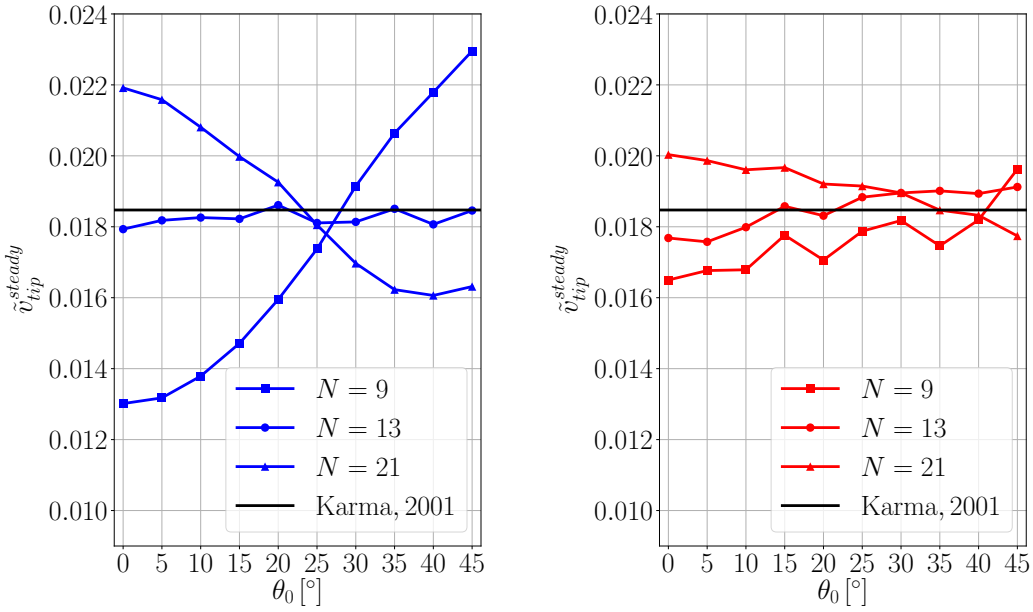

FIGURE 4.38: Steady-state growth velocity as a function of growth angle for $m_\Omega = 28$ by using RND (left) and SND (right).

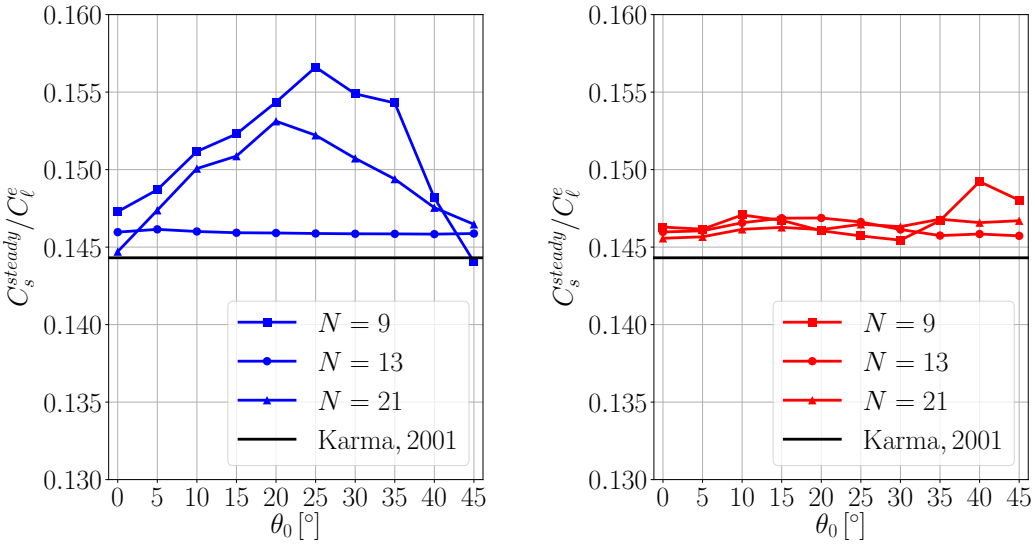

FIGURE 4.39: Steady-state normalised concentration as a function of growth angle for $m_\Omega = 28$ by using RND (left) and SND (right).

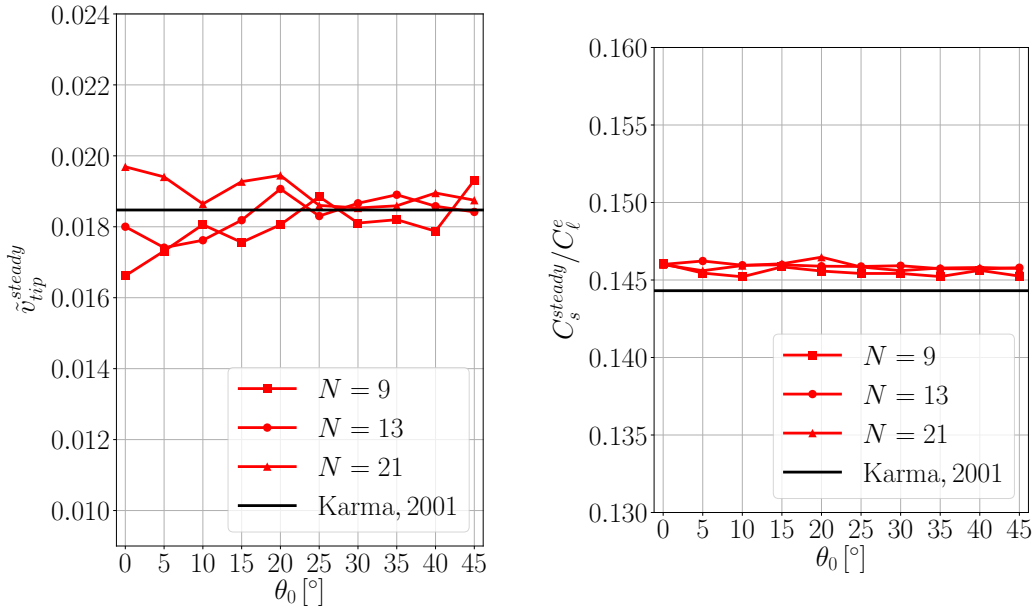

FIGURE 4.40: Steady-state growth velocity (left) and steady-state concentration in the solid phase (right) for $m_\Omega = 56$ by using SND.

4.2.6 Discussion

In Section 4.2, the newly developed numerical approach is analysed for the PF modelling of the isothermal dendritic solidification of binary alloys for arbitrary preferential growth directions. The growth velocity and the concentration in the solid phase are compared to the reference solution from (Karma, 2001). An almost identical observation as in the case of pure materials from Section 4.1 can be made regarding the accuracy. The use of the SND provides better accuracy in comparison to the use of the RND for $N = 9$ and $N = 21$. The quadtree domain decomposition in the ASP introduces regularity in the solution obtained by using the SND. A large enough quadtree sub-domain size/spacing ratio has to be used therefore to increase the accuracy if the SND is in use. The results are further comprehensively summarized and concluded in Section 5.

4.3 Solidification with a constant cooling rate for an Al-Cu alloy

In this section, the solidification of Al-Cu alloy with a constant cooling rate is considered. A 2-D example with the concentration $C_0 = 1\,\text{wt.\%Cu}$ and the side length of square computational domain $L = 1000\,\mu\text{m}$ from (Boukellal et al., 2018) is chosen as the reference solution to which the results of our newly developed numerical model are compared. In the article, 2-D and 3-D PF simulations in dilute Al-Cu alloys are performed with the purpose of finding scaling laws that govern the growth and interaction of equiaxed Al-Cu dendrites. The interaction between the dendrites is simulated by the zero-flux Neumann boundary conditions for PF and supersaturation.

The problem definition of the solidification with a constant cooling rate of the Al-Cu alloy is given in Section 4.3.1. The simulation parameters are discussed in Section 4.3.2. The time step in the forward Euler scheme is determined in Section 4.3.3. The results of the verification are presented in Section 4.3.4.

4.3.1 Problem definition

The computational domain Ω with the boundary Γ is a square with the southwest vertex $\boldsymbol{r}_{sw}$ and the side length L, as shown in Fig. 4.41. Solidification with the constant cooling rate of a dendrite from a binary alloy ($N_c = 2$) with negligible diffusivity of solute in the solid phase ($D_s = 0$) is considered. In this section, a dimensional version of the PF model is applied where the spatial coordinates and time are measured in units of micrometers and seconds. The system of two coupled governing equations for PF ϕ and dimensionless supersaturation U is given by Eqs. (2.84) and (2.85)

$$\begin{aligned}(1+(1-k_0)U)a^2(\boldsymbol{n})\tau_0\frac{\partial\phi}{\partial t} &= \phi-\phi^3-(1-\phi^2)^2\lambda(\theta+U)\\ &+\nabla\cdot\left(W_0^2a^2(\boldsymbol{n})\nabla\phi\right)+\sum_{\xi=x,y}\partial_\xi\left(W_0^2|\nabla\phi|^2a(\boldsymbol{n})\frac{\partial a(\boldsymbol{n})}{\partial(\partial_\xi\phi)}\right),\end{aligned} \tag{4.43}$$

and

$$\begin{aligned}\frac{1}{2}\left(1+k_0-(1-k_0)\phi\right)\frac{\partial U}{\partial t} &= \frac{1}{2}\left(1+(1-k_0)U\right)\frac{\partial \phi}{\partial t} \\ &+ \nabla\cdot\left(D_\ell\frac{1-\phi}{2}\nabla U+\frac{1}{2\sqrt{2}}W_0(1+(1-k_0)U)\frac{\partial\phi}{\partial t}\frac{\nabla\phi}{|\nabla\phi|}\right),\end{aligned} \tag{4.44}$$

The cubic anisotropy function $a(\boldsymbol{n})$ is given by Eq. (4.1). The dimensionless temperature as a function of time t is given as

$$\theta(t) = R_c t/\Delta T_{ref}, \tag{4.45}$$

where R_c is the constant cooling rate. The reference freezing range is given as $\Delta T_{ref} = -m_\ell(1-k_0)C_0$.

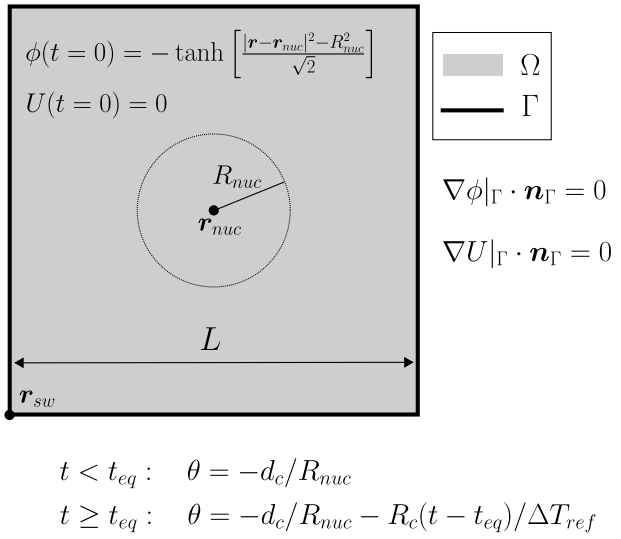

FIGURE 4.41: Illustration of a square computational domain Ω with boundary Γ. A domain is defined by the south-west coordinate $\boldsymbol{r}_{sw} = (-L/2, -L/2)$ and the side length of a square $L = 2000\,\mu$m. Solidification of small nucleus with radius $R_{nuc} = 50\,\mu$m and center $\boldsymbol{r}_{nuc} = (0,0)$ with a constant cooling rate R_c is considered. The equilibrium is achieved by properly selected temperature field $\theta(t)$. Zero flux Neumann boundary conditions are proposed for ϕ and U.

The constrained growth of a dendrite is simulated by a zero-flux boundary condition for ϕ and U from Eqs. (4.10) and (4.33), respectively. The initial condition for the PF is a circular nucleus with the origin $\boldsymbol{r}_{nuc}$ and the radius

R_{nuc}, already defined in Eq. (4.9) from the previous sub-section. Special care has to be given to the initial conditions for θ and U, since the nucleus starts to melt till θ is large enough due to capillary effects if the initial condition is simply set to $U(0) = 0$ and $\theta(0) = 0$. In (Boukellal et al., 2018), the initial conditions are set to $U(0) = -d_c/R_{nuc}$ and $\theta(0) = -U(0)$. Temperature θ is then varied with decreasing amplitude in order to achieve a quasi-equilibrium state with an interface velocity arbitrarily close to zero.

In the dissertation, a slightly different strategy is applied to achieve the equilibrium state. The initial supersaturation is set to $U(0) = 0$ and the initial temperature is held at $\theta = -d_c/R_{nuc}$ until the growth velocity is arbitrarily close to zero. The dimensionless initial temperature $\theta = -d_c/R_{nuc}$ corresponds to the actual initial temperature $T_0 = T_{liq} - \Gamma_{s\ell}/R_{nuc}$. The equilibrium solid-liquid interface is given as $T^* = T_{liq} - \Delta T_c = T_{liq} - \Gamma_{s\ell}(a(\varphi) - a''(\varphi))/R_{nuc}$ according to the conditions at the solid-liquid interface from Chapter 2. The kinetic undercooling ΔT_k is negligible for Al alloys under the considered solidification conditions. The initial and equilibrium temperatures for $a(\varphi) = 1 + \epsilon_4 \cos 4\varphi$ are shown in Fig. 4.42. For $\varphi < \pi/8$ and $\varphi > 3\pi/8$, the initial temperature T_0 is below the equilibrium temperature T^*, which results in solidification in those ranges. For $\pi/8 < \varphi < 3\pi/8$, the initial temperature T_0 is above the equilibrium temperature T^*, which results in the melting in this range.

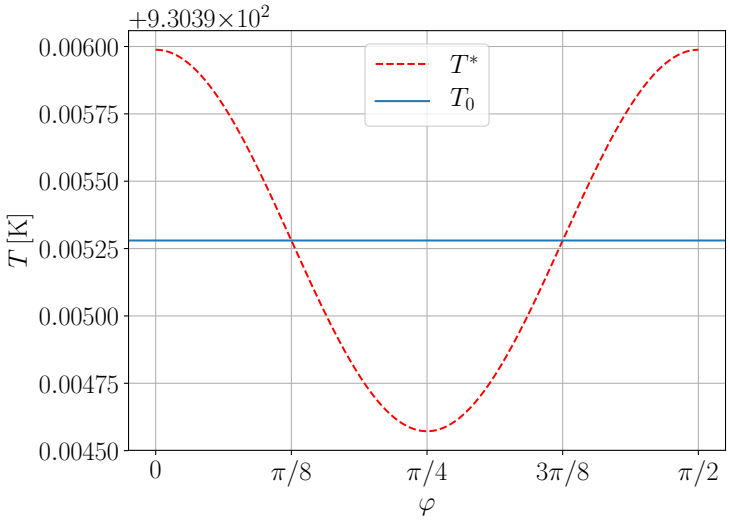

FIGURE 4.42: Equilibrium and initial temperatures as a function of the angle φ for $\theta_0 = 0$ in the first quadrant.

The solid-liquid interface at $t = 0$ s and $t = 30$ s and the growth velocity as a function of time with the simulation parameters from Table 4.17 for $\theta(t) = -d_c/R_{nuc}$ are shown in Fig. 4.43. For $\varphi < \pi/8$ and $\varphi > 3\pi/8$, the curvature is slightly increased due to solidification that shifts T^* towards T_0. For $\pi/8 < \varphi < 3\pi/8$, curvature is slightly decreased due to the melting, which also shifts T^* towards T_0. In both cases, the growth velocity eventually approaches zero, which we consider as the quasi-equilibrium. To conclude, the initial supersaturation is set to $U(0) = 0$, while the dimensionless temperature as a function of time is given as

$$\theta(t) = \begin{cases} -d_c/R_{nuc}, & t < t_{eq} \\ -d_c/R_{nuc} - R_c(t - t_{eq})/\Delta T_{ref}, & t \geq t_{eq} \end{cases}, \tag{4.46}$$

where t_{eq} is the equilibrium time. It is set to $t_{eq} = 30\,\text{s}$ since the growth velocity is almost zero for $t > 30\,\text{s}$, as seen in Fig. 4.43.

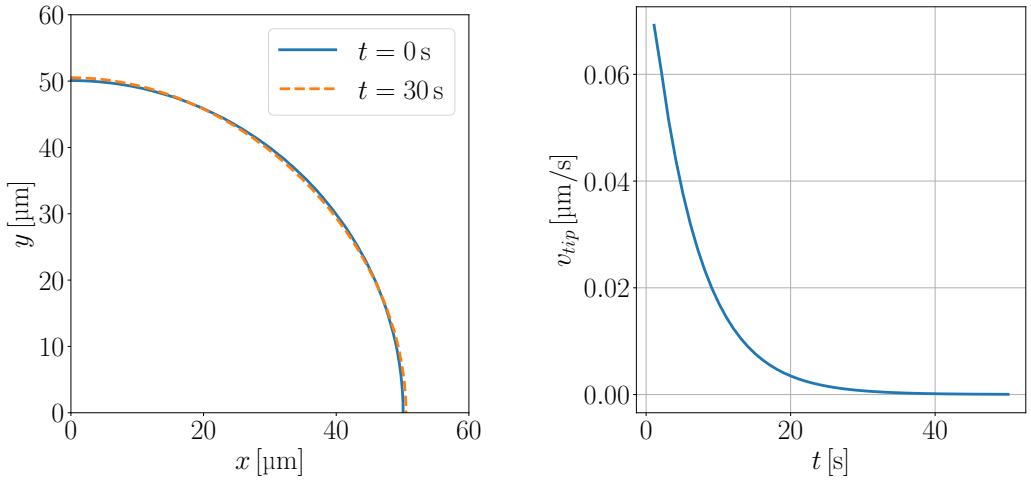

FIGURE 4.43: The solid-liquid interface at two times (left) and the growth velocity as a function of time for $\theta(t) = -d_c/R_{nuc}$ (right).

4.3.2 Simulation parameters

In the considered case, the initial concentration and the side length of a square domain are set to $C_0 = 1\,\text{wt.\%Cu}$ and $L = 1000\,\mu\text{m}$, respectively. A solid

nucleus with radius $R_{nuc} = 50\,\mu\text{m}$ is put in the south-west corner of the computational domain. A constant cooling rate $R_c = 0.5\,\text{K/min}$ is applied in the computational domain. The ratio between the interface thickness and chemical capillary length is set to $W_0/d_c = 24$. The properties of the Al-Cu alloy and the used PF parameters are shown in Table 4.17. The solid nucleus is in the quasi-equilibrium at $t = 0$ s by setting $t_{start} = -30$ s and $t_{eq} = 0$ s. The interface thickness and the attachment time are equal to

$$W_0 = (W_0/d_c)d_c = 2.53\,\mu\text{m}, \tag{4.47}$$

and

$$\tau_0 = \frac{d_c^2}{D_\ell}\frac{1}{\alpha_1^2\alpha_2^2}(W_0/d_c)^3 = 0.028\,\text{s}, \tag{4.48}$$

where $d_c = \Gamma_{s\ell}/(-m_\ell(1-k_0)C_0) = 0.106\,\mu\text{m}$.

TABLE 4.17: Simulation parameters.

Al-Cu alloy physical properties	
Partition coefficient (k_0)	0.14
Strength of anisotropy (ϵ_4)	0.01
Liquidus slope (m_ℓ)	$-2.6\,\text{K/wt.\%Cu}$
Copper concentration (C_0)	$1\,\text{wt.\%Cu}$
Copper diffusivity in the liquid phase (D_ℓ)	$3000\,\mu\text{m}^2/\text{s}$
Gibbs-Thomson coefficient ($\Gamma_{s\ell}$)	$0.236\,\text{K}\mu\text{m}$
Solidification parameters	
Growth angle (θ_0)	0°
Center of nucleus ($\boldsymbol{r}_{nuc}$)	$(0\,\mu\text{m}, 0\,\mu\text{m})$
Radius of nucleus (R_{nuc})	$50\,\mu\text{m}$
Equilibrium time (t_{eq})	$0\,\text{s}$
Cooling rate (R_c)	$0.5\,\text{K/min}$
Initial time (t_{start})	$-30\,\text{s}$
Final time (t_{end})	$200\,\text{s}$
PF parameters	
Constant (α_1)	0.8839
Constant (α_2)	0.6267
Interface thickness/capillary length ratio (W_0/d_c)	24
Coupling parameter (λ)	$\alpha_1 W_0/d_c$

The considered case is computationally much more demanding in comparison to the cases from previous two sub-sections due to the large computational domain and long computational time. In (Boukellal et al., 2018), computational efficiency is increased by recasting the PF model with a pre-conditioned PF (Glasner, 2001), which allows larger spacings Δh and by applying the GPU acceleration (Yamanaka et al., 2011).

In the preliminary simulations, we found that the simulations of only one-quarter of the dendrite can be very inaccurate due to very small strength of anisotropy since the dendrite tip is directly at the boundary of the computational domain, which leads to instabilities in the current implementation of the RBF-FD method. Consequently, the nucleus is put in the middle of the computational domain, which requires side length L that is twice as long. The growth velocity as a function of time is compared to the reference solution from (Boukellal et al., 2018). The algorithm from sub-section 4.1.4 with the parameters $t_0^{mea} = 0.1\,\mathrm{s}$ and $\Delta t^{mea} = 0.1\,\mathrm{s}$ is applied for the calculation of the growth velocity. The averaging with thirty points from the data set $\{t_i^{mea}, v_{tip}(t_i^{mea})\}$ is applied in the representation of the velocity $v_{tip}(t)$. The concentration as a function of x along the $y = 0$ line is also analysed.

4.3.3 Stability criterion in the forward Euler scheme

The time step in this case is given as

$$\Delta t(\Delta h) = \alpha_{\Delta t} \frac{1}{4} \frac{\Delta h^2}{\max(\bar{D}_\ell, 1/(1-\epsilon_4))} \frac{\tau_0}{W_0^2} \tag{4.49}$$

The parameters from Table 4.17 yield

$$\Delta t(\Delta h) = \alpha_{\Delta t} \Delta h^2 / (4 D_\ell), \tag{4.50}$$

since $\bar{D}_\ell = D_\ell \tau_0 / W_0^2 = 13.12$ and therefore $\bar{D}_\ell > 1/(1-\epsilon_4)$. The actual time step in a extended quadtree sub-domain Ω_i^* with spacing Δh_i is according to Eq. (3.30) from sub-section 3.4.6 given as

$$\Delta t_i(\Delta h_i) = \alpha_{\Delta t} \min\left(\Delta h_i^2, 2^{2m_{\Delta t}} \Delta h_{min}^2\right) / (4 D_\ell), \tag{4.51}$$

since the restriction parameter has to be additionally considered in the ASP.

4.3.4 Simulation results

The PF model is solved by the ASP with the numerical parameters from Table 4.18. We found that the minimum spacing has to be set to $\Delta h_{min} = 0.6W_0 = 1.52\,\mu\text{m}$ (or lower) in order to properly resolve the case with a very small strength of anisotropy $\epsilon_4 = 0.01$.

TABLE 4.18: Numerical parameters for the simulation of solidification of Al-Cu alloy at constant cooling rate.

Computational domain parameters	
Side length of domain (L)	$2040\,\mu\text{m}$
Forward Euler scheme	
Stability parameter ($\alpha_{\Delta t}$)	0.3
Time step (Δt)	$\alpha_{\Delta t}\Delta h^2/(4D_\ell)$
RBF-FD method	
Number of nodes in sub-domain (N)	$9, 13, 21$
PHS power (n)	5
Highest monomial order (P)	2
Adaptive algorithm	
Type of node distribution	RND, SND
Sub-domain size/spacing ratio (m_Ω)	21
Overlapping parameter (n^*)	2
Minimum spacing (Δh_{min})	$1.52\,\mu\text{m}$
Maximum spacing (Δh_{max})	$L/(2m_\Omega)$
Time step-restriction parameter ($m_{\Delta t}$)	2

The side length of the computational domain in the ASP is given as

$$L = 2^{\mathcal{N}_{max}} m_\Omega \Delta h_{min}, \tag{4.52}$$

due to quadtree domain decomposition. It is therefore impossible to simulate the case where the distance between the center of the dendrite and the boundary is exactly equal to $1000\,\mu\text{m}$. The closest configuration with $\Delta h_{min} = 0.6W_0$ is achieved by using parameters $\mathcal{N}_{max} = 6$ and $m_\Omega = 21$, which yield the distance $\approx 1020\,\mu\text{m}$. As in the previous two sections, the PF model is solved for three different values of N using RND and SND.

Morphology and growth velocity

The evolution of the solid-liquid interface (evolution of $\phi = 0$ contour) and the growth velocity as a function of time by using RND is shown in Fig. 4.44. The morphologies and the growth velocities are almost identical and very close to the reference velocity for all values of N for $t \lessapprox 30$ s. As θ is further decreased, the configuration with $N = 9$ can no longer correctly resolve the solid-liquid interface which yields the evolution of a seaweed-like structure. It is evident that some directions are more favourable. This is the consequence of the mesh-induced anisotropy (Mullis, 2006), which has also been observed in the PF modelling of the solidification on the regular node distribution using other numerical methods.

For $N = 13$ and $N = 21$, a dendrite with four primary trunks is developed. At higher undercoolings, secondary dendrite arms are developed too. They, however, do not disturb the growth velocity at the tip of the dendrite, which is of main interest in this analysis. The maximum growth velocities v_{tip}^{max} and the times t_{tip}^{max} at which the maximum occurs are tabulated in Table 4.19.

TABLE 4.19: Maximum velocity v_{tip}^{max} and time t_{tip}^{max} for BSP and ASP.

Node distribution	N	v_{tip}^{max} [µm/s]	t_{tip}^{max} [s]
RND	9	7.67	156
	13	12.32	129
	21	14.41	120
SND	9	11.89	129
	13	12.08	129
	21	13.21	126
Boukelall et al., 2018	-	11.25	119

Velocity v_{tip}^{max} at $N = 9$ is naturally far away from the velocities at $N = 13$ and $N = 21$. In the case of $N = 13$, v_{tip}^{max} is for ≈ 1 µm/s higher than reference v_{tip}^{max}, while time t_{tip}^{max} is shifted for 10 s to the right. In the case of $N = 21$, v_{tip}^{max} is for ≈ 3 µm/s higher than reference v_{tip}^{max}, while time t_{tip}^{max} is shifted for 1 s to the right. The reasons for these discrepancies are addressed later in this section.

The evolution of the solid-liquid interface and the growth velocity as a function of time by using SND are shown in Fig. 4.45. In this case, a dendrite with four primary trunks is developed for all three values of N. There

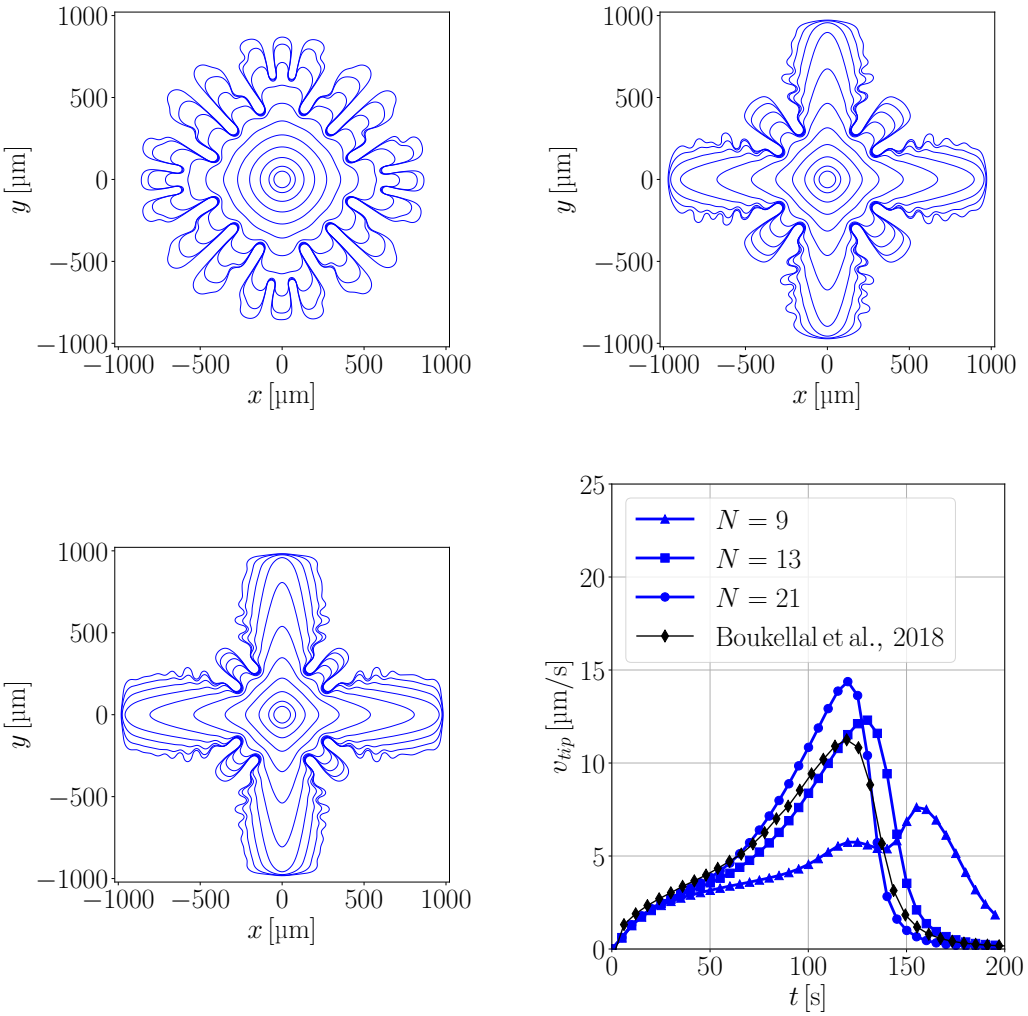

FIGURE 4.44: The evolution of the solid-liquid interface for $N = 9$ (top-left), $N = 13$ (top-right), and $N = 21$ (bottom-left) in the case of RND. The solid-liquid interface is plotted every 20 seconds. The growth velocity as a function of time (bottom-right) for three values of N in the case of RND.

is not a large difference between the dynamics at the tip of a dendrite for different values of N; however, the maximum velocity at $N = 21$ is again the highest. In the case of $N = 9$ and $N = 13$, v_{tip}^{max} is for less than $1\,\mu m/s$ higher than reference v_{tip}^{max}, while time t_{tip}^{max} is shifted for $10\,s$ to the right. In the case of $N = 21$, v_{tip}^{max} is for $\approx 2\,\mu m/s$ higher than reference v_{tip}^{max} while time t_{tip}^{max} is shifted for $7\,s$ to the right. Different values of N, however, affect the evolution of secondary dendrite branches. In the case of RND, the secondary branches

are totally symmetric, which is not the case for SND. Some quasi-symmetry is observed using SND too, since only one SND is generated at the beginning of the simulation and is during simulation re-scaled and saved for the calculation in a newly created quadtree sub-domain in the refinement/de-refinement procedure. The regular quadtree decomposition additionally introduces some symmetry. The quasi-symmetry can be observed between the north and west trunk or between the east and south trunk for $N = 9$ and $N = 13$.

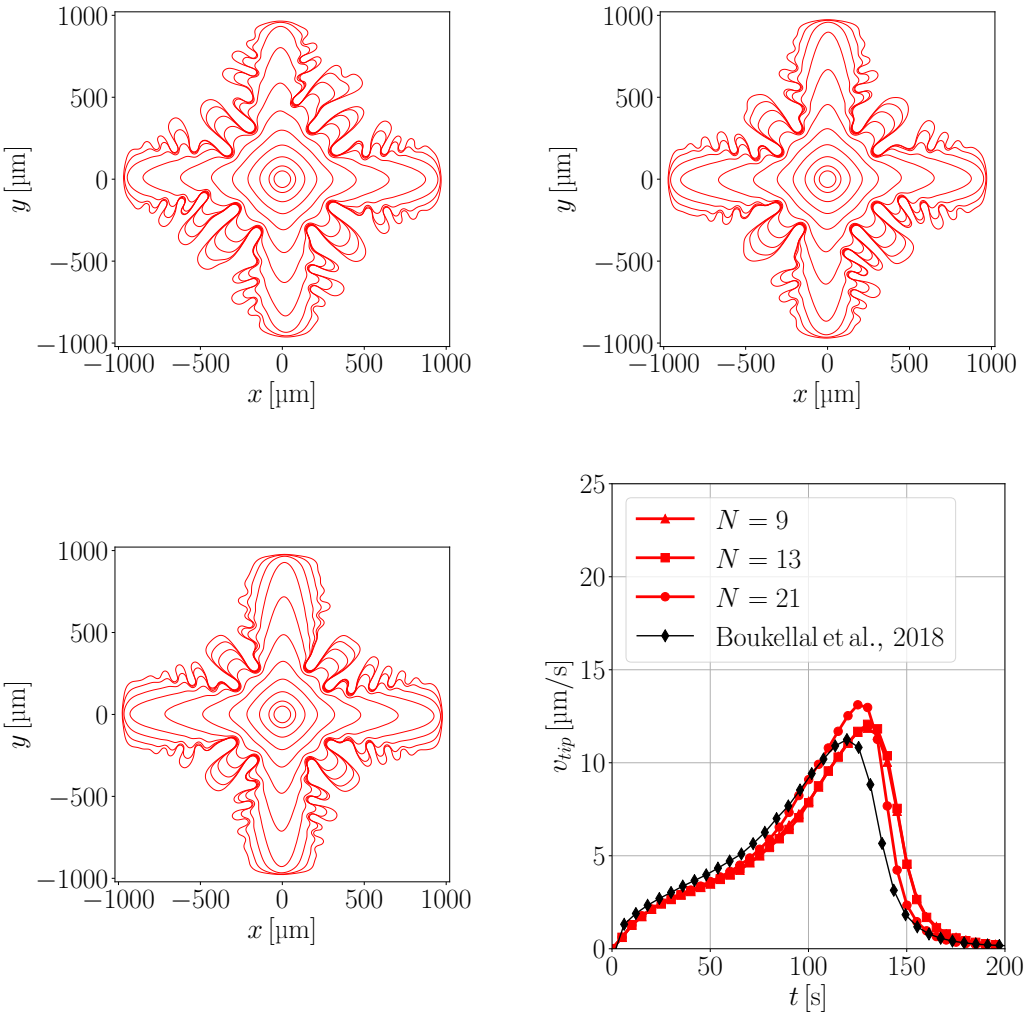

FIGURE 4.45: The evolution of the solid-liquid interface for $N = 9$ (top-left), $N = 13$ (top-right), and $N = 21$ (bottom-left) in the case of SND. The solid-liquid interface is plotted every 20 seconds. The growth velocity as a function of time (bottom-right) for three values of N in the case of SND.

Cu concentration

The concentration profile and the concentration along the x-axis at different times for $N = 13$ and RND are shown in Fig. 4.46. The quadtree sub-domains are also shown in order to emphasize that a large area of the computational domain is refined in the last stage of the simulation, which reduces the ASP speed-up and makes the simulation computationally extremely demanding. The concentration in the liquid and solid phases is an increasing function of time due to the applied constant cooling rate. One can also see how the gradient of the concentration in the liquid phase at the solid-liquid interface is approximately zero at the beginning and at the end of the simulation, which signals low growth velocities.

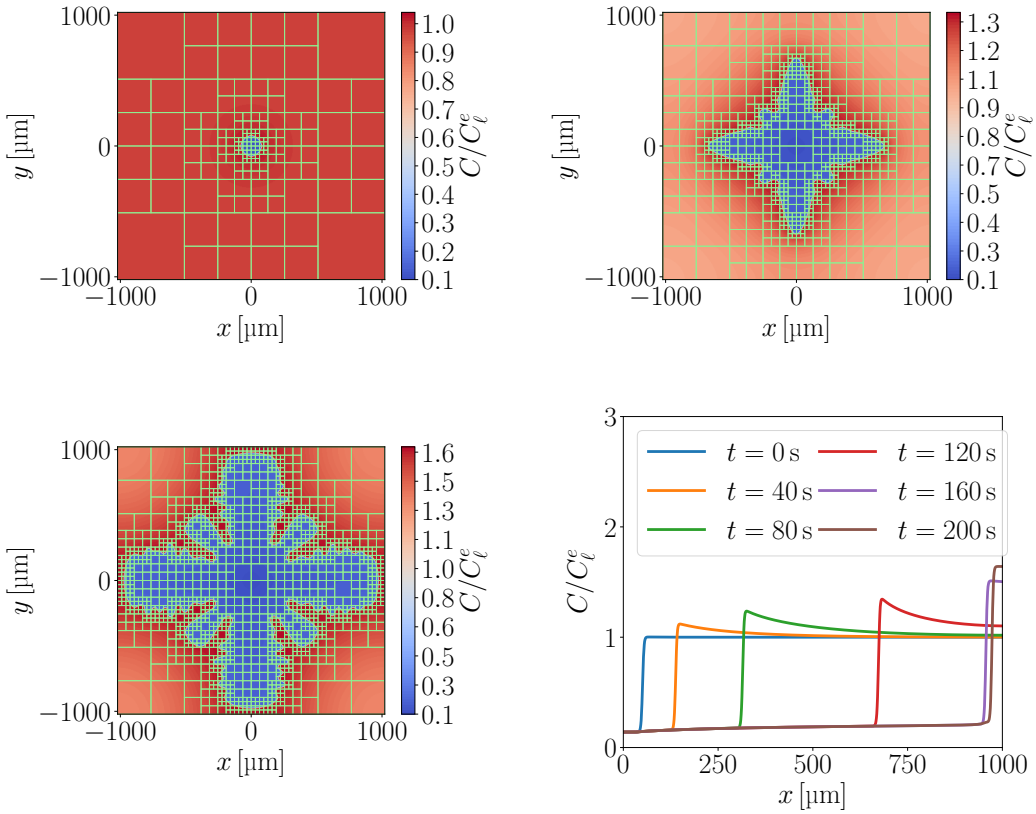

FIGURE 4.46: The concentration field at $t = 20$ s (top-left), $t = 120$ s (top-right), and $t = 200$ s (bottom-left). The concentration as a function of x at $y = 0\,\mu$m at six sequential times (bottom-right). Configuration with $N = 13$ on RND is used.

The concentration profile and the concentration in the solid phase along the x-axis at different values of N in the case of RND are shown in Fig. 4.47. The concentration in the middle of the trunk at $N = 9$ is far away from the concentration at $N = 13$ and $N = 21$. This is of course expected since the concentration profiles are directly determined by the growth velocity as a function of time (or more precisely, the size of dendrite trunk as a function of time). This is also the reason for the difference between the concentration at $N = 13$ and $N = 21$.

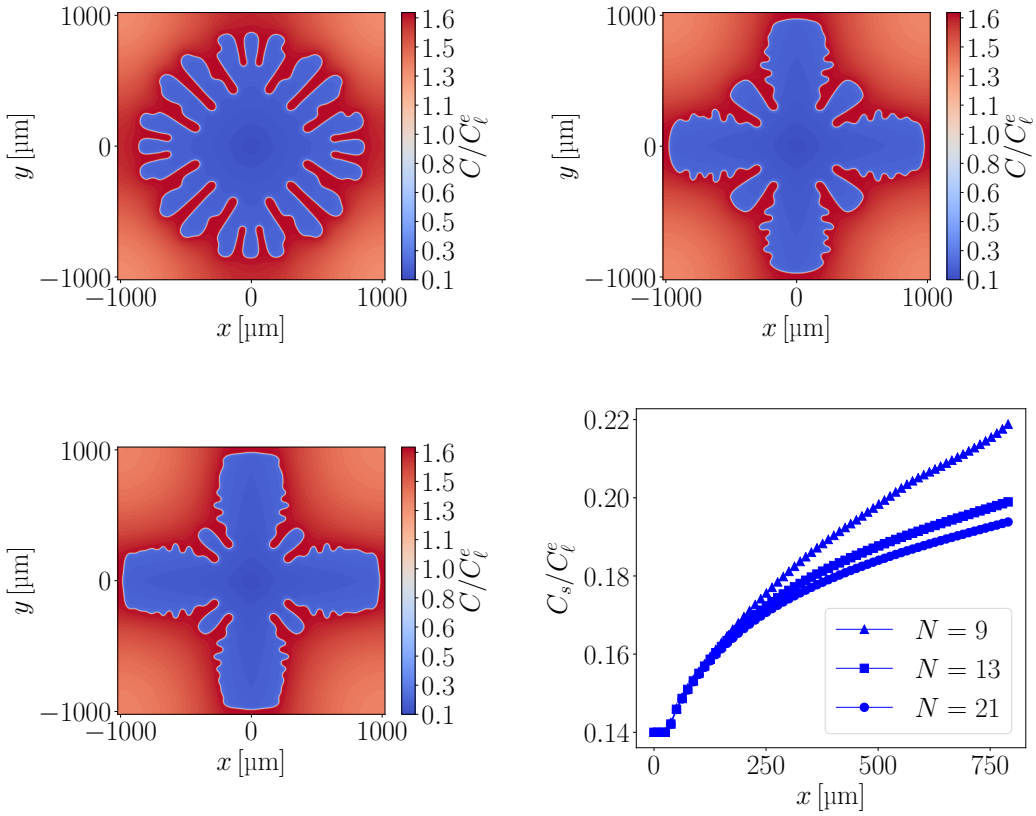

FIGURE 4.47: The concentration field at $t = 200\,\text{s}$ for $N = 9$ (top-left), $N = 13$ (top-right), and $N = 21$ (bottom-left) in the case of RND. The concentration in the solid phase as a function of x at $y = 0\,\mu\text{m}$ for three values of N (bottom-right) in the case of RND.

The concentration profile and the concentration in the solid phase along the x-axis at different values of N in the case of SND are shown in Fig. 4.48. For $N = 9$ and $N = 13$, the concentrations as a function of x almost coincide. A small deviation is observed for $N = 21$, which is again the consequence of a

different growth velocity as a function of time in comparison to $N = 9$ and $N = 13$.

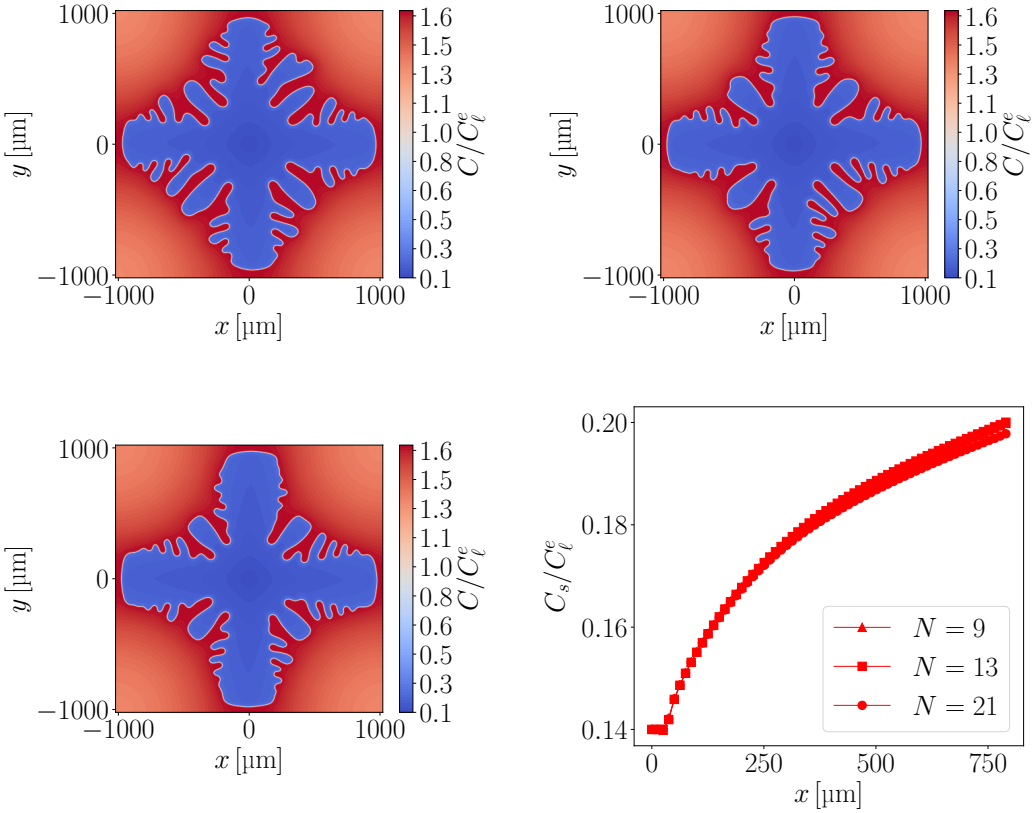

FIGURE 4.48: The concentration field at $t = 200\,\text{s}$ for $N = 9$ (top-left), $N = 13$ (top-right), and $N = 21$ (bottom-left) in the case of SND. The concentration in the solid phase as a function of x at $y = 0\,\mu\text{m}$ for three values of N (bottom-right) in the case of SND.

Analysis of the discrepancy with the reference results

We managed to qualitatively reproduce the reference results for $N = 13$ and $N = 21$ in the case of RND and for all three values of N in the case of SND. There is, however, a quantitative discrepancy between the growth velocities as seen in Table 4.19. The highest discrepancy of $\approx 28\%$ is observed for the case with $N = 21$ on RND. The lowest discrepancy of $\approx 5.6\%$ is observed for $N = 9$ on SND. In general, the results with SND are closer to the reference results. The discrepancy is attributed to

- the side length of the computational domain is for $\approx 20\,\mu$m larger in our case,
- the initial conditions are not precisely equal,
- in (Boukellal et al., 2018), the PF model from (Echebarria et al., 2004) is applied, while in our case we apply the PF model from (Ohno, 2012). The difference between the models is the term $1 + (1 - k_0)U$ on the left-hand side of Eq. (4.43), which is in (Boukellal et al., 2018) set to $1 - (1 - k_0)\theta$,
- the PF model in (Boukellal et al., 2018) is re-cast with a pre-conditioned PF (Glasner, 2001),
- the PDEs are discretised by different numerical methods.

The analysis of the importance of each reason for the discrepancy is the aim of the post-doctoral research.

4.3.5 Discussion

In Section 4.3, the newly developed numerical approach is analysed for the PF modelling of dendritic solidification of an Al-Cu alloy with constant cooling rate. The growth velocity is compared to the reference solution from (Boukellal et al., 2018). It is once again shown that the use of the SND is superior to the use of the RND. A quantitative discrepancy compared to the reference solution is observed. The discrepancy is more prominent if the RND is in use. The results are further comprehensively summarized and concluded in Section 5.

5 Summary and conclusions

The main aim of this dissertation was to develop a numerical approach for the accurate and computationally efficient modelling of dendritic solidification based on the PF formulation. In this chapter, the observations and conclusions regarding the performance of the newly developed approach are given. The main advantages and limitations of the approach along with the possible future research directions are discussed.

5.1 Summary of the performed work

The following research was performed in the framework of the dissertation:

- The PF formulation is applied for the modelling of the dendritic solidification of pure materials and dilute multi-component alloys. In the modelling of the solidification of dilute multi-component alloys, an externally imposed temperature approximation is applied where the temperature is considered as an input parameter. The approximation is valid for materials where the diffusion of heat is a few orders of magnitude faster than the diffusion of solutes.

- The meshless RBF-FD method and the forward Euler scheme are applied for the spatial and temporal discretisation of the PDEs. The fifth-degree PHS are used as shape functions in the RBF-FD method. The second-degree monomial augmentation is applied to ensure a well-posed interpolation problem and a second-order spatial convergence.

- The spatio-temporal ASP, based on dynamic quadtree domain decomposition, is developed in order to increase the computational efficiency of the numerical approach. The ASP dynamically ensures the highest density of computational nodes at the solid-liquid interface. A RND or

SND is applied to generate computational nodes in each quadtree sub-domain.

- The PF model for the solidification of pure materials is solved by the BSP. The influence of
  - time step stability parameter $\alpha_{\Delta t}$ (=$0.3, 0.15, 0, 075, 0.0375, 0.01875$),
  - node spacing Δh (=$0.8, 0.6, 0.4, 0.2$),
  - size of the local sub-domain N (=$9, 13, 21$), and
  - the type of node distribution (=RND, SND),

  on the accuracy and stability is analysed. The accuracy for different preferential growth directions is assessed. The influence of the magnitude of the thermal noise F_u (=$0, 10^{-5}, 10^{-4}$) to the steady-state growth velocity at different preferential growth directions is analysed.

- The analysis is repeated by the ASP at $\Delta h_{min} = \Delta h$ in order to test the accuracy of the ASP in comparison to the BSP. The influence of the ratio m_Ω (=$15, 21, 28, 30, 60$) between the size of a quadtree sub-domain and the node spacing on the accuracy is analysed.

- The speed-up of the ASP in comparison to the BSP is assessed for different values of minimum node spacing Δh_{min} (=$0.4, 0.8$) and m_Ω (=$5, 10, 20, 40, 80$). The `OpenMP` speed-up is analysed on a laptop with 6 processor cores.

- The PF model for the isothermal solidification of binary alloys is solved by the ASP. The influence of the
  - $\alpha_{\Delta t}$ (=$0.3, 0.15, 0, 075, 0.0375$),
  - Δh_{min} (=$0.6, 0.4$),
  - N (=$9, 13, 21$),
  - type of node distribution (=RND, SND), and
  - m_Ω (=$21, 28, 56$),

  on the accuracy is analysed. The accuracy for different preferential growth directions is assessed.

- The PF model for solidification of the Al-Cu alloys at a constant cooling rate is solved by the ASP. The influence of N (=$9, 13, 21$) and the type of node distribution (RND, SND) on the accuracy is analysed.

5.2 Findings

The main findings of the dissertation are overviewed in this section.

5.2.1 Modelling of solidification of pure materials

The findings of the 2-D modelling of the solidification of pure materials are given in this sub-section. The analysis of the performance of a novel numerical approach is based on the example from (Karma and Rappel, 1998). The assessment of the accuracy and stability of the BSP gives:

- The forward Euler scheme is stable for $\alpha_{\Delta t} \leq 0.3$ for all three considered values of N using the RND and SND ($\Delta t = \alpha_{\Delta t}(1 - \epsilon_4)\Delta h^2/4$). The first order of convergence is observed for all configurations, except for configuration with $N = 21$ using the RND. The first order of convergence is observed for $\alpha_{\Delta t} \leq 0.15$ in this case. This finding needs to be further analysed.

- Re-scaled growth velocity $\tilde{v}_{tip}$, obtained using the RND, converges to $\tilde{v}_{tip}$, obtained by the MST, for $N = 13$ and $N = 21$. $\tilde{v}_{tip}$ does not converge to $\tilde{v}_{tip}$, obtained by the MST, for $N = 9$.

- $\tilde{v}_{tip}$ converges to the velocity, obtained by the MST, for all three tested values of N using the SND.

- The expected second order of convergence of the RBF-FD method is observed for $N = 13$ using the RND. The algorithm for the determination of the size of the dendrite trunk experiences a larger error in the case of SND in comparison to the RND; hence, a small deviation from the second-order convergence line is observed for $N = 13$ using the SND.

- The accuracy at different values of the preferential growth direction angle θ_0 using RND and SND is analysed. The analysis at five different node

distributions for each tested value of θ_0 is performed in the case of SND. We define the maximum relative deviation of a configuration as

$$\Delta\tilde{v}_{tip}/\tilde{v}_{tip} = ||\tilde{v}_{tip}(\theta_0 = 0^\circ) - \tilde{v}_{tip}(\theta_0)||_\infty / \tilde{v}_{tip}(\theta_0 = 0^\circ), \quad \theta_0 \in [0^\circ, 45^\circ]. \tag{5.1}$$

The definition from Eq. (5.1) applies to the median of the growth velocity at each θ_0 in the case of SND.

- The case with $N = 13$ is analysed first. $\Delta\tilde{v}_{tip}/\tilde{v}_{tip}$ is equal to 6.1% and 3.6% at $\Delta h = 0.8$ and $\Delta h = 0.6$, respectively, using the RND. $\Delta\tilde{v}_{tip}/\tilde{v}_{tip}$ is equal to 0.5% and 0.4% at $\Delta h = 0.8$ and $\Delta h = 0.6$, respectively, using the SND.

- The analysis at different values of θ_0 and $\Delta h = 0.8$ is also performed for $N = 9$ and $N = 21$. $\Delta\tilde{v}_{tip}/\tilde{v}_{tip}$ is equal to 45.9% and 16.1% for $N = 9$ and $N = 21$, respectively, using the RND. $\Delta\tilde{v}_{tip}/\tilde{v}_{tip}$ is equal to 3.4% and 1.7% for $N = 9$ and $N = 21$, respectively, using the SND.

- The analysis at different values of θ_0 and F_u for $\Delta h = 0.8$ and $N = 13$ is performed by using RND and SND. The thermal noise introduces scatter in the variables used for characterisation of dendrite growth. The absolute scatter of $\tilde{v}_{tip}$ is approximately twice as larger when SND is in use in comparison to the use of RND. The scatter of $\tilde{v}_{tip}$ increases with F_u.

The following findings can be made regarding the accuracy and stability of the ASP:

- The same findings as for the BSP can be made regarding the stability and convergence of the forward Euler method.

- The same findings as for the BSP can be made regarding the convergence of the growth velocity to the velocity, obtained by the MST, using the RND.

- The same findings as for the BSP can be made regarding the convergence of the RBF-FD method.

- The analysis at different values of θ_0 is first performed for $N = 13$ at $\Delta h_{min} = 0.8$ and $\Delta h_{min} = 0.6$. The values $m_\Omega = 21$ and $m_\Omega = 28$ are used

for $\Delta h_{min} = 0.8$ and $\Delta h_{min} = 0.6$, respectively. $\Delta\tilde{v}_{tip}/\tilde{v}_{tip}$ is equal to 3.5% and 1.9% at $\Delta h_{min} = 0.8$ and $\Delta h_{min} = 0.6$, respectively, using the RND. $\Delta\tilde{v}_{tip}/\tilde{v}_{tip}$ is equal to 2.6% and 1.2% at $\Delta h_{min} = 0.8$ and $\Delta h_{min} = 0.6$, respectively, using the SND. The analysis in the case of SND is repeated for twice as large values $m_\Omega = 42$ and $m_\Omega = 56$ for $\Delta h_{min} = 0.8$ and $\Delta h_{min} = 0.6$, respectively. $\Delta\tilde{v}_{tip}/\tilde{v}_{tip}$ is equal to 2.8% and 1.4% at $\Delta h_{min} = 0.8$ and $\Delta h_{min} = 0.6$, respectively.

- The analysis at different values of θ_0 and $\Delta h = 0.8$ is also performed for $N = 9$ and $N = 21$ at $m_\Omega = 21$. $\Delta\tilde{v}_{tip}/\tilde{v}_{tip}$ is equal to 45.1% and 12.6% for $N = 9$ and $N = 21$, respectively, using the RND. $\Delta\tilde{v}_{tip}/\tilde{v}_{tip}$ is equal to 18.9% and 6.0% for $N = 9$ and $N = 21$, respectively, using the SND. The analysis in the case of SND is repeated for the twice as large value $m_\Omega = 42$. $\Delta\tilde{v}_{tip}/\tilde{v}_{tip}$ is equal to 11.0% and 4.8% for $N = 9$ and $N = 21$, respectively.

The comparison between different configurations for the modelling of dendritic growth at arbitrary values of θ_0 yields

- RND vs. SND using BSP: The configuration with the SND outperforms the configuration with the RND for all three tested values of N.
- RND vs. SND using ASP: The configuration with the SND outperforms the configuration with the RND. The difference is especially prominent at $N = 9$ and $N = 21$.
- BSP vs. ASP using RND: The configuration with the ASP interestingly outperforms the configuration with the BSP for $N = 13$. The behaviour of the configurations for other two values of N is identical.
- BSP vs. ASP using SND: The configuration with the BSP outperforms the configuration with the ASP. The increase of m_Ω is beneficial for $N = 9$ and $N = 21$. For $N = 13$, the accuracy is interestingly slightly reduced as m_Ω is increased.

The following findings can be made regarding the computational efficiency of the ASP:

- The ERT has three contributions: iteration time, communication time, and adaptation time.

- Iteration time represents the majority of the whole computational time.
- The percentage of the iteration time is an increasing function of m_Ω.
- The ASP speed-up is a decreasing function of the time.
- The ASP speed-up is a decreasing function of Δh_{min}.
- The highest ASP speed-up is equal to 7.3 and 10.5 at $\Delta h_{min} = 0.4$ and $\Delta h_{min} = 0.8$, respectively. The highest ASP speed-up for $\Delta h_{min} = 0.4$ and $\Delta h_{min} = 0.8$ is observed at $m_\Omega = 10$ and $m_\Omega = 5$, respectively.
- For $m_\Omega > 10$, the ASP speed-up is a decreasing function of m_Ω.
- The ASP speed-up is primarily decreased due to communication between the quadtree sub-domains.
- The `OpenMP` speed-up as a function of N_{cores} is very close to the ideal speed-up for $N_{cores} \leq 4$ using a personal laptop with total of 6 available cores on a processor. The deviation from the ideal speed-up is more prominent for $\Delta h_{min} = 0.8$ in comparison to $\Delta h_{min} = 0.4$.
- The maximum `OpenMP` speed-up is equal to 3.9 and 4.8 at $\Delta h_{min} = 0.8$ and $\Delta h_{min} = 0.4$, respectively. The maximum `OpenMP` speed-up at $\Delta h_{min} = 0.8$ is observed at $m_\Omega = 5$ and $N_{cores} = 5$. The maximum `OpenMP` speed-up at $\Delta h_{min} = 0.4$ is observed at $m_\Omega = 20$ and $N_{cores} = 6$.

5.2.2 Modelling of isothermal solidification of binary alloys

The findings of the 2-D modelling of solidification of binary alloys are given in this sub-section. The analysis of the performance of a novel numerical approach is based on the example from (Karma, 2001). The assessment of the accuracy and stability of the ASP gives:

- The forward Euler scheme is stable for $\alpha_{\Delta t} \leq 0.3$ for all three considered values of N using the RND and SND ($\Delta t = \alpha_{\Delta t} \Delta h^2 / (4 \bar{D}_\ell)$). First order of convergence is observed for all configurations.
- Re-scaled growth velocity $\tilde{v}_{tip}$ for different configuration is compared to the reference $\tilde{v}_{tip}$ from (Karma, 2001). The ASP with $\Delta h_{min} = 0.6$ and $m_\Omega = 28$ is used first.

- $\tilde{v}_{tip}$ converges to the reference $\tilde{v}_{tip}$ for $N = 13$ using the RND. $\tilde{v}_{tip}$ is too low and too high at $N = 9$ and $N = 21$, respectively.

- $\tilde{v}_{tip}$ converges to the reference $\tilde{v}_{tip}$ for $N = 13$ and $N = 21$ using the SND. $\tilde{v}_{tip}$ is too low at $N = 9$. $\tilde{v}_{tip}$ converges to the reference $\tilde{v}_{tip}$ for $N = 9$ when m_Ω is increased from $m_\Omega = 28$ to $m_\Omega = 56$.

- $\tilde{v}_{tip}$ converges to the reference $\tilde{v}_{tip}$ for all three tested values of N using the SND when Δh_{min} is decreased from $\Delta h_{min} = 0.6$ to $\Delta h_{min} = 0.4$. The deviation from the reference $\tilde{v}_{tip}$ at $N = 9$ and $N = 21$ using the RND is decreased when Δh_{min} is decreased from $\Delta h_{min} = 0.6$ to $\Delta h_{min} = 0.4$.

- Re-scaled concentration in the solid phase C_s/C_ℓ^e is compared to the reference C_s/C_ℓ^e from (Karma, 2001).

- C_s/C_ℓ^e converges towards to the reference C_s/C_ℓ^e with the increase of N. The relative deviation from the reference C_s/C_ℓ^e is for $N = 9$, $N = 13$, and $N = 21$ equal to 2.07%, 1.04%, and 0.17%, respectively, using the RND. The relative deviation from the reference C_s/C_ℓ^e is at $N = 9$, $N = 13$, and $N = 21$ equal to 1.40%, 1.36%, and 0.95%, respectively, using the SND.

- The analysis at different values of θ_0 is first performed for $\Delta h_{min} = 0.6$ and $m_\Omega = 28$. The behaviour of the growth velocity is very similar to the behaviour in the case of pure materials. In this case, the accuracy of a single SND is analysed. $\Delta\tilde{v}_{tip}/\tilde{v}_{tip}$ is equal to 76.3%, 3.8%, and 26.7% at $N = 9$, $N = 13$, and $N = 21$, respectively, using the RND. $\Delta\tilde{v}_{tip}/\tilde{v}_{tip}$ is equal to 18.9%, 8.1%, and 11.4% at $N = 9$, $N = 13$, and $N = 21$, respectively, using the SND. The analysis using the SND is also performed for twice as large m_Ω, i.e., $m_\Omega = 58$. $\Delta\tilde{v}_{tip}/\tilde{v}_{tip}$ is in this case equal to 16.2%, 5.9%, and 5.9% at $N = 9$, $N = 13$, and $N = 21$, respectively.

- The behaviour of C_s/C_ℓ^e as a function of θ_0 is also analysed. The maximum deviation is in this case defined as

$$\Delta C_s/C_s = ||C_s(\theta_0 = 0^\circ) - C_s(\theta_0)||_\infty / C_s(\theta_0 = 0^\circ), \quad \theta_0 \in [0^\circ, 45^\circ]. \tag{5.2}$$

- $\Delta C_s/C_s$ is equal to 6.3%, 0.1%, and 5.8% at $N = 9$, $N = 13$, and $N = 21$, respectively, using the RND and $m_\Omega = 28$. $\Delta C_s/C_s$ is equal to 2.0%, 0.6%,

and 0.8% at $N = 9$, $N = 13$, and $N = 21$, respectively, using the SND and $m_\Omega = 28$. $\Delta C_s/C_s$ is equal to 0.6%, 0.2%, and 0.3% at $N = 9$, $N = 13$, and $N = 21$, respectively, using the SND and $m_\Omega = 56$.

Comparison between the use of RND and SND at different values of θ yields:

- The use of SND hugely outperforms the use of RND for $N = 9$ and $N = 21$. The use of RND outperforms the use of SND for $N = 13$.

5.2.3 Modelling of solidification with a constant cooling rate of Al-Cu alloy

The findings of the 2-D modelling of solidification with a constant cooling rate of an Al-Cu alloy are given in this sub-section. The analysis of the performance of a novel numerical approach is based on the example from (Boukellal et al., 2018). The assessment of the accuracy of the ASP gives:

- A seaweed-like morphology is developed instead of a dendrite at $N = 9$ using the RND. A dendrite is developed for $N = 13$ and $N = 21$. The same trend of the growth velocity as a function of time as in the reference solution is observed. The maximum growth velocity for $N = 13$ and $N = 21$ is $\approx 9\%$ and $\approx 28\%$ higher in comparison to the reference solution.

- A dendrite is developed for all three values of N when the SND is used. The same trend of the growth velocity as a function of time as in the reference solution is observed. The maximum growth velocity for $N = 9$ and $N = 13$ is $\approx 6\%$ higher in comparison to the reference solution. The maximum growth velocity is $\approx 17\%$ higher for $N = 21$.

- The final morphology at $N = 13$ is very similar to the final morphology at $N = 21$ using the RND. The final morphologies, obtained using the RND, are very different to the final morphologies, obtained using the SND. The secondary branches are developed to a greater extent when SND is used. There is also a big difference between the morphologies of secondary branches at different values of N in this case.

- The concentration in the solid phase is directly linked to the growth velocity as a function time. Consequently, the concentration profiles at different values of N are very similar using the SND. The concentration

profiles at different values of N do not follow the same trends using the RND.

- The final morphology is not symmetric when the SND is used. At the beginning of the simulation, the growing dendrite is symmetric for all values of N. As the temperature is decreasing, the driving force of solidification increases which in turn also amplifies the small local numerical error determined by the non-symmetrically distributed computational nodes in the local sub-domains in the RBF-FD method. This primarily effects the evolution of secondary branches while the dynamics at the tip of the primary trunk is still properly resolved. The final morphology of a dendrite is symmetric when the RND is used which is the consequence of the symmetrically distributed computational nodes in local sub-domains and consequently symmetric local numerical error. A decrease of W_0 or Δh would decrease the local numerical error on both node distributions.

- Four non-physical diagonal secondary branches appear in all cases, except at $N = 9$ by using RND where a dendrite morphology is not even developed. The branches are developed in the last stage of solidification when the solidification driving force is very large. The main reason for the development of diagonal branches is probably very small strength of anisotropy of surface energy. The numerical model evidently does not capture the physics at the minimum surface energy correctly, hence, additional simulations with lower values W_0 and Δh should be performed in order to analyse this phenomenon.

- There is a quantitative discrepancy between our and reference results. The solution of the considered physical problem is very sensitive to the numerical parameters due to very small strength of anisotropy. The main reason for the discrepancy is attributed to the difference between the considered PDEs, which describe otherwise the same physical problem, and different numerical methods for the spatial discretisation of the PDEs. This finding needs to be further analysed.

5.3 Conclusions

The main conclusions are:

- The use of the SND in the BSP and ASP provides higher accuracy in comparison to the use of the RND for otherwise same numerical parameters when the growth for an arbitrary preferential growth direction is considered. The use of the RND provides higher accuracy only when the isothermal dendritic solidification of binary alloys is simulated with the ASP at $N = 13$.
- The solution is much more sensitive to the number of computational nodes in a local sub-domain N using the RND in comparison to the use of the SND.
- The configurations with $N = 9$ and $N = 21$ using the RND are not suitable for the PF modelling of dendritic solidification at arbitrary values of θ_0. The configuration with $N = 9$ using the SND in the ASP is not suitable for the PF modelling of dendritic solidification at arbitrary values of θ_0. The assessment of these facts needs additional research.
- The solution is much more sensitive to θ_0 using the RND.
- The RND or SND type of the node distribution and the size of the local sub-domain N critically determine the morphology of the secondary branches (if they are developed).
- The RBF-FD method proves to be very suitable for the PF modelling of dendritic solidification since the consideration of the SND in the RBF-FD method is simple and straightforward. In a lot of the PF studies of dendritic solidification (Karma and Rappel, 1998; Karma, 2001; Ohno, 2012; Greenwood et al., 2018; Bollada et al., 2015; Yamanaka et al., 2011) etc., the mesh-based FDM is used for the spatial discretisation. The FDM is used exclusively in combination with RND and is therefore much more sensitive to the mesh-induced anisotropy effects.
- A straightforward application of the SND represents one of the distinctive advantages of the present numerical approach.

- The accuracy is an increasing function of m_Ω when the SND is used in the ASP since the quadtree domain decomposition introduces regularity in the solution of the PF model.
- The number of the nodes in the BSP is proportional to $L^2/\Delta h^2$. The number of the nodes in the ASP is approximately proportional to $L_{int}/\Delta h$, where L_{int} stands for the length of the solid-liquid interface. The ASP speed-up $(L^2/\Delta h^2)/(L_{int}/\Delta h) = L^2/(L_{int}\Delta h)$ is therefore an increasing function of the area of the computational domain and a decreasing function of the length of the solid-liquid interface and the spacing.
- The solid-liquid interface can be optimally resolved by decreasing m_Ω, which results in a small number of all computational nodes and therefore short iteration times. Decrease of m_Ω, however, increases the number of quadtree sub-domains and therefore the communication and adaptation times. The optimal value of m_Ω with the highest speed-up is a consequence of the interplay of these phenomena.
- The compromise has to be made in the selection of parameter m_Ω in the ASP since the accuracy and the computational efficiency are an increasing and decreasing function of m_Ω, respectively.
- The `OpenMP` can be successfully used for the speed-up of the ASP. The break from the ideal speed-up is observed. One of the reasons for the break is the load imbalance. The memory bandwidth represents a bottleneck of the hardware. This is another important reason for the break, since the computational tasks cannot be performed simultaneously on multiple processor cores due to data starvation.

5.4 Further work

The present work demonstrates that the RBF-FD method is very suitable and promising for the PF modelling of dendritic solidification of the pure materials and dilute multi-component alloys. The plan for the use of the developed model for the simulation of dendritic growth in industry and the possible further research of this topic is presented in this section.

5.4.1 The use in the industry

The PF model for the simulation of solidification of dilute multi-component alloys will be built in the simulation system (Šarler et al., 2019) for the prediction of solidification phenomena in the direct-chill casting of aluminium alloys. The simulation system contains three coupled models

- thermofluid model,
- thermomechanics model,
- microstructure model.

The thermofluid model considers the macroscopic equations for the conservation of mass, momentum, heat, and species. The thermomechanics model obtains the temperature field, solid fraction and pressure field from the thermofluid module and considers the elastic strain, viscoplastic strain and the thermal strain. The microstructure module requires the thermal and the chemical history of a small piece of solidified material from the thermofluid model and considers nucleation and grain growth in that piece by the point-automata method (Lorbiecka and Šarler, 2010). The output of the current microstructure model is the average grain size and a rough estimation of the microsegregation.

The PF model will be built in the microstructure model in order to provide a more accurate estimation of the microsegregation and the morphology of an average grain. The thermofluid model will provide the temperature as a function of time in the PF model. The input parameters of the PF model obtained by the point-automata model will be the average grain size and the maximum growth velocity. The average grain size will be used to determine the size of the computational domain where the effect of the neighbouring grains will be simulated by the zero-flux Neumann boundary conditions. The maximum growth velocity from the point-automata model will be used as v^* in the validity condition for the PF model. To recall, interface thickness W is the only free parameter of the PF model for the simulation of solidification of dilute multi-component alloys. It has to be set according to the condition $W \ll \min(D_{\ell,i})/v^*$.

5.4.2 PF modelling of microstructure evolution

The first step in the PF modelling of the solidification is the re-casting of the implemented PF models with the preconditioned PF (Glasner, 2001) in order to increase the computational efficiency by larger allowed spacings Δh. In the industrial casting of commercial alloys, multiple differently oriented dendrites are growing from the melt. The implementation of a PF model for polycrystalline alloy solidification (Ofori-Opoku and Provatas, 2010; Granasy et al., 2004) therefore represents an important next step in the modelling of solidification phenomena for industrially relevant cases. Modelling of melt convection during the dendritic solidification (Beckermann et al., 1999) is also planned for the future research. PF modelling of other types of solidification (Folch and Plapp, 2005; Gyoon Kim et al., 2004), e.g., eutectic and peritectic solidification, is also relevant in the industrial casting processes. PF modelling of other free-boundary problems like solid-state phase transformation (Zhu et al., 2019; Duong et al., 2020; Kovačević and Šarler, 2005) is also an interesting possible further step of research.

5.4.3 ASP

The first further step regarding the developed ASP is an upgrade to the 3-D using an octree data structure (Greenwood et al., 2018) since the 2-D simulations can only be used for the qualitative prediction (Boukellal et al., 2018) of the dendritic solidification in the casting of commercial alloys. The GPU acceleration (Yamanaka et al., 2011) is also an important next step, especially for 3-D PF modelling of solidification.

The ASP has been developed for the solution of the parabolic PDEs by explicit methods for the time stepping. The upgrade of the ASP for the solution of other types of PDEs and the implementation of the implicit methods for the time stepping are also interesting possibilities for further development. The consideration of computational domains of arbitrary shapes is another possibility for the upgrade of the developed ASP.

5.5 Dissemination of the results

The journal papers, the conference papers, and the conference talks presenting the results of this dissertation are given in the list below. The results obtained by the BSP from Section 4.1.5 are presented in (Dobravec et al., 2020). The developed quadtree data structure used in the dissertation is presented in (Dobravec et al., 2017a). In (Dobravec et al., 2017a), cellular automata modelling of dendritic and eutectic solidification of binary alloys using adaptive FVM is considered. Several other journal papers with the results from dissertation are planned, in particular, a paper with the results obtained by the ASP in the case of pure materials from Sections 4.1.6 and 4.1.7 and a paper with the results obtained by the ASP in the case of binary alloys from Section 4.2. The developed numerical approach will be incorporated in the simulation system for prediction of solidification phenomena in aluminium alloys (Šarler et al., 2019) with the purpose of providing more accurate estimation of the final microstructure.

Journal papers

- Dobravec, T., Mavrič, B., Šarler, B. (2020). Reduction of discretisation-induced anisotropy in the phase-field modelling of dendritic growth by meshless approach. *Computational Materials Science*, 172: 109166.
- Šarler, B., Dobravec, T., Glavan, G., Hatić, V., Mavrič, B., Vertnik, R., Cvahte, P., Gregor, F., Jelen, M., and Petrovič, M. (2019). Multi-physics and multiscale meshless simulation system for direct-chill casting of aluminium alloys. *Strojniški vestnik – Journal of Mechanical Engineering*, 65: 658–670.
- Dobravec, T., Mavrič, B., Šarler, B. (2017). A cellular automaton – finite volume method for the simulation of dendritic and eutectic growth in binary alloys using an adaptive mesh refinement. *Journal of Computational Physics*, 349: 351-375.

Conference papers

- Dobravec, T., Mavrič, B., Šarler, B. (2020). Phase field modelling of dendritic solidification by using an adaptive meshless solution procedure. *MCWASP XV : International Conference on Modelling of Casting, Welding and Advanced Solidification Processes - Online, Djurönäset, Stockholm, Sweden, June 22-23, IOP conference series, Materials science and engineering, Bristol: IOP Publishing*, 861: 1-7.

- Dobravec, T., Mavrič, B., Šarler, B. (2018). Meshless phase field modeling of dendritic growth. *VII International Conference on Solidification and Gravity, Miskolc-Lillafüred, Hungary, September 3-6, 2018, Selected, peer reviewed papers from the 7th International Conference on Solidification and Gravity, Miskolc: Hungarian Academy of Sciences - University of Miskolc*, 52-58.

Conference talks

- Dobravec, T., Mavrič, B., Šarler, B. (2019). Development of meshless method for an accurate phase-field modelling of dendrites with arbitrary orientations. *27th International Conference on Materials and Technology, Portorož, Slovenia, October 16-18, 2019*. (awarded as a best presentation of a young researcher)

- Dobravec, T., Mavrič, B., Šarler, B. (2019). Meshless phase field modeling of dendritic growth by using an h-adaptive computational node arrangement. *Joint 5th International Conference on Advances in Solidification Processes (ICASP-5) and 5th International Symposium on Cutting Edge of Computer Simulation of Solidification, Casting and Refining (CSSCR-5), Salzburg, Austria, June 17-21, 2019*.

- Dobravec, T., Mavrič, B., Šarler, B. (2018). Phase field modelling of dendritic growth based on local meshless solution procedure. *26th International Conference on Materials and Technology, Portorož, Slovenia, October 3-5, 2018*.

Bibliography

Atluri, S. N. (2004). *The Meshless Method (MLPG) for Domain and BIE Discretizations*. Tech Science Press, Forsyth, Georgia, USA.

Atluri, S. N. and Shen, S. (2002). *The Meshless Local Petrov-Galerkin (MLPG) Method*. Tech Science Press, Encino, California, USA.

Atluri, S. N. and Sladek, J. (editors) (2009). *Advances in the MLPG Meshless Methods*. Tech Science Press, Hendersen, Nevada, USA.

Atluri, S. N. and Zhu, T. (1998). A new meshless local Petrov-Galerkin (MLPG) approach in computational mechanics. *Computational Mechanics*, 22: 117–127.

Barbieri, A. and Langer, J. S. (1989). Predictions of dendritic growth rates in the linearized solvability theory. *Physical Review A*, 39: 5314–5325.

Barrat, J.-L. and Hansen, J.-P. (2003). *Basic Concepts for Simple and Complex Liquids*. Cambridge University Press, New York, USA.

Bayona, V., Flyer, N., Fornberg, B., and Barnett, G. A. (2017). On the role of polynomials in RBF-FD approximations: II. Numerical solution of elliptic PDEs. *Journal of Computational Physics*, 332: 257–273.

Beckermann, C., Diepers, H. J., Steinbach, I., Karma, A., and Tong, X. (1999). Modeling melt convection in phase-field simulations of solidification. *Journal of Computational Physics*, 154: 468–496.

Belinha, J. (2014). *Meshless Methods in Biomechanics: Bone Tissue Remodelling Analysis*. Lecture Notes in Computational Vision and Biomechanics. Springer International Publishing, New York, USA.

Belytschko, T., Lu, Y. Y., and Gu, L. (1994). Element-free Galerkin methods. *International Journal for Numerical Methods in Engineering*, 37: 229–256.

Ben-Jacob, E., Goldenfeld, N., Langer, J. S., and Schön, G. (1983). Dynamics of interfacial pattern formation. *Physical Review Letters*, 51: 1930–1932.

Ben-Jacob, E., Goldenfeld, N., Langer, J. S., and Schön, G. (1984). Boundary-layer model of pattern formation in solidification. *Physical Review A*, 29: 330–340.

Berger, M. J. and Colella, P. (1989). Local adaptive mesh refinement for shock hydrodynamics. *Journal of Computational Physics*, 82: 64–84.

Berger, M. J. and Oliger, J. (1984). Adaptive mesh refinement for hyperbolic partial differential equations. *Journal of Computational Physics*, 53: 484–512.

Berghoff, M., Selzer, M., Choudhury, A., and Nestler, B. (2013). Efficient techniques for bridging from atomic to mesoscopic scale in phase-field simulations. *Journal of Computational Methods in Sciences and Engineering*, 13: 441–454.

Bhaskar, M. S. (2018). Quantitative phase field modelling of precipitate coarsening in Ni-Al-Mo alloys. *Computational Materials Science*, 146: 102–111.

Boettinger, W. J., Warren, J. A., Beckermann, C., and Karma, A. (2002). Phase-field simulation of solidification. *Annual Review of Materials Research*, 32: 163–194.

Bollada, P. C., Goodyer, C. E., Jimack, P. K., Mullis, A. M., and Yang, F. W. (2015). Three dimensional thermal-solute phase field simulation of binary alloy solidification. *Journal of Computational Physics*, 287: 130–150.

Boukellal, A. K., Debierre, J.-M., Reinhart, G., and Nguyen-Thi, H. (2018). Scaling laws governing the growth and interaction of equiaxed Al-Cu dendrites: A study combining experiments with phase-field simulations. *Materialia*, 1: 62–69.

Brower, R. C., Kessler, D. A., Koplik, J., and Levine, H. (1984). Geometrical models of interface evolution. *Physical Review A*, 29: 1335–1342.

Buhmann, M. D. (2003). *Radial Basis Functions: Theory and Implementations*. Cambridge University Press, Cambridge, UK.

Caginalp, G. (1989). Stefan and Hele-Shaw type models as asymptotic limits of the phase-field equations. *Physical Review A*, 39: 5887–5896.

Cahn, J. and Allen, S. (1977). A microscopic theory for domain wall motion and its experimental verification in Fe-Al alloy domain growth kinetics. *Journal de Physique Colloques*, 38: C7–51–C7–54.

Cahn, J. W. (1961). On spinodal decomposition. *Acta Metallurgica*, 9: 795–801.

Cahn, J. W. and Hilliard, J. E. (1958). Free energy of a nonuniform system. I. Interfacial free energy. *The Journal of Chemical Physics*, 28: 258–267.

Campbell, J. (2003). *Castings*. Butterworth-Heinemann, Oxford, UK.

Chapman, B., Jost, G., and Pas, R. v. d. (2008). *Using OpenMP: Portable Shared Memory Parallel Programming*. MIT Press, Cambridge, Massachusetts, USA.

Chen, L.-Q. (2002). Phase-field models for microstructure evolution. *Annual Review of Materials Research*, 32: 113–140.

Chen, W., Fu, Z.-J., and Chen, C. S. (2014). *Recent Advances in Radial Basis Function Collocation Methods*. Springer-Verlag, Heidelberg, Germany.

Chen, Y., Lee, J., and Eskandarian, A. (2006). *Meshless Methods in Solid Mechanics*. Springer-Verlag, New York, USA.

Collins, J. B. and Levine, H. (1985). Diffuse interface model of diffusion-limited crystal growth. *Physical Review. B, Condensed Matter*, 31: 6119–6122.

Dantzig, J. and Rappaz, M. (2017). *Solidification, Second Edition*. EPFL Press, Lausanne, Switzerland.

Dehghan, M. and Abbaszadeh, M. (2017). The meshless local collocation method for solving multi-dimensional Cahn-Hilliard, Swift-Hohenberg and phase field crystal equations. *Engineering Analysis with Boundary Elements*, 78: 49–64.

Dehghan, M. and Mohammadi, V. (2016). The numerical simulation of the phase field crystal (PFC) and modified phase field crystal (MPFC) models via global and local meshless methods. *Computer Methods in Applied Mechanics and Engineering*, 298: 453–484.

Dobravec, T., Mavrič, B., and Šarler, B. (2017a). A cellular automaton – finite volume method for the simulation of dendritic and eutectic growth in binary alloys using an adaptive mesh refinement. *Journal of Computational Physics*, 349: 351–375.

Dobravec, T., Mavrič, B., and Šarler, B. (2020). Reduction of discretisation-induced anisotropy in the phase-field modelling of dendritic growth by meshless approach. *Computational Materials Science*, 172: 109166.

Dobravec, T., Mavrič, B., Vertnik, R., and Šarler, B. (2017b). Meshless modelling of microstructure evolution in the continuous casting of steel. *Proceedings of the VII International Conference on Coupled Problems in Science and Engineering*, vol. VII, pp. 156–166. International Center for Numerical Methods in Engineering (CIMNE), Rhodes Island, Greece.

Dong, X., Xing, H., Weng, K., and Zhao, H. (2017). Current development in quantitative phase-field modeling of solidification. *Journal of Iron and Steel Research, International*, 24: 865–878.

Dubey, A., Almgren, A., Bell, J., Berzins, M., Brandt, S., Bryan, G., Colella, P., Graves, D., Lijewski, M., Löffler, F., O'Shea, B., Schnetter, E., Van Straalen, B., and Weide, K. (2014). A survey of high level frameworks in block-structured adaptive mesh refinement packages. *Journal of Parallel and Distributed Computing*, 74: 3217–3227.

Duong, T. C., Hackenberg, R. E., Attari, V., Landa, A., Turchi, P. E. A., and Arróyave, R. (2020). Investigation of the discontinuous precipitation of U-Nb alloys via thermodynamic analysis and phase-field modeling. *Computational Materials Science*, 175: 109573.

Dyn, N., Leviatan, D., Levin, D., and Pinkus, A. (editors) (2001). *Multivariate Approximation and Applications*. Cambridge University Press, Cambridge, UK.

Echebarria, B., Folch, R., Karma, A., and Plapp, M. (2004). Quantitative phase-field model of alloy solidification. *Physical Review E*, 70: 061604.

Fasshauer, G. F. (2007). *Meshfree Approximation Methods with MATLAB*. World Scientific Publishing Co., Inc., River Edge, New Jersey, USA.

Finkel, R. A. and Bentley, J. L. (1974). Quad trees a data structure for retrieval on composite keys. *Acta Informatica*, 4: 1–9.

Fix, G. J. (1982). Phase field methods for free boundary problems. *Free Boundary Problems: Theory and Applications*, vol. 2, p. 580. Piman, Boston, Massachusetts, USA.

Flyer, N., Fornberg, B., Bayona, V., and Barnett, G. A. (2016). On the role of polynomials in RBF-FD approximations: I. Interpolation and accuracy. *Journal of Computational Physics*, 321: 21–38.

Folch, R. and Plapp, M. (2005). Quantitative phase-field modeling of two-phase growth. *Physical Review E*, 72: 011602.

Fornberg, B. and Flyer, N. (2015). Fast generation of 2-D node distributions for mesh-free PDE discretizations. *Computers & Mathematics with Applications*, 69: 531–544.

Galenko, P. and Sobolev, S. (1997). Local nonequilibrium effect on undercooling in rapid solidification of alloys. *Physical Review E*, 55: 343–352.

Galenko, P. K. and Danilov, D. A. (1999). Model for free dendritic alloy growth under interfacial and bulk phase nonequilibrium conditions. *Journal of Crystal Growth*, 197: 992–1002.

Galenko, P. K., Danilov, D. A., Reuther, K., Alexandrov, D. V., Rettenmayr, M., and Herlach, D. M. (2017). Effect of convective flow on stable dendritic growth in rapid solidification of a binary alloy. *Journal of Crystal Growth*, 457: 349–355.

Galenko, P. K., Reutzel, S., Herlach, D. M., Danilov, D., and Nestler, B. (2007). Modelling of dendritic solidification in undercooled dilute Ni–Zr melts. *Acta Materialia*, 55: 6834–6842.

Glasner, K. (2001). Nonlinear preconditioning for diffuse interfaces. *Journal of Computational Physics*, 174: 695–711.

Glicksman, M. E. (1984). Free dendritic growth. *Materials Science and Engineering*, 65: 45–55.

Glicksman, M. E. (2011). *Principles of Solidification*. Springer New York, New York, USA.

Goulart, P. R., Osório, W. R., Spinelli, J. E., and Garcia, A. (2007). Dendritic microstructure affecting mechanical properties and corrosion resistance of an Al-9 wt% Si alloy. *Materials and Manufacturing Processes*, 22: 328–332.

Granasy, L., Pusztai, T., and Warren, J. A. (2004). Modelling polycrystalline solidification using phase field theory. *Journal of Physics-Condensed Matter*, 16.

Greengard, L. and Lee, J.-Y. (2004). Accelerating the nonuniform fast Fourier transform. *SIAM Review*, 46: 443–454.

Greenwood, M., Shampur, K. N., Ofori-Opoku, N., Pinomaa, T., Wang, L., Gurevich, S., and Provatas, N. (2018). Quantitative 3D phase field modelling of solidification using next-generation adaptive mesh refinement. *Computational Materials Science*, 142: 153–171.

Griebel, M. and Schweitzer, M. A. (editors) (2017). *Meshfree Methods for Partial Differential Equations VIII*. Lecture Notes in Computational Science and Engineering. Springer International Publishing, New York, USA.

Gu, Y. and Liu, G. (2003). A boundary radial point interpolation method (BRPIM) for 2-D structural analyses. *Structural Engineering and Mechanics*, 15.

Gu, Y. T. and Liu, G. R. (2002). A boundary point interpolation method for stress analysis of solids. *Computational Mechanics*, 28: 47–54.

Guo, Z., Mi, J., and Grant, P. S. (2012). Phase field simulation of multi-dendrite growth in a coupled thermal-solute-convective environment. *IOP Conference Series: Materials Science and Engineering*, 33: 012101.

Guo, Z. and Xiong, S. M. (2015). On solving the 3-D phase field equations by employing a parallel-adaptive mesh refinement (Para-AMR) algorithm. *Computer Physics Communications*, 190: 89–97.

Gyoon Kim, S., Tae Kim, W., Suzuki, T., and Ode, M. (2004). Phase-field modeling of eutectic solidification. *Journal of Crystal Growth*, 261: 135–158.

Haar, D. T. (2013). *Collected Papers of L.D. Landau*. Elsevier, Pergamon, Oxford, UK.

Hanoglu, U. and Šarler, B. (2018). Multi-pass hot-rolling simulation using a meshless method. *Computers & Structures*, 194: 1–14.

Hatić, V. (2019). *Modelling of Macrosegregation of a Low-Frequency Electromagnetic Direct Chill Casting by a Meshless Method*. Ph.D. thesis, University of Nova Gorica, Nova Gorica, Slovenia.

Hatić, V., Cisternas Fernández, M., Mavrič, B., Založnik, M., Combeau, H., and Šarler, B. (2019). Simulation of a macrosegregation benchmark in a cylindrical coordinate system with a meshless method. *International Journal of Thermal Sciences*, 142: 121–133.

Hatić, V., Mavrič, B., and Šarler, B. (2018). Simulation of a macrosegregation benchmark with a meshless diffuse approximate method. *International Journal of Numerical Methods for Heat & Fluid Flow*, 28: 361–380.

Hohenberg, P. C. and Halperin, B. I. (1977). Theory of dynamic critical phenomena. *Reviews of Modern Physics*, 49: 435–479.

Horvay, G. and Cahn, J. W. (1961). Dendritic and spheroidal growth. *Acta Metallurgica*, 9: 695–705.

Iserles, A. (2000). *Acta Numerica*. Cambridge University Press, Cambridge, UK.

Ivantsov, G. P. (1947). Temperature field around a spherical, cylindrical, and needle-shaped crystal, growing in a pre-cooled melt. *Doklady Akademii Nauk*, 58: 567–571.

Jokisaari, A. M., Voorhees, P. W., Guyer, J. E., Warren, J. A., and Heinonen, O. G. (2018). Phase field benchmark problems for dendritic growth and linear elasticity. *Computational Materials Science*, 149: 336–347.

Kalikmanov, V. (2001). *Statistical Physics of Fluids: Basic Concepts and Applications*. Springer, Berlin, Germany.

Kansa, E. J. (1990a). Multiquadrics—A scattered data approximation scheme with applications to computational fluid-dynamics—I surface approximations and partial derivative estimates. *Computers & Mathematics with Applications*, 19: 127–145.

Kansa, E. J. (1990b). Multiquadrics—A scattered data approximation scheme with applications to computational fluid-dynamics—II solutions to parabolic, hyperbolic and elliptic partial differential equations. *Computers & Mathematics with Applications*, 19: 147–161.

Karma, A. (2001). Phase-field formulation for quantitative modeling of alloy solidification. *Physical Review Letters*, 87: 115701.

Karma, A. and Rappel, W.-J. (1998). Quantitative phase-field modeling of dendritic growth in two and three dimensions. *Physical Review E*, 57: 4323.

Karma, A. and Rappel, W. J. (1999). Phase-field model of dendritic sidebranching with thermal noise. *Physical Review. E, Statistical Physics, Plasmas, Fluids, and Related Interdisciplinary Topics*, 60: 3614–3625.

Karma, A. and Tourret, D. (2016). Atomistic to continuum modeling of solidification microstructures. *Current Opinion in Solid State and Materials Science*, 20: 25–36.

Kessler, D. A. and Levine, H. (1986). Velocity selection in dendritic growth. *Physical Review B*, 33: 7867.

Kessler, D. A. and Levine, H. (1988). Pattern selection in three dimensional dendritic growth. *Acta Metallurgica*, 36: 2693–2706.

Kim, S. G. (2007). A phase-field model with antitrapping current for multicomponent alloys with arbitrary thermodynamic properties. *Acta Materialia*, 55: 4391–4399.

Kim, S. G., Kim, W. T., and Suzuki, T. (1999). Phase-field model for binary alloys. *Physical Review E*, 60: 7186–7197.

Knuth, D. E. (1997). *The Art of Computer Programming, Vol. 1: Fundamental Algorithms, 3rd Edition*. Addison-Wesley Professional, Reading, Massachusetts, USA.

Kosec, G. and Šarler, B. (2011). H-adaptive local radial basis function collocation meshless method. *Computers, Materials and Continua*, 26: 227–253.

Kosec, G. and Šarler, B. (2014). Simulation of macrosegregation with mesosegregates in binary metallic casts by a meshless method. *Engineering Analysis with Boundary Elements*, 45: 36–44.

Kovačević, I. and Šarler, B. (2005). Solution of a phase-field model for dissolution of primary particles in binary aluminum alloys by an r-adaptive mesh-free method. *Materials Science and Engineering: A*, 413–414: 423–428.

Kurz, W., Fisher, D. J., and Trivedi, R. (2019). Progress in modelling solidification microstructures in metals and alloys: dendrites and cells from 1700 to 2000. *International Materials Reviews*, 64: 311–354.

Kurz, W., Rappaz, M., and Trivedi, R. (2021). Progress in modelling solidification microstructures in metals and alloys. Part II: dendrites from 2001 to 2018. *International Materials Reviews*, 66: 30–76.

Langer, J. S. (1986). Models of pattern formation in first-order phase transitions. *Directions in Condensed Matter Physics*, vol. 1 of *Series on Directions in Condensed Matter Physics*, pp. 165–186. World Scientific, Singapore.

Langer, J. S. and Müller-Krumbhaar, H. (1978). Theory of dendritic growth—I. Elements of a stability analysis. *Acta Metallurgica*, 26: 1681–1687.

Lee, C. K., Liu, X., and Fan, S. C. (2003). Local multiquadric approximation for solving boundary value problems. *Computational Mechanics*, 30: 396–409.

Lee, J.-Y. and Greengard, L. (2005). The type 3 nonuniform FFT and its applications. *Journal of Computational Physics*, 206: 1–5.

Leitao, V. M. A., Alves, C. J. S., and Duarte, C. A. (editors) (2007). *Advances in Meshfree Techniques*. Computational Methods in Applied Sciences. Springer Netherlands, Dordrecht, Netherlands.

Lewis, R. W., Morgan, K., Thomas, H. R., and Seetharamu, K. N. (1996). *The Finite Element Method in Heat Transfer Analysis*. Wiley, Chichester, New York, USA.

Li, H. and Mulay, S. S. (2013). *Meshless Methods and Their Numerical Properties*. CRC Press, Boca Raton, Florida, USA.

Li, S. and Liu, W. K. (2004). *Meshfree Particle Methods*. Springer-Verlag, Berlin, Germany.

Li, Y. and Kim, J. (2012). Phase-field simulations of crystal growth with adaptive mesh refinement. *International Journal of Heat and Mass Transfer*, 55: 7926–7932.

Lipton, J., Glicksman, M. E., and Kurz, W. (1984). Dendritic growth into undercooled alloy metals. *Materials Science and Engineering*, 65: 57–63.

Lipton, J., Glicksman, M. E., and Kurz, W. (1987). Equiaxed dendrite growth in alloys at small supercooling. *Metallurgical Transactions A*, 18: 341–345.

Liszka, T. and Orkisz, J. (1980). The finite difference method at arbitrary irregular grids and its application in applied mechanics. *Computers & Structures*, 11: 83–95.

Liu, G. R. (2009). *Meshfree Methods: Moving Beyond the Finite Element Method, Second Edition*. CRC Press, Boca Raton, Florida, USA.

Liu, G. R. and Gu, Y. T. (2001a). A local radial point interpolation method (LRPIM) for free vibration analyses of 2-D solids. *Journal of Sound and Vibration*, 246: 29–46.

Liu, G. R. and Gu, Y. T. (2001b). A point interpolation method for two-dimensional solids. *International Journal for Numerical Methods in Engineering*, 50: 937–951.

Liu, G. R. and Gu, Y. T. (2003). A meshfree method: meshfree weak–strong (MWS) form method, for 2-D solids. *Computational Mechanics*, 33: 2–14.

Liu, G. R. and Gu, Y. T. (2005). *An Introduction to Meshfree Methods and Their Programming*. Springer Netherlands, Dordrecht, Netherlands.

Liu, G.-R. and Liu, M. B. (2003). *Smoothed Particle Hydrodynamics: A Meshfree Particle Method*. World Scientific, Singapore.

Liu, Q. G. and Šarler, B. (2018). Non-singular method of fundamental solutions for elasticity problems in three-dimensions. *Engineering Analysis with Boundary Elements*, 96: 23–35.

Liu, W. K., Jun, S., and Zhang, Y. F. (1995). Reproducing kernel particle methods. *International Journal for Numerical Methods in Fluids*, 20: 1081–1106.

Liu, X., Liu, G. R., Tai, K., and Lam, K. Y. (2002). Radial basis point interpolation collocation method for 2-D solid problem. *Advances in Meshfree and X-FEM Methods*, pp. 35–40. World Scientific, Singapore.

Lorbiecka, A. Z. and Šarler, B. (2010). Simulation of dendritic growth with different orientation by using the point automata method. *CMC: Computers, Materials & Continua*, 18: 69–104.

Lu, X., Li, C., Tie, Y., Hou, Y., and Zhang, C. (2019). Crack propagation simulation in brittle elastic materials by a phase field method. *Theoretical and Applied Mechanics Letters*, 9: 339–352.

Mathew, T. (2008). *Domain Decomposition Methods for the Numerical Solution of Partial Differential Equations*. Lecture Notes in Computational Science and Engineering. Springer-Verlag, Heidelberg, Germany.

Mavrič, B. (2017). *Meshless Modeling of Thermo-Mechanics of Low-Frequency Electromagnetic Direct Chill Casting*. Ph.D. thesis, University of Nova Gorica, Nova Gorica, Slovenia.

Mavrič, B. and Šarler, B. (2015). Local radial basis function collocation method for linear thermoelasticity in two dimensions. *International Journal of Numerical Methods for Heat & Fluid Flow*, 25: 1488–1510.

Mavrič, B. and Šarler, B. (2017). Application of the RBF collocation method to transient coupled thermoelasticity. *International Journal of Numerical Methods for Heat & Fluid Flow*, 27: 1064–1077.

Moshkelgosha, E. and Mamivand, M. (2020). Phase field modeling of crack propagation in shape memory ceramics – Application to zirconia. *Computational Materials Science*, 174: 109509.

Mramor, K., Vertnik, R., and Šarler, B. (2014). Simulation of laminar backward facing step flow under magnetic field with explicit local radial basis function collocation method. *Engineering Analysis with Boundary Elements*, 49: 37–47.

Mukherjee, Y. X. and Mukherjee, S. (1997). The boundary node method for potential problems. *International Journal for Numerical Methods in Engineering*, 40: 797–815.

Mullins, W. W. and Sekerka, R. F. (1963). Morphological stability of a particle growing by diffusion or heat flow. *Journal of Applied Physics*, 34: 323–329.

Mullins, W. W. and Sekerka, R. F. (1964). Stability of a planar interface during solidification of a dilute binary alloy. *Journal of Applied Physics*, 35: 444–451.

Mullis, A. M. (2006). Quantification of mesh induced anisotropy effects in the phase-field method. *Computational Materials Science*, 36: 345–353.

Nash, G. E. and Glicksman, M. E. (1974). Capillarity-limited steady-state dendritic growth—I. Theoretical development. *Acta Metallurgica*, 22: 1283–1290.

Nestler, B. and Choudhury, A. (2011). Phase-field modeling of multicomponent systems. *Current Opinion in Solid State and Materials Science*, 15: 93–105.

Nestler, B., Garcke, H., and Stinner, B. (2005). Multicomponent alloy solidification: Phase-field modeling and simulations. *Physical Review E*, 71: 041609.

Nguyen, V. P., Rabczuk, T., Bordas, S., and Duflot, M. (2008). Meshless methods: A review and computer implementation aspects. *Mathematics and Computers in Simulation*, 79: 763–813.

Oñate, E., Idelsohn, S., Zienkiewicz, O. C., and Taylor, R. L. (1996). A finite point method in computational mechanics. applications to convective transport and fluid flow. *International Journal for Numerical Methods in Engineering*, 39: 3839–3866.

Ofori-Opoku, N. and Provatas, N. (2010). A quantitative multi-phase field model of polycrystalline alloy solidification. *Acta Materialia*, 58: 2155–2164.

Ohno, M. (2012). Quantitative phase-field modeling of nonisothermal solidification in dilute multicomponent alloys with arbitrary diffusivities. *Physical Review E*, 86: 051603.

Oldfield, W. (1973). Computer model studies of dendritic growth. *Materials Science and Engineering*, 11: 211–218.

Perrone, N. and Kao, R. (1975). A general finite difference method for arbitrary meshes. *Computers & Structures*, 5: 45–57.

Perumal, R., Selzer, M., and Nestler, B. (2019). Concurrent grain growth and coarsening of two-phase microstructures; large scale phase-field study. *Computational Materials Science*, 159: 160–176.

Plapp, M. and Karma, A. (2000). Multiscale random-walk algorithm for simulating interfacial pattern formation. *Physical Review Letters*, 84: 1740–1743.

Provatas, N. and Elder, K. (2010). *Phase-Field Methods in Materials Science and Engineering*. Wiley-VCH, Weinheim, Germany.

Provatas, N., Goldenfeld, N., and Dantzig, J. (1998). Efficient computation of dendritic microstructures using adaptive mesh refinement. *Physical Review Letters*, 80: 3308–3311.

Provatas, N., Goldenfeld, N., and Dantzig, J. (1999). Adaptive mesh refinement computation of solidification microstructures using dynamic data structures. *Journal of Computational Physics*, 148: 265–290.

Reuther, K. and Rettenmayr, M. (2014). Simulating dendritic solidification using an anisotropy-free meshless front-tracking method. *Journal of Computational Physics*, 279: 63–66.

Reuther, K., Sarler, B., and Rettenmayr, M. (2012). Solving diffusion problems on an unstructured, amorphous grid by a meshless method. *International Journal of Thermal Sciences*, 51: 16–22.

Rippa, S. (1999). An algorithm for selecting a good value for the parameter c in radial basis function interpolation. *Advances in Computational Mathematics*, 11: 193–210.

Rowlinson, J. S. (1979). Translation of J. D. van der Waals' "The thermodynamik theory of capillarity under the hypothesis of a continuous variation of density". *Journal of Statistical Physics*, 20: 197–200.

Ruan, Y., Mohajerani, A., and Dao, M. (2016). Microstructural and mechanical-property manipulation through rapid dendrite growth and undercooling in an Fe-based multinary alloy. *Scientific Reports*, 6: 1–11.

Sadat, H. and Prax, C. (1996). Application of the diffuse approximation for solving fluid flow and heat transfer problems. *International Journal of Heat and Mass Transfer*, 39: 214–218.

Saito, Y., Goldbeck-Wood, G., and Müller-Krumbhaar, H. (1988). Numerical simulation of dendritic growth. *Physical Review A*, 38: 2148–2157.

Samet, H. (1989). Neighbor finding in images represented by octrees. *Computer Vision, Graphics, and Image Processing*, 46: 367–386.

Shimokawabe, T., Aoki, T., Takaki, T., Endo, T., Yamanaka, A., Maruyama, N., Nukada, A., and Matsuoka, S. (2011). Peta-scale phase-field simulation for dendritic solidification on the TSUBAME 2.0 supercomputer. *Proceedings of 2011 International Conference for High Performance Computing, Networking, Storage and Analysis*, SC '11, pp. 3:1–3:11. ACM, New York, NY, USA.

Sladek, J. and Sladek, V. (editors) (2006). *Advances in Meshless Methods*. Tech Science Press, Hendersen, Nevada, USA.

Sun, W., Yan, R., Zhang, Y., Dong, H., and Jing, T. (2019). GPU-accelerated three-dimensional large-scale simulation of dendrite growth for Ti6Al4V alloy based on multi-component phase-field model. *Computational Materials Science*, 160: 149–158.

Šarler, B. (1995). Stefan's work on solid-liquid phase changes. *Engineering Analysis with Boundary Elements*, 16: 83–92.

Šarler, B. and Atluri, S. N. (editors) (2010). *Recent Studies in Meshless & Other Novel Computational Methods*. Tech Science Press, Duluth, Minessota, USA.

Šarler, B., Dobravec, T., Glavan, G., Hatić, V., Mavrič, B., Vertnik, R., Cvahte, P., Gregor, F., Jelen, M., and Petrovič, M. (2019). Multi-physics and multi-scale meshless simulation system for direct-chill casting of aluminium alloys. *Strojniški vestnik – Journal of Mechanical Engineering*, 65: 658–670.

Šarler, B. and Vertnik, R. (2006). Meshfree explicit local radial basis function collocation method for diffusion problems. *Computers & Mathematics with Applications*, 51: 1269–1282.

Širca, S. and Horvat, M. (2018). *Computational Methods in Physics: Compendium for Students*. Springer International Publishing, NYC, USA.

Talat, N., Mavrič, B., Belšak, G., Hatić, V., Bajt, S., and Šarler, B. (2018a). Development of meshless phase field method for two-phase flow. *International Journal of Multiphase Flow*, 108: 169–180.

Talat, N., Mavrič, B., Hatić, V., Bajt, S., and Šarler, B. (2018b). Phase field simulation of Rayleigh–Taylor instability with a meshless method. *Engineering Analysis with Boundary Elements*, 87: 78–89.

Temkin, D. E. (1960). Growth velocity of a needle crystal in a supercooled melt. *Doklady Akademii Nauk*, 132: 1307–1310.

Tolstykh, A. I. and Shirobokov, D. A. (2003). On using radial basis functions in a "finite difference mode" with applications to elasticity problems. *Computational Mechanics*, 33: 68–79.

Tourret, D. and Karma, A. (2015). Growth competition of columnar dendritic grains: A phase-field study. *Acta Materialia*, 82: 64–83.

Tourret, D., Song, Y., Clarke, A. J., and Karma, A. (2017). Grain growth competition during thin-sample directional solidification of dendritic microstructures: A phase-field study. *Acta Materialia*, 122: 220–235.

Trefethen, L. N. (1996). *Finite Difference and Spectral Methods for Ordinary and Partial Differential Equations*. Cornell University, Ithaca, New York, USA.

Versteeg, H. and Malalasekera, W. (2007). *An Introduction to Computational Fluid Dynamics: The Finite Volume Method*. Pearson, Harlow, England, UK.

Vertnik, R. and Šarler, B. (2011). Local collocation approach for solving turbulent combined forced and natural convection problems. *Advances in Applied Mathematics and Mechanics*, 3: 259–279.

Vertnik, R., Mramor, K., and Šarler, B. (2019). Solution of three-dimensional temperature and turbulent velocity field in continuously cast steel billets with electromagnetic stirring by a meshless method. *Engineering Analysis with Boundary Elements*, 104: 347–363.

Wang, K., Wen, S., Zahoor, R., Li, M., and Šarler, B. (2016). Method of regularized sources for axisymmetric Stokes flow problems. *International Journal of Numerical Methods for Heat & Fluid Flow*, 26: 1226–1239.

Wendland, H. (2010). *Scattered Data Approximation*. Cambridge University Press, Cambridge, UK.

Wrobel, L. C. and Aliabadi, M. H. (2002). *The Boundary Element Method, Applications in Thermo-Fluids and Acoustics*. Wiley, Hoboken, New Jersey, USA.

Yamanaka, A., Aoki, T., Ogawa, S., and Takaki, T. (2011). GPU-accelerated phase-field simulation of dendritic solidification in a binary alloy. *Journal of Crystal Growth*, 318: 40–45.

Zhu, J., Zhang, T., Yang, Y., and Liu, C. T. (2019). Phase field study of the copper precipitation in Fe-Cu alloy. *Acta Materialia*, 166: 560–571.

Zhu, T., Zhang, J., and Atluri, S. N. (1998). A meshless local boundary integral equation (LBIE) method for solving nonlinear problems. *Computational Mechanics*, 22: 174–186.